

**Mechanism of Solidification Cracking during Welding
of High Strength Steels for Subsea Linepipe**

Thesis submitted for the degree of

Doctor of Philosophy

at the University of Leicester

by

Lee Alan Aucott

Department of Engineering

University of Leicester

2015

Publications

- [1] The role of Ti carbonitride precipitates on strength-toughness of submerged arc welded pipeline joints

Lee Aucott, Shuwen Wen, Hongbiao Dong

Materials Science and Engineering: A, Volume 622, 12 January 2015, Pages 194–203

DOI: 10.1016/j.msea.2014.10.057

Details of contribution: I wrote the paper and carried out all experimental work, apart from TEM sample preparation and image collation. Dr Hiroto Kitaguchi of the University of Oxford prepared TEM samples and images for the paper.

- [2] On the relationship of microstructure, toughness, and hardness properties in a submerged arc welded API-5L grade X65 pipeline steel section

Lee Aucott, Shuwen Wen, Hongbiao Dong

Proceedings of the ASME 2014 33rd International Conference on Ocean, Offshore and Arctic Engineering, OMAE2014. June 8-13, 2014, San Francisco, California, USA

DOI: 10.1115/OMAE2014-23858

Details of contribution: I carried out all experimental work, wrote the paper and gave conference presentation.

- [3] Multiscale, Multiphysics, Numerical Modelling of Fusion Welding with Experimental Characterization and Validation

Mingming Tong, Gregory Duggan, Jun Liu, Yu Xie, Mike Dodge, Lee Aucott, Hongbiao Dong, Ruslan L. Davidchack, Jon Dantzig, et al.

JOM (2013) 65:99-106

DOI 10.1007/s11837-012-0499-6, ISSN 1047-4838

Details of contribution: I co-authored section “Experimental Characterization of Hot Cracking and Melt Flow”.

- [4] Testing of solidification cracking susceptibility of MAG welded overlays on S355JR steel using the Transvarestraint test

Lee Aucott, Tomasz Pfieler, Aleksander Zak

Institute of Welding Bulletin (2013), Volume 57, Number 3, Pages: 5-11

ISSN 2300-1674

Details of contribution: I carried out all experimental work and wrote the paper.

- [5] Assessment of the Resistance to Weld Solidification Cracking of X65 Pipeline Steel Using a Transvarestraint Test

Lee Aucott, Shuwen Wen, Andrew Sullivan, Hongbiao Dong

4th International Integrity of High Temperature Welds Conference

IOM3, London, UK. 25th – 27th September 2012

Details of contribution: I carried out all experimental work, wrote the paper and gave conference presentation.

Lee Aucott

Mechanism of Solidification Cracking during Welding of High Strength Steels for Subsea Linepipe

Abstract

Weld solidification cracking is an important issue in fusion welding. If undetected, the cracking defects can act as stress concentration sites which lead to premature failure via fatigue, as well as offer favourable sites for hydrogen assisted cracking and stress corrosion cracking. For welded steel products such as deep sea oil and gas transportation pipes, such defects heighten the risk of catastrophic in-service failures. Such failures can lead to devastating environmental, economic, and social damage.

In this thesis, a comprehensive review of literature associated with steel linepipe and solidification cracking defects is first presented. Fluid flow prior to solidification is then observed and quantified *in situ* using a novel synchrotron X-ray radiography approach. The flow is dynamic at velocities up to 0.52 m/s and primarily driven via Marangoni flow.

The relationship between the microstructure and mechanical properties of the welded linepipe are extensively characterised, with a new equation derived to assess fracture toughness based on the size and distribution of carbonitride precipitates. Weld residual stresses are measured both before and after linepipe expansion in the U-forming, O-forming and expansion process for the first time using a neutron diffraction technique.

To further understand the fundamental mechanisms of solidification cracking during welding of high strength steels for subsea linepipe, a novel small-scale Varestriant test rig was developed for use in synchrotron X-ray imaging experiments and a Transvarestriant test rig utilised for industrial scale weldability tests. Solidification cracking during the welding of steel is observed *in situ* for the first time using a micro-radiography approach and the 3D crack network is rebuilt using a micro-tomography technique. It is proposed that solidification cracks nucleate from sub-surface cavities associated with: i) residual liquid high in solute and impurity concentration (hot cracks), ii) Ti (C,N) precipitated during solidification (that induce ductile microvoids). Solidification cracks then propagate via inter-dendritic hot tearing.

Acknowledgements

I would like to express my great appreciation to Professor Hongbiao Dong for his supervision, support, and extensive knowledge throughout my time at University.

My thanks are extended to those at Tata Steel, particularly Shuwen Wen and John Marsden, whose scientific and technical expertise comes second only to their hospitality and patience. Similarly, I would like to thank Mick Bugdol and Zulfiqar Husain for aiding and training me in the skills necessary to undertake my studies.

I would like to thank those within the Mechanics of Materials group at The University of Leicester. Graham Clarke is also thanked for his time and patience in training me on the fundamentals of the laboratory equipment.

I would like to thank beam scientists at ISIS ENGIN-X, Rutherford Appleton Laboratory (Shu Yan Zhang, Joe Kelleher and Saurabh Kabra), Diamond Light Source I12 (Robert Atwood) and the European Synchrotron Radiation Facility ID19 (Alexander Rack) for their hospitality and expertise, often during the course of extremely long and strenuous days. Their patience and knowledge are truly amazing.

Special thanks also go to my friends and fellow research students: Mike Dodge, Tristram Broadbent, Adam Brown, Scott Simmonds, Mykhailo Melnykov, Manish Javahar, and Xingzhong Liang. Thanks for making my time in Leicester such an enjoyable period - I will undoubtedly look back on the last few years with fond memories.

MintWeld partners, Ding Huang and Alan Cocks of The University of Oxford, are thanked for their contributions.

Financially, this work was funded by Tata Steel, the Engineering and Physical Sciences Research Council (EPSRC) and MintWeld, a European Commission Seventh Framework Programme (FP7) sponsored project (contract No: NMP3-SL-2009-229108). I feel privileged to have had the opportunity to work on this project, thanks.

To you all, I am very grateful!

Contents

i. List of figures	12
ii. List of tables.....	23
iii. Nomenclature.....	25
1. Introduction.....	28
1.1. Seam welded linepipe for subsea pipeline application	28
1.2. Subsea linepipe manufacturing process	31
1.3. The weldability of steel and solidification cracking defects.....	35
1.3.1. Types of weld cracking defect	35
1.4. Terminology to be used in the thesis	37
1.5. Objectives of the research.....	39
1.6. Scope of the thesis	41
2. Literature survey on processing, microstructures and residual stresses in welded linepipe.....	42
2.1. HSLA steel for welded subsea oil and gas linepipe.....	42
2.1.1. Processing high strength steel for subsea linepipe.....	43
2.1.2. Microstructures within HSLA steel for subsea linepipe.....	49
2.2. Welding of subsea oil and gas transportation linepipes.....	53
2.2.1. The submerged arc welding process	53
2.2.2. Heat flow during welding	55
2.2.3. Fluid flow during welding	58
2.2.4. Solidification structure in the submerged arc weld joint	64

2.2.5.	Microstructure development in the submerged arc weld joint	66
2.2.6.	Strength and toughness of the submerged arc welded joint.....	69
2.2.7.	Phase transformations and grain growth in the heat affected zone.....	74
2.2.8.	Weld residual stresses	78
3.	Literature survey on solidification cracking during welding	88
3.1.	Introduction.....	88
3.1.1.	The solidification stages when cracking can occur	88
3.1.2.	The Trans(Varestraint) weldability test	90
3.2.	Solidification cracking theories and criterion.....	92
3.3.	Metallurgical factors which affect solidification cracking in welds.....	98
3.3.1.	Solidification temperature range.....	98
3.3.1.	Solubility of solute elements in the primary solidification phase.....	100
3.3.2.	Ductility of the solidifying weld metal	101
3.3.2.1.	Ductility curve (brittle temperature range)	101
3.3.2.2.	Solidification cracking temperature range	103
3.3.3.	Surface tension of grain boundary liquid.....	105
3.3.4.	Solidification grain structure	106
3.4.	Application of synchrotron X-ray in solidification cracking research	107
3.4.1.	Introduction to synchrotron X-ray imaging	108
3.4.2.	A review of synchrotron X-ray used in solidification cracking research	110

4. Evolution of weld pool and fluid flow	115
4.1. Introduction.....	115
4.2. Materials and experimental methods	116
4.2.1. Materials and welding process.....	116
4.2.2. Synchrotron based micro-radiography.....	117
4.2.3. Image processing and flow analysis	118
4.2.4. Selection of 2D flow patterns in the 3D volume	119
4.3. Results.....	120
4.3.1. Weld evolution and fluid flow in low S content steel.....	120
4.3.2. Weld evolution and fluid flow in high S content steel	122
4.3.3. Metallographic examination of the solidified weld geometries.....	124
4.4. Discussion.....	126
4.5. Chapter summary.....	130
5. Microstructure and mechanical properties of linepipe SAW seam weld	131
5.1. Introduction.....	131
5.2. Materials	133
5.3. Microstructural and mechanical properties characterisation	135
5.3.1. Experimental methods	135
5.3.1.1. Optical microscopy	135
5.3.1.2. Scanning electron microscopy	135
5.3.1.3. Transmission electron microscopy.....	137
5.3.1.4. Vickers hardness	137
5.3.1.5. Charpy impact toughness	138
5.3.1.6. K_{Ic} fracture toughness	139
5.3.2. Weld geometry and chemical analysis.....	141

5.3.3.	Microstructure analysis.....	143
5.3.3.1.	Base metal	143
5.3.3.2.	Heat affected zone.....	145
5.3.3.3.	Fusion zone	147
5.3.4.	Mechanical properties of the welded joint.....	150
5.3.5.	Fractography analysis of toughness samples	152
5.3.5.1.	Base metal	152
5.3.5.2.	Heat affected zone.....	153
5.3.5.3.	Fusion zone	153
5.3.6.	Discussion.....	157
5.4.	The role of Ti carbonitride precipitates on strength-toughness	162
5.4.1.	Identification and distribution of precipitates	162
5.4.2.	Effect of size and volume fraction of precipitates on strength	164
5.4.3.	Effect of the size/spacing of precipitates on fracture toughness.....	166
5.5.	Residual stress in UOE linepipe seam weld	172
5.5.1.	Neutron diffraction experiment	172
5.5.1.1.	Sample preparation.....	172
5.5.1.2.	Measurement plan	174
5.5.1.3.	ENGIN-X virtual laboratory	175
5.5.1.4.	Sample orientations for strain measurements	177
5.5.1.5.	Experiment execution and data analysis	178
5.5.2.	Results.....	179
5.5.2.1.	Raw data – TOF diffraction spectrums	179
5.5.2.2.	Calculated weld residual stresses	180
5.5.3.	Discussion.....	187
5.6.	Chapter summary	189

6.	X-ray imaging of solidification cracking during welding of steel.....	192
6.1.	Introduction.....	192
6.2.	Materials and thermodynamic property characterisation methods	193
6.2.1.	Materials	193
6.2.2.	Methods of thermodynamic property characterisation	193
6.2.2.1.	Thermo-Calc computational thermodynamics	193
6.2.2.2.	Gleeble hot ductility tests.....	194
6.3.	Equipment and experimental methods for X-ray imaging.....	196
6.3.1.	Design and manufacture of test apparatus	196
6.3.1.1.	Design considerations	197
6.3.1.2.	3D Solidworks model.....	199
6.3.1.3.	2D engineering drawings	200
6.3.2.	Procedure for the <i>in situ</i> imaging of weld solidification cracking.....	201
6.3.2.1.	Varestraint weldability test	201
6.3.2.2.	Synchrotron based micro-radiography	205
6.3.3.	Procedure for ex-situ synchrotron X-ray micro-tomography	206
6.4.	Results.....	207
6.4.1.	Visual analysis of welds and solidification cracking.....	207
6.4.2.	<i>In situ</i> radiography imaging of weld solidification cracking.....	210
6.4.3.	Temperature and phase when solidification cracking initiates.....	214
6.4.4.	Tomographic reconstruction of the crack network	218
6.4.5.	Microscopic examination of fracture surfaces.....	222
6.5.	Mechanisms proposed for solidification cracking during welding of low-alloy high-impurity steels	225
6.6.	Discussion.....	230

7. Industrial application	232
7.1. Introduction.....	232
7.2. Materials	232
7.3. Industrial scale Transvarestraint weldability test.....	233
7.3.1. Test rig setup.....	233
7.3.2. Transvarestraint weldability test procedure	234
7.4. Results.....	235
7.4.1. Material solidification characteristics	235
7.4.2. Quantification of weld geometry and solidification cracking	236
7.4.3. Identification of solidification crack initiation sites	238
7.4.4. Identification of solidification crack propagation mechanism	240
7.5. Mechanisms proposed for solidification cracking during welding of HSLA subsea linepipe steel.....	241
7.6. Discussion.....	252
8. Conclusions and recommendations	255
8.1. Conclusions.....	255
8.2. Recommendations for further work	259
Appendix	260
Appendix A – Evaluation of measurement errors in Chapter 4.	261
Appendix B – Evaluation of measurement errors in Chapter 5.	266
Appendix C – Evaluation of measurement errors in Chapter 6.	267
References.....	269

i. List of figures

Figure 1-1: A typical subsea oil and gas retrieval and transportation network (image taken from Genesis Oil and Gas company webpage).	29
Figure 1-2: Temperature dependant manufacturing lifecycle of a typical steel linepipe.	31
Figure 1-3: Schematic illustration of the manufacturing steps at Tata Steel’s DSAW UOE linepipe mill in Corby. Plate edges are prepared and crimped before being U-formed, then O-formed. Next, the seam is tack welded; SAW welded on the inner diameter, and then SAW welded on the outer diameter. After welding, stringent NDT is carried out to check for weld defects. If no defects are detected, the linepipe is then mechanically expanded to the nominal outer diameter, submitted for final inspection and prepared for shipping [9].....	33
Figure 1-4: Macro image of the different zones in a double submerged arc welded joint, the base metal, heat affected zone (which is sub-categorised as the fine grained heat affected zone (FG-HAZ) and the coarse grained heat affected zone (CG-HAZ)) and fusion zone.	34
Figure 1-5: Schematic illustration of typical weld “hot” cracking defects and the regions in which they typically develop [11].	36
Figure 1-6: Centreline weld solidification cracks, a) buried sub-surface [12], b) surface penetrating [13].....	36
Figure 1-7: Schematic illustration of the structure and mechanical properties at various stages of the solidification sequence [35].	38
Figure 2-1: Strengthening mechanisms in modern HSLA steel for linepipe application [1].....	45
Figure 2-2: Schematic illustration of a typical TMCR process with various accelerated cooling schedules [62].	46
Figure 2-3: Role of Nb based precipitates at each stage of the TMCR process showing their effects on the refinement of ferrite grains and precipitation hardening [62].....	48
Figure 2-4: Schematic of the various accelerated cooling regimes used by [70].	51

Figure 2-5: Schematic illustration of the submerged arc welding process showing, a) overview of system components, b) detailed view of the welding process and interaction with the base metal (Adapted from [13]).	54
Figure 2-6: Schematic illustration showing the welding of a stationary workpiece. The co-ordinate system (x, y, z) moves with the heat source [81].	55
Figure 2-7: Schematic illustration of two-dimensional heat flow during welding of thin sample [13].	56
Figure 2-8: Schematic illustration of three-dimensional heat flow during welding of thick sample [13].	57
Figure 2-9: Effect of weld bead shape on state of stress at centre of outer surface (Adapted from [88]).	58
Figure 2-10: Schematic illustration of the various driving forces that stimulate fluid flow within a molten weld pool.	59
Figure 2-11: YAG laser welds in two stainless steels with a) 40 ppm S and b) 140 ppm S [13].	61
Figure 2-12: Heiple's model for Marangoni convection in a weld pool (a,b,c) low S steel, (d,e,f) high S steel [13].	62
Figure 2-13: Marangoni convection with an outward surface flow in a NaNO_3 pool, showing a) a schematic representation of tension-temperature peaks, and b) experimental observations in NaNO_3 pool [103].	63
Figure 2-14: Illustration of common solidification modes, a) factors controlling the growth mode during the solidification of liquid metals, b) planar solidification of C tetrabromide, c) cellular solidification of C tetrabromide with a small amount of impurity, d) columnar dendritic solidification of C tetrabromide with several percent of impurity, e) equiaxed dendritic solidification of cyclohexanol with impurity [107].	64
Figure 2-15: CCT diagram for low C steel weld metal (Adapted from [112]).	66
Figure 2-16: A schematic diagram of the sub-zones of the heat affected zone explained in terms of the Fe-C equilibrium phase diagram for a 0.15 wt.% C alloy [79].	74
Figure 2-17: Two β precipitates of radius r_1 and r_2 dispersed in an α matrix. The radii r_1 and r_2 are less than and greater than the average particle radius [155].	76
Figure 2-18: Schematic illustration of grain boundary diffusion [155].	77
Figure 2-19: Methods of residual stress measurement [158].	80

Figure 2-20: Penetration and the spatial resolution of the various techniques. The destructive and semi destructive methods are coloured grey [158].	80
Figure 2-21: Plan of the ISIS facility (spallation source and instruments) [174].	82
Figure 2-22: Schematic diagram of a time-of-flight neutron strain scanner. The elastic strain is measured along the directions of the impulse exchange vector, q_1 and q_2 . The volume of the sample explored by the instrument corresponds to the intersection of incident and diffracted beams, as defined by slits and collimators [176].	83
Figure 2-23: Typical TOF diffraction spectrum on ENGIN-X, in this case for a stainless-steel specimen. The elastic strain is calculated from the shift in the peak positions defined through a least-squares refinement. The macroscopic strain is obtained from the change in lattice parameter given by a full-pattern refinement [176].	84
Figure 2-24: Schematic illustration of strain components in a linepipe.	85
Figure 3-1: Schematic illustration of the (Trans)Varestraint test, showing a) Varestraint and b) Transvarestraint tests.	91
Figure 3-2: Summary of mechanisms, conditions and causes of solidification cracking proposed to date.	93
Figure 3-3: Effect of alloying elements on the solidification temperature range of carbon and low alloy steels [219].	99
Figure 3-4: Effect of impurities on grain boundary liquid during weld solidification [13].	99
Figure 3-5: Ductility of solidifying weld metal (Adapted from [13]).	101
Figure 3-6: MCD vs applied strain ~ Transvarestraint test [205].	103
Figure 3-7: Method for determining the SCTR using the cooling rate through the solidification temperature range and MCD at saturated strain [205].	104
Figure 3-8: Effect of liquid grain boundary morphology on crack susceptibility (Adapted from [13]).	105
Figure 3-9: Schematic illustration of the key components within Diamond Light Source synchrotron.	108
Figure 3-10: Schematic showing the key microstructural features active during semi-solid tensile deformation: (a) strain localization and flow of liquid towards this location and (b) semi-solid necking in combination with damage nucleation and growth; formation of micro-necks and final fracture [240].	111

Figure 4-1: Illustration of experimental setup within Diamond Light Source's I12. ...	116
Figure 4-2: Identification of image components and resolution using a) schematic diagram and b) radiograph from imaging.	118
Figure 4-3: Illustration of methodology for selecting in-plane 2D flow patterns for analysis within the 3D flow volume.	119
Figure 4-4: Time dependent evolution of the molten weld pool in the low S steel, showing minimum intensity z-stacks of raw data (Figs. a,b,c) and the corresponding geometry measured (Figs. d,e,f) at 3 time intervals.....	121
Figure 4-5: Fluid flow observed in low S steel at $t = \sim 1$ s, showing shallow outward and upward re-circulation zones. Specifically, a) the outward and upward flow after 0.05 s tracking, b) the repeated recirculation zone 0.08 s tracking, c) a schematic illustration of the flow coupled with the results of velocity quantification.....	121
Figure 4-6: Fluid flow observed in low S steel at $t = \sim 2$ s, showing shallow outward and upward re-circulation zones. Specifically, a) the outward and upward flow after 0.04s tracking, b) the repeated recirculation zone 0.08 s tracking, c) a schematic illustration of the flow coupled with the results of velocity quantification.....	121
Figure 4-7: Time dependent evolution of the molten weld pool in the high S steel, showing minimum intensity z-stacks of raw data (Figs. a,b,c) and the corresponding geometry measured (Figs. d,e,f) at 3 time intervals.....	123
Figure 4-8: Fluid flow observed in high S steel at $t = \sim 2$ s, showing deep inward and downward re-circulation zones. Specifically, a) the inward and downward flow after 0.07 s tracking, b) the repeated recirculation zone 0.11 s tracking, c) a schematic illustration of the flow coupled with the results of velocity quantification.	123
Figure 4-9: Cross sectional macrographs of welded samples after full 3 s of welding showing; a) shallow and wide weld geometry of low S steel and corresponding outward flow pattern, b) deep and wide weld geometry of high S steel and corresponding inward flow pattern.	124
Figure 4-10: Schematic illustration of surface tension-temperature behaviour for iron; curve A defines a high purity Fe, curve B defines an Fe alloy containing S, curve C defines an Fe alloys containing oxygen [92]	127
Figure 5-1: Schematic illustration of the location and orientation of Charpy V-notch samples taken from the X65 linepipe.	139

Figure 5-2: Transverse weld macrograph highlighting the various weld region: fusion zone, fine grain heat affected zone (FG-HAZ), coarse grain heat affected zone (CG-HAZ), base metal, and location of Vickers hardness indentations.	141
Figure 5-3: Primary ferrite (F) and second phase degenerate pearlite (DP) microstructure observed in the API 5L grade X65 base metal under a) optical microscope, b) SEM.	144
Figure 5-4: a) SEM image of large cuboidal Ti (C, N) precipitate and Al ₂ O ₃ inclusion, b) Direction of EDX line mapping, c) Qualitative EDX line mapping results.	145
Figure 5-5: CG-HAZ observed under a) optical microscope, showing the grain growth region in the immediate vicinity to the fusion line, b) SEM, illustrating the upper bainite (UB), polygonal ferrite (PF), and degenerate pearlite (DP) microstructure	146
Figure 5-6: Predominantly acicular ferrite (AF) microstructure found in the fusion zone, observed under a) optical microscope, showing AF, and grain boundary ferrite (GBF) phases SEM, b) showing AF and polygonal ferrite (PF) phases, and c) SEM, showing small AF plates which have nucleated heterogeneously and grown from a non-metallic inclusion.	148
Figure 5-7: TEM bright field image of a coarse particle in the weld fusion zone (a) and two SADPs (b) and (c). The circles in the figures correspond to the area chosen in (a) for the acquisition of the diffraction patterns in (b) and (c). The rectangle box in (a) will be explained in Figure 5-8.	149
Figure 5-8: EDX mapping results for Al (red) and Ti (green) of the same precipitate in Figure 5-7. The region analysed by EDX mapping was indicated by the rectangle box in Figure 5-7. The positions of the SADP circles from Figure 5-7 are also shown.	149
Figure 5-9: a) Lightly-etched optical micrograph showing the distribution of coarse particles (dark circular phase) in the weld fusion zone, b) the distribution of particle size observed in Fig.5-9(a).	150
Figure 5-10: Vickers hardness and impact toughness measured by Charpy V-notch tests over a weld joint.	151
Figure 5-11: a) Macro image identifying delamination on the X65 base metal CVN fracture surface, b) SEM image detailing dimpled fracture surfaces close to the delamination origin.	152
Figure 5-12: Ductile dimple fracture surfaces observed in CVN samples tested at 0°C under SEM; a) base metal, b) HAZ, and c) fusion zone.	153

Figure 5-13: a) Macro image of fusion zone Charpy V-notch fracture surface, b) SEM image showing fully ductile fracture in centre of CVN sample, c) Direction of EDX line mapping across a chosen particle, d) SEM image showing large particles in the centre of microvoids, e) Qualitative EDX line mapping results along direction marked in c). 154

Figure 5-14: Fractography analysis of K_{Ic} fracture toughness specimens, showing; a) macrograph of specimen fracture surface, b) Secondary electron micrograph of area under examination showing fully ductile fracture, c) Very large (12 μm) second phase particle inherent to the centre of the large fracture void under investigation, d) some of the smaller and more frequently distributed second phase particles..... 155

Figure 5-15: Chemical analysis of second phase particles found within the ductile fracture micro voids of the K_{Ic} fracture toughness specimens defining, a) particle under investigation and direction of EDX line map, b) EDX spectra of particle showing Al and Ti enrichment, c) Qualitative line mapping analysis highlighting Al, Ti, Mn, and V enrichment. 156

Figure 5-16: Variation in precipitate strengthening contribution calculated from the Ashby-Orowan equation for a range of average precipitate sizes at varying volume fractions. 165

Figure 5-17: Schematic idealization of microscopic fracture criteria pertaining to critical stress-modified, critical strain controlled model for microvoid coalescence. Adapted from [137, 138, 271]...... 167

Figure 5-18: Predicted fracture initiation toughness in the fusion zone as a function of precipitate size, calculated from Eq. 5-12..... 170

Figure 5-19: Relationship between mean particle size and spacing at different volume fractions. 171

Figure 5-20: Schematic illustration of pipe section showing sub-ring to be removed to machine stress relieved D_0 samples. 173

Figure 5-21: Schematic illustration and geometry of the stress relieved D_0 samples... 173

Figure 5-22: Type 1 D_0 sample stress relieved with slots and etched to reveal weld... 174

Figure 5-23: Schematic illustration of measurement locations on pipe samples..... 174

Figure 5-24: The ENGIN-X virtual laboratory. Three-dimensional models of the laboratory and sample are used for planning of experiments, in this case to measure the axial and radial directions of the strain tensor of the pipe. The three-dimensional model

of the sample is produced by a co-ordinate measuring machine. The virtual model is then uploaded to SSCANSS to input measurement co-ordinates and scan times (Fig. b). Simulations are then ran to determine stage translation sequence (Fig. c) and path lengths (Fig. d).....	176
Figure 5-25: Orientation of pipe samples for axial and radial strain measurements. ...	177
Figure 5-26: TOF diffraction spectrum in radial direction of linepipe, showing clearly defined peaks relating to lattice planes	179
Figure 5-27: Residual stresses measured in the unexpanded and expanded 15.4 mm walled pipe. Measurements taken through thickness in the weld centre line.	181
Figure 5-28: Residual stresses measured in the unexpanded and expanded 15.4 mm walled pipe. Measurements taken through thickness in the heat affected zone.	182
Figure 5-29: Residual stresses measured in the unexpanded and expanded 15.4 mm walled pipe. Measurements taken horizontally away from the weld centre line, 3 mm in from the inner diameter.....	184
Figure 5-30: Residual stresses measured in the unexpanded and expanded 15.4 mm walled pipe. Measurements taken horizontally away from the weld centre line, 3 mm in from the outer diameter.....	185
Figure 5-31: Residual stresses measured in the unexpanded and expanded 15.4 mm walled pipe. Measurements taken horizontally away from the weld centre at mid-thickness.....	186
Figure 6-1: a) Schematic illustration of Varestraint weldability test rig, b) Varestraint test rig integrated to the ESRF's ID19 experimental hutch.	196
Figure 6-2: Schematic of angular displacement.	198
Figure 6-3: 3D Solidworks model of Varestraint test rig assembly.	199
Figure 6-4: 2D engineering drawings of, a) bending block sub-assembly, and b) bending block.....	200
Figure 6-5: Varestraint test rig integrated into the ESRF's ID19 experimental hutch. The broken red boxes highlight the location of sample and test rig, while the broken blue boxes highlight the detector location (7.2 m away from the sample).....	201
Figure 6-6: Experimental setup within ID19 showing the test apparatus both before testing (showing an un-deformed sample, with both the horizontal and vertical actuators retracted) and after testing (showing the sample deformed around the bending radius with both the vertical and horizontal actuators fully extended). The yellow arrow	

dictates the approximate path of the X-ray through the 8 mm thickness of the samples towards the detector.	202
Figure 6-7: Schematic illustration of the Vareststraint test for in situ synchrotron X-ray micro-radiography experiments.	204
Figure 6-8: a) Macro image of typical deformed sample, b) detailed view of the weld which exhibits good quality with induced solidification cracking defects.	207
Figure 6-9: The array of weld solidification cracking observed in EN1A, C, and S303 materials tested at 135, 115, and 95 mm/s bending speeds.	208
Figure 6-10: Total length of surface solidification cracking observed in the weld after Vareststraint testing at a range of bending speeds.	209
Figure 6-11: Results of synchrotron radiography analysis on the EN1A sample tested with a 135 mm bending speed, showing a) the initiation of weld solidification cracking at 0.134 s of bending with an approximate strain of 3.25 %, the broken blue line depicts the fusion boundary measured from post-test microscopic observations b) the end of solidification cracking at 0.832 s of bending and an approximate strain of 10.53 %, c) a magnified image of the weld solidification crack initiating trailing the welding electrode by 2.69 mm at 1.45 mm sub-surface, d) a magnified image of the full solidification cracking at the end of testing, showing propagation through the surface.	211
Figure 6-12: Sub-surface depth of solidification cracking nucleation site, plotted as a function of Vareststraint bending speed.	212
Figure 6-13: Strain that initiated solidification cracking plotted as a function of bending speed.	213
Figure 6-14: Strain range over which solidification cracking was observed to propagate plotted as a function of Vareststraint bending speed.	213
Figure 6-15: Schematic illustration of solidification stages relating to solidification cracking, adapted to include values calculated from the results of EN1A alloy Thermo-Calc simulations under equilibrium and non-equilibrium (Scheil) conditions.	214
Figure 6-16: Results of Gleeble hot ductility tests showing, a) Fracture samples and corresponding test temperatures. The lower temperature samples show clear elongation and ductile fracture. Based on visual observations, it appears the ZDT is between 1410-1430 °C and the ZST between 1430-1450 °C, b) Plot of stress and reduced area vs temperature from the Gleeble hot ductility tests on the EN1A alloy.	215

Figure 6-17: Results of thermocouple recordings within the molten weld pool during Vareststraint testing. $T_{cracking}$ has been extrapolated from the observations on crack initiation made in the in situ radiography sequence reported in Figure 6-11.217

Figure 6-18: 3D reconstruction of the solid EN1A sample tested at 135 mm/s bending speed with weld and solidification cracks visible on the surface of the reconstruction. An orthogonal co-ordinate system is defined in the image.218

Figure 6-19: a) Macro image of surface cracking visible to the eye, b) View of the air (solidification cracking network) inherent to the sample from the z-y plane. The broken blue line highlights the bulk of the solidification cracking. It essentially one crack that propagates the largest surface area on sample surface and is the point at which the cracks first initiate. The broken red line highlights the solidification cracks initiated at later times during testing. This region is made up of hundreds of isolated cracks, the majority of which are sub-surface219

Figure 6-20: Plan view on the z-x plane of the solidification cracks showing somewhat symmetric features in terms of the angle of cracking either side of weld centreline....220

Figure 6-21: Detailed observation of fracture initiation site. The yellow broken square highlights the fracture initiation site observed in the micro-radiography sequence and is viewed in more detail in Figure 6-22.....221

Figure 6-22: Cavitation ahead of the crack tip. Some of the cracks are isolated, some coalesce with each other, but not the bulk crack and some coalesce with each other and the bulk crack.....221

Figure 6-23: Observations made on the fracture surface of the Gleeble hot ductility sample tested at 1430 °C showing, a) macro image of the full fracture surface, b) SEM image of the as-solidified faceted ferritic grains in the centre of the Gleeble sample. The facets results from brittle inter-granular fracture, c) magnified SEM image of the porosity inherent to the faceted grains in the centre of the Gleeble sample, d) SEM image of the fracture surface typical to the outer fracture surface. The orange broken circles highlight two low melting point Type III MnS particles while the broken red circle highlights the presence of numerous globular particles enriched in solute elements (Si in particular) inherent to grain boundaries.....223

Figure 6-24: Dendritic fracture morphology observed on the bulk fracture surface at later stages of cracking showing clear inter-dendritic fracture associated with stage 2 hot tearing.224

Figure 6-25: 2D schematic of inter-granular hot crack initiation, formed upon low melting point eutectic segregates after the transition from the dendrite to the grain structure. Co-ordinate system used in bottom left of the figure is defined in Figure 6-26.225

Figure 6-26: 3D schematic of hot crack initiation in respect to weld pool. The red globules depict hot cracks initiated in the solidifying weld.....226

Figure 6-27: 2D schematic illustration of the hot crack coalescence mechanism. Sometimes the hot cracks remain isolated and sometimes they coalesce with each other but not the bulk crack. Eventually the coalescence of the hot cracks propagates through the grain structure to the solidifying dendritic structure.....227

Figure 6-28: 2D schematic of hot tears nucleated from hot cracks. Hot tears form from inter-granular hot cracks that coalesce and propagate into the solidifying dendrite structure.228

Figure 6-29:3D illustration of hot tearing propagation direction towards the heat source.229

Figure 7-1: Transvarestraint weldability test rig.....233

Figure 7-2: Schematic illustration of welding and bending points during Transvarestraint test.....234

Figure 7-3: Results of thermodynamic analysis displaying the mass-fraction of equilibrium phases during solidification of the experimental alloys.....235

Figure 7-4: Weld solidification cracking observed in: a) initial observations on the X65 weld bead; b) backscattered electron micrograph of metallographically prepared X65 specimen.236

Figure 7-5: Transverse weld macrographs of weld geometries in test alloys showing, the fusion zone (area enclosed by the white broken line) and HAZ (area enclosed by the red broken line) shape and size.....237

Figure 7-6: Fractography examination of solidification cracking in X65 steel, showing; a) macro image of full solidification crack interface (dark region encircled by broken white line), b) SEM image of fracture surface highlighted by the broken yellow square in Fig. a., c) SEM image of ductile microvoids at the base of the solidification crack around 1 mm sub-surface. The microvoids are located within the solidification cracking region and are surrounded by dendritic fracture morphologies, d) SEM image of microvoid detailed in Fig. c by broken yellow arrow, showing the presence of a void

initiating second phase particle. The fracture surface in and around the microvoid appears to be smooth highlighting possible presence of liquid at failure.239

Figure 7-7: Results of SEM and EDX analysis depicting the through-liquid-film, intergranular, fracture propagation mechanism in X65 alloy, showing; a) SEM image of upper fracture surfaces displaying both interlinked and separated primary dendrite arms. The fracture surface is covered in eutectics. b) detailed SEM image of a eutectic with direction of EDX line scan transposed, c) results of EDX line mapping across the eutectic presented in Fig. b, showing enrichment in solute elements (C, N, Al, Si, P, S, and Cu) as well as strengthening (solution and precipitation) elements (Ti, Mo, Nb). 240

Figure 7-8: 3D schematic illustration of base metal microstructure prior to welding, the black circles represent Ti (C,N) particles inherent to the fine grained microstructure depicted by the grey hexagons.241

Figure 7-9: 3D schematic of weld pool formation and grain growth in the HAZ. The large black dots represent Ti (C,N) enlarged from thermal exposure during welding. The large green hexagons represent the HAZ grain growth region and the purple semi-circle depicts the molten weld pool.242

Figure 7-10: 3D schematic of solidification initiation. Coarse and columnar grains grow directly from the coarse HAZ grains.243

Figure 7-11: 3D schematic of competitive growth of columnar dendrites and precipitation of Ti (C,N) which triggers coalescence of primary dendrite trunks.244

Figure 7-12: 2D schematic of Ti (C,N) precipitation and dendrite coalescence.245

Figure 7-13: 3D schematic of transverse tensile strain application.246

Figure 7-14: 2D schematic of microvoid nucleation mechanism.247

Figure 7-15: 2D schematic of microvoid coalescence mechanism.248

Figure 7-16: 2D schematic of hot tears nucleated from microvoids. Hot tears form from microvoids that coalesce and propagate into the solidifying dendrite structure.250

Figure 7-17: 3D illustration of hot tearing propagation direction towards the heat source.251

ii. List of tables

Table 3-1: Summary of solidification cracking mechanisms proposed to date (Adapted from [20]).....	92
Table 4-1: Nominal chemistries of sample materials.	117
Table 4-2: Summary of the measured weld geometrical parameters in the low S steel. The measurements were made in situ at various time intervals	125
Table 4-3: Summary of the measured weld geometrical parameters in the high S steel. The measurements were made in situ at various time intervals	125
Table 5-1: Nominal chemistries of linpipes used for microstructure and mechanical property testing.	134
Table 5-2: Nominal and measured chemistries obtained through optical emission spectroscopy.....	143
Table 5-3: Mean results from six fracture toughness (ASTM 1820) tests made on the fusion zone.....	150
Table 5-4: Average weld region Vickers hardness (10 kg load) results.	159
Table 5-5: Average micro-Vickers hardness (10 g load) values for the individual phases present in the respective weld regions.	160
Table 6-1: Nominal chemistries of sample materials used for X-ray imaging experiments.....	193
Table 6-2: Input parameters for sample deflection calculations.....	197
Table 6-3: Predicted deflection and angular displacement as a function of sample temperature.	198
Table 6-4: Summary of Vareststraint weldability test parameters.	203
Table 6-5: Summary of properties observed from in situ micro-radiography.....	212
Table 6-6: Summary of solidification thermodynamic results	216
Table 7-1: Chemical composition of the alloys used for industrial scale weldability tests.	232
Table 7-2: Summary of welding and Transvareststraint test parameters	234
Table 7-3: Summary of the thermodynamic parameters predicted in Thermo-Calc simulations that affect weld solidification cracking susceptibility.	235

Table 7-4: Quantification of cracking observed in the weld bead after Transvarestraint testing.....236

Table 7-5: Measured weld geometries (width and depth) mid-weld on Transvarestraint test samples.....237

iii. Nomenclature

AF	Acicular Ferrite
API	American Petroleum Industry
B	Bainitic Ferrite
BTR	Brittle Temperature Range
CCT	Continuous Cooling Transformation
CFD	Computational Fluid Dynamics
CG-HAZ	Coarse-Grained Heat Affected Zone
CSC	Cracking Susceptibility Coefficient
CST	Critical Strain Rate for Temperature Drop
CT	Computed Tomography
CTOD	Crack Tip Opening Displacement
CVN	Charpy V-notch
DBTT	Ductile to Brittle Transition Temperature
DLS	Diamond Light Source
DP	Degenerate Pearlite
DSAW	Double Submerged Arc Weld
DSC	Differential Scanning Calorimetry
EDM	Electrical Discharge Machining
EDX	Electron Dispersive X-ray
ESRF	European Synchrotron Radiation Facility

GB	Granular Bainite
GBF	Grain Boundary Ferrite
HAZ	Heat Affected Zone
HIC	Hydrogen Induced Cracking
HSLA	High Strength Low Alloy
ID	Inner Diameter
LBZ	Local Brittle Zone
LIT	Liquid Impenetrable Temperature
M/A	Martensite/Austenite
MCD	Maximum Crack Distance
MCL	Maximum Crack Length
NDT	Non-destructive Testing
OD	Outside Diameter
OES	Optical Emission Spectroscopy
PF	Polygonal Ferrite
QF	Quasi-polygonal Ferrite
RA	Reduction of Area
SADP	Selected Area Diffraction Pattern
SAW	Submerged Arc Welding
SCTR	Solidification Cracking Temperature Range
SEM	Scanning Electron Microscope
SMYS	Specified Minimum Yield Strength

STR	Solidification Temperature Range
T _L	Liquidus Temperature
T _s	Solidus Temperature
TCL	Total Crack Length
TEM	Transmission Electron Microscope
TIG	Tungsten Inert Gas
TMCR	Thermo-mechanically Controlled Rolled
TOF	Time of Flight
UB	Upper Bainite
UOE	<u>U</u> -forming, <u>O</u> -forming and <u>E</u> xpansion process
ZDT	Zero Ductility Temperature
ZST	Zero Strength Temperature

1. Introduction

1.1. Seam welded linepipe for subsea pipeline application

Welding is an integral part of the steel pipeline industry. It has long been the most common and economical way of joining metals. The history of joining metals goes back several millennia; however, it wasn't until the 1920's that notable advances towards modern arc welding technology began. To this day, the joining of modern day linepipes is commonly performed using a submerged arc welding (SAW) technique that was first developed in the early 1930's.

Today, the linepipes used for the transportation of oil and gas are commonly made of micro-alloyed low C steels, originally termed High Strength Low Alloy (HSLA) steels. Micro-alloyed HSLA steels were first introduced in the late 1930's [1]. In these early HSLA steels, the elements Nb, V and Ti were added separately, in amounts as low as 0.005 to 0.010 percent. Later, the elements were added in tandem as strengths increased and the metallurgical approach became more refined [1].

The micro-alloying technology was first introduced to ship plates, beams, bridge steels, reinforcing bar and heat treated forgings. The technology was not introduced into linepipe steels until 1959 [2]. However, the escalating technological demands of high pressure pipeline systems can be credited with the rapid evolution of HSLA linepipe technology since then. Some of the technological gains and escalating end user expectations have evolved naturally as competitive producers applied technology developed primarily for other steel products. Nevertheless, other requirements may have been provoked by catastrophic and costly failures.

Today's pipelines operate in extremely complex production systems deep below sea level. A typical subsea oil and gas retrieval and transportation system is depicted in Figure 1-1.

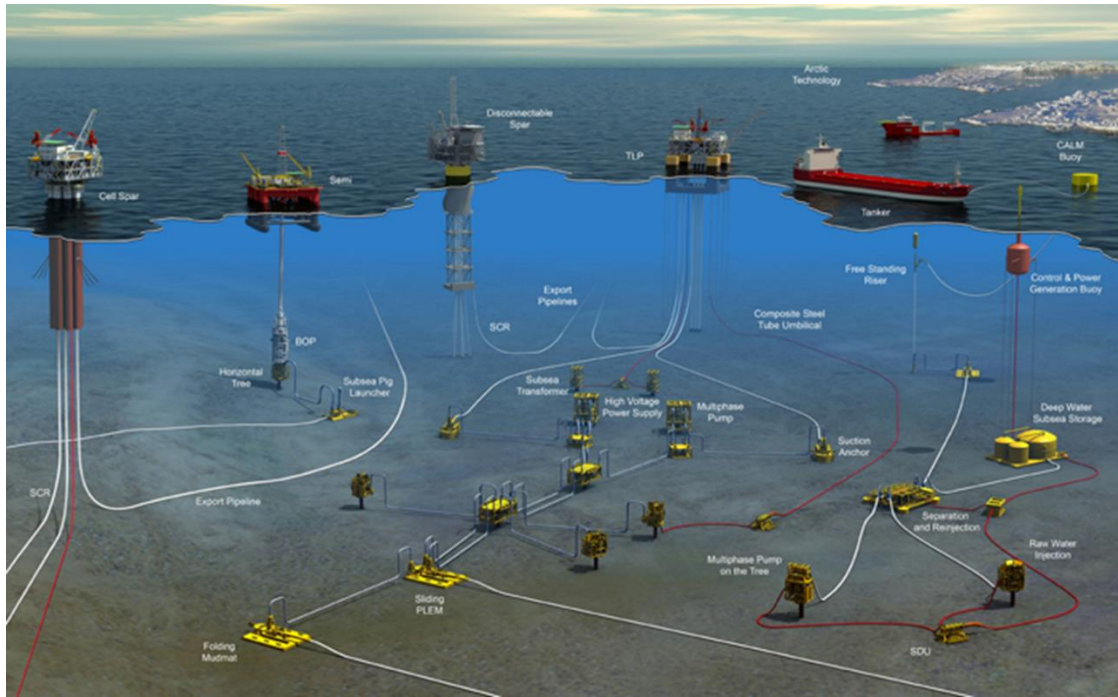


Figure 1-1: A typical subsea oil and gas retrieval and transportation network (image taken from Genesis Oil and Gas company webpage).

The linepipes used in deep sea pipelines are typically used to export oil and gas across large distances, at depths of over 2 km below sea level. The external pressure acting upon the pipes at this depth is around 22 MPa [3]. In service the pipe must survive in a harsh, corrosive environment for periods of 20 years or more. Furthermore, the oil and gas which the pipelines transport internally are also highly pressured and corrosive. Therefore, pipeline design considers all aspects of performance, including; strength, toughness, weldability, fatigue and collapse resistance, strain tolerance, as well as environmental degradation such as stress corrosion cracking, and resistance to sour hydrocarbons containing H₂S and CO₂. Modern linepipe manufacturers must achieve a combination of these properties at affordable prices to remain viable in what is a highly competitive market place.

The linepipe manufacturing process is explained in detailed in the next chapter. Following the processing route described in chapter 1.2, linepipe manufacturers are able to stringently develop homogenous base metals for use in the subsea linepipes that exhibit excellent mechanical properties. However, the control of the weld joint that

binds the linepipe along its seam is much more difficult to control and often offers significantly different mechanical properties to the base metal. As such, the improvement and understanding of the welded joint is required.

Currently, the annual production of steel linepipe is around 25 Mt (~1.9% of the total global steel production) [3]. This huge scale of production, coupled with a fiercely competitive post-recession market place dictates a strong desire within the industry for new approaches to cost saving to be established. Weld solidification cracking, also known as hot cracking during welding, is an important issue in fusion welding. If undetected, the cracking defects can act as stress concentration sites which lead to premature failure via fatigue, as well as offer favourable sites for hydrogen assisted cracking [4, 5] and stress corrosion cracking [6]. For welded steel products such as deep sea oil and gas transportation linepipes, such defects heighten the risk of catastrophic in-service failures. Such failures can lead to devastating environmental, economic, and social damage. Therefore, welding manufacturers are forced to include rigorous post-weld non-destructive testing (NDT) to examine welded products prior to being sent for service, increasing both lead-time and cost. If solidification cracks are detected in NDT, whole sections of linepipe products can be scrapped, again increasing costs and lead-time. Because of this, solidification cracks are considered the most deleterious of all welding defects.

Within this thesis, the factors which influence solidification cracking in welded steel linepipe are assessed and quantified. The mechanisms of solidification cracking are then examined using a novel X-ray imaging experiment coupled with industrial scale weldability tests.

1.2. Subsea linepipe manufacturing process

To further understand the scope of the research encompassed in this thesis, an understanding of the manufacture process involved in the production of welded subsea oil and gas transportation linepipes is required. Figure 1-2 describes the various manufacturing stages in chronological order as a function of temperature.

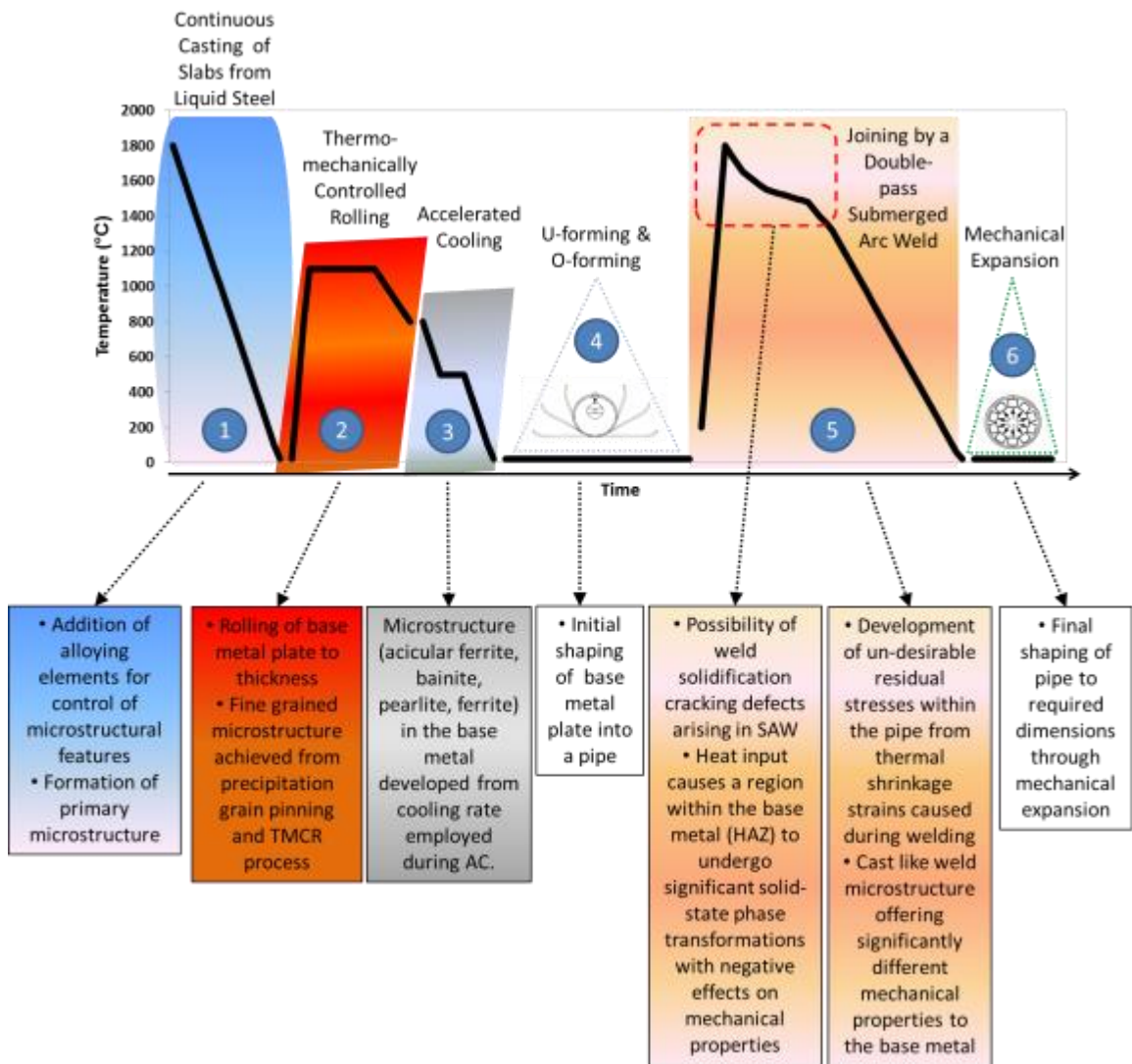


Figure 1-2: Temperature dependant manufacturing lifecycle of a typical steel linepipe.

At stage 1 in Figure 1-2 rough slabs are initially continuously cast from liquid steel containing complex and stringently controlled micro-alloying additions. The rough slabs are then reheated into the austenite region (circa 1100°C, dependant on alloy and manufacturer) and thermo-mechanically controlled rolled (TMCR). During this stage, precipitates formed as a result of micro-alloying additions, pin grain boundaries and allow for fine grains to be rolled by mechanical formers until the desired wall thickness is achieved. Once fine austenite grains are attained within the optimal wall thickness, the plates are then rapidly cooling during using accelerated cooling in stage 3 of Figure 1-2. The cooling rate employed during this stage contributes significantly towards the composition of the final microstructural constituents as well as precipitate size and distribution within the base metal.

Once the base plate of the pipe has been rolled to the required thickness, with the desired microstructural features inherent to the plate, it is then shaped into the cylindrical geometry associated with a linepipe through a U-forming, O-forming and Expansion process (UOE) [7]. A detailed schematic of the UOE and SAW welding process is illustrated in Figure 1-3. The plate edges are prepared and crimped before being U-formed, then O-formed. Next, the seam is tack welded; submerged arc welded (SAW) on the inner diameter, and then SAW welded on the outer diameter. This is known as a double submerged arc weld (DSAW) [8]. It is during the solidification of the SAW joint that detrimental cracking defects known as solidification cracking defects can arise. Furthermore, the high heat input associated with the SAW can lead to significant solid-state phase transformations to occur in the un-melted region in close proximity to the re-solidified weld joint. The region, known as the heat affected zone (HAZ), often has inferior mechanical properties as a result of the heat input and corresponding phase transformations. A demonstration of the resultant weld regions is defined in Figure 1-4.

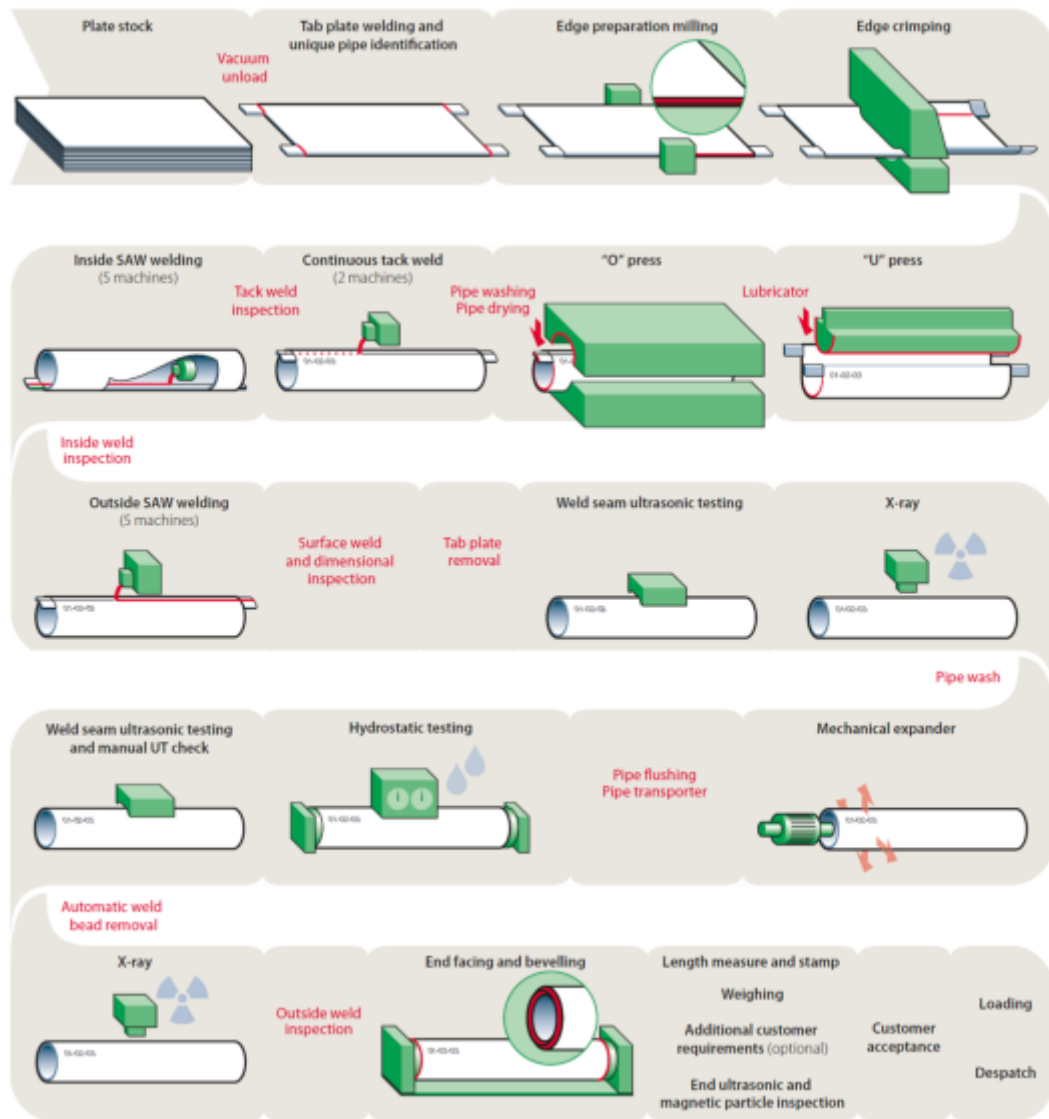


Figure 1-3: Schematic illustration of the manufacturing steps at Tata Steel's DSAW UOE linepipe mill in Corby. Plate edges are prepared and crimped before being U-formed, then O-formed. Next, the seam is tack welded; SAW welded on the inner diameter, and then SAW welded on the outer diameter. After welding, stringent NDT is carried out to check for weld defects. If no defects are detected, the linepipe is then mechanically expanded to the nominal outer diameter, submitted for final inspection and prepared for shipping [9].

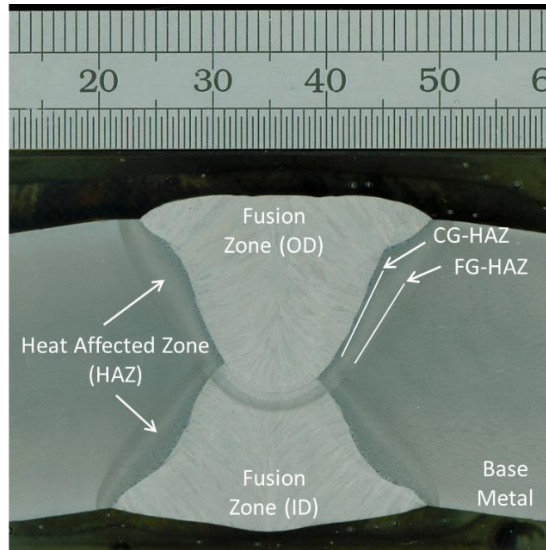


Figure 1-4: Macro image of the different zones in a double submerged arc welded joint, the base metal, heat affected zone (which is sub-categorised as the fine grained heat affected zone (FG-HAZ) and the coarse grained heat affected zone (CG-HAZ)) and fusion zone.

Once the SAW has solidified, the intense thermal contraction strains inherent to the weld solidifying and cooling can cause significant residual stresses to develop within the SAW joint and into the linepipe base metal. Also, the continuously cooled SAW can have considerably different microstructural and mechanical properties in comparison to the rigorously controlled cooling processes (TMCR and accelerated cooling) used in the manufacture of the base plate.

Once joined, the linepipe is then mechanically expanded to normalise the pipe to the desired diameter, ready for service.

1.3. The weldability of steel and solidification cracking defects

Weldability is a term most commonly used to define a materials resistance to cracking during fabrication. Specifically the American Welding Society (AWS) define weldability as [10]:

“The capacity of a material to be welded under fabrication conditions imposed into a specific, suitably designed structure and to perform satisfactorily in the intended service.”

Thus a material that has “good weldability” would be resistant to various forms of cracking during welding.

In the previous section, it was highlighted that solidification cracks can occur during the solidification of the SAW joint. In this section, weld solidification cracking, also known as hot cracking during welding will be introduced in more detail. The prior sentence and literature as a whole often lack consistency in the terminology used to describe weld cracking defects. The purpose of this chapter is to introduce the various types of weld cracking defects and to define the terminology that is used in the remainder of the thesis to describe them.

1.3.1. Types of weld cracking defect

A number of cracking mechanisms have been identified within steels. They can be grouped by the temperature range at which they occur:

- Hot Cracking – Includes cracking phenomena associated with the presence of liquid in the system. If localized in the fusion zone, then the cracks are solidification cracks. If localized in the partially melted zone (PMZ) region of the HAZ, then the cracks are HAZ liquation cracks.
- Warm Cracking – Occurs at elevated temperature in the solid-state, where no liquid is present. These defects may occur in both the fusion zone and HAZ.
- Cold Cracking – Occurs at near room temperature and is usually synonymous with hydrogen induced cracking.

The hot cracking phenomenon can be used to describe a number of specific modes of cracking. However, only weld metal solidification cracking will be discussed within this thesis. In Figure 1-5, the weld metal solidification cracks form in the centre of the weld pool, both on the outer surface of the weld, and internally. These are the most undesirable of all the cracking mechanisms and shall be the main focus for review.

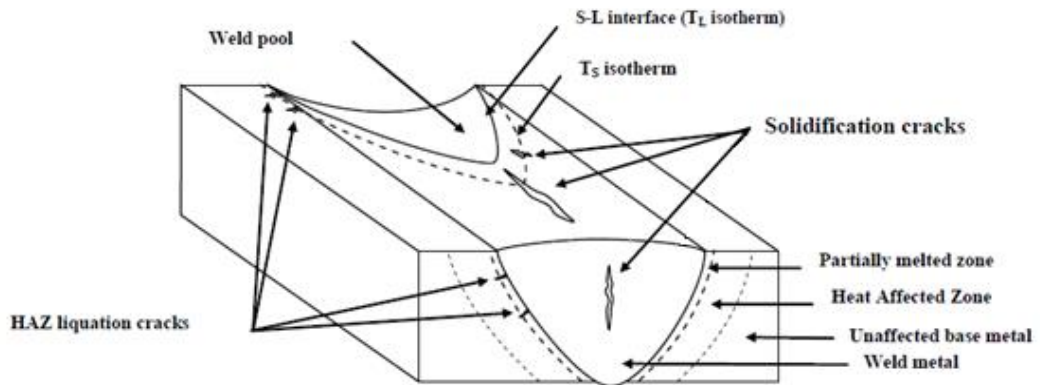


Figure 1-5: Schematic illustration of typical weld “hot” cracking defects and the regions in which they typically develop [11].

Solidification cracks can appear in several locations, and orientations, but most commonly are longitudinal centreline cracks (coincident with the intersection of grains growing from opposite sides of the weld), that are either buried Figure 1-6(a) or surface penetrating Figure 1-6(b).

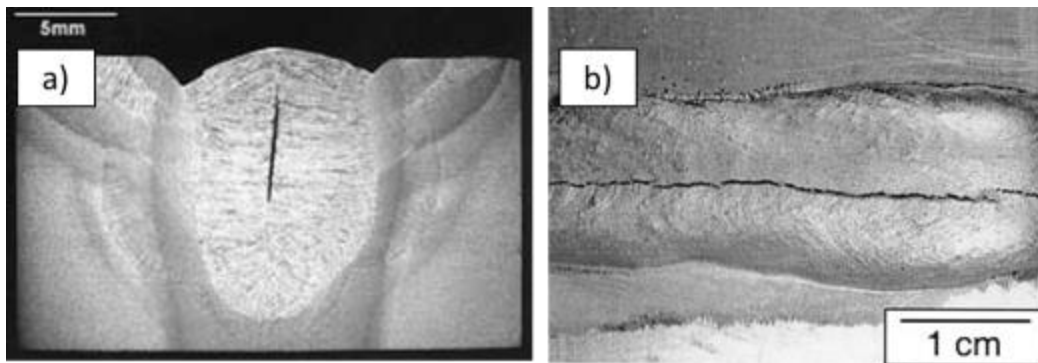


Figure 1-6: Centreline weld solidification cracks, a) buried sub-surface [12], b) surface penetrating [13]

1.4. Terminology to be used in the thesis

Historically, in literature, there has often been disparity between terminologies that describe these solidification defects. In the previous section, it was highlighted that the term “hot cracking” can be used to describe both weld metal solidification cracking and HAZ liquation cracking, two relatively different forms of welding defect. To highlight the issue, the term “hot crack” is used by [14-18], “hot tear” is used by [19-26] and “solidification crack” is used by [4, 5, 27-34].

More recently, in the field of casting research, more concise and consistent terminology has been introduced. Authors have reclassified the defects based on the liquid fraction at which they form, with clear identification between “hot cracks” and hot tears” being made as follows using Figure 1-7 from [35].

At Stage 2b in Figure 1-7 ($f_s \sim 0.8-0.9$), with increasing solid fraction, liquid is isolated in pockets or immobilized by surface tension. During this sub stage, as liquid is trapped between interlocking dendrites, the free passage for liquid is blocked, transforming continuous liquid films into isolated liquid droplets. As a result, the strength of the material is very low due to the existence of this non continuous liquid film between the primary dendrites. If an external stress is applied to the material, then hot tearing can easily occur. The hot tears have inter-dendritic fracture morphologies

Stage 3 in Figure 1-7 ($f_s > 0.9$) marks the transition from the dendritic to the grain structure. At this stage, the boundaries of the primary dendrites become invisible on polished sections. A thin liquid film can still be present at the grain boundaries due to the presence of segregated elements in the liquid, lowering the melting point of this film. Solidification cracks formed at this stage are named hot cracks to distinguish them from the hot tears formed during stage 2b. The hot cracks have inter-granular fracture morphologies.

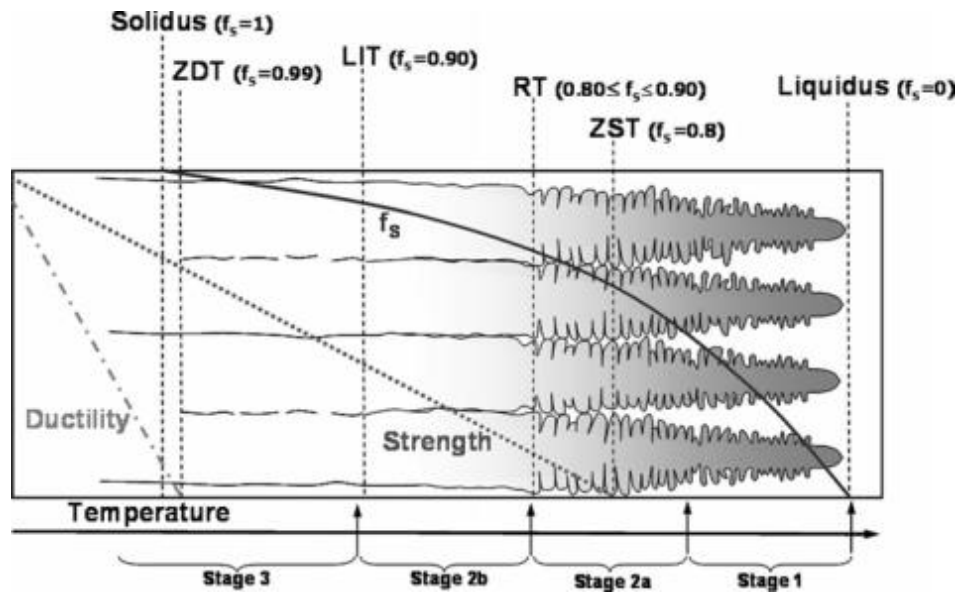


Figure 1-7: Schematic illustration of the structure and mechanical properties at various stages of the solidification sequence [35].

In welding, standardised terminology is very much needed to describe solidification defects. Typically, the cracking is simply assessed as a single entity; A weld solidification crack. For this research the following terminology will be used to describe the weld metal defects in a more concise and distinguishable manner:

Solidification crack:

A general term used to describe cracking defects formed in the weld metal during solidification. Solidification cracks can then be sub-categorised as follows:

Hot tear:

A crack formed during solidification when high volume fraction of liquid ($f_s > 0.9$) exists. Hot tears exhibit inter-dendritic fracture morphologies.

Hot crack:

A crack formed during solidification when low volume fraction of liquid ($f_s < 0.9$) exists. Hot cracks exhibit inter-granular fracture morphologies.

1.5. Objectives of the research

Objective 1: Observe and quantify weld evolution and fluid flow *in situ* prior to solidification.

Hypothesis: Deep and narrow welds with a low width/depth ratio can be susceptible to weld solidification cracking. This is because of the steep angle of abutment between columnar grains growing from opposite sides of the weld pool. Also, concave bead enforcement has been found to increase surface tension. Both lead to reduced solidification cracking resistance. Therefore, it is important to further understand the phenomena which control how the weld evolves during welding in order to achieve high width/depth ratio welds with convex bead enforcement shapes. Quantification of fluid flow velocity and path using the novel technique will also provide interesting experimental data for use by computational fluid dynamics (CFD) research groups that computationally model welding processes and fluid flow.

Objective 2: Characterise and measure microstructure-mechanical property relationships in subsea linepipe in terms of solidification structure, strength and residual stresses induced during welding.

Hypothesis: Without tensile thermal contraction stresses during solidification, cracking would not occur. Therefore it is important to measure the orientation and magnitude of the residual stresses induced by welding. Also, the solidification structure, strength and ductility of the material are key contributing factors to solidification cracking in welding. The results will also provide steel linepipe makers with valuable data on the microstructure-mechanical property relationships in the SAW weld joints, stimulating improved welding and metallurgical approaches to linepipe design and manufacture.

Objective 3: Explore the feasibility of using synchrotron X-ray imaging to observe, identify and understand the mechanisms of solidification cracking during the welding of steel for subsea linepipe applications.

Hypothesis: The hypothesis is that it is now possible to make a significant step forward in understanding the mechanisms (initiation and propagation) of weld solidification cracking defects using synchrotron X-ray imaging coupled with advanced microscopy and computational modelling. The observation of solidification crack nucleation and propagation is almost an unexplored phenomenon. Only recently have experimental observations on solidification cracking started to emerge: first for transparent analogues [23], then for real metals [22] and binary alloys [27]. Some of the mechanisms for solidification crack formation and propagation have been elucidated from observations of fracture surfaces. Based on these observations, the following crack nuclei have been suggested: 1) liquid film or liquid pool [36]; 2) pore or series of pores [24, 37]; 3) grain boundary located in the place of stress concentration; and 4) inclusions that can be easily separated from the liquid or solid phase [38, 39]. However, in previous studies emphasis is placed on the continuous casting of Al alloys.

The outcome of the research will allow for a much more quantitative understanding of how to avoid these defects in high value, high integrity steel products, such as deep sea oil and gas transportation linepipes.

Revisiting this topic is timely and novel because third generation synchrotron sources are now capable of penetrating sufficiently thick (8-10 mm) steel samples to observe welding phenomena *in situ*. Software packages for the analysis of radiographic/tomographic image data are now readily available. Advanced microscopy techniques are standard tools for observing and quantifying the morphology and chemistry of fracture surface features contributing to weld solidification cracking.

1.6. Scope of the thesis

The proceeding chapters aim to address the objectives set out in Chapter 1.5. Following this introduction chapter, Chapter 2 introduces the materials and processes that are used to manufacture subsea linepipe. The factors which contribute towards solidification cracking during welding, such as processing, microstructure and residual stresses are identified with the historical research relating to each of the fields being presented and evaluated based on their contribution to solidification cracking in the weld. Chapter 3 presents a detailed literature survey on historical and current research in the field of solidification cracking during welding. Specific emphasis is placed on modern experimental techniques and identifying the current challenges that need to be addressed. In Chapter 4, objective 1 will be addressed. Weld evolution and fluid flow prior to solidification are reported and evaluated in Chapter 4 using a novel synchrotron X-ray radiography approach. Chapter 5 tackles objective 2. The chapter identifies the microstructure and mechanical properties of the welded linepipe joint using advanced microscopy analysis, mechanical tests and residual stress analysis via the neutron diffraction technique. In Chapter 6, key objective 3 is addressed. The mechanisms of solidification cracking during welding are identified using a novel synchrotron X-ray imaging approach. In Chapter 7, the results are up-scaled to address industrial scale weldability issues in advanced steels for subsea linepipe applications. Finally, conclusions and recommendations for future work are made in Chapter 8.

2. Literature survey on processing, microstructures and residual stresses in welded linepipe

In this chapter, the materials and processes that are used to manufacture subsea linepipe are introduced. The factors which contribute towards solidification cracking during welding are identified with the historical research relating to each of the fields being presented and evaluated. In summary, this chapter identifies the following factors that influence solidification cracking during welding:

- The microstructure and mechanical properties of HSLA steel substrate
- The submerged arc welding process that joins the HSLA steel linepipe
- The phenomenon controlling fluid flow and weld geometry
- The solidification microstructure in the submerged arc weld joint
- The strength and toughness of the submerged arc welded joint
- Residual stresses induced from the submerged arc welding process

2.1. HSLA steel for welded subsea oil and gas linepipe

As discussed within the introduction, modern welded linepipe is made of HSLA steel plate. HSLA steels are preferred for manufacture of seam welded linepipe due to the steels combined quality in strength, ductility/formability and weldability. The steels also exhibit excellent toughness for high resistance to fracture and fatigue failures.

The HSLA plate is shaped by the UOE process described in Figure 1-3 and then joined with a submerged arc welding process. The properties of the linepipe can therefore be assessed as multiple entities i.e. the unaffected base metal, heat affected zone, and weld joint due to the inhomogeneous features within the respective regions. This section specifically looks at the HSLA steel base metal. The term “solidification cracking during welding” doesn’t immediately identify with the unaffected HSLA base metal. However, as welding wires are designed to exhibit similar chemistries and mechanical properties as the substrate, it is important to examine the complex nature of the HSLA base metals used in deep sea linepipe.

2.1.1. Processing high strength steel for subsea linepipe

The manufacture of HSLA steel base metal for linepipe application is a stringently controlled process and has been a focus of study for nearly a century. There are five basic strengthening mechanisms in steel making:

(1) work hardening, (2) solution strengthening [40] through: (i) interstitials (C, and N) and, (ii) solids (e.g. Mn, Si, Ni, Mo, etc. These alloying elements are usually added for other reasons, e.g. Si to achieve de-oxidation, Mn to combine with S or Mo to promote hardenability. Therefore, the solid solution hardening contribution can be viewed as a useful bonus), (3) precipitation hardening [41], (4) transformation strengthening [42], and (5) grain refinement. The final three result in part from micro-alloying; that is, the addition of elements such as Nb, V and Ti at a level of only a few hundredths of a weight percent to the alloy.

The first reports on the positive effects of micro-alloying within the manufacture of steel were presented in the late 1930's when patents [43, 44] were filed on the influence that Nb had upon increasing the strength of hot-rolled C-Mn steels. Later, in the mid 1940's similar increases in strength were reported in normalized steels containing V. The exact mechanisms of the strengthening were unclear at the time, but it was proposed that the beneficial strength occurred predominantly due to the grain refining effects of the Nb and V carbides and nitrides.

It was around this time that the first reported use of micro-alloying techniques in linepipe steels arose. This was later extended to API grade X56 and X60 in 1953 and 1962, respectively [45, 46]. API standard categorises linepipe grade by its specified minimum yield strength (SMYS) in a designation format of a numeral preceded by the character "X", such as X65 where the numeral 65 represents the SMYS in ksi.

Other reports at the time [47] indicated that the new steels had poor notch toughness due to the formation of cementite networks on ferrite grain boundaries, also because of the formation of Widmanstätten ferrite during normal air cooling [48]. Later it was discovered that hardening or strengthening by the precipitation of V or Nb carbonitrides could also harm toughness [49].

Soon enough these toughness issues were eradicated by increasing Mn content [50] and refining the austenite grain size during hot rolling. In 1967 the effect of Nb in retarding austenite recrystallization was discovered [51] which later became the foundation for the large scale introduction of controlled rolling and other thermo-mechanical processing methods of austenite. Ti, and V, plus Mo and Al retard austenite recrystallization to some degree but Cuddy *et al* [52] found that Nb was the most effective and was later termed indispensable by Kosazu *et al* [53].

In the subsequent years, the strengthening mechanisms operational in micro-alloyed steels were further understood and quantified. In the last thirty years, considerable research has been placed on the development of X100 and X120 steel [54-58] although linepipe with strengths above 80 ksi have yet to see widespread commercial application in an offshore environment. However, the trend towards these higher strength levels has been led by developments in onshore double SAW linepipe whereby the high strength benefits have translated into the use of lighter wall thicknesses for high pressure, long distance onshore pipelines. The thinner walled pressure vessels offer attractive cost reduction possibilities in the future for manufacturers.

The metallurgy of X90 to X120 linepipe is based on very low C micro-alloyed steels, additionally alloyed with Mo, Cr, Ni, Cu and occasionally B, combined with elegant TMCR practices. Most of these practices have now been adopted in second generation X60 to X80 steels. The available strengthening mechanisms used today in HSLA linepipe steel can be depicted as simple incremental building blocks as illustrated in Figure 2-1.

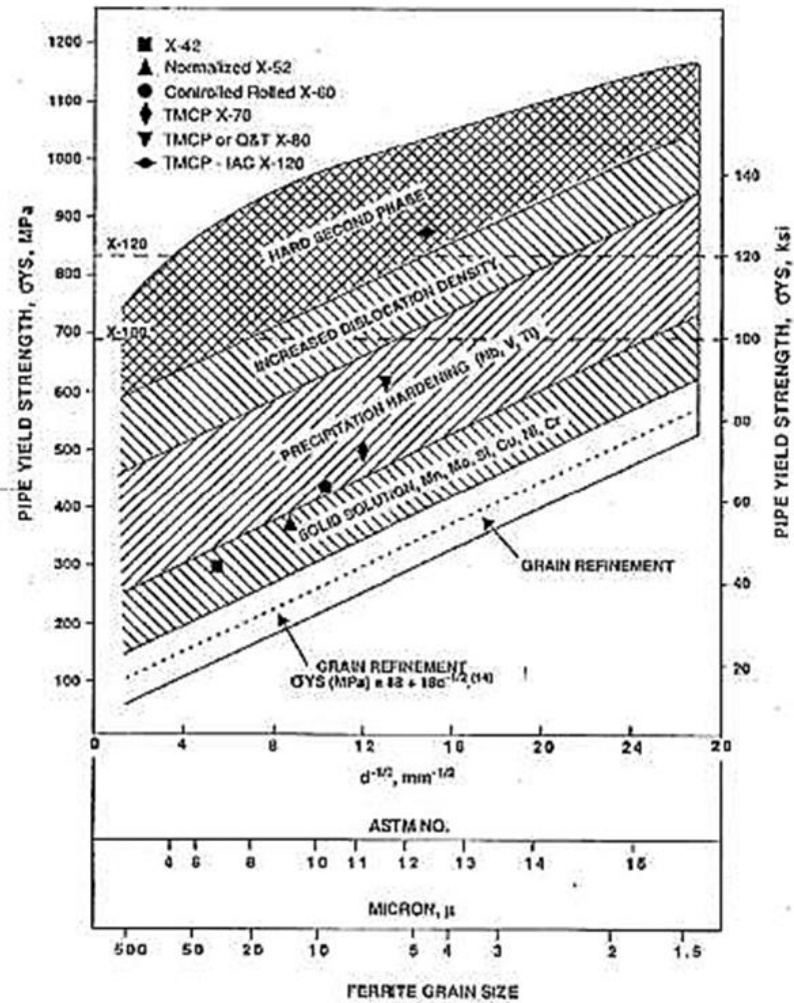


Figure 2-1: Strengthening mechanisms in modern HSLA steel for linepipe application [1].

It is clear from Figure 2-1 that the strength of the HSLA base metal for linepipe application is heavily dependent on micro-alloying and the control of grain size through TMCR.

In this study, API-5L grade X65 steel has been the focus of research as it is widely used as the main linepipe material for transporting sour loads in offshore locations [59]. From Figure 2-1 it is possible to assume that the strength of the API-5L grade X65 steel (65 ksi yield strength) is governed via a combination of solid solution strengthening, precipitation hardening and grain refinement through TMCR.

The concept of microstructural control by TMCR is schematically presented in Figure 2-2. The thermo-mechanical treatment involves the simultaneous application of heat and a deformation process, in order to change the shape and refine the microstructure. The TMCR process has been added to the manufacture cycle of micro-alloyed HSLA linepipe steel to manage the conflicting requirements of strength, toughness and weldability through grain refinement [60, 61].

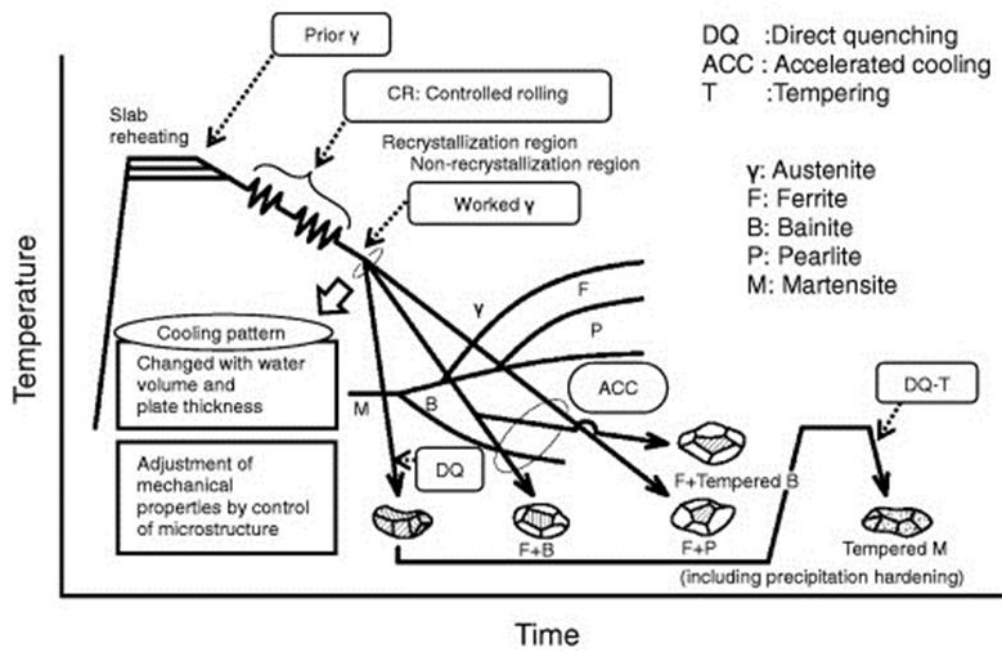


Figure 2-2: Schematic illustration of a typical TMCR process with various accelerated cooling schedules [62].

The primary grain refinement mechanism in TMCR is the recrystallization of austenite during hot deformation, known as dynamic recrystallization. The HSLA plates are reheated into the 1200–1300°C range and rolled to the desired wall thickness. The process is influenced by the temperature and degree of deformation which takes place during each rolling pass. The deformation leads to a breaking down of the original coarse microstructure by repeated recrystallization of the steel while in the austenitic condition, and by the gradual reduction in the chemical segregation introduced during casting. Also, non-metallic inclusions, i.e. oxides, sulphides and silicates, are broken

up, deformed and distributed throughout the steel in a more refined and uniform manner [40].

The fine crystalline grains resulting from the TMCR process contribute considerably to the favourable yield strength and toughness properties of HSLA linepipe steels. Yield strength can be expressed by the Hall-Petch relationship [63-65]:

$$\sigma_y = \sigma_o + k_1 d^{-1/2} \quad (2-1)$$

Where σ_y is the yield strength. σ_o and k_1 are constants independent of grain size. σ_o is a friction stress, which includes contributions from solutes and particles but not from dislocations. d is the grain size.

Similarly, the ductile to brittle impact transition temperature (DBTT) for low C ferrite-pearlite steels can also be expressed as a function of the grain size [66]:

$$DBTT = -19 + 44(Si) + 700(\sqrt{N_f}) + 2.2(Pearlite) - 11.5d^{-1/2} \quad (2-2)$$

Where, Si , N_f , and *pearlite* are the respective weight percentages of Si, free N and pearlite.

Clearly then, from a strengthening and fracture mechanics perspective the control of grain size is paramount. However, in austenite devoid of second-phase particles, the high temperatures involved in TMCR lead to distinct grain growth, resulting in inadequate refinement of the grain structure and reduced strength and toughness properties. The situation is greatly improved if fine particles are introduced into the austenitic matrix. The particles are commonly introduced with the addition of elements such as Nb, V and Ti at a level of only a few hundredths of a weight percent to the alloy. The micro-alloying elements have a very strong affinity for the interstitial elements such as C and N and stimulate grain pinning, as expressed by the well-established Zener equation [67-69].

$$R = \left(\frac{4}{3}\right) \left(\frac{r}{f}\right) \quad (2-3)$$

Here R is the radius of an austenite crystal grain, r is the radius of a second-phase particle and f is the volume fraction of second-phase particles. From equation 2-3 it is

clearly beneficial that a finer and more widely dispersed particle distribution would be favourable on the control of the austenite grain size.

A schematic of this pinning effect for Nb based particles is depicted in Figure 2-3 at various stages of the TMCR process. During re-heating, the austenite grains are pinned by the 300 nm Nb precipitates. During rolling the precipitates are dispersed into 50 nm sizes and distributed more extensively to retard recrystallization. To be effective in either of these phenomena and guard against harming toughness properties, there is a critical particle size that needs to be achieved. The control of particle size will be further discussed in chapter 2.2.7.

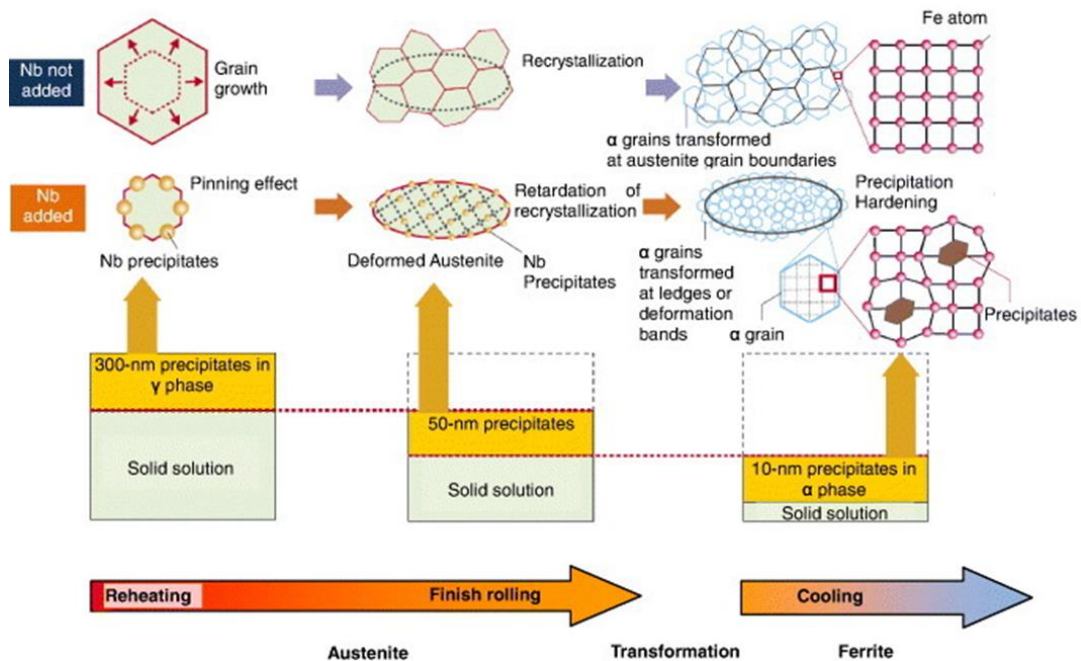


Figure 2-3: Role of Nb based precipitates at each stage of the TMCR process showing their effects on the refinement of ferrite grains and precipitation hardening [62].

2.1.2. Microstructures within HSLA steel for subsea linepipe

Once the grain refinement is completed, the HSLA linepipe steel is then water cooled in an accelerated cooling process to either promote, or avoid, specific microstructural features. The most notable feature that is avoided during accelerated cooling is the formation of a banded pearlite and ferrite microstructure commonly associated with low alloy steel. The minimum cooling rate employed during the accelerated cooling process is usually only sufficient for a homogenous structure of degenerate pearlite (DP) to form. The structure of the DP phase, which is referred as pseudo-pearlite without the banding pattern, is different from that of typical pearlite evolved by normalizing and slow cooling. The high cooling rate associated with the accelerated cooling process retards the C diffusion efficiency during cooling to a point at which is insufficient for the lamellar structure of cementites, more commonly associated with pearlite, to form [70, 71].

By increasing the cooling rate during accelerated cooling even further the formation of pearlite can be completely avoided. Therefore, the predominant microstructural feature in linepipe steels is ferrite. The ferrite however can assume many different morphologies [72].

- Polygonal ferrite (PF) which is transformed at the highest temperatures and slowest cooling rate, assumes equiaxed grains with smooth continuous boundaries under the scale of optical microscopy.
- Quasi-polygonal ferrite (QF) which is produced by transformation through short range diffusion across ferrite/austenite interface, assumes grains with irregular and jagged boundaries containing high density of dislocations, sub-boundaries and martensite/austenite (M/A) constituents. M/A constituents are inherently brittle and often contribute to reduced toughness properties [70, 73].
- Granular bainitic ferrite (GB) which forms at the same transformation temperature as bainite, but at slower cooling rate with granular equiaxed retained austenite or M/A islands dispersed in ferritic matrix.

- Bainitic ferrite (B) which is characterized by many elongated ferritic lath bundles with high density of dislocations separated with high angle grain boundaries.
- Acicular ferrite (AF) which is a complex structure consisting of QF, GF, BF and few PF with dispersed islands of second phases in the matrix it is characterized with relatively high density of dislocations and fine grains [41]. AF within HSLA steel base metals usually has irregular grain boundaries and a number of small-sized sub-grain boundaries in the grain. This is different from AF formed during welding, which has randomly-oriented grain boundaries and showed a needle-like shape [74].

Many variations in the types and volume fractions of these individual microstructural constituents can be found in the API-5L grade X65 steel under investigation in this study. Fraigel *et al* [75] reported on the variation in microstructural characteristics within X65 steel from different commercial manufacturers. However, the X65 grade typically exhibits a ferrite-pearlite microstructure, whereas higher strength grades, i.e. X80 upwards often exhibit hard phases such as bainite and martensite with varied volume fractions to maximise strength, as described in Figure 2-1, while reducing toughness.

Later, Yu *et al* [76] reported upon the fracture anisotropy in the X65 grade. The study found that fracture toughness was almost 50% lower in the longitudinal rolling direction in comparison to the circumferential. Texture intensity revealed that the anisotropy of toughness may be attributed to the lower volume fraction of the densely packed [110] preferential slip plane in the longitudinal direction when compared to the transverse. More recently, Bhadeshia *et al* [77] proposed that rather than the alignment of preferential slip planes, directionally dependent delamination and texture effects were a more likely basis for reduced Charpy V-notch (CVN) impact toughness in hot rolled HSLA steels.

Hashemi [78] proposed an empirical formula in an attempt to statistically correlate strength and hardness properties in a fine grained ferrite-bainite API-5L grade X65 steel.

Park *et al* [70] utilised a range of accelerated cooling schemes (Figure 2-4) to assess the hydrogen trapping efficiency and hydrogen induced cracking (HIC) susceptibility of various microstructural constituents in API-5L grade X65 steel.

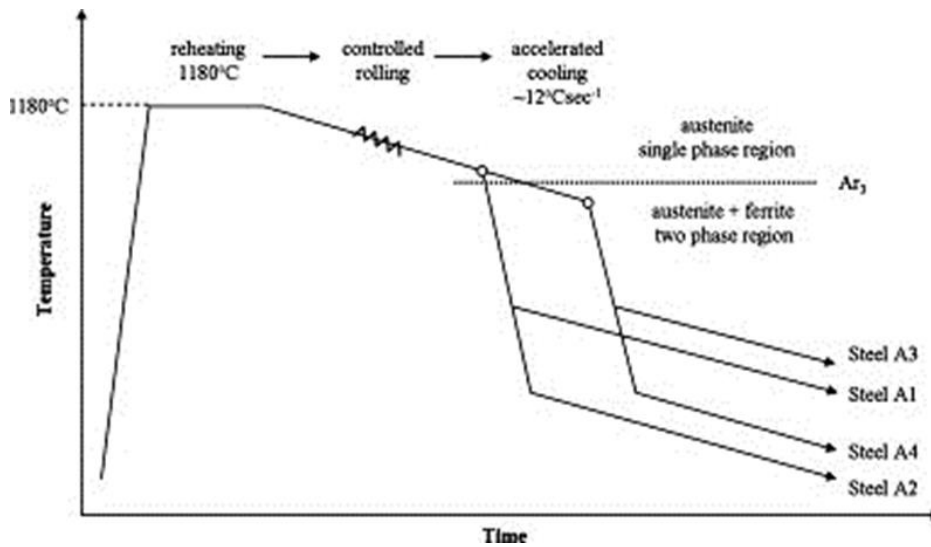


Figure 2-4: Schematic of the various accelerated cooling regimes used by [70].

To exemplify the importance of the accelerated cooling regime on microstructural development within API-5L grade X65 steel, steels A1 and A3 in Figure 2-4 produced a ferrite (PF/QF)-DP microstructure. Steel A2 produced a ferrite (PF/QF)-AF microstructure and steel A4 had a ferrite (PF/QF)-B microstructure. Micro-hardness tests revealed the cementite enriched DP and B phases to be significantly harder than the PF and QF. The study concluded that AF was the most potent microstructural site for hydrogen trapping (followed by B then DP). M/A constituents were found to be the initiation site of fracture during HIC testing due to them being easily embrittled by hydrogen.

Once the API-5L grade X65 steel plate has been thermo-mechanically processed, it is then shaped by U-formed and O-forming process and joined with a submerged arc weld along the seam of the pipe. A schematic of the shaping and welding process is defined in Figure 1-3. The UOE forming process will have a significant influence on the mechanical properties of the finished linepipe product, which is however outside the

scope of the current study. The focus of this research work is on the seam welding and the resultant weld joining the UOE linepipe. The various associated issues and aspects relating to the welding and weld joint are systematically dealt with in the following chapters.

To summarise, the literature survey presented in 2.1 has introduced the historical advancement of micro-alloyed HSLA steels usage in linepipe applications. The strengthening mechanisms within the linepipe were presented with particular focus made towards the grain refinement achieved via austenite grain pinning and TMCR. The key microstructural features that develop in the HSLA base metal were then discussed in relation to the accelerated cooling process.

The next section will introduce the welding process.

2.2. Welding of subsea oil and gas transportation linepipes

2.2.1. The submerged arc welding process

Once the base metal has been cast, processed and shaped, it is then joined along its seam using a submerged arc welding process. The submerged arc welding process illustrated in Figure 2-5 joins the pipe by heating the seam with an arc established between a consumable wire electrode and the HSLA steel. The arc is shielded by a molten slag and granular flux that is supplied from a hopper, which travels with the torch, so no shielding gas is needed because the molten metal is already separated from the air. The protecting and refining action of the slag helps produce clean welds. Since the arc is submerged, spatter and heat losses to the surrounding air are eliminated even at high welding currents. Both alloying elements and metal powders can be added to the granular flux to control the weld metal composition and increase the deposition rate, respectively. Using two or more electrodes in tandem further increases the deposition rate. Because of the high deposition rate, thick samples can easily be welded by SAW. However, the relatively large volumes of molten slag and metal pool often limit SAW to flat-position welding and circumferential welding (of pipes) [13].

The submerged arc welding technique was first developed in the early 1930's and is still commonly used for the joining of HSLA steel linepipe due to the favourable deposition rates, penetration depth and consistency of the welds produced.

Submerged arc welding is a high energy welding process. The heat input of the SAW process can be estimated by [79]:

$$HI = n \frac{I \times V}{1000 \times s} \text{ (kJ mm}^{-1}\text{)} \quad (2-4)$$

where V is the arc voltage in volts, I is the welding current in amps, S is the welding speed in mm s^{-1} and n is the arc efficiency. Typically, the heat input from the submerged arc welding process to join thick walled HSLA steels for deep sea oil and gas linepipe is between $3\text{-}7 \text{ kJ mm}^{-1}$ [80]. The high deposition rates are achieved by utilising multi-wire welding heads with four or five welding wires operating in conjunction.

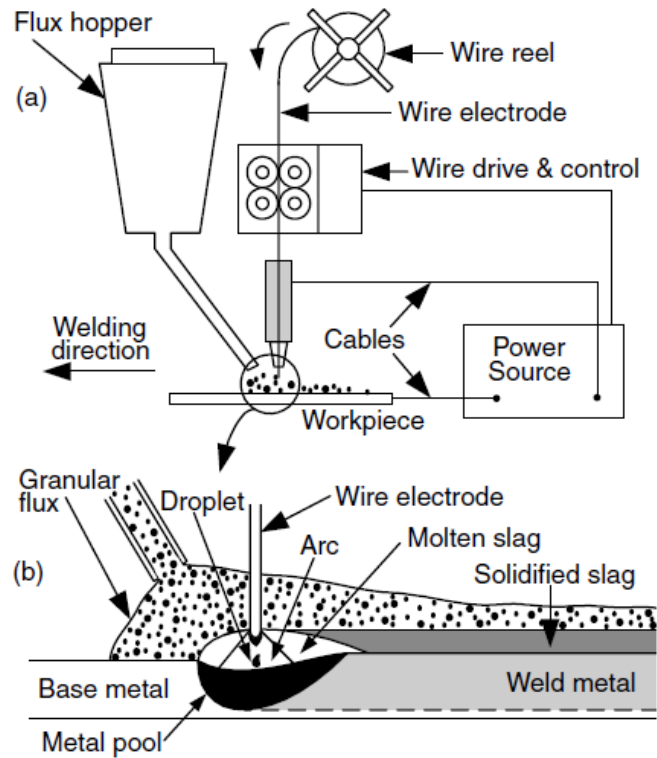


Figure 2-5: Schematic illustration of the submerged arc welding process showing, a) overview of system components, b) detailed view of the welding process and interaction with the base metal (Adapted from [13]).

The molten welding wires mix with the partially molten HSLA base metal along the seam of the U-formed and O-formed pipe. Weld pool phenomena during the weld's liquidus state will be discussed in detail, along with the microstructure and properties of the solidified weld joint in the following sections.

2.2.2. Heat flow during welding

Figure 2-6 is a schematic showing the welding of a stationary workpiece [81]. The origin of the coordinate system moves with the heat source at a constant speed V in the negative- x direction. Except for the initial and final transients of welding, heat flow in a workpiece of sufficient length is steady, or quasi-stationary, with respect to the moving heat source. In other words, for an observer moving with the heat source, the temperature distribution and the pool geometry do not change with time. This steady-state assumption was first used by Rosenthal [82] to simplify the mathematical treatment of heat flow during welding.

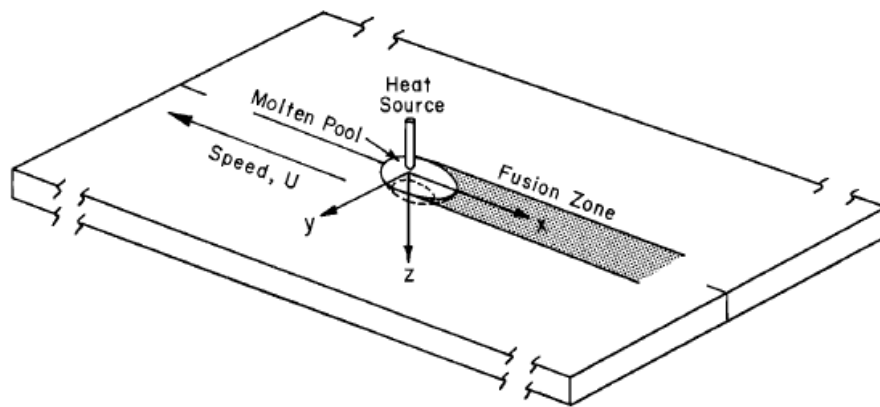


Figure 2-6: Schematic illustration showing the welding of a stationary workpiece. The coordinate system (x, y, z) moves with the heat source [81].

Rosenthal [82] used the following simplifying assumptions to derive analytical equations for heat flow during welding:

1. Steady-state heat flow,
2. Point heat source,
3. Negligible heat of fusion,
4. Constant thermal properties,
5. No heat losses from the workpiece surface, and
6. No convection in the weld pool.

A. Rosenthal's two-dimensional equation

Figure 2-7 is a schematic showing the welding of thin sheets. Because of the small thickness of the workpiece, temperature variations in the thickness direction are assumed negligible and heat flow is assumed two dimensional.

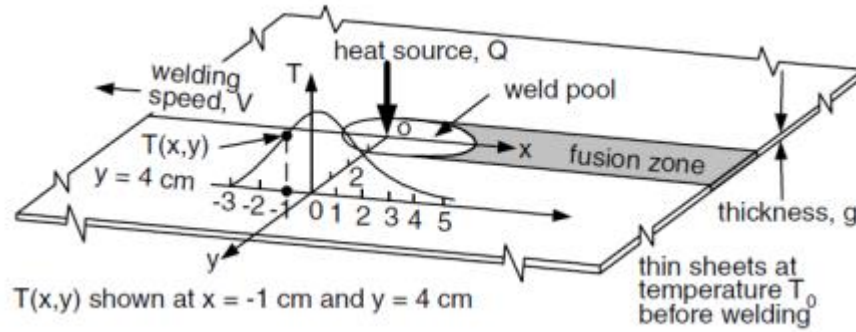


Figure 2-7: Schematic illustration of two-dimensional heat flow during welding of thin sample [13].

Rosenthal [82] derived the following equation for two-dimensional heat flow during the welding of thin sheets of infinite width:

$$\frac{2\pi(T-T_0)kg}{Q} = \exp\left(\frac{Vx}{2\alpha}\right) K_0\left(\frac{Vr}{2\alpha}\right) \quad (2-5)$$

Where,

T = Temperature, T_0 = Workpiece temperature before welding, k = Workpiece thermal conductivity, g = Workpiece thickness, Q = Heat transferred from heat source to workpiece, V = Travel speed, α = Workpiece thermal diffusivity, namely, $k/\rho C_p$, where ρ and C_p are density and specific heat of the workpiece, respectively, K_0 = Modified Bessel function of second kind and zero order, r = Radial distance from origin, namely, $(x^2 + y^2)^{1/2}$.

Equation (2-5) can be used to calculate the temperature $T(x, y)$ at any location in the workpiece (x, y) with respect to the moving heat source, for instance, at $x = -1\text{cm}$ and $y = 4\text{ cm}$ shown in Figure 2-7. The temperatures at other locations along $y = 4\text{ cm}$ can also be calculated, and the temperature distribution along $y = 4\text{ cm}$ can thus be determined.

B. Rosenthal's three-dimensional equation

The analytical solution derived by Rosenthal for three-dimensional heat flow in a semi-infinite workpiece during welding, Figure 2.17, is as follows [82]:

$$\frac{2\pi(T-T_0)kR}{Q} = \exp\left[\frac{-V(R-x)}{2\alpha}\right] \quad (2-6)$$

Where R is the radial distance from the origin, namely, $(x^2 + y^2 + z^2)^{1/2}$. For a given material and a given welding condition, an isotherm T on a plane at a given x has a radius of R . In other words, Equation (2-6) implies that on the transverse cross section of the weld all isotherms, including the fusion boundary and the outer boundary of the heat-affected zone, are semi-circular in shape. Equation (2-6) can be used to calculate the steady-state temperature $T(x, y, z)$, with respect to the moving heat source, at any location in the workpiece (x, y, z) , for instance, at $x = 1$ cm, $y = 4$ cm, and $z = 0$ cm, as shown in Figure 2-8. The temperatures at other locations along $y = 4$ cm can also be calculated, and the temperature distribution along $y = 4$ cm can thus be determined.

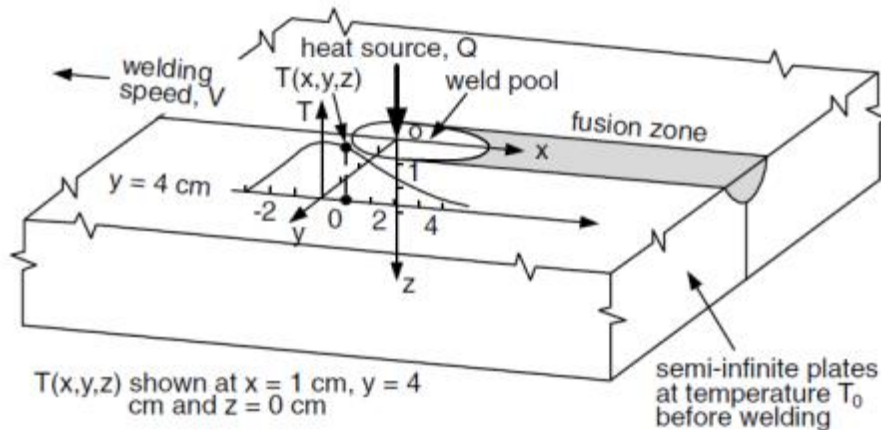


Figure 2-8: Schematic illustration of three-dimensional heat flow during welding of thick sample [13].

Equations (2-5) and (2-6) can be used to calculate the temperature distribution in the workpiece during welding. The temperature distribution in the welding direction, for instance, the $T-x$ curves in Figure 2-7 and Figure 2-8, are of particular interest. They can be readily converted into temperature–time plots, namely, the thermal cycles, by converting distance x into time t through $t = (x - 0)/V$.

2.2.3. Fluid flow during welding

As the welding wires and base metal are heated by the submerged arc, the two melt and form a liquidus pool across the seam of the linepipe. At this point the crystallographic structure of the solid steels has disappeared and instead molten liquidus steel is able to flow.

Fluid flow and solidification are two important subjects in fusion welding. Solidification affects the microstructure [83, 84], mechanical properties [85, 86], and defects [24, 87] in the resultant weld joint. However, solidification and the geometry of weld joint are highly dependent upon the prior fluid flow. It is well understood that the geometry of the weld contributes to solidification cracking during welding.

Blodgett [88] found that concave weld surface geometries can leave the outer surface in tension. By making the outer surface convex the surface tension is reduced, which in turn lowers the welds solidification cracking susceptibility. Tsai and Kou [89] demonstrated the deformation of the weld pool surface caused by Marangoni flow and density changes. The study found that fast outward surface flow can make the pool surface concave.

The weld width-depth ratio is also an important factor, as illustrated in Figure 2-9. Deep narrow welds with a low width/depth ratio can be susceptible to weld solidification cracking, because of the steep angle of abutment between columnar grains growing from opposite sides of the weld pool.

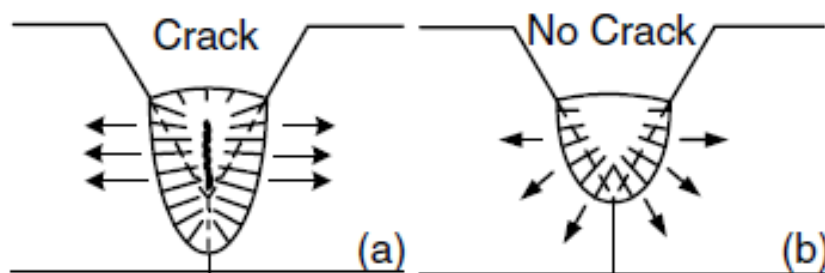


Figure 2-9: Effect of weld bead shape on state of stress at centre of outer surface (Adapted from [88]).

Therefore, a greater understanding and control of the fluid flow during welding is of particular interest to industries such as the oil and gas sector in order to optimise weld shape, penetration, solidification structure and solidification cracking resistance.

Several phenomena have been identified to influence the flow within molten weld joints, as schematically illustrated in Figure 2-10. These include surface tension force (Marangoni flow), arc drag force, electromagnetic (Lorentz) force and buoyancy force [90, 91]. However, it has been reported that surface tension driven Marangoni flow dominates the flow behaviour in the weld pool and consequently determines the shape and penetration of the solidified weld bead [92-94].

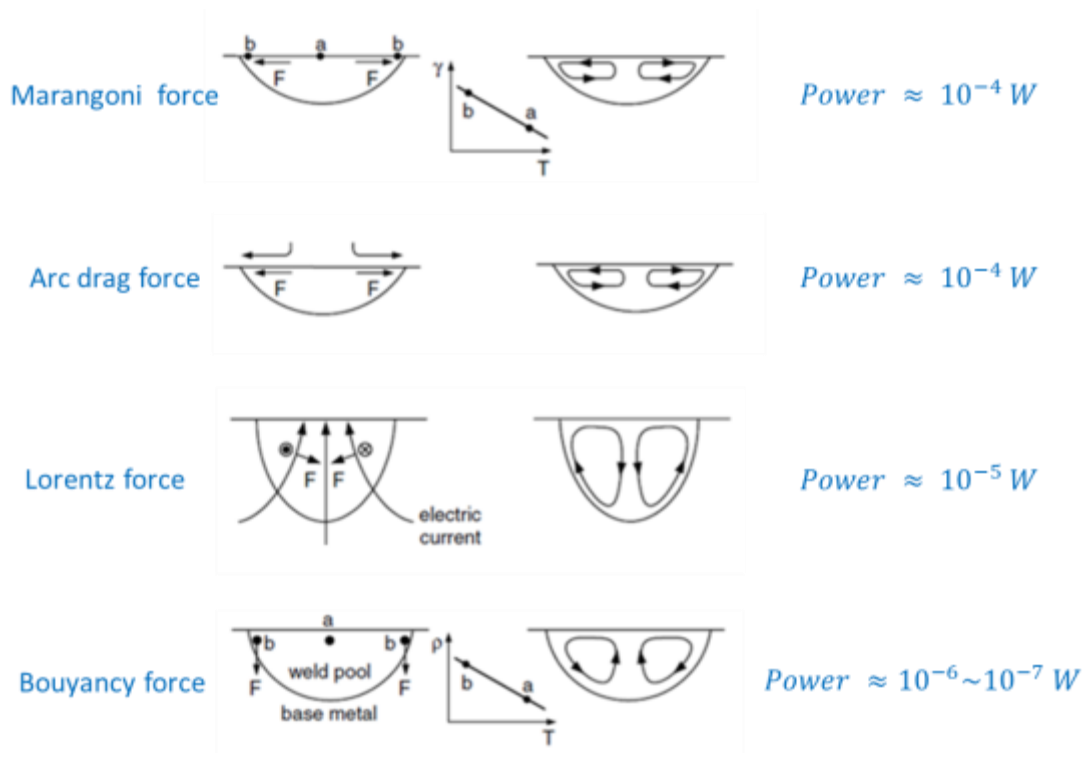


Figure 2-10: Schematic illustration of the various driving forces that stimulate fluid flow within a molten weld pool.

Marangoni flow is driven by the surface tension gradient along the weld pool surface $d\gamma/dl$, where γ is the surface tension and l the distance along the weld pool surface. The surface tension of a pure liquid metal tends to decrease with increasing temperature, that is:

$$\frac{d\gamma}{dT} < 0 \quad (2-7)$$

Thus, when the welding heat source induces a temperature gradient dT/dl along the pool surface, it also induces $d\gamma/dl$ because [95]:

$$\frac{d\gamma}{dl} = \left(\frac{d\gamma}{dT}\right) \times \left(\frac{dT}{dl}\right) \quad (2-8)$$

Heiple *et al* [92] described that a surface tension gradient with consequent fluid flow can be imposed on the surface of a fluid for at least two reasons:

- (1) If there is a temperature gradient along the surface, there will be a surface tension gradient because the surface tension is temperature dependant. A temperature gradient clearly exists within a weld with the temperature reducing with distance away from the region directly under the arc.
- (2) If there is a composition gradient along the surface there will be a surface tension gradient because the surface tension is generally composition dependant. This situation may also occur in weld pools through increased vaporization or reduced surface segregation of certain impurities on the hotter portion of the weld pool surface.

Small concentrations of residual impurities have been found to have significant effects on surface tension within welds. S is an impurity always present in steels and stainless steels. It acts as a surface-active element (that is, an element which segregates preferentially to the surface of the liquid metal) and affects weld pool shape by altering surface tension gradients on the weld pool surface and thereby changing the magnitude and/or direction of fluid flow in the weld pool.

In addition, impurities which are not surface active may affect weld pool shape. This can occur if they react with surface active impurities (also present in the weld pool) to

form compounds which are not surface active, and thus prevent the surface active impurities from influencing surface tension gradients.

In the absence of significant concentrations of surface active elements, the surface tension of molten metals and alloys decreases with increasing temperature

Experimental data shows that with low S (~40 ppm) $d\gamma/dT < 0$, but with increasing S (~150 ppm) $d\gamma/dT$ can become positive [92]. Heiple and Roper [92] proposed a theory to explain the significant effect of the surface-active agent on weld penetration. According to the theory, when sufficient surface active agent is present to make $d\gamma/dT > 0$, Marangoni flow is reversed and the weld pool can become significantly deeper. The theory is illustrated in Figure 2-11 and Figure 2-12.

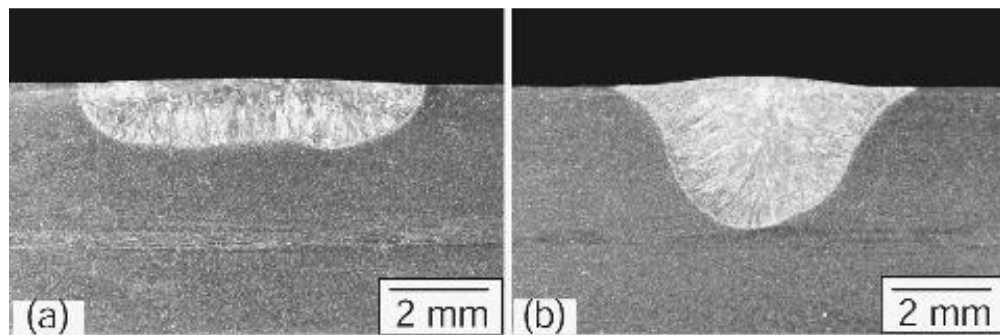


Figure 2-11: YAG laser welds in two stainless steels with a) 40 ppm S and b) 140 ppm S [13].

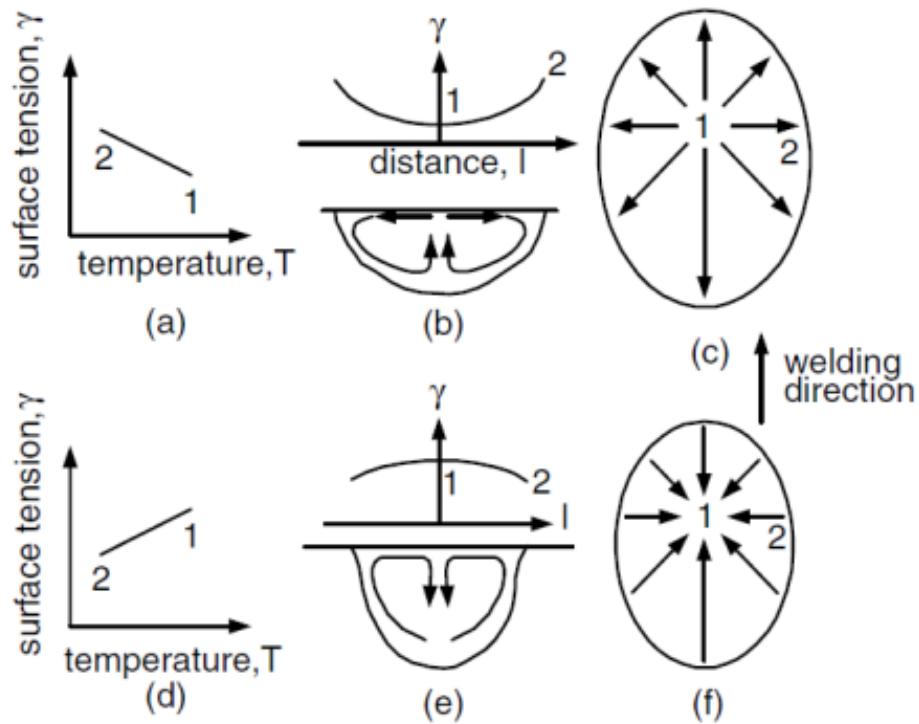


Figure 2-12: Heiple's model for Marangoni convection in a weld pool (a,b,c) low S steel, (d,e,f) high S steel [13].

In the absence of surface active agent (Figure 2-12(a-c)), the warmer liquid metal of lower surface tension near the centre of the pool surface is pulled outward by the cooler liquid metal of higher surface tension at the pool edge. Alternatively, in the presence of a surface active agent (Figure 2-12(d-f)), the cooler liquid metal of lower surface tension at the edge of the pool surface is pulled inward by the warmer liquid metal of higher surface tension near the centre of the pool surface. The resultant flow pattern (Figure 2-12(e)) favours convective heat transfer from the heat source to the pool bottom. I.e. the liquid metal carries heat from the heat source to the pool bottom more effectively, thus increasing weld penetration.

In order for this phenomenon to be better understood, significant efforts [89, 96-102] have been placed upon the computational modelling of fluid flow and heat transfer in welding. Until now, validation of these models has been performed on simulated alloys such as NaNO_3 [103-105].

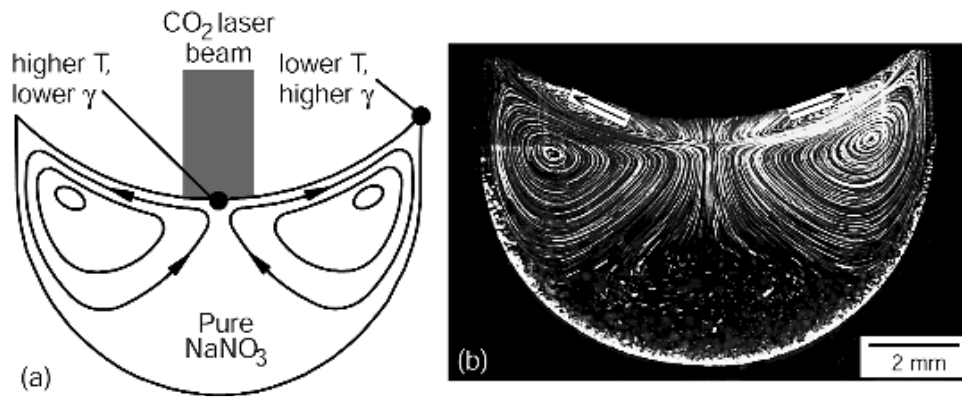


Figure 2-13: Marangoni convection with an outward surface flow in a NaNO_3 pool, showing a) a schematic representation of tension-temperature peaks, and b) experimental observations in NaNO_3 pool [103].

These experiments go some way to validating computational models, however, there is almost no experimental data available for weld fluid flow in steels or other commercial metals. Until now, experimental techniques available have not been advanced enough to capture this phenomenon. However, the emergence of third generation synchrotron X-ray sources has opened interesting new avenues for experimental exploration. Zabler *et al* [106] recently used an *in situ* micro-radioscopy technique to observe particle and liquid motion in semi-solid Al alloys. Using the technique, the authors were able to quantify the flow in terms of both orientation and velocity in a thin walled injection sample. The technique offers interesting possibilities in order to observe fluid flow during welding.

2.2.4. Solidification structure in the submerged arc weld joint

As the liquid metal cools, solidification begins. Solidification modes within the weld can be described by transparent organic materials with similar behaviour to metals, such as those given in Figure 2-14. In the first instance, Figure 2-14(b), a planar solid liquid (S-L) interface is observed, a common mode of solidification in pure metals without severe undercooling. In the second image, Figure 2-14(c), the planar S-L interface has broken down into a cellular solidification front.

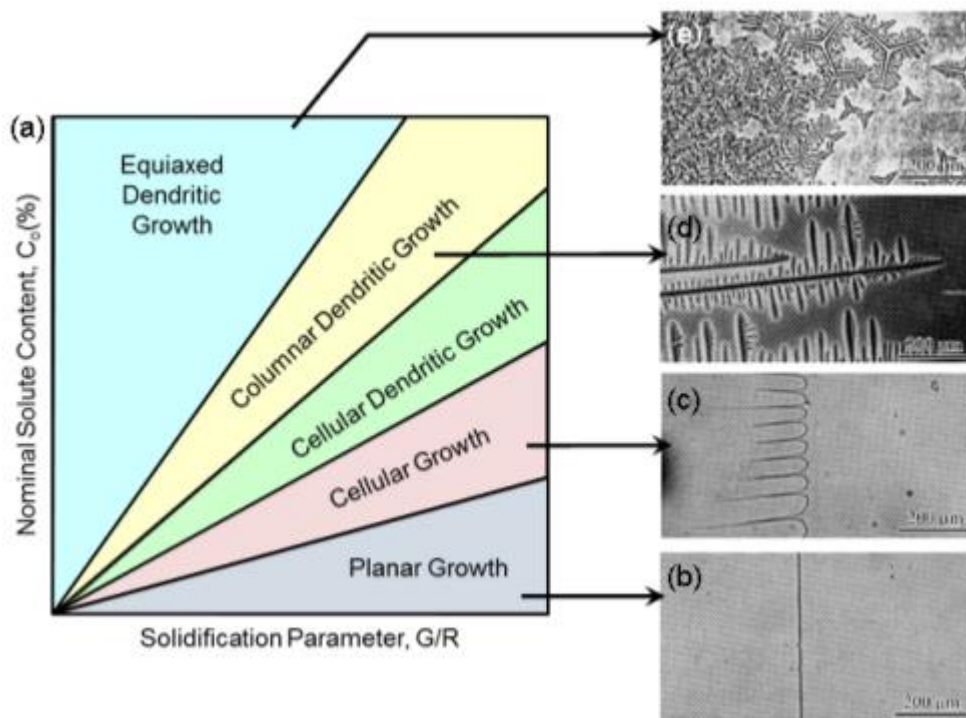


Figure 2-14: Illustration of common solidification modes, a) factors controlling the growth mode during the solidification of liquid metals, b) planar solidification of C tetrabromide, c) cellular solidification of C tetrabromide with a small amount of impurity, d) columnar dendritic solidification of C tetrabromide with several percent of impurity, e) equiaxed dendritic solidification of cyclohexanol with impurity [107].

As the fusion boundary continues the grains grow in a columnar fashion, followed by equiaxed dendritic growth, Figure 2-14(d) and (e). The chemistry of the welding wires used in the SAW process is very similar to that of the base metal, and when welding materials of a similar composition, epitaxial growth rather than nucleation occurs [108, 109]. Epitaxial growth describes the process by which the molten liquid solidifies and develops new grains directly from the solid in the underlying base material. The grains

are anisotropic because they grow along the direction of heat flow. Those grains with their (100) directions parallel to the direction of heat-flow grow fastest and stifle the growth of unsuitably oriented grains. This solidification path results in a columnar solidification structure depicted in Figure 2-14(d), with the width of the columns related to the size of the grains in the underlying base material.

Fine equiaxed grains are often less susceptible to solidification cracking than coarse columnar grains [110]. Fine equiaxed grains can deform to accommodate contraction strains more easily (more ductile) than columnar grains. Liquid feeding and healing of incipient cracks can also be more effective in fine-grained material. In addition, the grain boundary area is much greater in fine-grained material. Therefore, harmful low-melting-point segregates are less concentrated at the grain boundary. Because of this, it is important to understand the grain structure and underlying microstructure in the weld metal and the effect it has upon mechanical properties.

Once all of the remaining liquid has solidified, the bonding of the linepipe seam is complete. However, the microstructure and subsequent mechanical properties of the final weld joint (and linepipe as a whole) are heavily dependent upon the solid state transformations which occur as the weld cools from the solidus to room temperature.

2.2.5. Microstructure development in the submerged arc weld joint

Several studies have been undertaken to examine the development of the weld metal microstructure in HSLA steels [111-113]. All studies employed continuous cooling transformation (CCT) diagrams, as seen in Figure 2-15, to schematically describe the solidification process in terms of microstructural development. The hexagons (Figure 2-15 A, B, C, and D) represent the transverse cross section of columnar austenite grains in the weld metal.

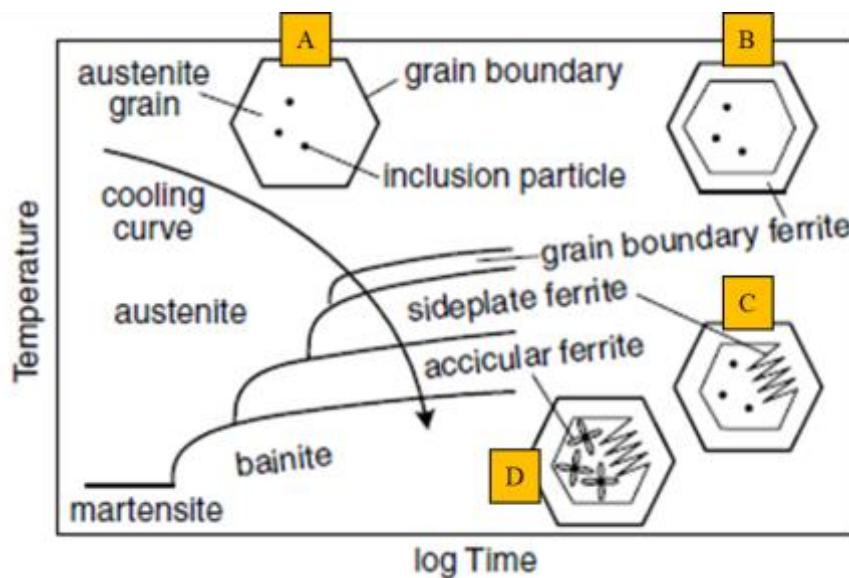


Figure 2-15: CCT diagram for low C steel weld metal (Adapted from [112])

As austenite is cooled down from high temperature, grain boundary ferrite (GBF) nucleates at the grain boundary (Figure 2-15 B). It nucleates at the columnar austenite grain boundaries as these are easy diffusion paths. The boundaries become decorated with thin continuous layers of ferrite and under isothermal condition the thickness of the ferrite layers, q , increase parabolically with time, t :

$$q = \alpha_1 t^{\frac{1}{2}} \quad (2-9)$$

Where α_1 is the parabolic rate constant. As the transformation in welds occurs as it cools, the GBF thickness has to be integrated over temperature:

$$q = \int_{t=0}^{t_1} 0.5\alpha_1 t^{-0.5} + \frac{\delta\alpha_1}{\delta t} t^{0.5} dt \quad (2-10)$$

As thickness of the ferrite varies with the square root of time, the rate of growth decreases as the ferrite layer gets thicker. This is because the distance at which the C has to diffuse over increases with time. The growth rate for a given alloy goes through a maximum as a function of temperature, because the driving force for transformation increases with undercooling, whereas the diffusivity decreases. Consequently as the weld cools to a temperature less than around 600 °C, the diffusional growth of ferrite slows down so much that the layers of GBF reach a limiting thickness. Widmanstatten ferrite formation does not involve the diffusion of substitutional solutes, and therefore its growth is not sluggish at low temperatures. The remaining austenite therefore begins to form Widmanstatten ferrite [40, 114].

The growth of Widmanstatten ferrite is eventually hampered by acicular ferrite plates which nucleate at non-metallic inclusions throughout the weld (Figure 2-15 D). The formation of Widmanstatten and acicular ferrite is therefore competitive. Anything that increases the number density of inclusion sites, favours the formation of acicular ferrite at the expense of Widmanstatten ferrite [40, 114].

The term “acicular” means shaped and pointed like a needle, although it is generally recognized that the three dimensional morphology of acicular ferrite is liken to that of thin, lenticular plates. In two-dimensional sections, the acicular ferrite always appears like a plate rather than a section of a rod. Serial sectioning experiments carried out by Wu *et al* [115] confirmed that the shape of acicular ferrite is between that of a lath or plate, with the length, width and thickness normally less than about 36, 6 and 3 μm , respectively.

The previously mentioned, highly organized, microstructures found in steels, e.g. ferrite can grow in the form of packets containing parallel plates which are in the same crystallographic orientation. This can be harmful to mechanical properties such as cleavage cracks, or deformation processes, can extend readily across the packets. The effects of the individual plates within these packets then have a minimal effect on the mechanical properties.

Acicular ferrite, however, is far from organized; this microstructure is better described as chaotic. The plates of acicular ferrite nucleate heterogeneously on small non-metallic inclusions and radiate in many different directions from these 'point' nucleation sites. Ti oxide, Ti nitride, and galaxite have often been noted as effective nucleants of acicular ferrite [116-119].

In the SAW joint of HSLA steel linepipe, acicular ferrite is regarded as the most desirable microstructural feature, in view of the favourable strength and toughness properties it offers. The main strengthening and toughening mechanisms will be discussed further in the next chapter.

2.2.6. Strength and toughness of the submerged arc welded joint

The mechanical properties of the weld joint are intrinsically related to the chemistry and microstructure that reside after solidification and cooling to room temperature is achieved.

The Hall-Petch criteria [63-65] for strengthening via inoculation of the grain structure is clearly not realised in the case of the coarse columnar structure of the submerged arc weld joint that undergoes no TMCR process. Yet, the welding wires that are employed for the welding of deep sea oil and gas linepipe are commonly over-matched; that is, to have a higher yield strength than that of the base metal. The overmatched welding wires are introduced to protect weld from localization of plastic strain in the event that the yield load of the structure is exceeded [120]. In the absence of strengthening by inoculation, solution strengthening becomes paramount in order to achieve the overmatched yield strength in the fusion zone.

Solution strengthening of the SAW joint is achieved via the addition of the alloying elements Ti, Nb, and V to the HSLA steel welding wires. The alloying element atoms are a different size to the iron atoms, and their presence prevents dislocation slip in the crystal lattice by filling vacancies in the lattice (interstitial solution strengthening), or, if they are large, by causing distortion of the crystal lattice (substitutional solution strengthening) [121]. The distortion prevents the slippage of the metal atoms relative to each other.

The Ashby – Orowan equation is commonly used for assessing the solution strengthening contribution of precipitates given the assumption that all the precipitates are incoherent globular particles that are randomly dispersed [122-124]:

$$\Delta\sigma_p = \frac{0.538.Gb.f_p^{1/2}}{X} \ln\left(\frac{X}{2b}\right) \quad (2-11)$$

Where $\Delta\sigma_p$ is increment of yield strength in MPa, G is shear modulus, b is Burger's vector in mm, X is the average diameter of precipitates in mm, and f_p is the volume fraction of precipitates. The two process variables X and f_p , are crucial in facilitating solution strengthening, with fine and closely dispersed precipitates being the most favourable.

Both interstitial and substitutional solution strengthening increase the strength of the SAW joint by reducing the ductility, therefore considerations must be made in regards to the SAW joints toughness properties.

Second phase particles are commonly found to initiate fracture, especially when large in size. Studies [125, 126] have shown that TiN particles that form in the molten or semisolid matrix can grow large ($>0.5 \mu\text{m}$) in size. As such, Ti and N levels, as well as the process parameters such as solidification rate, need to be carefully controlled in order for optimum toughness levels to be achieved.

Yan, *et al* [127] demonstrated that large TiN inclusions were found to affect the toughness of micro-alloyed steel. It was shown, that when the product of the Ti and N content is larger than the solubility product of TiN at the solidus temperature, TiN manifests in the liquid as large inclusions. On the other hand, if the contents are such that TiN does not form until the solid state, fine precipitates result. Moreover, the inherently brittle non-metallic inclusions have often been reported to initiate cleavage [128-131]. The investigations have been conducted on the stress distribution when a Charpy V-notch (CVN) specimen is in the completely elastic state, with the results helping to explain TiN cleavage initiation at a characteristic distance away from the notch tip at low temperature [132-134]. Noticeably, in the case of room temperature, where considerable plastic fracture is present on the fracture surface, less attention has been paid to the function of the TiN particles.

In order to quantify how precipitation size effects fracture toughness in terms of initiation and propagation of ductile fracture by microvoid initiation and coalescence, several researchers have developed models to predict the fracture toughness based on the so-called “fracture micro-mechanisms” which incorporate a local failure criterion and consider salient microstructural features, such as large precipitates or inclusions, under plane stress/strain conditions.

For small scale yielding (ssy), a stress-modified critical strain criterion has been proposed by various authors [135, 136]. According to Rice and Johnson [137], at the fracture initiation toughness, J_{Ic} , or critical crack tip opening displacement (CTOD), δ_{Ic} ,

the local equivalent plastic strain, $\bar{\varepsilon}_p^*$, must exceed a critical fracture strain or ductility, $\bar{\varepsilon}_f^*(\sigma_m/\bar{\sigma})$, where the stress triaxiality, $(\sigma_m/\bar{\sigma})$, can be written as [138]:

$$(\sigma_m/\bar{\sigma}) = \frac{1}{3} \left[1 + 2 \ln \left(1 + \frac{2X}{\delta} \right) \right] \quad (2-12)$$

The critical fracture strain or ductility, $\bar{\varepsilon}_f^*(\sigma_m/\bar{\sigma})$, is specific to the relevant stress state over a characteristic distance, l_0^* , comparable with the mean spacing (d_p) of the void initiating particles.

Following the approach of Ritchie *et al* [139], the near tip strain distribution, $\bar{\varepsilon}_p$, is considered in terms of distance ($r = x$) directly ahead of the crack, normalised with respect to the CTOD, δ :

$$\bar{\varepsilon}_p \propto \left(\frac{J}{\sigma_0 r} \right)^{\frac{1}{n}+1} \sim c_1 \left(\frac{\delta}{x} \right) \quad (2-13)$$

Where c_1 is of order unity and n is the strain hardening exponent. The crack initiation criterion of $\bar{\varepsilon}_p$ exceeding the critical fracture strain or ductility, $\bar{\varepsilon}_f^*(\sigma_m/\bar{\sigma})$, over $x = l_0^* \sim d_p$ at fracture initiation, J_{Ic} , now implies a ductile fracture toughness [139]:

$$\delta_i = \delta_{Ic} \sim \bar{\varepsilon}_f^* l_0^*, \quad (2-14.a)$$

or,
$$J_{Ic} \sim \sigma_0 \bar{\varepsilon}_f^* l_0^* \quad (2-14.b)$$

or,
$$K_{Ic} \equiv \sqrt{J_{Ic} E'} \quad (2-14.c)$$

Where σ_0 is the yield strength of the material and E' is the young's modulus. The stress modified critical strain criterion (Eq. 2-14), now implies that fracture initiation toughness, J_{Ic} for ductile fracture is proportional to strength times ductility. This is a physically realistic concept and permits rationalization of the toughness-strength relationship for cases where microstructural changes which increase strength also cause a more rapid reduction in the critical fracture strain.

According to Ritchie and Thompson [140], for an array of void initiating particles of diameter (D_p) and mean spacing (d_p), the critical fracture strain ($\bar{\varepsilon}_f^*$) is given by:

$$\bar{\epsilon}_f^* \approx \frac{\ln(d_p/D_p)}{0.28 \exp(1.5\sigma_m/\bar{\sigma})} \quad (2-15)$$

Substitution of Eq. 2-15 into Eq. 2-14 allows for the SAW joint toughness properties to be assessed in terms of the size and distribution of the precipitation inherent to the welded joint as a result of solution strengthening.

Although the micro-alloying additions to welding wires can contribute towards reduced toughness properties within the weld joint, the additions aren't completely negative from a fracture mechanics perspective. Various authors presented the effect of alloying elements upon microstructural development within SAW linepipe joints.

Bhole *et al* [141] examined the effects of Ni (on its own), Mo (on its own), and Ni and Mo (together) alloy additions on the impact toughness of submerged arc welding linepipe. Ni additions individually resulted in low impact toughness and an increased fracture appearance transition temperature. The influences of Ni were attributed to the formation of acicular ferrite being suppressed as the Ni content increased. Conversely, the combined presence of Ni and Mo in the SAW joint decreased the volume fractions of grain-boundary ferrite and promoted formation of high toughness acicular ferrite. The increase of Mo content created an acicular ferrite-predominant weld metal microstructure with impressively improved toughness. Mo addition of 0.881 wt.% in the welding wires gave the optimal impact toughness at -45 °C with a microstructure of 77% AF and 20% granular bainite.

Bose-Filho *et al* [142] analysed the effects of Ti, Ni, Mo and Cr on microstructural development and the chemical composition of non-metallic inclusions in HSLA weld metal. The study found that increasing the Ti content, in the range of 50 to 400 ppm, caused no major effects on microstructural development. With a further increase in the hardenability, by Ni, Mo and Cr additions, the microstructure changed from a mixture of GBF, Widmanstätten ferrite, acicular ferrite and microphases to a mixture of acicular ferrite, bainite, low C martensite and microphases. In weld metals with low Ti content, Mn and Si were the main chemical elements present in inclusions. Increasing the Ti content in the weld metal leads to an increase in the Ti content of the inclusions.

Beidokhti *et al* [143] focussed solely on the effect that Ti additions had upon the microstructure in the SAW joint of API-5L grade X70 pipeline steel. The relationship

between microstructure and toughness of the weld deposit was studied by means of full metallographic, longitudinal tensile, Charpy-V notch and HIC tests on the specimens cut transversely to the weld beads. The best combination of microstructure and impact properties was obtained in the range of 0.02–0.05% Ti. By further increasing of Ti content, the microstructure was changed from a mixture of acicular ferrite, grain-boundary ferrite and Widmanstätten ferrite to a mixture of acicular ferrite, grain-boundary ferrite, bainite and ferrite with M/A micro constituent. Therefore, the mode of fracture also changed from dimpled ductile to quasi-cleavage. The results showed an increase in the Ti content of inclusions with increased Ti levels of weld metal. Ti-base inclusions improve impact toughness by increasing the formation of acicular ferrite in the microstructure. No HIC susceptibility was found in the weld metals with Ti contents less than 0.09%.

The high heat input from the SAW process subjects the area in the immediate vicinity to the fusion line temperatures close to melting point. The effect that this has upon the microstructure and mechanical properties within the region will now be discussed.

2.2.7. Phase transformations and grain growth in the heat affected zone

The term heat affected zone describes the weld region in the immediate vicinity to the weld joint. The thermal exposure from the submerged arc welding process described in Chapter 2.2.1 isn't high enough to cause melting in this region, but, it is sufficient enough to cause significant re-crystallisation, grain growth, and solid state phase transformations to develop. Figure 2-16 describes temperature dependant phase transformations in terms of the Fe-C equilibrium phase diagram. The thermal exposure decreases with distance from the SAW joint until a point at which the base metal is completely unaffected by the heat input of the welding process.

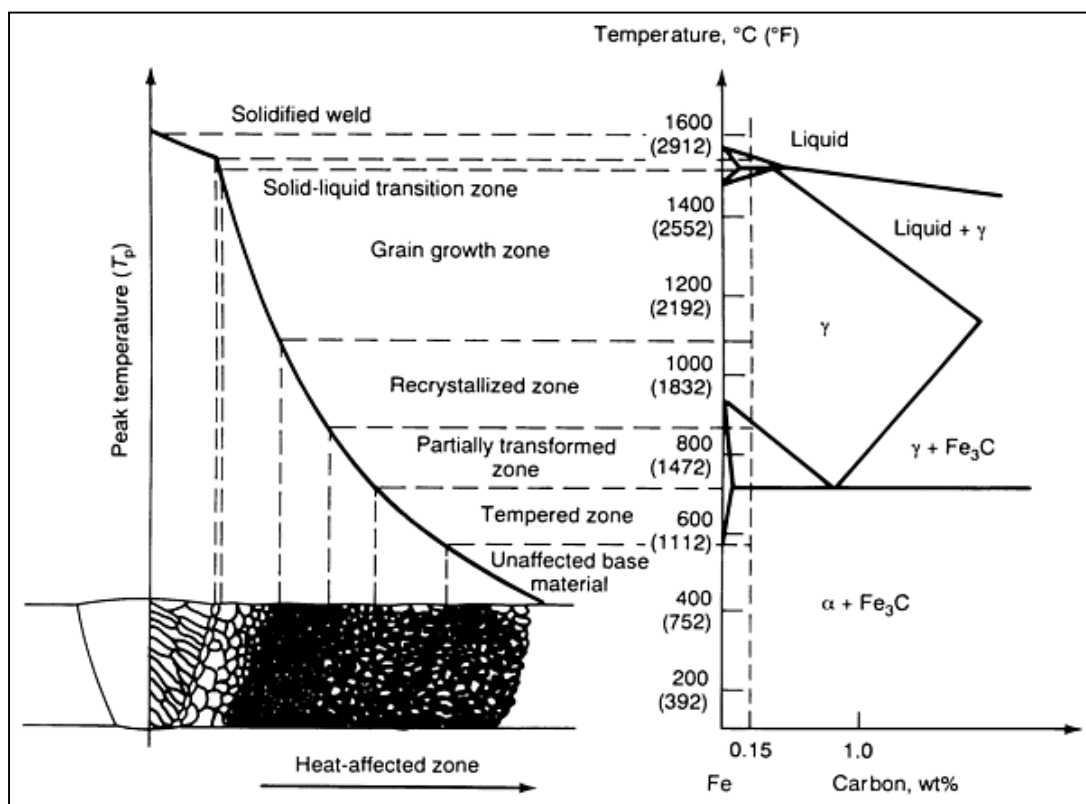


Figure 2-16: A schematic diagram of the sub-zones of the heat affected zone explained in terms of the Fe-C equilibrium phase diagram for a 0.15 wt.% C alloy [79].

The most widely studied HAZ region is the grain growth zone; more commonly termed the coarse-grained heat affected zone (CG-HAZ). The CG-HAZ is generally found as the location for the initiation for brittle fracture [73]. The low toughness properties in

the CG-HAZ are commonly attributed to its large prior austenite grain size which increases the DBTT, and also the presence of low toughness microstructures such as M/A constituents [144, 145].

To improve HAZ toughness, Ti is commonly added to HSLA linepipe steel to enhance weldability. The enhanced weldability is due to the Ti forming thermally stable TiN particles which at a suitable size will suppress austenite grain coarsening in the weld HAZ [125, 146]. However, coarse (over 0.5 μm) TiN particles formed through excessive Ti additions, or particle coarsening at high temperature have been found to be ineffective in pinning the grain boundaries and instead act as cleavage initiation sites [125, 130, 131, 147, 148].

In view of this, considerable effort has been placed on the development of mathematical models to simulate and predict precipitate nucleation and growth with HSLA steels. Deschamps [149] considered the time evolution of the density number of precipitates and the mean precipitate radius, while Kampmann and Wagner [150] introduced the modelling of a size distribution function of precipitates, which evolves using growth and nucleation laws.

In practice, the control of precipitate size can be difficult. The TiN particles inherently have a lower solubility in the matrix and a high resistance to particle coarsening [151, 152]. However, the particles still grow and dissolve in the CG-HAZ where temperatures easily exceed 1200°C. The growth of precipitates at high temperature is commonly discussed in terms of Ostwald ripening [153, 154]. Ostwald suggested that the solute (Ti and N atoms) atoms from the dissolution of less stable nitride and carbide particles (of lower dissolution temperature) would supersaturate and uniformly distribute in the austenite matrix. Figure 2-17 is a schematic illustration of the theory.

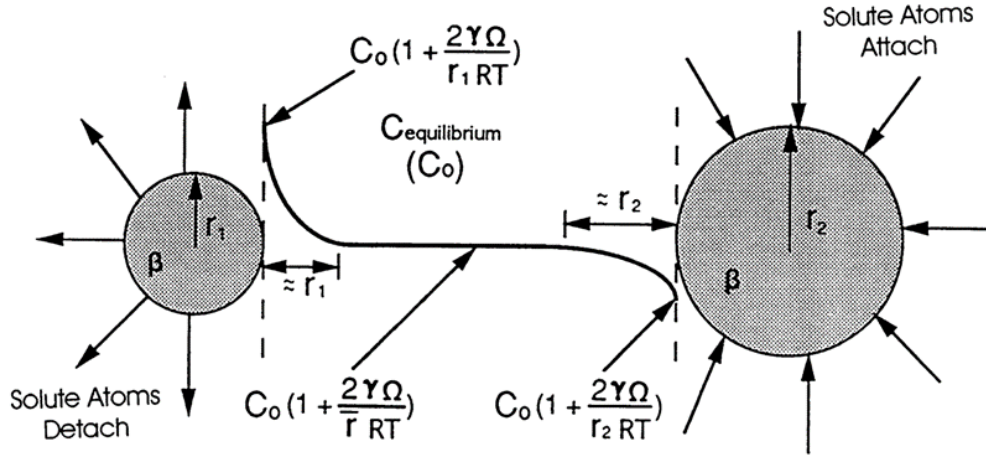


Figure 2-17: Two β precipitates of radius r_1 and r_2 dispersed in an α matrix. The radii r_1 and r_2 are less than and greater than the average particle radius [155].

The smaller particle is assumed to be smaller than the average particle size and the larger particle, larger than the average particle size of the population. Both precipitates are surrounded by a matrix supersaturated with solute atoms.

Due to the Gibbs-Thomson effect [156], the solute concentration in the matrix adjacent to a particle will increase as the radius of curvature decreases. Therefore, there will be concentration gradients in the matrix which will cause solute to diffuse in the direction of the largest precipitates away from the smallest. Figure 2-17 shows that solute atoms detach from the smaller particle, diffusing through the matrix of equilibrium solute concentration (C_0), and then attach onto the surface of the larger particle. The diffusion is driven by the chemical potential gradient that exists between these two different size particles as expressed in the following relationship [155]:

$$C_0 \left(1 + \frac{2\gamma\Omega}{r_1 RT} \right) > C_0 \left(1 + \frac{2\gamma\Omega}{r RT} \right) > C_0 \left(1 + \frac{2\gamma\Omega}{r_2 RT} \right) \quad (2-16)$$

The overall result is that the total number of precipitates decreases and the mean radius (\bar{r}) increases with time. By assuming volume diffusion is the rate controlling factor, it has been shown that the following relationship should be obeyed [157]:

$$(\bar{r})^3 - r_0^3 = kt \quad (2-17)$$

and,

$$k \propto D\gamma X_e \quad (2-18)$$

where, r_0 is the mean radius at time $t = 0$, D is the diffusion coefficient, γ is the interfacial energy and X_e is the equilibrium solubility of very large particles. Since D and X_e increase exponentially with temperature, the rate of coarsening will increase rapidly with increasing temperature – a key consideration in view of the high temperature welding process.

It is well known that precipitates such as Ti nitride can be distributed along the austenite grain boundaries. In this case, other diffusion mechanisms such as grain boundary diffusion are also expected to accelerate precipitate growth. A schematic illustration of precipitation growth by grain boundary diffusion can be seen in Figure 2-18.

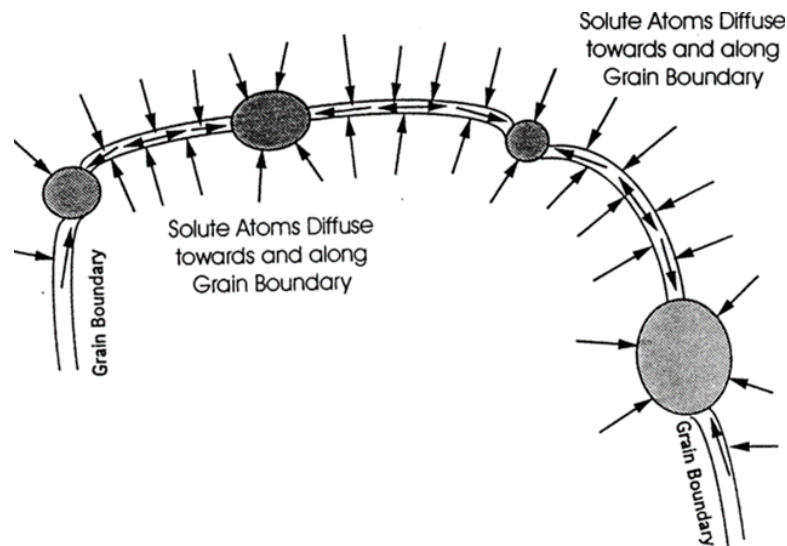


Figure 2-18: Schematic illustration of grain boundary diffusion [155].

Solute atoms, Ti and N, depending on their location, will first diffuse to the nearby austenite grain boundaries and then to the precipitates via the grain boundary. Meanwhile, the small precipitates anchored along the grain boundaries may also dissolve and release solute atoms to the grain boundary which then diffuse rapidly to the large precipitates, promoting growth of these particles.

2.2.8. Weld residual stresses

Residual stresses are self-equilibrating stresses within a stationary solid body when no external force is applied. As such, they are not particularly obvious and can be hard to measure. Residual stresses can be defined as either macro or micro-stresses and both may be present in a component at any one time. They can be classified as [158]:

- Type I: Macro residual stresses that develop in the body of a component on a scale larger than the grain size of the material.
- Type II: Micro residual stresses that vary on the scale of an individual grain.
- Type III: Micro residual stresses that exist within a grain, essentially as a result of the presence of dislocations and other crystalline defects.

Residual stresses are generated during most manufacturing processes involving material deformation, heat treatment, machining or processing operations that transform the shape or change the properties of a material. They originate from a number of sources and can be present in unprocessed raw material, introduced during manufacturing or arise from in-service loading. Typically, residual stresses originate from:

- Differential plastic flow;
- Differential cooling rates;
- Phase transformations with volume changes.

Shape misfits between the unstressed shapes of different parts, regions, or phases within a component are the root of the stresses. In welded linepipe, they are formed in the structure as the result of differential contractions which occur as the weld metal solidifies and cools to ambient temperature. In fact, welding introduces high heat input to the material being welded. As a result of this, non-uniform heat distributions, plastic deformations and phase transformations are induced in the material. Residual stresses induced by shrinkage of the molten region are usually tensile. Transformation induced residual stresses occur in the parts of the HAZ where the temperature exceeds the critical values for phase transformations. When the effect of phase transformations is dominant compressive residual stresses are formed in the transformed areas [159].

Tensile residual stress, in particular, can be a very important factor in affecting the reliability and integrity of the pipeline. The formation of tensile residual stress may result in reduced fatigue life [160], distortion, dimensional stability, corrosion resistance, stress corrosion cracking [161], or other types of fracture [162, 163].

For solidification cracking during welding to occur, tensile stresses must be present during the solidification process. As such, residual stresses have to be considered as a crucial data input for accurate engineering critical assessments of offshore pipelines [164, 165]. Engineering critical assessments for offshore pipelines have so far been based on the assumption that the residual stresses in the UOE pipe seam weld are equal to the yield strength of the parent material [164, 165]: an assumption that is likely to cause over-conservatism in conventional pipeline design. It is therefore necessary to understand the development residual stresses in the UOE linepipe manufacturing process to provide quantitative knowledge in order to challenge such over-conservatism. The over-conservatism must be addressed without compromising safety, especially at times of economic uncertainty [166].

The role of residual stresses in engineering failure has drawn significant attention from scientists and researchers in recent years [167, 168]. As such, several techniques for measuring residual stresses have been developed as summarised in Figure 2-19. However, the techniques are limited by their spatial resolution and penetration depth of measurements, as described in Figure 2-20.

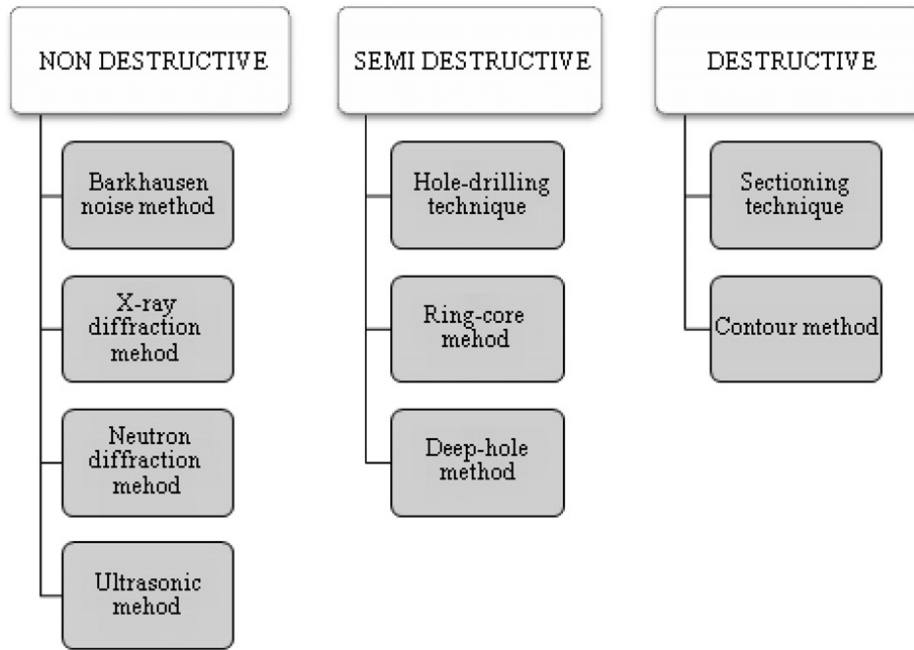


Figure 2-19: Methods of residual stress measurement [158].

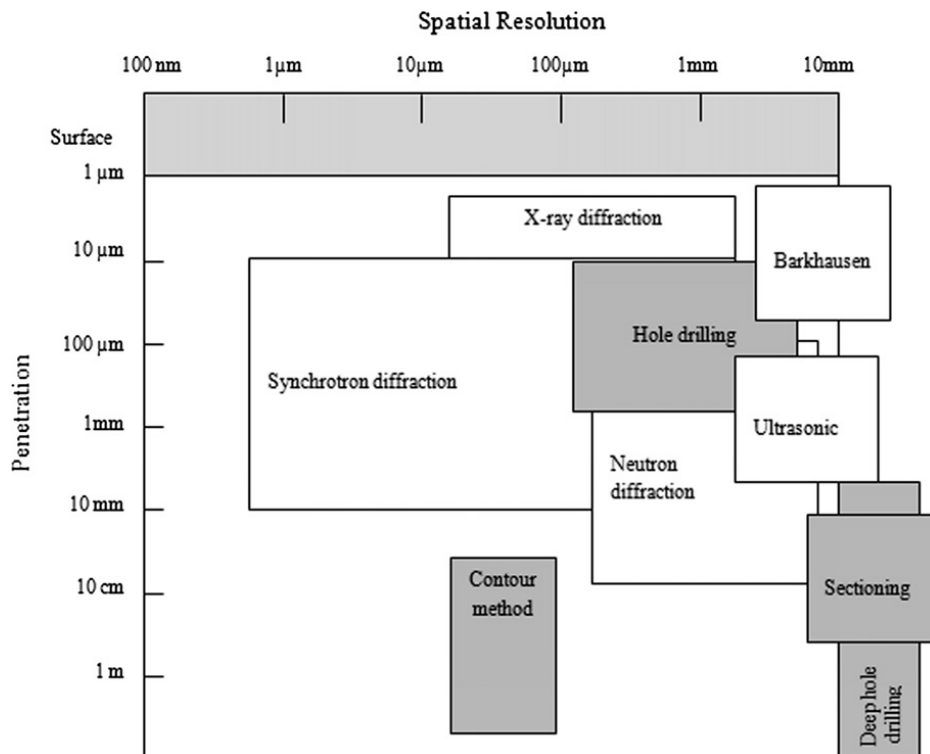


Figure 2-20: Penetration and the spatial resolution of the various techniques. The destructive and semi destructive methods are coloured grey [158].

Of the non-destructive methods, for fairly large diameter linepipes, the contour method appears most appropriate. The contour method, first proposed in 2000 [169], is a newly invented relaxation method that enables a 2D residual stress map to be evaluated on a plane of interest. The contour method provides higher spatial resolution, while the sectioning technique is easier to apply since almost no calculations are needed. The theory of the contour method is based on a variation of Buckner's elastic superposition principle [170] and primarily involves four steps: specimen cutting, contour measurement, data reduction and stress analysis. The method is favourable for its high-resolution maps of the stress normal to the cut surface and application to large structures. However, it can be hard to interpret results and non-destructive methods are preferred when available.

Non-destructive techniques such as the magnetic Barkhausen noise method [171], and the x-ray diffraction technique [172] have been utilised to measure weld residual stresses. Yet the development of neutron diffraction techniques over the past two decades has put the methodology at the forefront due to the improved penetration characteristics offered by the neutrons [173], essential for the analysis of thick walled steel linepipes.

The production of neutron particles is difficult and expensive. Presently, two sources produce beams of thermal neutrons: nuclear fission (steady state) reactors and neutron spallation (pulsed) sources. A schematic illustration of ISIS neutron spallation facility is given in Figure 2-21.

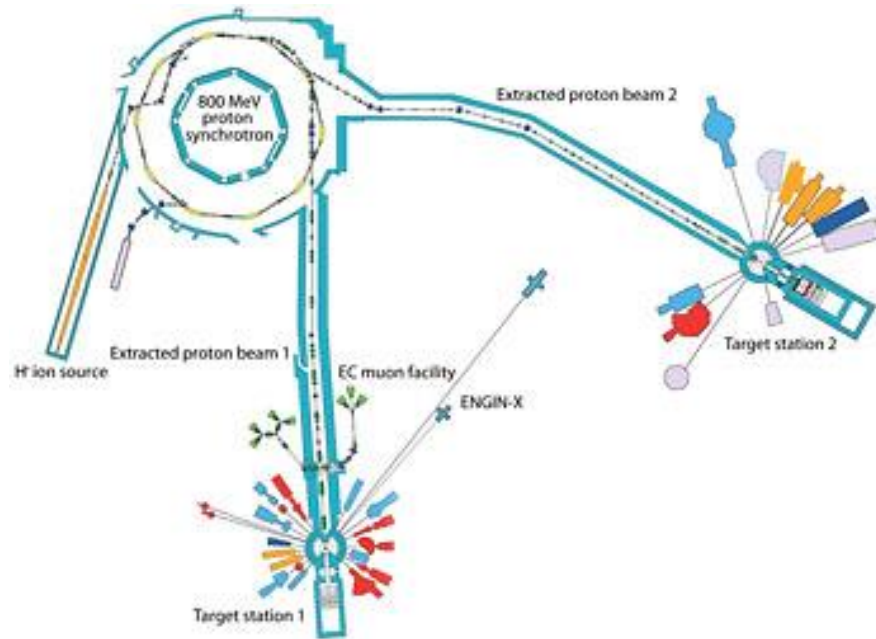


Figure 2-21: Plan of the ISIS facility (spallation source and instruments) [174].

In a neutron spallation source, sharp pulses of high energy protons accelerated in a synchrotron hit a target of high atomic mass (Pb, W, Ta or U). As a consequence of the subsequent nuclear reactions, the target nuclei are put in a highly excited state. The nuclei then decay by “evaporating” neutrons. Because of the pulsed nature of the incident proton beam, the spallation reaction produces sharp pulses of neutrons of very high energy (in the MeV range). The spallation process has the advantage of a much lower heat production in the target, and high neutron brightness in the pulse [175].

Instruments on pulsed sources generally use a polychromatic (white) neutron beam and are based on time of flight (TOF) techniques, such as neutron strain scanning (neutron diffraction). The aim of TOF neutron strain scanner is to define the macroscopic elastic strain tensor at definite locations in the bulk of a specimen; a schematic is shown in Figure 2-22.

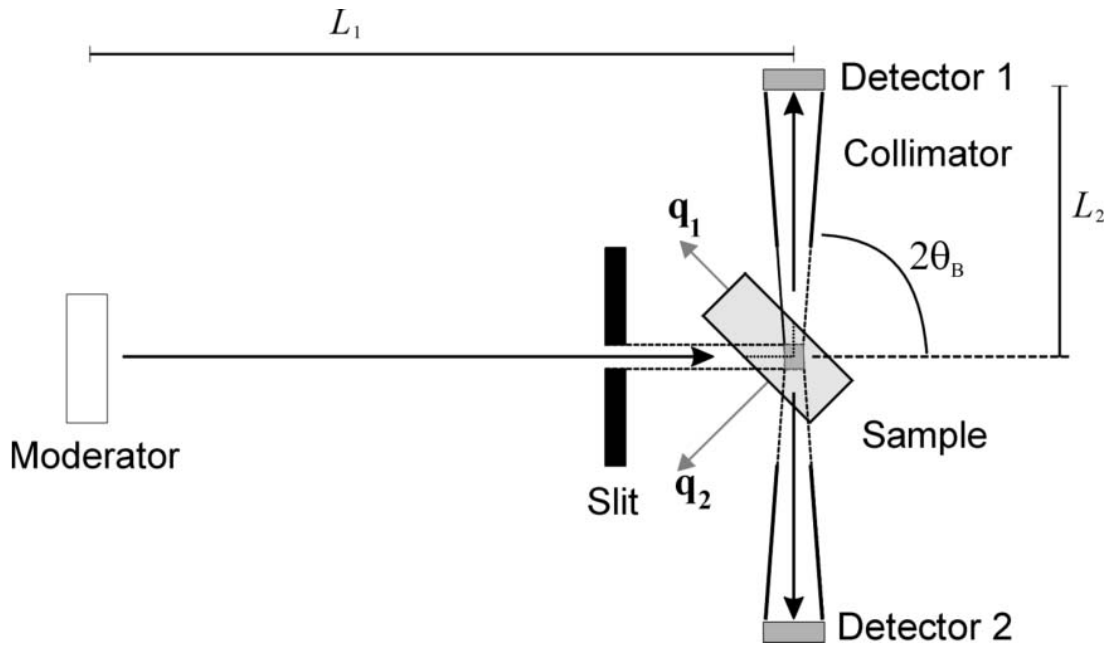


Figure 2-22: Schematic diagram of a time-of-flight neutron strain scanner. The elastic strain is measured along the directions of the impulse exchange vector, q_1 and q_2 . The volume of the sample explored by the instrument corresponds to the intersection of incident and diffracted beams, as defined by slits and collimators [176].

A pulsed beam of neutrons with a wide energy range travels to the sample, where a small fraction of the beam is scattered into a detector at an angle $2\theta_B$. Assuming an elastic collision, the wavelength of the detected neutrons is defined from its TOF t :

$$\lambda = \frac{h}{m(L_1+L_2)} t \quad (2-19)$$

with h being Planck's constant, m the neutron mass and L_1 and L_2 the primary and secondary flight paths, respectively. A typical spectrum diffracted by a polycrystalline material is shown in Figure 2-23.

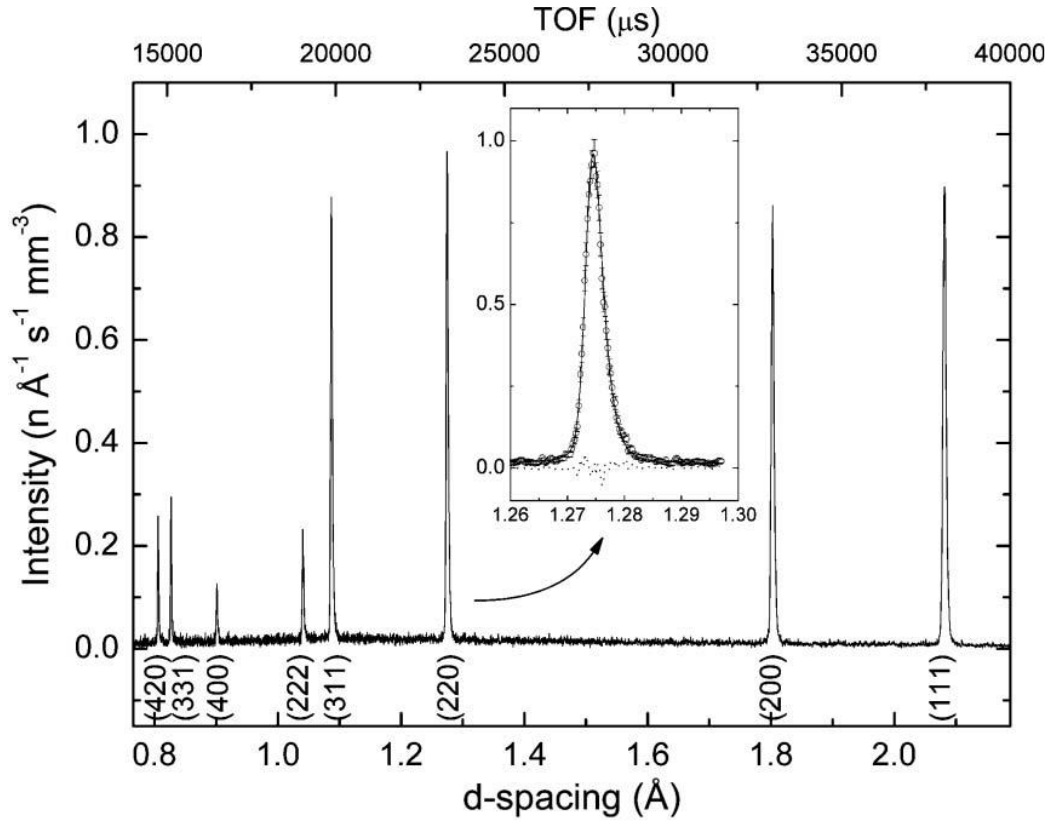


Figure 2-23: Typical TOF diffraction spectrum on ENGIN-X, in this case for a stainless-steel specimen. The elastic strain is calculated from the shift in the peak positions defined through a least-squares refinement. The macroscopic strain is obtained from the change in lattice parameter given by a full-pattern refinement [176].

Each peak corresponds to a (hkl) family of lattice planes as given by Bragg's law [177], $\lambda_{hkl} = 2d_{hkl} \sin \theta_B$, so the d -spacing is obtained from the position t_{hkl} of the peak in the TOF spectrum:

$$d_{hkl} = \frac{h}{2 \sin \theta_B m(L_1 + L_2)} t_{hkl} \quad (2-20)$$

Peak positions can be precisely determined by least-squares refinement of the peaks. The elastic strain is determined from the change in the atomic inter-planar distances between the strained and unstrained sample ($\Delta d = d - d_0$). Any change in lattice spacing, will result in a change in λ or θ and strain ε is given by:

$$\varepsilon = \frac{d - d_0}{d_0} \quad (2-21)$$

The volume of material contributing to the diffraction pattern corresponds to the intersection of the incident and diffracted beams, typically defined by slits and collimators, respectively. The centroid of this gauge volume (typically of the order of cubic millimetres) defines the location of the measurement. In a neutron strain scanning instrument, the gauge volume is fixed at a position in the laboratory, so the strain variation across the sample is explored by moving the sample using a translation stage.

The measured strain gives the component of the strain tensor along the direction of the neutron wave-vector change q , which bisects the incident and diffracted beams (Figure 2-22). For pipe samples, the principal components coincide with the hoop, axial, and radial directions defined in Figure 2-24.

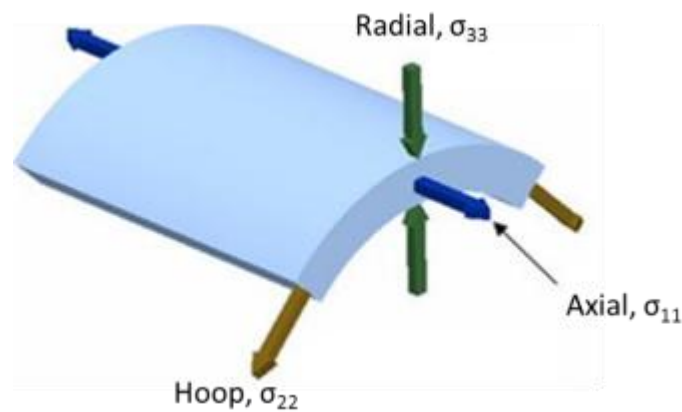


Figure 2-24: Schematic illustration of strain components in a linepipe.

Measurements of strain in these three orientations are required to completely define the stress tensor at any given point. When the principal directions coincide with these coordinate directions and the material is isotropic with a Young's modulus E and Poisson's ratio ν , the principal stresses are obtained from Hooks law of linear elasticity:

Axial Direction:

$$\sigma_{11} = \frac{E}{1-\nu} \left[\varepsilon_{11} + \frac{\nu}{1-2\nu} (\varepsilon_{11} + \varepsilon_{22} + \varepsilon_{33}) \right]$$

Hoop Direction:

$$\sigma_{22} = \frac{E}{1-\nu} \left[\varepsilon_{22} + \frac{\nu}{1-2\nu} (\varepsilon_{11} + \varepsilon_{22} + \varepsilon_{33}) \right]$$

Radial Direction:

$$\sigma_{33} = \frac{E}{1-\nu} \left[\varepsilon_{33} + \frac{\nu}{1-2\nu} (\varepsilon_{11} + \varepsilon_{22} + \varepsilon_{33}) \right] \quad (2-22)$$

The NSS technique is conceptually very simple but its practical application can be time-consuming. Very long counting times are required when small gauge volumes and large penetration depths are involved, which effectively dictates the range of problems that can be studied with this technique. Withers [178] defined a ‘maximum acceptable acquisition time’ for neutron strain scanning when measuring strain deep within materials. This is an important concept because NSS experiments are performed at large facilities, where the experimenter is granted a limited amount of beam time, under competitive review. Hence, a minimization of the experimental time required for an accurate determination of peak positions (and hence strain) is the first goal of an optimized strain scanner.

Previous residual stress studies on SAW pipeline steels using the neutron diffraction technique [179, 180] have shown that the maximum residual stresses developed as a result of the SAW are well below the materials yield strength. This knowledge has insinuated that current pipelines are quite possibly being designed with a much higher safety factor than what may ultimately be required. In a highly competitive industry, quantitative proof of this design conservatism is paramount for the refinement of pipeline design. Refinement to pipeline design will promote cost reduction through the application of thinner walled vessels to more adverse operation conditions.

Previously, FE techniques were developed for prediction of weld residual stress and distortion [181, 182]. These techniques were then used in the through-process modelling of UOE linepipe manufacture to investigate the initiation of weld residual stresses due to SAW seam welding and its subsequent evolution due to mechanical expansion [183-185]. However, experimental data for model validation was scarce [185]. Although neutron diffraction has been shown to be a well-established technique for weld residual stress measurement [186, 187], only a few papers were found in the literature dealing with pipe girth welds [188, 189]. Even scarcer are investigations of UOE pipe seam welds.

3. Literature survey on solidification cracking during welding

Weld solidification cracking defects were first introduced in Chapter 1.3 and some of the contributing factors to solidification cracking during welding have been defined in Chapter 2. In this chapter, a comprehensive review on the historical research and current work in the area of solidification cracking will be presented.

3.1. Introduction

3.1.1. The solidification stages when cracking can occur

As the liquid weld pool cools, solidification begins. The solidification process in steel is usually divided into three different stages based on the permeability of the solid network. Stage 1 represents the formation of dendrites during solidification and mass feeding. As the steel weld metal starts to solidify, it does so in a dendritic structure. While cooling, secondary dendrite arms form at a short distance behind the primary dendrite tips. These dendrites have no mechanical bond with each other, as they are separated by liquid steel. Consequently, the shell at this location has little or no strength as both liquid and solid are free to move. At this stage, the name “mushy zone” is misleading, as it is actually a slurry with the newly formed dendrites suspended in the liquid. Only after the temperature has dropped below the coherency point, a real mush is formed [190]. If thermal strain is imposed on the semisolid material at this early stage of solidification, the resulting opening in the structure can be filled by inter-granular or inter-dendritic liquid [191].

Upon further cooling, at stage 2, dendrites coarsen and impinge on one another. This stage can be divided into two sub-stages, as follows:

(a) Coarsening of dendrites during solidification and inter-dendritic feeding: Secondary dendrite arms begin to reach out and interlock with each other and the individual dendrites start to connect with each other giving the solidified shell some strength. However, at this stage, the permeability of the network is still large enough to prevent defect formation by melt feeding.

(b) Coarsening of dendrite arms and inter-dendritic separation: Dendrites reach the stage when the interlocked secondary dendrite branches become indistinguishable. As the temperature drops further, the structure starts to resemble columns without visible dendrite branching.

In terms of weld solidification cracking, only the final stages of solidification (stage 2b and 3) are of interest. At Stage 2b ($f_s \sim 0.8-0.9$), with increasing solid fraction, liquid is isolated in pockets or immobilized by surface tension. During these sub stages, as liquid is trapped between interlocking dendrites, the free passage for liquid is blocked, transforming continuous liquid films into isolated liquid droplets. As a result, the strength of the material is very low due to the existence of this non continuous liquid film between the primary dendrites. If an external stress is applied to the material, then solidification cracking (hot tearing) can easily occur.

Stage 3 ($f_s > 0.9$) marks the transition from the dendritic to the grain structure. At this stage, the boundaries of the primary dendrites become invisible on polished sections. A thin liquid film can still be present at the grain boundaries due to the presence of segregated elements in the liquid, lowering the melting point of this film. Solidification cracks formed at this stage are named grain-boundary or inter-granular cracks, or hot cracks to distinguish them from the hot tears formed during stage 2b. Solid-state creep is the only way to accommodate solidification shrinkage and thermal stresses at this stage.

Weld solidification cracking is an important issue in fusion welding. If undetected, the defects act as stress concentration sites which lead to premature failure via fatigue, as well as offering favourable sites for hydrogen assisted cracking [4, 5] and stress corrosion cracking [6]. Because of this, solidification cracks are considered the most deleterious of all the welding defects. They are widely studied [29] and have been the subject of investigation for several decades [192-198].

3.1.2. The Trans(Varestraint) weldability test

In the welding industry, the (Trans)Varestraint test is widely used for assessing the weldability of steel [4, 11, 15, 18, 29, 30, 87, 199-202]. However, the test itself has never been fully standardized and many variations (over 200) are currently used around the world [203] making comparisons between tests unreliable.

The Variable Restraint, or Varestraint test was developed in the 1960's by Savage and Lundin at Rensselaer Polytechnic Institute [204]. The test itself is fairly simple in nature and can operate under strain control, strain rate control, or stress control [205]. The test is designed to separate the metallurgical variables that cause solidification cracking during welding. A tungsten inert gas (TIG) welding process is the most commonly used welding method for these tests, although other fusion welding processes can also be used. Welds are normally autogenous, although filler deposits can be tested using special samples [205].

The weld is laid on the top surface of a sample either longitudinal (Varestraint, Figure 3-1(a)) or transverse (Transvarestraint, Figure 3-1(b)) to a loading device/bending block. Near the end of welding, a load is applied to ends of the sample. Bending (strain) is normally applied very rapidly, and is provided by accurate loading devices, capable of maintaining high linear strain accuracy. The bending load can be applied during welding, or exactly when the arc is extinguished, at the time when the welding torch is positioned at a pre-determined point over the dye curvature. [206]

The load deforms the sample around the radius of a bending block. The deformation induces a strain to the weld. The strain is controlled by the sample thickness, t , and radius of the die block, R , as described below:

$$\varepsilon = \frac{t}{2R+t} \quad (3-1)$$

The augmented strain cause's solidification cracks to develop in the weld metal, and sometimes HAZ as liquation cracks.

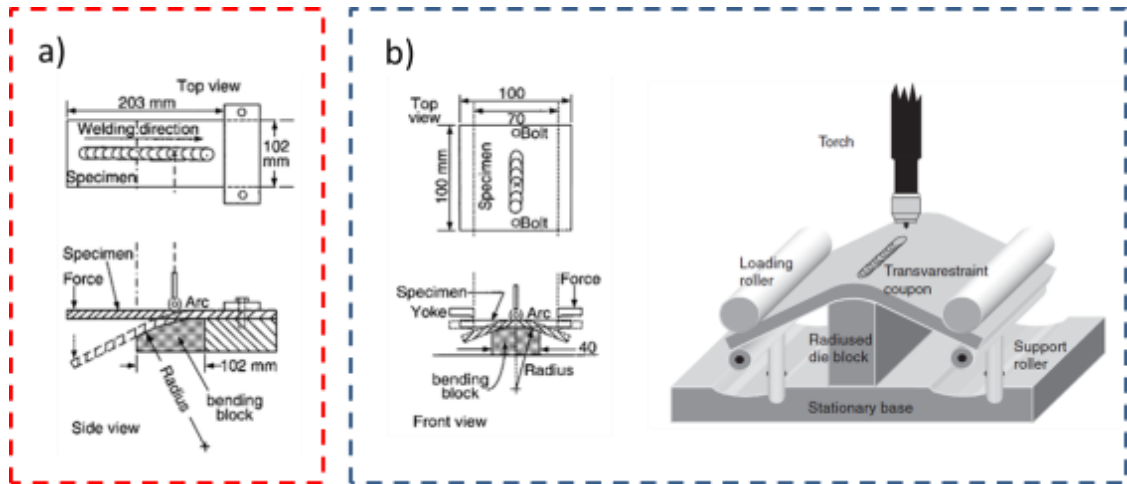


Figure 3-1: Schematic illustration of the (Trans)Varestraint test, showing a) Varestraint and b) Transvarestraint tests.

The key criterion for assessing the susceptibility of a metal to weld solidification cracking is defined below:

Total Crack Length (TCL) – The summation of all the individual crack lengths.

Maximum Crack Length (MCL) – The length of the largest crack observed on the sample surface.

Maximum Crack Distance (MCD) – A more recently developed concept created to allow more accurate determination of the cracking temperature range.

Brittleness Temperature Range (BTR) – Temperature range of cracking during solidification.

Threshold Strain – Strain at which cracking initiates.

Saturated Strain – Critical strain level at which damage stops with increasing strain.

Solidification Cracking Temperature Range (SCTR) – Temperature range over which cracking occurs, and a subset of the BTR.

In the Varestraint test, the TCL and cracking threshold strain are considered the most important assessment criteria [207], while in the Transvarestraint test the MCL is used for assessment.

3.2. Solidification cracking theories and criterion

A compilation of the prior research in this field has been reported by Sigworth [25] and Eskin [190]. Several mechanisms for solidification cracking and the conditions which stimulate it are already suggested in literature, as outlined in Table 3-1.

Mechanisms and Conditions	Suggested and Developed by
Cause of solidification cracking	
Thermal contraction	Heine (1935), Pellini (1952), Dobatkin (1948)
Liquid film distribution	Vero (1936)
Liquid pressure drop	Prokhorov (1962), Niyama (1977)
Vacancy supersaturation	Fredriksson et al. (2005)
Nucleation	
Liquid film or pore as stress concentrator	Patterson et al. (1953, 1967), Niyama (1977), Rappaz et al. (1999); Braccini et al. (2000), Suyitno et al. (2002)
Oxide bi-film entrained in the mush	Campbell (1991)
Vacancy clusters at a grain boundary or solid/liquid interface	Fredriksson et al. (2005)
Propagation	
Through liquid film by sliding ;	Patterson (1953), Williams and Singer (1960, 1966), Novikov and Novik (1963)
By liquid film rupture	Pellini (1952), Patterson (1953), Saveiko (1961), Dickhaus (1994)
By liquid metal embrittlement	Novikov (1966), Sigworth (1996)
Through liquid film or solid phase depending on the temperature range	Guen and Hunt (1988)
Diffusion of vacancies from the solid to the crack	Fredriksson et al. (2005)
Conditions	
Thermal strain cannot be accommodated by liquid flow and mush ductility	Pellini (1952), Prokhorov (1962), Novikov (1966), Magnin et al. (1996)
Pressure drop over the mush reaches a critical value for cavity nucleation	Niyama (1977), Guen and Hunt (1988), Rappaz et al. (1999), Farup and Mo (2000)
Strain rate reaches a critical value that cannot be compensated by liquid feeding and much ductility	Pellini (1952), Prokhorov (1962), Rappaz et al. (1999), Braccini et al. (2000)
Thermal stress exceed rupture or local critical stress	Lees (1946), Langlais and Griuzleski (2000), Lahaie and Bauchard (2001), Suyitno et al. (2002)
Stresses and insufficient feeding in the vulnerable temperature range	Bochvar (1942), Lees (1946), Pumphrey and Lyons (1948), Clyne and Davies (1975), Feurer (1977), Kargerman (1982)
Thermal stress exceeds rupture stress of the liquid film	Saveiko (1961)

Table 3-1: Summary of solidification cracking mechanisms proposed to date (Adapted from [20]).

Over the years, much more effort has been put on the conditions required for solidification cracking occurrence rather than on the mechanisms of crack initiation and propagation. When it comes to the nucleation and propagation of solidification cracks, an educated guess frequently replaces experimental proof. Figure 3-2 also shows that the conditions for and causes of solidification cracking can be considered on different length scales, from macroscopic to microscopic, and some of these conditions are important on both mesoscopic and microscopic scales.

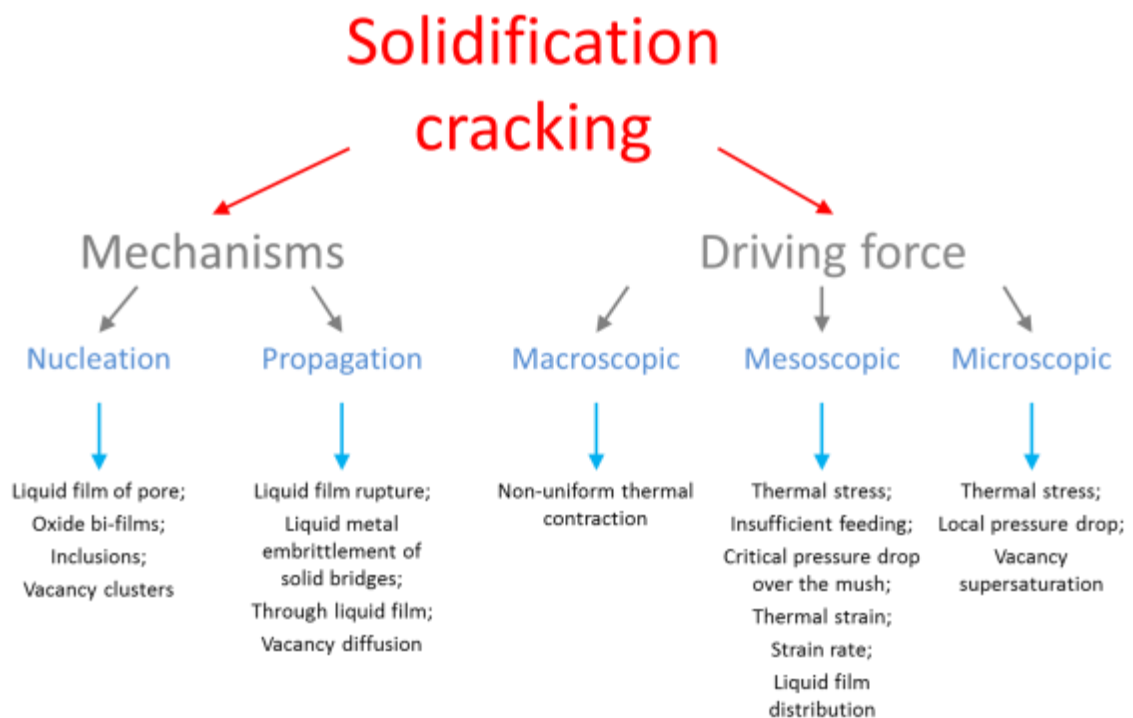


Figure 3-2: Summary of mechanisms, conditions and causes of solidification cracking proposed to date.

Today, the mesoscopic strain rate is believed to be the most important factor and some modern models are based on it. The physical explanation of this approach is that semisolid material during solidification can accommodate the imposed thermal strain by plastic deformation, diffusion-aided creep, structure rearrangement, and filling of the gaps and pores with the liquid. All these processes require some time, and the lack of time will result in fracture. Therefore, there exists a maximum strain rate that the semisolid material can endure without fracture during solidification [20].

However, it is worth noting that most of the existing solidification cracking criteria deals with the conditions rather than with the mechanisms of solidification cracking. In the following discussion, some of these mechanisms described in literature will now be evaluated in more detail.

The solidification cracking theories used in welding today originate from the studies of solidification to describe hot tearing in casting. Some of the first studies of importance were:

- Pellini's "Strain theory of hot tears" [196]
- Humphrey & Jennings "Shrinkage-Brittleness theory" [197].
- Borland's "Generalised theory" which later combined and modified both of the above [195].

All these solidification cracking theories are similar in the agreement that the presence of a liquid phase, when combined with thermally and mechanically induced strain increases the materials susceptibility to cracking. Pellini proposed the "strain theory" [196] relating to the formation of a continuous liquid film which separates the solidifying metal. The strength and ductility of these solid grains separated by a continuous liquid film is very low and was accepted as the "Film stage" [196]. As thermal contraction and shrinkage stresses increase appreciably near the solidus temperature, this film stage causes inter-granular rupture. Humphrey and Jennings shrinkage-brittleness theory on the other hand recognised the inability of the newly formed dendrites to accommodate strain [197]. Later, Borland proposed a new "generalized theory" [195] modified on some of the previous theories.

It is evident from these early studies, that solidification shrinkage and thermal contraction impose strains and stresses on the solid network, and without these shrinkage strains, solidification cracks would not develop. Therefore, it is argued that it is mainly the strain and the strain rate, which are critical for solidification cracking [39, 196].

Novikov and Novik [208] reported that at low strain rates, grain boundary sliding is the main mechanism of deformation of a semi-solid body. The load applied to the semi-solid body will be accommodated by a grain boundary displacement that is lubricated

by liquid film surrounding the grain. Prokhorov [209] proposed a model for deformation of the semi-solid body. It was proposed, if two tangential forces were applied to the equilibrium semi-solid body, the response of the body would manifest as grain movement and at some point the grains will touch each other. The liquid covering the grain will circulate to the lowest pressure point. Further deformation will be possible if the surface tension and resistance to liquid flow are sufficient to accommodate the stress imposed. If not, a brittle inter-granular fracture or solidification crack will occur. In relation to this theory, Prokhorov proposed that: (1) an increase in film thickness increases the fracture strain, (2) a decrease in grain size increases the fracture strain, (3) any non-uniformity of the grain size will decrease the fracture strain. Based on this theory, the main measure for solidification cracking is the ductility of the semi-solid body. A solidification crack will occur if the strain of the body exceeds its ductility.

The theory of shrinkage-related brittleness divides the solidification range into two parts. In the upper part the coherent solid-phase network does not exist. Cracks or defects occurring in this stage can be healed by liquid flow. As the solidification progresses and the solid fraction further increases a coherent network is formed. This stage is considered as the start of linear shrinkage. Continued cooling past the coherency point, imposes the shrinkage stress onto the semisolid body. Fracture or solidification cracking occurs if the shrinkage stress exceeds the rupture stress [198].

Pellini's strain theory [196] was based on strain accumulation with the following key considerations: (1) cracking occurs in a hot spot region, (2) solidification cracking is a strain-controlled phenomenon which occurs if the accumulated strain in the hot spot reaches a certain critical value, and (3) the strain accumulated at the hot spot depends on the strain rate and time required for a sample to pass through a film stage. The most important factor of solidification cracking based on this theory is the total strain on the hot spot region. Pellini's strain theory is also the basis for a solidification cracking criterion proposed by Clyne and Davies [210].

Some authors suggest that it is not the strain but the strain rate which is the critical parameter for solidification cracking. The physical explanation of this approach is that the strain rate during solidification is limited by the minimum strain rate at which the

material will fracture. Prokhorov [209] first suggested a criterion based on this approach. More recently, a strain-rate based hot tearing criterion is proposed by Rappaz *et al* [24].

Yet another approach to the solidification cracking phenomenon is the assumption that failure happens at a critical stress. The liquid surrounding the grain is considered as a stress riser of the semi-solid body [211]. In this theory, a liquid-filled crack is considered as a crack initiator. The propagation of the crack initiator is determined by the critical stress [211]. The critical stress is mostly determined using the modified Griffith energy balance approach.

Another approach within the fracture mechanics theory is proposed by Sigworth [25] who considers the possibility of applying a liquid-metal-embrittlement concept to the solidification cracking case.

Based on the theories proposed, several solidification cracking criteria have been developed in the past decades.

Feurer [193] used fluid flow through a porous network to calculate the after-feeding by liquid metal. The criterion showed that solidification cracks will initiate when the after-feeding cannot compensate the solidification shrinkage.

Clyne and Davies [212] defined a cracking susceptibility coefficient (CSC) as the ratio between the time during which the alloy is prone to solidification cracking and the time during which stress relaxation and after-feeding can take place. These times are defined as the periods during which the fraction liquid is between 0.1 and 0.01 and between 0.1 and 0.6 respectively. The criterion was combined with a heat flow model describing the DC casting process by Katgerman [213]. This enabled the determination of the cracking susceptibility coefficient as a function of the casting parameters. Unfortunately, the above criteria are restricted in their use because they give only a qualitative indication for the solidification cracking susceptibility.

The first two-phase model, which takes into account both fluid flow and deformation of the solid network, is the Rappaz–Drezet–Gremaud (RDG) solidification cracking criterion [24]. The RDG criterion is formulated on the basis of after-feeding, which is limited by the permeability of the mushy zone. At the solidification front the

permeability is high but deeper in the mushy zone the permeability is restricted. A pressure drop along the mushy zone exists which is a function of this permeability and the strain rate. If the local pressure becomes lower than a critical pressure, a cavity is initiated. The model is implemented in a thermo-mechanical model for DC casting by Drezet *et al* [214] to predict solidification cracking during billet casting.

A further development of the RDG criterion is carried out by Braccini *et al* [39]. They included plastic deformation of the solid phase and a criterion for the growth of a cavity. The model is based on two simplified geometric models, one for a columnar dendritic and one for an equiaxed dendritic structure. Explicit relations are developed for critical strain rates and they indicate that the critical strain rate decreases with increasing solid fraction.

To summarise, many mechanisms and criterion for solidification cracking have been proposed, as summarised in Figure 3-2. However, the studies are often biased in their applicability to the continuous casting of aluminium alloys. Greater understanding of the mechanisms of solidification cracking during welding of steel is required.

3.3. Metallurgical factors which affect solidification cracking in welds

There are a number of metallurgical factors that can affect the solidification cracking susceptibility of metals; the key factors can be seen as:

- a) The solidification temperature range.
- b) The primary solidification phase.
- c) The ductility of the solidifying weld metal.
- d) The surface tension of the grain boundary liquid.
- e) The grain structure.

These factors will be presented in further detail in this chapter.

3.3.1. Solidification temperature range

The weakest and most susceptible region to solidification cracking during welding is the mushy zone where both solid and liquid exists. Therefore, the larger this solid/liquid region is, the more susceptible the metal is to cracking. In steel welds, liquid films usually manifest as a result of the segregation of low melting point eutectics containing impurities such as S, P and alloying additions such as C, Ni, Ti, Mn and Nb [4, 13, 15, 29, 33, 215, 216].

A simple measure of a material's susceptibility to solidification cracks can be calculated from the empirical formula highlighted below, using chemical composition, where the elemental values are given in percent [113]:

$$UCS = 230 C + 190 S + 75 P + 45 Nb - 12.3 Si - 5.4 Mn - 1 \quad (3-2)$$

If the UCS value is less than 10, then the susceptibility to cracking is low, whereas a value higher than 30 means that this susceptibility is high. A UCS value of between 10 and 30 allows the welding procedures to become controllable. It is evident from the empirical formula that a strong emphasis is placed upon C and S concentrations.

The segregation of the solutes, generally speaking, increases the alloys solidification (freezing) temperature range (STR) as illustrated in Figure 3-3, with S showing the most detrimental increase to the STR. A large STR promotes solidification cracking due to the increased time in which the alloy spends in the susceptible state in which thin

liquid films exist between the dendrites [20, 30] as illustrated in Figure 3-4. Due to the complexity of the mechanisms involved in solidification crack formation, several models developed to date are based simply upon the STR being used as a gauge to measure the cracking susceptibility [20, 217].

Evidently, the control of segregation and in turn the STR then becomes interesting. Differential scanning calorimetry (DSC) studies have shown the STR is heavily dependent upon the solidification cooling rate [218], while the segregation can be somewhat controlled via the primary solidification phase.

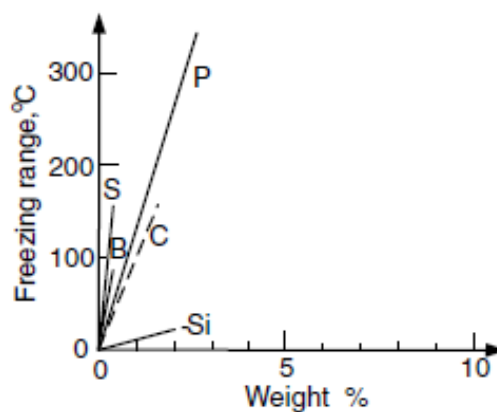


Figure 3-3: Effect of alloying elements on the solidification temperature range of carbon and low alloy steels [219].

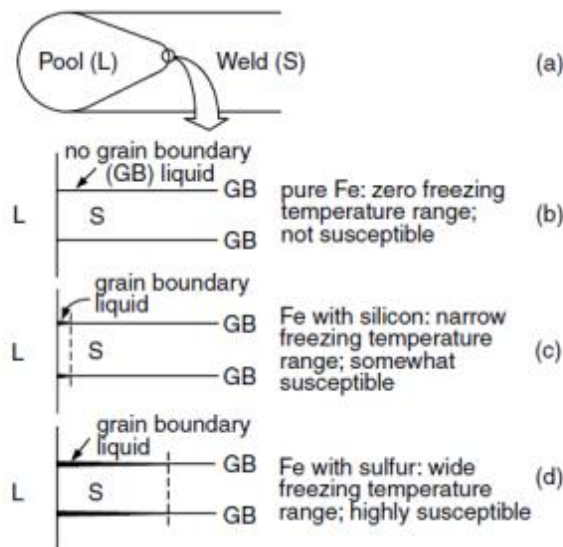


Figure 3-4: Effect of impurities on grain boundary liquid during weld solidification [13].

3.3.1. Solubility of solute elements in the primary solidification phase

In austenitic stainless steels a primary solidification phase of δ -ferrite is sought after as the harmful impurities, S and P, are less soluble in austenite than δ -ferrite [15, 29, 31, 216, 220]. However, the opposite has been found for low alloy steel weld metals [4]. In HSLA steel welds used for oil and gas applications, the continued improvements in steel making practice have resulted in impurity contents of typically only a few tens of ppm. In these low impurity welds cracking has mainly been attributed to segregation of C and Ni [221-223]. Particularly, in linepipe welding it has been found that increased cracking occurred in steels with C in the range 0.06-0.1 wt.% [224]. In addition, alloys which pass through a peritectic reaction during solidification have also been found to exhibit higher cracking susceptibilities [225] due to the associated volume shrinkage and elastic straining [226] with the former, in particular, contributing to an increasing cracking susceptibility [16].

3.3.2. Ductility of the solidifying weld metal

3.3.2.1. Ductility curve (brittle temperature range)

The less ductile a metal is, the more susceptible it will be to weld metal solidification cracking. Nakata *et al* [227] put forward a theory to determine the so called “ductility curve” of a metal, illustrated in Figure 3-5 using the (Trans)Varestraint test described in Chapter 3.1.2. Nakata stated that at any given strain, the ductility curve ranges from the liquidus temperature, T_L , to the temperature at the tip of the longest crack measured after the (Trans)Varestraint test [227].

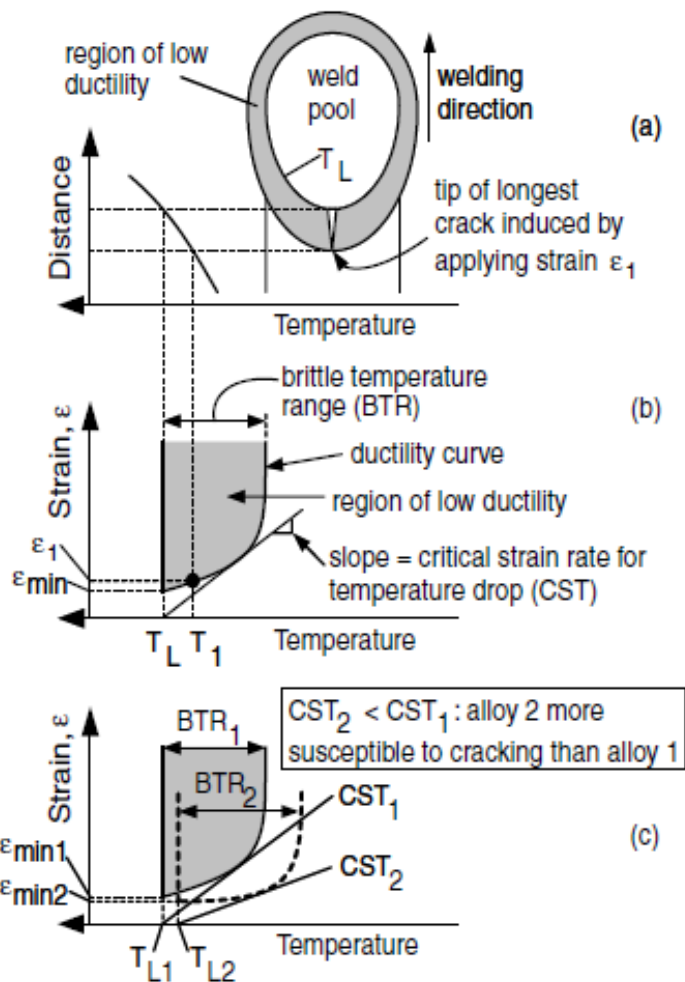


Figure 3-5: Ductility of solidifying weld metal (Adapted from [13]).

Using this theory, the ductility curve seen in Figure 3-5 can be constructed as follows:

1. A strain, ϵ_I , is applied during welding
2. Upon completion of the (Trans)Varestraint test, the maximum crack length within the weld examined and measured (Figure 3-5(a)).
3. By measuring the temperature history along the weld centreline using thermocouple recordings during welding, the temperature, T_I , at the tip of the longest crack. I.e. the point (T_I, ϵ_I) can be determined (Figure 3-5(b))
4. Repeat this procedure for various applied strains and measuring corresponding crack tip temperatures, the ductility curve can be plotted.

Figure 3-5(b) shows the maximum crack length and the temperature range of the ductility curve increasing fairly quickly initially, with the increasing strain applied. The increasing crack length and temperature range then level off as the strain is increased further.

The widest temperature range covered by the ductility curve is called the “brittle temperature range” (BTR). The weld metal is much less ductile in this temperature range in comparison with the fully solidified weld metal, or the liquidus weld pool, hence the term “brittle” in BTR.

There are two key factors that can be used to instantaneously assess the general susceptibility of a material: (i) the minimum strain required to initiate cracking, ϵ_{min} . (ii) critical strain rate for temperature drop (CST) ~ the slope of the tangent to the ductility curve seen in Figure 3-5(b) and Figure 3-5(c)

In general cases, the lower the ϵ_{min} , the greater the BTR. In other words, the smaller the CST is, the higher the susceptibility to solidification cracking, as highlighted in Figure 3-5(c).

In the case of steels and stainless steels, the solidification temperature range is relatively narrow [228], and impurities such as P and S are found to enlarge the BTR, by forming eutectics with a low melting point [15].

3.3.2.2. Solidification cracking temperature range

A similar technique was developed by Lin and Lippold [229] in which the maximum crack distance (MCD) measured over a range of augmented strains in the (Trans)Varestraint test is used to measure the solidification cracking temperature range (SCTR).

Above a critical strain level, the saturated strain, the MCD does not increase with increasing strain. This signifies that the solidification crack has propagated the full length of the crack susceptible region. By devising a test plan across a range of augmented strain, plots assessing MCD against the strain applied can be created, as shown in Figure 3-6.

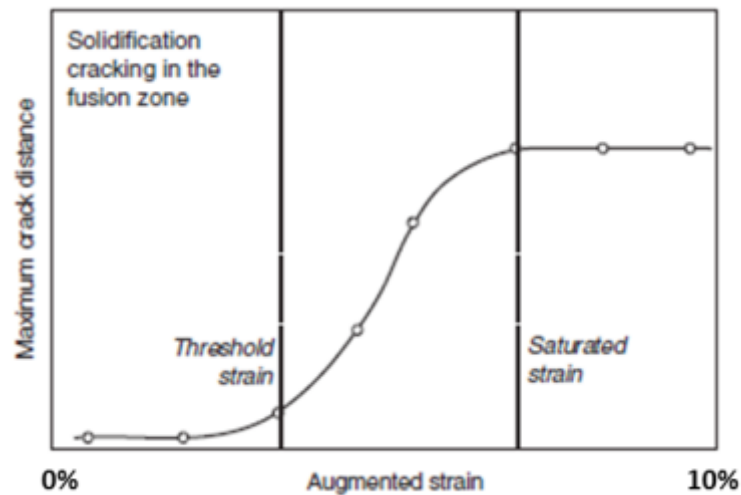


Figure 3-6: MCD vs applied strain ~ Transvarestraint test [205].

The typical strain range over which samples are tested is 0.5 – 7% [205]. The SCTR can then be determined using the following steps:

1. Measure the cooling rate across the solidification temperature range, via thermocouples located in the molten weld bead.
2. Approximate the time over which cracking occurs:

$$T_{cracking} \approx \frac{MCD \text{ above saturated strain}}{Solidification \text{ velocity}} \quad (3-3)$$

3. SCTR can then be calculated using the following relationship, where V = welding velocity:

$$SCTR = (\text{Cooling Rate}) \times \left(\frac{MCD}{V}\right) \quad (3-4)$$

The application of this method is illustrated in Figure 3-7. By using the temperature history, rather than the crack length as a measure of the materials susceptibility to cracking, variables associated with the weld (heat input, travel speed, etc) can be eliminated. SCTR then represents a metallurgically significant, material specific measure of weld solidification cracking susceptibility [203, 205].

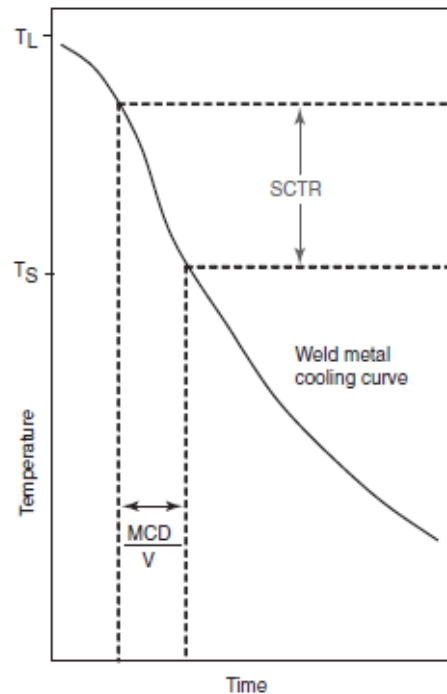


Figure 3-7: Method for determining the SCTR using the cooling rate through the solidification temperature range and MCD at saturated strain [205].

3.3.3. Surface tension of grain boundary liquid

If the surface tension between the solid grains and grain boundary liquid is very low, a liquid film will form between the grains. Figure 3-8(b) depicts the continuous liquid film and as a result of the continuous nature of the film, solidification cracking susceptibility will be high. If the surface tension is high, the liquid phase will be globular, as illustrated in Figure 3-8(c). Such discontinuous liquid globules do not significantly reduce the strength of the solid network, and therefore, are not as detrimental.

An example of this is between FeS and MnS. FeS forms films at the grain boundary, while MnS forms globules. As MnS has globular form, and a higher melting point it is preferred to FeS, as it's less susceptible to solidification cracking.

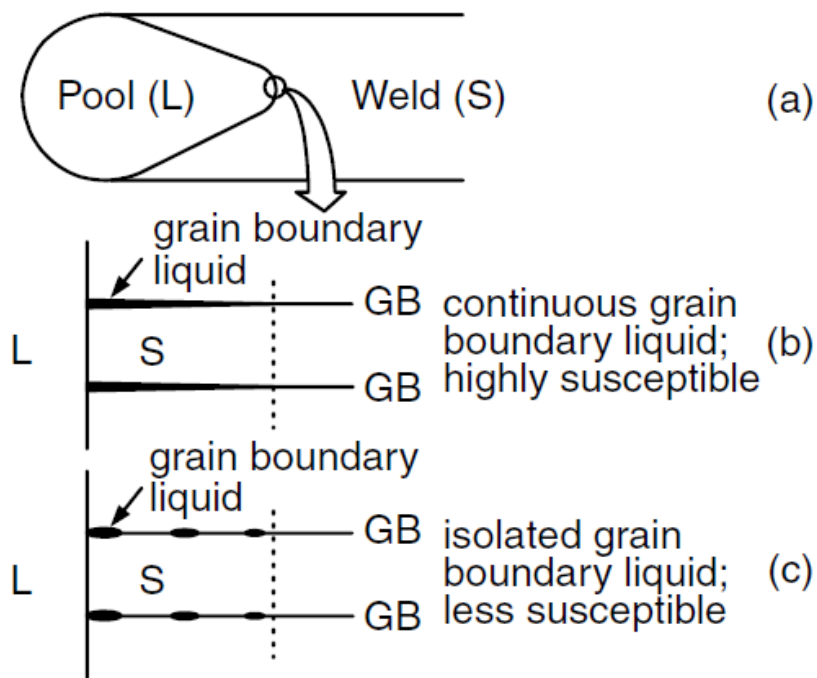


Figure 3-8: Effect of liquid grain boundary morphology on crack susceptibility (Adapted from [13]).

3.3.4. Solidification grain structure

Fine equiaxed grains are often less susceptible to solidification cracking than coarse columnar grains [227]. Fine equiaxed grains can deform to accommodate contraction strains more easily, that is, it is more ductile, than columnar grains. Liquid feeding and healing of incipient cracks can also be more effective in fine-grained material. In addition, the grain boundary area is much greater in fine-grained material and, therefore, harmful low-melting point segregates are less concentrated at the grain boundary.

It is interesting to note that, due to the steep angle of abutment between columnar grains growing from opposite sides of the weld pool, welds made with a teardrop-shaped weld pool tend to be more susceptible to centreline solidification cracking than welds made with an elliptical-shaped weld pool. A steep angle seems to favour the head-on impingement of columnar grains growing from opposite sides of the weld pool and the formation of the continuous liquid film of low-melting-point segregates at the weld centreline. As a result, centreline solidification cracking occurs under the influence of transverse contraction stresses.

3.4. Application of synchrotron X-ray in solidification cracking research

From the literature review presented of solidification cracking theory and criterion, it is evident that the potential driving forces for solidification cracking are well-established: solid contraction in a thermal gradient, solidification shrinkage, and a high sensitivity to solute segregation. However, the variation and disparity between theories is vast. This disparity needs to be addressed in terms of experimental evidence and validation of the proposed theories. The observation of solidification crack nucleation and propagation is almost an unexplored phenomenon. Only recently have experimental observations on solidification cracking started to emerge: first for transparent analogues [23], then for real metals [22] and binary alloys [27]. Some of the mechanisms for solidification crack formation and propagation have been elucidated from observations of fracture surfaces. Based on these observations, the following crack nuclei have been suggested: 1) liquid film or liquid pool [36]; 2) pore or series of pores [24, 37]; 3) grain boundary located in the place of stress concentration; and 4) inclusions that can be easily separated from the liquid or solid phase [38, 39]. Still, it is evident that the understanding of solidification cracking can be improved.

3.4.1. Introduction to synchrotron X-ray imaging

The development of third generation synchrotron sources has opened interesting new fields for experimental research to advance this understanding. A synchrotron is a huge scientific machine, typically around half a kilometre in circumference. A schematic illustration of the key components with a synchrotron source is depicted in Figure 3-9.

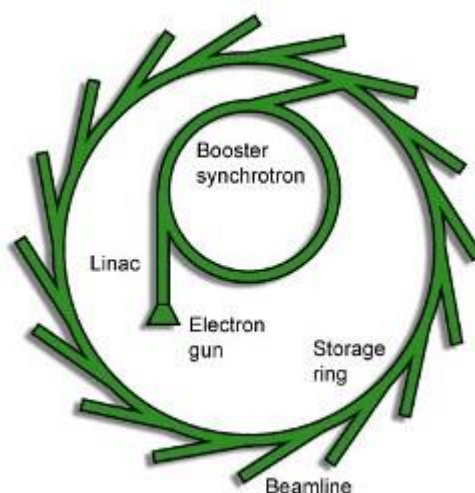


Figure 3-9: Schematic illustration of the key components within Diamond Light Source synchrotron.

The synchrotron is a source of electromagnetic radiation that is usually produced by a storage ring. Electron particles are generated in an electron gun and then fired out into the machine, where they are accelerated up to very high speeds through a series of particle accelerators. Once the high-energy electron beam has been generated, it is directed into auxiliary components such as bending magnets and insertion devices (undulators or wigglers) in storage rings and free electron lasers. These supply the strong magnetic fields perpendicular to the beam which is needed to convert the high-energy electron energy into photons. The photon light is then channelled into experimental hutches called beamlines [230]. The beamlines are typically designed specifically for an intended application, e.g. Diamond Light Source's (DLS) I12 beamline is designed specifically for high energy engineering applications, whereas the European Synchrotron Radiation Facility's (ESRF) ID19 beamline is specifically designed from high resolution imaging experiments.

The beamlines adopt a range of X-ray imaging techniques, however, only radiography and tomography X-ray imaging techniques will be discussed further.

Since the discovery of X-rays by Rontgen in 1895 [231] non-destructive imaging of objects has proven to be a powerful tool in materials science. For many tasks, a simple two-dimensional radiographic projection image is suitable. To create a two-dimensional radiograph, the beam of X-rays produced by the synchrotron is projected toward the object of interest. On collision with the sample, a certain amount of the X-rays are absorbed by the object. The level of localised absorption is dependent on the particular density and composition of the features within the object. The X-rays that pass through the object are captured behind the object by a detector (either photographic film or a digital detector). The detector can then provide a superimposed 2D representation of all the object's internal structures from the attenuation changes resulting from density mismatch intrinsic to the sample. This is commonly known as absorption contrast imaging. However, there is often a need for obtaining, in a non-destructive manner, information about the three-dimensional structure of objects. Cormack published his approach in the 1960s to derive the mass distribution inside an object from its radiographic projection images taken from different projection angles [232]. Based on this idea Hounsfield introduced in the 1970s the first scanner for non-invasive three-dimensional imaging — so called computed tomography (CT) [233]. Following the huge success of CT in medicine, the method was soon utilized in materials research and non-destructive testing [234]. With micro-focus X-ray tubes, spatial resolutions up to the micrometre scale can be reached — μ CT [235]. Compared to laboratory X-ray sources, synchrotron radiation offers a significant improvement with its nearly parallel beam propagation, a flux which is several orders of magnitudes higher and the possibility to work with a monochromatic beam. These advantages lead to higher reconstruction qualities, fewer artefacts, shorter acquisition times and improved contrast [235, 236]. The fundamentals of synchrotron based micro-tomography and radiography have been known since the 1990s with available resolutions up to sub-micrometre [237].

3.4.2. A review of synchrotron X-ray used in solidification cracking research

Synchrotron X-ray imaging (X-ray micro-tomography) was first used by Phillion *et al* [21] to observe the development of damage and strain during mushy zone tensile loading in Al alloy AA5182 specimens at 528 °C. The growth of hot tear damage was qualitatively assessed in 2D and 3D and quantitatively characterized in 3D. The results showed that in the early stages of loading, strain is accommodated mainly by specimen diameter reduction with only limited internal damage accumulation. At intermediate strains it is accommodated by a combination of as-cast porosity growth and damage-based void nucleation in the residual liquid present in the microstructure. At high strains, void coalescence and continued growth appears to be the main mechanism of damage accumulation and strain accommodation. Later the author published a more quantitative study [238] and observed that during the initial stages of semisolid deformation, strain was accommodated by both the growth of as-cast porosity and the detection of new damage-based voids. As the volume fraction of damage increased, the growth of voids occurred in an orientation perpendicular to the loading direction, both through expansion within the grain boundary liquid and void coalescence. The damage then localizes, causing failure. Phillion *et al* [239] then studied the effect of porosity on solidification cracking using a novel semi-solid tensile deformation methodology combined with X-ray micro-tomography. Semi-solid deformation tests were conducted on the commercial Al–magnesium alloy AA5182 in the as-cast state. This material was tested in two forms: as-received and hot isostatically pressed. In all cases, processing via hot isostatic pressing was found to increase the semi-solid tensile strength and ductility by reducing the number of pre-existing nucleation sites for strain accommodation. Further, it was shown that the failure in this material is localized to the fracture surface with very little internal damage occurring in other areas. These results support the hypothesis that as-cast porosity is intimately linked to the hot tearing susceptibility of Al alloys. The author later employed a radiography approach [240] to observe semi-solid deformation and failure in Al–Cu alloys. The combination of X-ray radiography with semi-solid tensile deformation in Al–Cu alloys enabled identification of mechanisms in semi-solid materials relating to (i) fluid flow during deformation and (ii) stress–strain response. At low to moderate fraction solids, bulk tensile deformation was accommodated by flow of the Cu-enriched inter-dendritic liquid and resulted in a

substantial increase in the amount of liquid in the region of strain localization. The liquid phase then ruptured, leading to final failure. Across this large range of fraction solid, the load required to initiate localized tensile deformation remained almost constant. This similarity exists because tensile deformation in the absence of grain coalescence induces bulk liquid flow. As the grain morphology remained un-coalesced across the low to moderate range of fraction solid, the load at yield will also remain similar. In contrast, there is only a limited amount of liquid flow at high fraction solids. Instead, due to the coalesced semi-solid grain structure, deformation is accommodated by early void formation and considerable deformation of the solid skeleton. The load at yield was also considerably higher as compared to the low to moderate fraction solid material, followed by an apparent hardening of the material with deformation.

Based on the observations presented above, a three-stage mechanism for semi-solid failure was proposed for the range of fraction solid between 0.35 and 0.66 and illustrated in Figure 3-10.

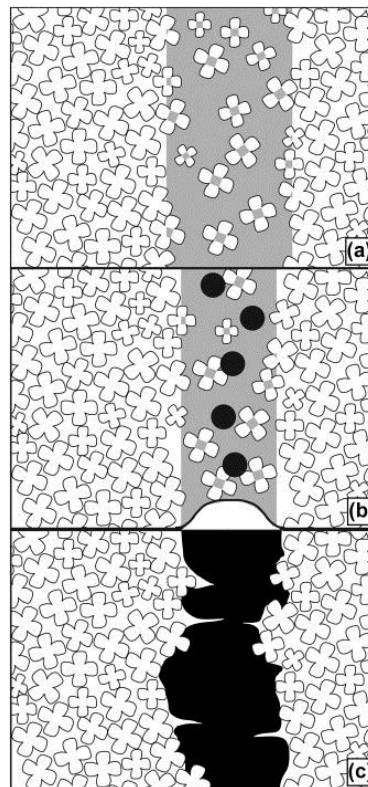


Figure 3-10: Schematic showing the key microstructural features active during semi-solid tensile deformation: (a) strain localization and flow of liquid towards this location and (b) semi-solid necking in combination with damage nucleation and growth; formation of micro-necks and final fracture [240].

Stage 1 (Figure 3-10(a)): Strain localization and flow of liquid towards this location.

Stage 2 (Figure 3-10(b)): Semi-solid necking in combination with damage nucleation and growth.

Stage 3 (Figure 3-10(c)): Formation of micro-necks, and final fracture.

A similar approach was then employed by Aveson *et al* [27], although at a much smaller scale, to observe the initiation and propagation of solidification cracks at the dendritic scale in an Al-Sn binary alloy.

Gourlay *et al* [241] demonstrated the existence and importance of granular behaviour in solidification using *in situ* radiography experiments. Vernede, Rappaz, and co-workers then adopted the granular simulation method for discrete element simulations of solidification cracking [242-244]. The studies show that solidification cracking is a highly complex phenomenon, which involves heat flow, fluid flow under capillary action and various other factors such as material chemistry and processing parameters.

Most recently, Sistaninia *et al* [19] compared the results of a hydro-mechanical granular model [245] with *in situ* X-ray tomographic observations made during tensile deformation of a mushy Al-Cu alloy specimen. The study found that during tensile testing, fluid flows toward the deformed region to compensate for deformation. Furthermore, the specimen continuously necks, allowing the liquid channels perpendicular to the tensile axis to open by feeding them with the liquid coming from neighbouring zones and from channels which are parallel to the tensile axis and tend to close. Once the liquid is no longer able to feed the deformed zone, cracks form in the structure. The 3D coupled hydro-mechanical granular model has been validated to directly predict, for the first time, solidification crack formation and stress-strain behaviour in metallic alloys during solidification. This granular model consists of four separate 3-D modules: (i) the solidification module is used to generate the solid-liquid geometry at a given solid fraction; (ii) the fluid flow module is used to calculate the solidification shrinkage and deformation-induced pressure drop within the inter-granular liquid; (iii) the semi-solid deformation module simulates the rheological behaviour of the granular structure; and (iv) the failure module simulates crack initiation and propagation. Since solid deformation, inter-granular flow and crack

initiation are deeply linked together, the fluid flow module, semi-solid deformation module and failure module are coupled processes. This has been achieved through the development of a new three-phase interactive technique that couples the interaction between inter-granular liquid, solid grains and growing voids. The results show that the pressure drop, and consequently solidification crack formation, depends also on the compressibility of the mushy zone skeleton, in addition to the well-known contributors (lack of liquid feeding and semi-solid deformation). The granular model also demonstrates that the grain size has a large effect on the ‘overpressure’ required to overcome the capillary forces at the liquid–void interface. Because of this dependence, the hot tearing susceptibility increases with increasing grain size.

Puncreobutr *et al* [246] quantitatively investigated the influence of Fe-rich β -intermetallics on solidification defect formation using 4-D (three spatial dimensions evolving with time) synchrotron X-ray tomographic microscopy. Two experiments were conducted in this work: an in situ solidification study of porosity formation and an in situ isothermal semi-solid deformation experiment simulating hot tearing. The experiments were performed on a commercial A319 alloy (Al–7.5Si–3.5Cu, wt.%) with 0.2 and 0.6 wt.% Fe, providing complex commercial-like casting microstructures with β -intermetallic particles equivalent to primary and recycled Al alloy products.

From the in situ solidification experiment, the results indicate that the presence of a large fraction of β -intermetallics strongly blocks the inter-dendritic channels and induces porosity formation as a result of permeability reduction and hydrogen supersaturation in the local subdivided domain. No β -intermetallics are seen directly nucleating a pore during solidification; instead they appear to physically block and constrain pore growth and contribute to an increase in pore tortuosity. In addition, β -intermetallics are found to facilitate pore growth, which may be due to a low interfacial energy between the gas and the intermetallic plates. The in situ semi-solid deformation experiments show that β -intermetallics increase hot-tearing susceptibility. The 0.6 wt.% Fe specimen sustained a relatively small amount of strain ($\varepsilon \sim 7\%$) prior to failure, and the failure event was brittle-like. In comparison, the 0.2 wt.% Fe specimen sustained triple the true strain upon failure, and the failure event was more ductile. High-resolution images of the β -intermetallic-rich post-failure microstructures also show that the internal pores near the fracture surface of the 0.6 wt.% Fe specimen were flatter,

less branched and preferentially aligned to existing β -intermetallics in comparison to the 0.2 wt.% Fe sample, which exhibited highly tortuous and branched pores. Such a change in the pore shape could concentrate strain and weaken the mush. These advancements in observing and quantifying intermetallics and defect formation highlight the very complex effect of secondary phase formation on the rheology and mechanical behaviour of semi-solid microstructures. The author later used the technique to carry out studies on the nucleation and growth of the intermetallics [247] along with the effect on permeability [248].

Unfortunately, steel has little attenuation contrast and good cracking resistance in comparison to the favourable Al and binary alloys carefully selected in studies listed above. Thus, similar experiments are unfeasible for steels. Furthermore, the literature presented above is based upon casting. Information regarding solidification cracking in steel welding is desperately lacking and needs will be addressed in the forthcoming results chapters.

4. Evolution of weld pool and fluid flow

4.1. Introduction

The solid steel weld joint which forms the bond along the seam of linepipe is initially formed from molten steel. The geometry of the solidified weld joint is highly dependent upon the fluid flow inherent to the steel in its liquid form. In Chapter 2.2.3 it was identified that solidification cracking during welding is influenced by the geometry of the weld joint. I.e. Deep and narrow welds with a low width/depth ratio can be susceptible to weld solidification cracking, because of the steep angle of abutment between columnar grains growing from opposite sides of the weld pool. Similarly, convex bead enforcement geometries can reduce the surface tension in the weld, which lowers the welds solidification cracking susceptibility. As such, a greater understanding and control of the fluid flow during welding is particularly interesting to optimise weld shape, penetration, solidification structure and solidification cracking resistance.

The phenomena controlling the flow of the liquid metal within the weld pool is well understood and described in Chapter 2.2.3. To date, experimental analysis has been limited by the opacity of metals and the dynamic nature of the flow. The results go some way to validating computational models, however, there is no quantitative experimental data available for weld fluid flow in steels or other commercial metals. Until now, experimental techniques available have not been advanced enough to capture this phenomenon. However, the emergence of third generation synchrotron X-ray sources has opened interesting new avenues for experimental exploration [106]. In this chapter, fluid flow within a molten steel weld has been observed. The flow and geometry of the weld joint is quantitatively analysed, with specific emphasis placed on the effect of S .

4.2. Materials and experimental methods

4.2.1. Materials and welding process

Figure 4-1 shows a schematic of the experimental setup within Diamond Light Source's I12 facility. Samples are held in a jig that is directly integrated to the computer controlled stage in I12's experimental hutch. The jig is specifically designed to fully insulate the sample stage from the welding current. Cylindrical samples (10 mm diameter x 50 mm long) were prepared from three commercially available steels with varying S contents. The nominal chemistries of the materials are defined in Table 4-1. Fine (~50 micron) tungsten and tantalum particles are placed on the welding surface. Fine (~50 micron) tungsten and tantalum particles are placed on the welding surface.

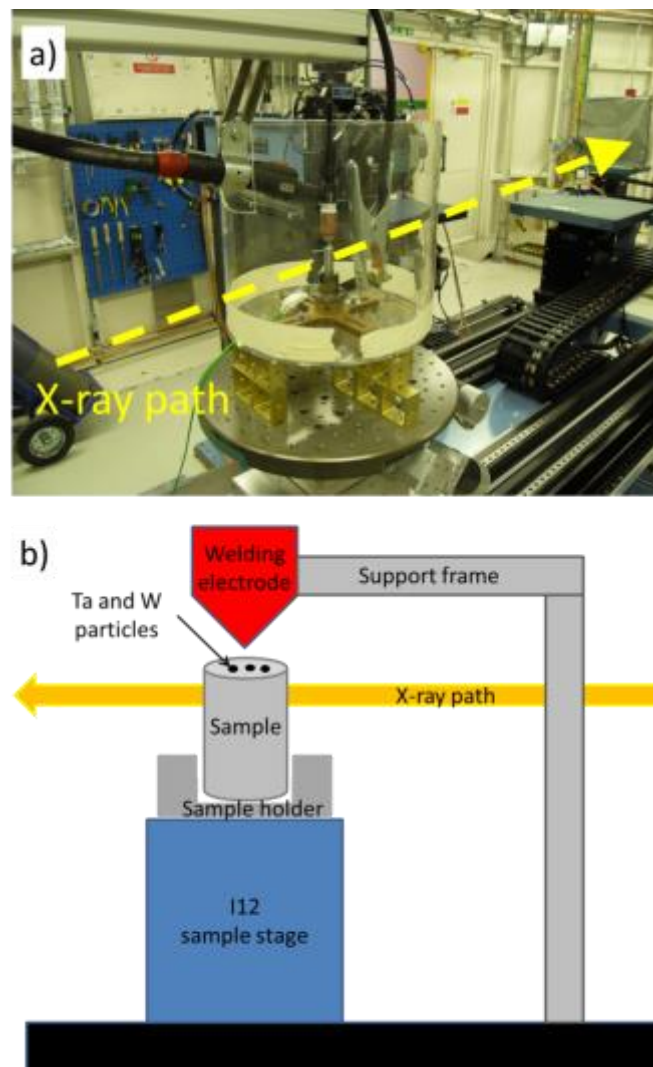


Figure 4-1: Illustration of experimental setup within Diamond Light Source's I12.

	C	Mn	Si	P	S	Cr	Ni
High S steel	0.15	2	1	0.2	0.3	19	10
Low S steel	0.145	1.02	0.014	0.001	0.0005	0.005	0.005

Table 4-1: Nominal chemistries of sample materials.

During the experiments, a three second (10 V, 125 A) tungsten inert gas (TIG) spot weld was made in the centre of the specimens in order to consume the tungsten and tantalum particles. The welding process used a non-consumable tungsten electrode in DCEP polarity. Argon was used as the shielding gas, with an 8 L/min flow rate.

4.2.2. Synchrotron based micro-radiography

In order to be able to distinguish between the solid and liquid phases, as well as quantitatively track the molten fluid flow, sufficient absorption contrast is essential. Hence, the high flux and high energy beamline I12 at Diamond Light Source was chosen to carry out the study. The beamline has an extremely high photon flux, and coherence demands are less stringent. I12 was operated in white beam mode, with a 15 mm (H) x 50 mm (W) beam size. For the imaging, a view window of 800 x 600 pixels was employed with a 13 μm /pixel resolution. A Vision Research Phantom v7.3 detector enabled the high capture rates (1000 FPS) sufficient to observe the dynamic flow.

As the phase contrast between liquid and solid steel is so small, tungsten and tantalum particles were added to the weld as tracers. The particles were utilized to visualize the melt flow by investigating their spatial and temporal distribution in the melt pool. The particles have good phase contrast ($Z=73-74$) in comparison to the iron ($Z=26$). This results in strong attenuation, appearing darker than the surrounding liquid steel on the recordings. Although, both have very high melting temperatures (Ta ~ 3017 °C, and W ~ 3422 °C) only the W particles remained solid throughout welding. As such, it appears that the maximum temperature within the weld pool is below 3422 °C. The Ta particles dissolved during welding. This led to an improved attenuation of the Ta enriched liquid phase during welding, enhancing the solid/liquid interface visualisation, as illustrated in Figure 4-2.

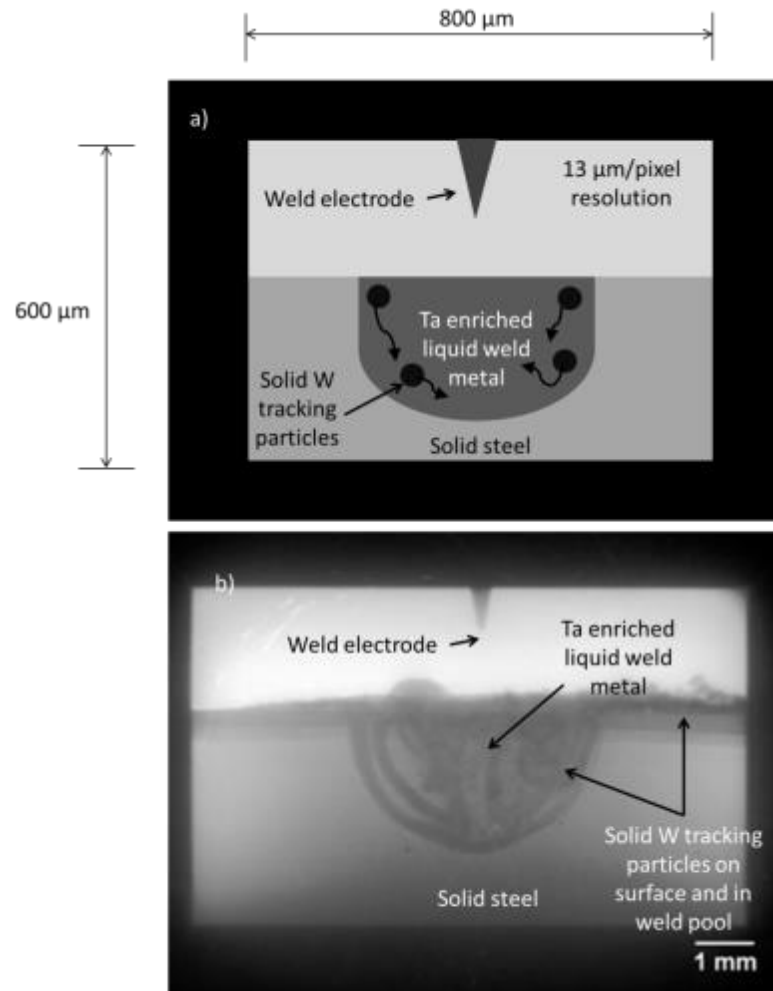


Figure 4-2: Identification of image components and resolution using a) schematic diagram and b) radiograph from imaging.

4.2.3. Image processing and flow analysis

All image analysis was completed using ImageJ software. To retain image integrity, minimal processing was implemented to the raw data. The routine started by applying a 3D Hybrid median filter (<http://rsb.info.nih.gov/ij/plugins/hybrid3dmedian.html>) to eliminate high contrast speckle noise. In order to observe the weld geometry, minimum intensity Z stacks were made of all the images in a test sequence. The overlay of the tracking particles, coupled with the density increase in the liquid phase, results in a clearly visible (darker) region where the molten weld had been. The increased density of the liquid phase has been attributed due to the partial melting of tantalum particles during welding. The tantalum enriched weld offers a higher absorption co-efficient to

that of the plain steel. Fluid flow analysis was carried out using the downloadable Manual Tracking plugin (<http://rsbweb.nih.gov/ij/plugins/track/track.html>). This plugin provides a way to retrieve XY coordinates as well as velocity, distance covered between two frames and intensity of the selected pixel or volume.

4.2.4. Selection of 2D flow patterns in the 3D volume

As a 3D flow is being observed in only a 2D plane, selecting flow patterns that were in plane was essential in order to obtain an accurate velocity recording. To ensure selection of in-plane flow, only particles that flowed at the extremities of the weld pool were tracked, as described in Figure 4-3 and described in more detail in Appendix A.

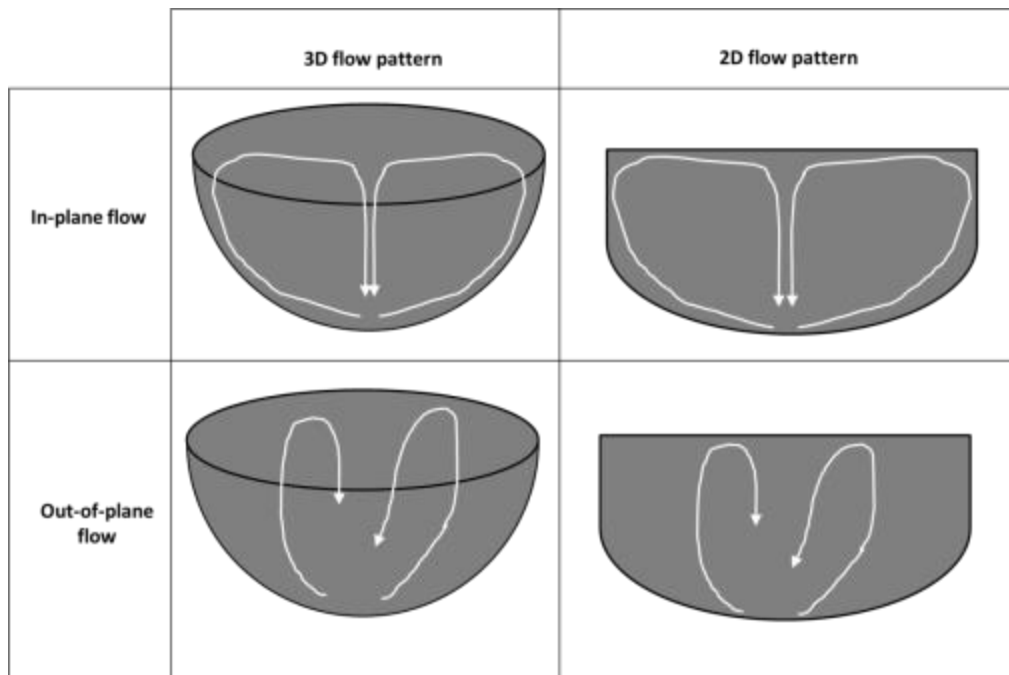


Figure 4-3: Illustration of methodology for selecting in-plane 2D flow patterns for analysis within the 3D flow volume.

4.3. Results

4.3.1. Weld evolution and fluid flow in low S content steel

Figure 4-4(a-c) shows three “minimum intensity Z-stacks” of the raw images collected for the low S (0.0005 wt.%) steel defined in Table 4-1. The stacks are made at three intervals to assess geometric evolution in respect to time. The pointed tip in the central upper part of the images is the tip of the welding electrode. The darkest region below the tip is created from both the enrichment of molten tantalum into the liquid steel, and also the result of the cumulative flow tracing of the solid tungsten particles. The weld retains a shallow and wide morphology throughout the welding process. After 500 ms of welding in Figure 4-4(a) and (d), the pool is only 0.69 mm deep and 3.81 mm wide. After a further 500 ms welding in Figure 4-4(b) and (e), the pool has grown only 0.1 mm in depth to 0.79 mm and a much larger 1.18 mm in width to 4.99 mm.

To understand weld pool growth further, the fluid flow was tracked over a 0.08s timeframe (across 80 consecutive frames) at $\sim t = 1$ s. The results in Figure 4-5 exhibit an outward and upward flow with a peak velocity of 0.3 m/s. The circular dot on the tracking lines represents the end point of the tracked flow. Similarly, flow was also tracked over the same time period (0.08s) at $\sim t = 2$ s. The results of the tracking in Figure 4-6 reveal an identical flow orientation to that observed in Figure 4-5. The flow velocities are also very similar ($V_{max} = 0.31$ m/s) even though the weld pool had become wider and deeper.

The flow orientation can be related to the S content within the steel. In the absence of the surface active agent, the warmer liquid metal of lower surface tension near the centre of the pool surface is pulled outward by the cooler liquid metal of higher surface tension at the pool edge. This phenomenon is observed in Figure 4-5 and Figure 4-6. The warmer liquid metal from under the welding arc is being convectively transported horizontally away from the weld centre towards the lateral extremities of the weld pool. This stimulates the growth of the shallow and wide weld depicted in Figure 4-4.

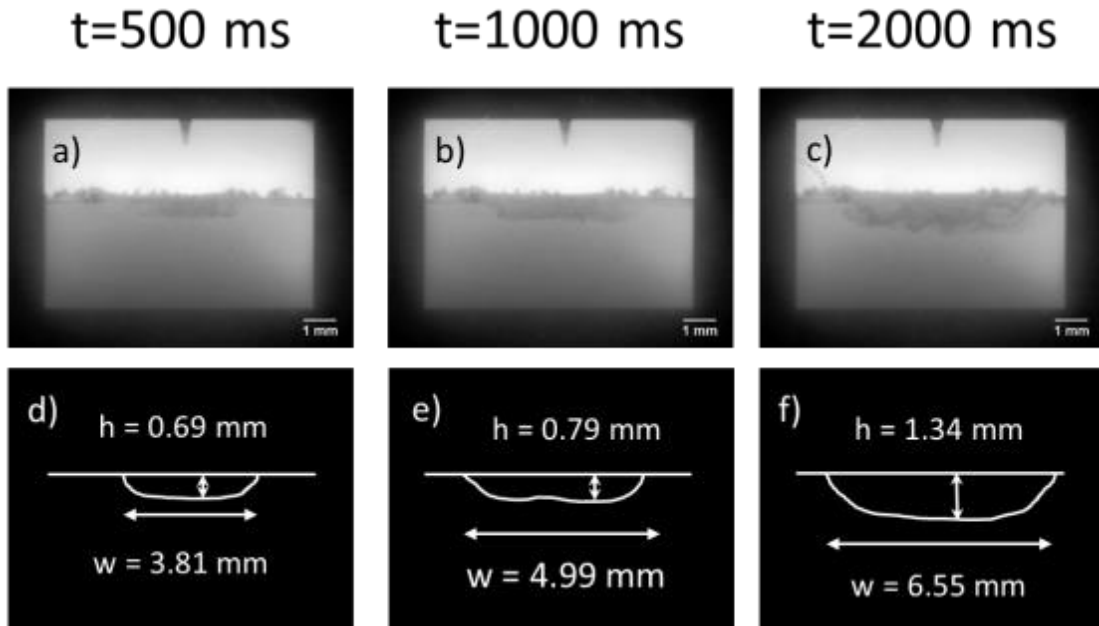


Figure 4-4: Time dependent evolution of the molten weld pool in the low S steel, showing minimum intensity z-stacks of raw data (Figs. a,b,c) and the corresponding geometry measured (Figs. d,e,f) at 3 time intervals.

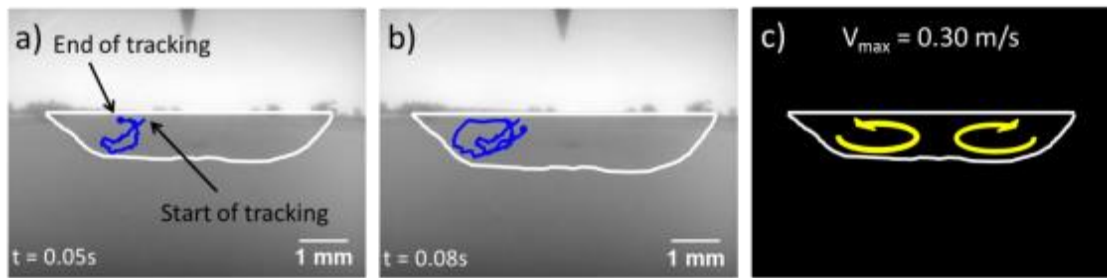


Figure 4-5: Fluid flow observed in low S steel at $t \sim 1$ s, showing shallow outward and upward re-circulation zones. Specifically, a) the outward and upward flow after 0.05 s tracking, b) the repeated recirculation zone 0.08 s tracking, c) a schematic illustration of the flow coupled with the results of velocity quantification.

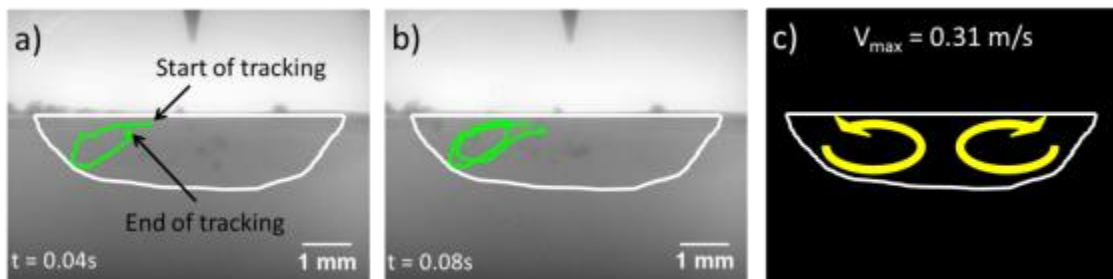


Figure 4-6: Fluid flow observed in low S steel at $t \sim 2$ s, showing shallow outward and upward re-circulation zones. Specifically, a) the outward and upward flow after 0.04 s tracking, b) the repeated recirculation zone 0.08 s tracking, c) a schematic illustration of the flow coupled with the results of velocity quantification.

4.3.2. Weld evolution and fluid flow in high S content steel

Figure 4-7(a-c) shows three “minimum intensity Z-stacks” of the raw images collected for the high S (0.3 wt.%) steel defined in Table 4-1. The geometry of the weld differs significantly to the geometries observed in the low S sample. After only 500 ms welding, the molten weld joint is already deeper (1.86 mm) than the low S sample (1.34 mm) became after 2000 ms of welding. Yet, the initial width in the high S sample after 500 ms welding is very similar (3.89 mm) to that of the low S sample (3.81 mm). After further welding in Figure 4-7(b) and (c) the weld appears to favour downward growth to create a deep (3.59 mm) weld geometry.

To understand this growth further, the fluid flow was tracked over a 0.11 s timeframe (across 110 consecutive frames) at $\sim t = 2$ s. The results in Figure 4-8 reveal a flow pattern opposite to that observed in the low S steel (Figure 4-5 and Figure 4-6). The flow exhibits an inward and downward motion with a peak velocity of 0.52 m/s.

The flow orientation can again be related to the S content. In the presence of the surface active agent, the cooler liquid metal of lower surface tension at the edge of the pool surface is pulled inward by the warmer liquid metal of higher surface tension near the centre of the pool surface. The resultant flow pattern in Figure 4-8 favours convective heat transfer from the heat source to the pool bottom. I.e. the liquid metal carries heat from the heat source to the pool bottom more effectively, thus increasing weld penetration as seen in Figure 4-7(c).

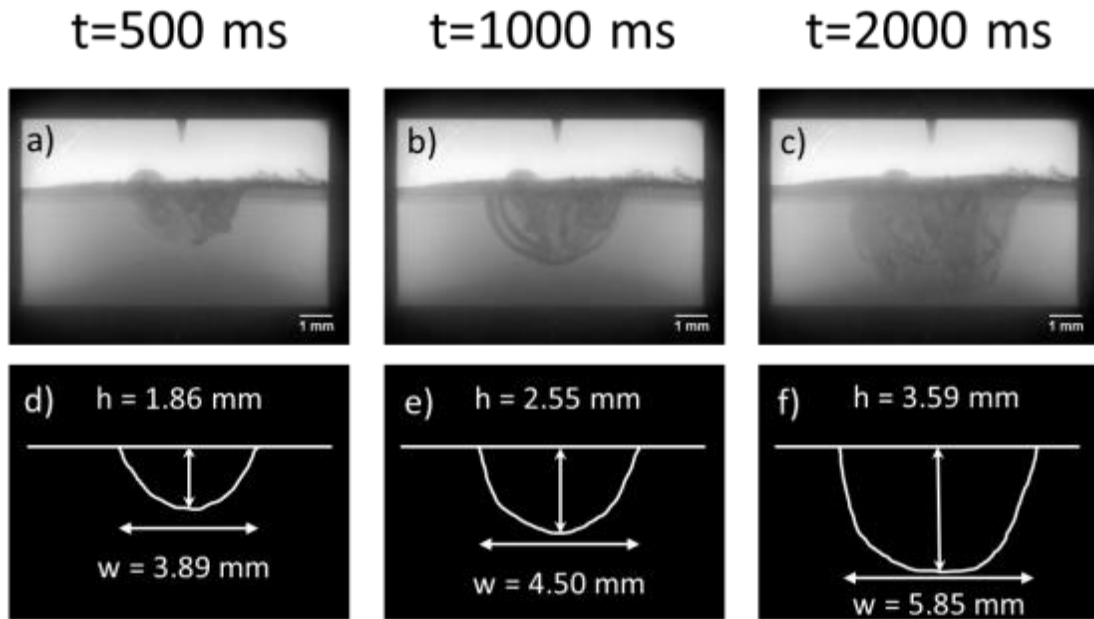


Figure 4-7: Time dependent evolution of the molten weld pool in the high S steel, showing minimum intensity z-stacks of raw data (Figs. a,b,c) and the corresponding geometry measured (Figs. d,e,f) at 3 time intervals.

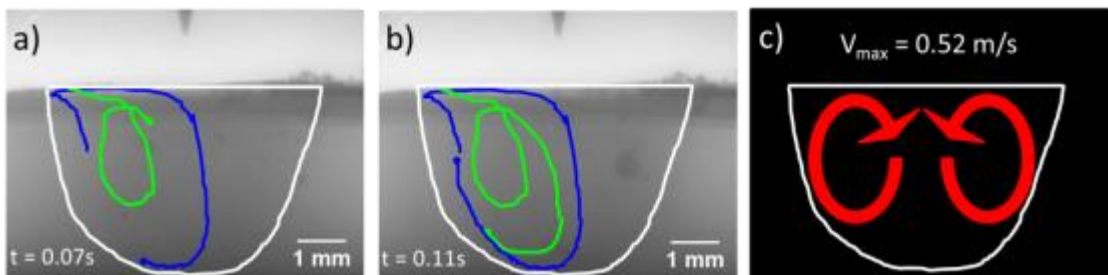


Figure 4-8: Fluid flow observed in high S steel at $t \approx 2$ s, showing deep inward and downward re-circulation zones. Specifically, a) the inward and downward flow after 0.07 s tracking, b) the repeated recirculation zone 0.11 s tracking, c) a schematic illustration of the flow coupled with the results of velocity quantification.

4.3.3. Metallographic examination of the solidified weld geometries

Figure 4-9 displays the results of metallographic analysis made on the samples after the full 3 seconds welding. The geometries observed agree well with the corresponding *in situ* figures presented in chapter 4.3.1 and 4.3.2. The weld in the low S steel (Figure 4-9(a)) is wide (9.34 mm) and shallow (2.24 mm). The weld in the high S sample (Figure 4-9(b)) is deep (5.03 mm) and narrow (7.21 mm).

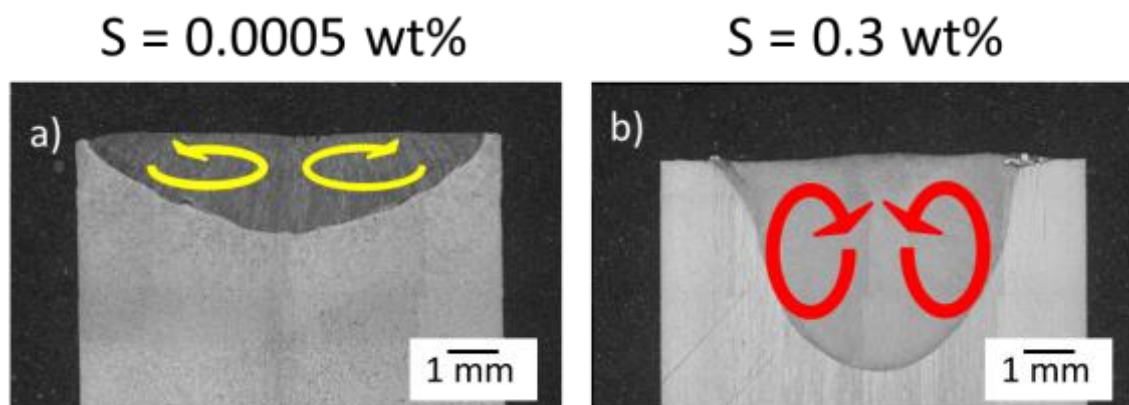


Figure 4-9: Cross sectional macrographs of welded samples after full 3 s of welding showing; a) shallow and wide weld geometry of low S steel and corresponding outward flow pattern, b) deep and wide weld geometry of high S steel and corresponding inward flow pattern.

Table 4-2 and Table 4-3 summarise the geometric evolution measured through the welding process in the low and high S steels respectively. It is clear that the low S steel offers a higher width/depth ratio while the width/depth ratio in the high S steel appears to decrease as welding time increases. To summarise, using uniform welding variables, other than sample material chemistry, a substantial variation in weld geometry has been achieved. The low S steel has a width 68% greater than the high S steel, while the high S steel has 124% more penetration than the low S steel. The geometries can be related to the orientation of the fluid flow observed *in situ* during welding.

Weld pool development - low S steel			
Time (s)	Width (mm)	Penetration (mm)	Width/penetration ratio
0.5	3.81	0.69	5.52
1	4.99	0.79	6.32
2	6.55	1.34	4.89
3	9.34	2.24	4.17

Table 4-2: Summary of the measured weld geometrical parameters in the low S steel. The measurements were made in situ at various time intervals.

Weld pool development - high S steel			
Time (s)	Width (mm)	Penetration (mm)	Width/penetration ratio
0.5	3.89	1.86	2.09
1	4.5	2.55	1.76
2	5.85	3.59	1.63
3	7.21	5.03	1.43

Table 4-3: Summary of the measured weld geometrical parameters in the high S steel. The measurements were made in situ at various time intervals.

4.4. Discussion

It is well understood that welding parameters influence the penetration characteristics of the weld and that the effects are sensitive to S concentrations. Shirali *et al* [249] made the following conclusions based on the effects of welding parameters and S concentrations in steel TIG welds:

- 1) Weld penetration decreases with increasing welding speed for low, medium and high S casts.
- 2) Increased welding current increases the weld penetration in high S steel but decreased penetration in low S steel.
- 3) Increasing linear energy (which is dependent upon both welding speed and current) increases penetration for low and medium S steels but had little effect on penetration in high S steels.
- 4) Increases in arc length decrease weld penetration.
- 5) Weld penetration increases with increasing vertex angle of the electrode for medium and low sulfur casts.
- 6) Additions of 1 % O or SO₂ reduce weld penetration.

For this study, the welding parameters (current, voltage, arc length and electrode tip geometry) were uniform for each test. As such, the contribution of welding parameters can be discounted from further discussion.

For the surface tension driven flow proposed here to be valid, surface active elements must alter the temperature dependence of the surface tension. Since S and O are known to be surface active (segregate to the surface) in liquid iron, surface properties can be altered substantially by low average bulk concentrations of these elements. Measurements of the surface tension coefficient dy/dT are available for both the Fe-S and Fe-O binary systems. The reports [250, 251] suggest that the surface tension of Fe-S melts increases with increasing temperature above the melting point for at least 200 °C when the S concentration exceeds approximately 40 ppm. The surface active elements lower the surface tension of the base metal at the melting point. For example,

the surface tension of liquid iron is reduced by more than a factor of two near 1570 °C by 1 wt.% S [250, 252]. However, as the temperature is increased, the resulting increase in entropy favours reduced segregation of the surface active elements on the surface, thereby increasing the surface tension. As temperature is raised, a point will be reached at which the species will no longer be concentrated on the surface and no longer surface-active [92]. Gogiberidze et al [253] determined this temperature by extrapolation to be 2025 °C for S in a ball bearing steel.

Figure 4-10 is used to illustrate the above discussions visually. Pure iron has a negative dy/dT as expected for a pure metal. The surface tension of pure iron is indicated schematically by curve A in Figure 4-10, iron containing S by curve B, and iron containing oxygen by curve C. The slopes and surface depression at the melting point are dependent on the actual concentrations of S and oxygen present in the alloy.

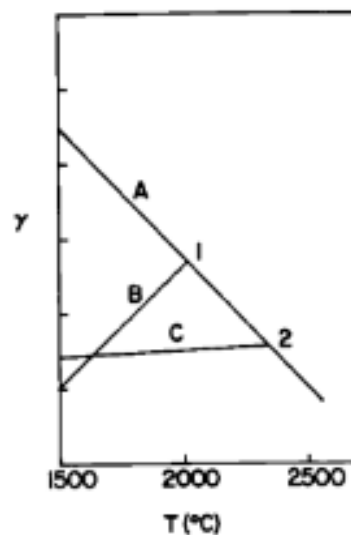


Figure 4-10: Schematic illustration of surface tension-temperature behaviour for iron; curve A defines a high purity Fe, curve B defines an Fe alloy containing S, curve C defines an Fe alloys containing oxygen [92]

As relatively low concentrations of surface active elements are adequate to produce a positive surface tension temperature coefficient and good penetration, poor penetration is only normally expected in steels with particularly low S contents, as observed in the 0.0005 wt.% alloy presented in Chapter 4.3.1.

The high speed micro-radiography technique described in Chapter 4.2.2 has demonstrated a substantial difference in fluid flow pattern between low penetration (Chapter 4.3.1) and high penetration (Chapter 4.3.2) welds. These observations are consistent with the high speed motion pictures of TIG weld pools presented by Heiple *et al* [94]. Heiple's observations led, in part, to the development of the surface tension driven fluid flow model [92] and the results presented in this thesis are consistent with it.

Turbulent fluid flow is observed in the X-ray analysis of the low and high S steel and the symmetric recirculation zones are consistent with previous models and experimental techniques [254].

The flow velocity has also been quantified between 0.3-0.52 m/s (max velocity) using the high speed micro-radiography technique. However, due to the considerations described in Appendix A, the flow could possibly be as high as 5.87 m/s. Therefore, when considering all possibilities, the fluid flow shall be reported at maximum velocities of between 0.3-5.87 m/s.

Heiple [255] estimated surface fluid flow velocity from measurements taken from the motion of Al oxide particles on the weld pool surface using high speed motion pictures. All measurements were made after S was added to the weld pool so that the particles were moving toward the centre of the pool. The speeds of 17 particles measured lay between 0.05 and 0.14 m/s, with an average speed of 0.09 m/s. These speeds are consistent with the results presented in chapter 4.3 and also those observed by Brimacombe and Weinberg [256] for surface fluid flow on a pool of liquid tin in the presence of an imposed surface tension gradient. Furthermore, the flow velocities quantified could explain the lack of unwanted slag inclusions and oxide film entrapments in the weld. Campbell [257] classified two types flow within metal castings; i) bulk turbulence, which is assessed by Reynolds Number, and describes the chaotic eddying flow of the bulk liquid, and ii) surface turbulence, which is the chaotic breaking up of the surface of the liquid, allowing the surface oxide film to become incorporated into the bulk melt. While the avoidance of bulk turbulence is probably impossible, Campbell derived a critical velocity of approximately 0.5 m/s whereby surface turbulence in liquid metals would be avoided. In this study, the flow velocity

has been characterised below this critical value and such the avoidance of oxide film entrapments in the solidified weld have been achieved.

In terms of solidification cracking during welding, it is beneficial to achieve a wide and shallow weld with a high width/depth ratio along with convex bead enforcement. Welds with narrow and deep geometries can be susceptible to weld solidification cracking, because of the steep angle of abutment between columnar grains growing from opposite sides of the weld pool. As such, it appears that steels with low concentrations of active elements, such as S, would be preferred. S is an impurity in steel that is also undesirable as it easily segregates during solidification to form low melting point eutectic films at grain boundaries. Therefore it seems that the reduction of impurity element S will offer multi-dimensional benefits to solidification cracking resistance.

4.5. Chapter summary

An advanced imaging technique – *in situ* synchrotron X-ray micro-radiography – has been used to study weld pool fluid flow. Two distinct flow patterns, which have been speculated upon in literature, have been realistically visualised within the weld pool during welding. The results provide solid evidence for confirmation and verification, of the surface tension driven flow model of Heiple [92] which is mainly attributed to the difference in S content.

In steels with a low sulfur content (0.0005 wt.%) shallow and wide weld joints were produced as a result of an outward and upward flow orientation. The warmer liquid metal of lower surface tension near the centre of the pool surface being pulled outward by the cooler liquid metal of higher surface tension at the pool edge. As sulphur content is increased (>0.3 wt.%) the flow orientation changes to take on an inward and downward orientation. The cooler liquid metal of lower surface tension at the edge of the pool surface is pulled inward by the warmer liquid metal of higher surface tension near the centre of the pool surface. The resultant flow pattern favours convective heat transfer from the heat source to the pool bottom, increasing weld penetration.

The velocities of weld pool fluid flow have been calculated through extensive X-ray image analysis with a maximum value ranging between 0.3-0.52 m/s. However, this could reach velocities as high as 5.87 m/s due to considerations evaluated in Appendix A. All these are in good agreement with previous experimental and numerical results.

To reduce solidification cracking susceptibility, a wide and shallow weld with a high width/depth ratio is desired to reduce the abutment angle of columnar grains growing from opposing sides of the weld, while convex bead enforcement is preferred to reduce surface tension. As such, the reduction of S is proposed to improve weld geometry for solidification cracking resistance. As S is an impurity in steel that easily segregates during solidification to form low melting point eutectic films at grain boundaries, it seems that the reduction of impurity element S will offer multi-dimensional benefits to solidification cracking resistance. I.e. an improved weld geometry, and lower eutectic segregation. The X-ray imaging results from this study are a valuable source of experimental data that can also be used to verify and validate numerical models.

5. Microstructure and mechanical properties of linepipe SAW seam weld

5.1. Introduction

As the liquid weld metal cools, solidification begins. As presented in Chapter 2, to further understand solidification cracking in the welding of subsea linepipe, it is essential to quantify the following features within the submerged arc weld joint:

- Solidification structure
- Microstructural constituents
- Strength and ductility
- Residual stresses

Analysis of the submerged arc weld solidification structure, microstructure, and mechanical properties will also provide data for the improvement of the welded joint. A need for cost savings within the currently turbulent and uncertain market place has been highlighted throughout the literature survey presented. One way of achieving this is through the reduction of material usage i.e. reducing the wall thickness of linepipes. In order for reduced thickness linepipe to succeed in their current subsea operating environments, improvements must be made to mechanical properties. In this chapter, advanced microscopy analysis will be used to identify key microstructural features in welded deep sea linepipe. The microstructural properties will be related to the mechanical properties of the structure and how they contribute to solidification cracking. The relationships between microstructure and mechanical properties will be quantified using novel mathematic formula. The findings can then be used to guide improvements of linepipe chemistry and mechanical properties.

Preliminary research by Wen [185] on residual stress evolution through the manufacture process of UOE linepipe was simulated using a FE technique. The model predicts that high levels of tensile axial residual stress exist in and near the seam weld area after SAW seam welding ranging from 350 to 530 MPa. This is in agreement with the general understanding of weld residual stress in terms of pattern and magnitude. Tensile stresses during weld solidification contribute significantly to initiating solidification cracking defects. However, after mechanical expansion, the FE model predicts that the residual stress distribution and magnitude are completely modified due

to the plastic deformation resulting from the expansion operation. The model predicts that the axial residual stress in the weld area is now mainly compressive, ranging between -30 and -240 MPa. Meanwhile, the maximum tensile axial residual stress found in the whole pipe after expansion is outside the seam weld, being only about 130 MPa.

The results are interesting and in need of validation. In this chapter, welding residual stresses in a 15.7 mm walled steel UOE linepipe are measured with a neutron diffraction technique both before and after the mechanical expansion process. The results will be used to validate FE model predictions of residual stress distributions. The results will also provide information towards better understanding and control of welding, the resultant residual stresses it induces, and how the mechanical expansion process affects the residual stress distribution/magnitude. A better understanding of these factors will open the door to a more educated design of the expansion process. It should also confirm the current trend in design over-conservatism, and offer qualitative data to support the reduction of wall thicknesses in linepipe. In turn this could stimulate cost reductions in the industry.

5.2. Materials

For microstructure and mechanical property analysis, a 0.5 m long section of SAW API-5L grade X65 linepipe was acquired for the study. Table 5-1 highlights the nominal chemistry of the 25.4 mm gauge thickness, API-5L grade X65 steel source plate, along with the welding wires used for the SAW. The API-5L grade X65 source plate was manufactured through a TMCR route with accelerated cooling and shaped with a UOE process to achieve a pipe with an outside diameter (OD) of 457.2 mm. Prior to expansion, the formed pipe was joined using a multi-wire SAW in two main passes from inner diameter (ID) and OD. The ID welding was performed first using 4 wire welding heads with a travel speed of 1.65 m/min. Next, the OD welding was carried out using 5 wire welding heads with a travel speed of 1.9 m/min. The inter-pass temperature was controlled at below 50°C in order to improve toughness performance. Prior to ID welding the pipe was tack welded from the OD using a single wire gas metal arc welding process. The tack weld was then consumed by the subsequent OD welding. Analysis of Table 5-1 reveals the weld filler metal to be overmatched, primarily to protect weld from localization of plastic strain in the event that the yield load of the structure is exceeded [120].

For the residual stress experiments 15.9 mm walled API-5L grade X65 linepipe sections (~3300 mm long) were obtained from Tata Steel production line. The OD of the linepipe was 508 mm. Two linepipes were measured; one that had been U-formed, O-formed, and SAW seam welded. The other, which had been U-formed, O-formed, SAW seam welded, and mechanically expanded to complete the standard UOE manufacture process. The nominal chemistry of the materials is listed in Table 5-1.

		C	Si	Mn	P	S	Cr	Ni	Mo	Cu
Microstructure/ mechanical property analysis	X65 Base Metal	0.026	0.32	1.49	0.004	0.0003	0.17	0.009	0.002	0.011
	Welding Wire 1	0.07	0.26	1.1	0.013	0.003	0.04	0.021	0.51	0.02
	Welding Wire 2	0.08	0.27	1.14	0.013	0.002	0.035	0.024	0.5	0.02
Residual stress measurement	X65 Base Metal	0.07	0.31	1.59	0.011	0.0008	0.035	0.036	0.013	0.025
		V	Al	Nb	Sn	B	N	Ti	C_{eq}	Ti/N
Microstructure/ mechanical property analysis	X65 Base Metal	0.004	0.034	0.043	--	0.0002	0.005	0.012	0.122	2.4
	Welding Wire 1	0.006	0.011	--	0.001	0.017	0.003	0.012	0.274	4
	Welding Wire 2	0.007	0.011	--	--	0.01	0.002	0.01	0.233	5
Residual stress measurement	X65 Base Metal	0.0008	0.033	0.039	--	0	0.004	0.0018	0.35	0.45

Table 5-1: Nominal chemistries of linpipes used for microstructure and mechanical property testing.

5.3. Microstructural and mechanical properties characterisation

5.3.1. Experimental methods

5.3.1.1. *Optical microscopy*

Samples were extracted from the SAW seam weld of the UOE linepipe section for specimen preparation and examination in the cross section transverse to the welding direction. All specimens were ground by Si carbide abrasive paper, up to a final grade 1200. Specimens were then polished to a 3 µm finish and lightly etched using nital solution (a mixture of 2% nitric acid and ethanol). The microstructures of the fusion zone, HAZ, and base metal were then examined at $t/4$ (t is the thickness of the plate) from the OD using an Olympus BX51 optical microscope. Optical microscopes have a wide variety of applications, and are very powerful tools for inspecting the microstructure of a great range of materials [258]. There are three variations of the technique: reflected light microscopy, transmission mode, and polarized light microscopy. It is important to select the correct technique for the specimen under examination and the results that are required. For this study reflected light microscopy was utilized. Contrast between different regions when viewed in reflected light can arise from variations in surface topography and differences in reflectivity (e.g. of different phases, different grain orientations, or boundary regions) [258].

5.3.1.2. *Scanning electron microscopy*

The scanning electron microscope (SEM) permits the observation and characterisation of materials on a nanometre to micrometre scale.

In the SEM, the area to be examined is irradiated with a finely focussed electron beam. The beam maybe swept in a raster across the surface of the specimen to form images, or be static to obtain analysis at one position [259]. The types of signals produced from the interaction of the electron beam with the sample include secondary electrons, backscattered electrons, characteristic X-rays, and other photons of various energies. These signals are obtained from specific emission volumes within the sample and can

be used to examine many characteristics of the sample. I.e. surface topography, crystallography, composition, etc.

For imaging purposes, the secondary and back scattered electrons are utilised. Zworykin [260] first recognised that secondary electron emission would be responsible for topographic contrast. The secondary electron emission permits images to be obtained at a resolution approximating the size of the focussed electron beam. The three dimensional appearance of the images is due to the large depth of field of the SEM as well as the shadow relief effect of the secondary and backscattered electron contrast [259]. The field emission electron source uses a very small source, so that a probe of nanometre size with very high brightness can be obtained for improved imaging quality.

For elemental analysis, the characteristic x-rays are utilised, with the addition of an energy-dispersive X-ray spectrometer (EDS or EDX). At rest, an atom within the sample contains ground state (or unexcited) electrons in electron shells bound to the nucleus. The incident beam may excite an electron in an inner shell, ejecting it from the shell while creating an electron hole where the electron was. An electron from an outer, higher-energy shell then fills the hole, and the difference in energy between the higher-energy shell and the lower energy shell may be released in the form of an X-ray. The number and energy of the X-rays emitted from a specimen can be measured by an energy-dispersive spectrometer. As the energy of the X-rays is characteristic of the difference in energy between the two shells, and of the atomic structure of the element from which they were emitted, this allows the elemental composition of the specimen to be measured.

In this research, for microstructural examinations all specimens were ground by Si carbide abrasive paper, up to a final grade 1200. Specimens were then polished to a 3 μm finish and lightly etched using nital solution (a mixture of 2% nitric acid and ethanol). The fusion zone, HAZ, and base metal microstructures were then examined at $t/4$ (t is the thickness of the plate) from the OD using an FEI Sirion 200 field emission gun SEM. EDX analysis was performed on the SEM using Spirit software package. The fracture surfaces of Charpy impact and fracture toughness test samples were opened to reveal the fracture surface. The fracture surfaces were then analysed with SEM and EDX.

5.3.1.3. *Transmission electron microscopy*

All TEM sample preparation and analysis was carried out at Oxford University by Dr Hiroto Kitaguchi. A FIB microscope (FEI FIB200) and a dual-column FIB (Carl Zeiss Nvision N40) were used to prepare TEM specimens. The TEM specimen preparation methodology for steel samples has been documented in [261, 262].

5.3.1.4. *Vickers hardness*

The Vickers hardness test was developed in 1921 [263] as an alternative to the Brinell method to measure the hardness of materials. The basic principle of Vickers hardness testing is to observe a material's ability to resist plastic deformation under load from a standardised pyramid shaped diamond indenter.

The indenter was pressed into the polished surface of the sample by an accurately controlled test force and maintained for a 10 second dwell time. After the dwell time was complete, the indenter was removed and the size of the resulting indent was determined optically by measuring the two diagonals of the square indent. The plastic deformation was then measured in terms of the mean diagonal impression and the Vickers hardness value, HV, is derived from the following equation:

$$HV = \frac{2P \sin(\frac{\alpha}{2})}{d^2} = \frac{1.8544P}{d} \quad (5-1)$$

Where, P is the Force (kgf), d is the mean diagonal of impression, $\frac{d_1 + d_2}{2}$ (mm), and α is the face angle of diamond = 136° .

The Vickers test has two distinct force ranges, micro (10 g to 1000 g) and macro (1 kg to 100 kg). For this study, a Mitutyo DT-10 micro-Vickers hardness test machine was used with a 10 g load following ASTM E384 (micro force ranges – 10 g to 1 kg) to determine the hardness properties of the individual phase constituents within the sub-regions (base metal, HAZ, fusion zone, etc) of the weld joint. A Zwick Roell Indentec macro-Vickers hardness test machine was also used with a 10 kg load following ASTM E92 (macro force ranges – 1 kg to 100 kg) to determine the bulk hardness properties across the welded joint. Measurements were made at $t/4$ from the OD of the pipe.

5.3.1.5. Charpy impact toughness

The Charpy impact test was developed around 1900. The test became known as the Charpy test in the early 1900s due to the technical contributions and standardization efforts by Georges Charpy [264]. The test was pivotal in understanding the fracture problems of ships during WWII [265].

The purpose of the Charpy impact test is to measure the energy that a material can absorb under impact. This is particularly useful for ferritic steels that show a ductile to brittle transition with decreasing temperature. A brittle metal will absorb a small amount of energy when impact tested whereas a tough ductile metal absorbs a large amount of energy. The appearance of a fracture surface also gives information about the type of fracture that has occurred; a brittle fracture is bright and crystalline, a ductile fracture is dull and fibrous. The results are qualitative, and can only be compared with each other or with a requirement in a specification.

For this research, Charpy V-notch samples (50 mm x 10 mm x 10 mm, with 2mm notch depth and 0.25 mm root radius) were produced and tested at 0°C in accordance with API standard [266]. However, rather than notching transverse to the weld as stipulated in API standard, the notch was made longitudinal to the weld (Figure 5-1) in order to enable better control of the notch position in relation to position within the HAZ. The samples were taken from the base metal, HAZ, and fusion zone at the same location in which microstructure and hardness observations were made ($t/4$ from the OD).

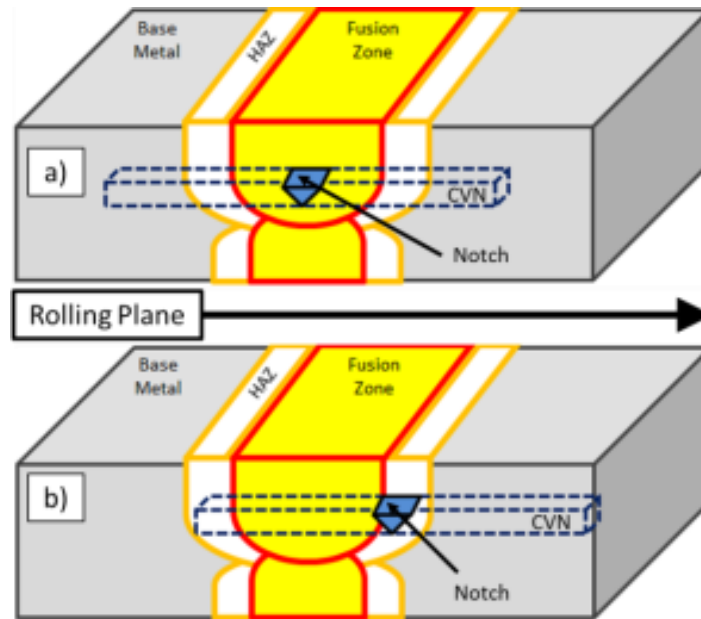


Figure 5-1: Schematic illustration of the location and orientation of Charpy V-notch samples taken from the X65 linepipe.

The standard Charpy V-notch specimens were supported at two ends on an anvil and struck by the pendulum on the face opposite to the notch. The pendulum swung from a set height with a controlled weight. The impact with the test sample on the downswing absorbs energy from the swinging pendulum. The height of the follow-through swing is then measured to ascertain the amount of energy absorbed in fracturing the specimen.

5.3.1.6. K_{Ic} fracture toughness

The intention of a fracture toughness test is to measure the resistance of a material to the presence of a flaw in terms of the load required to cause brittle or ductile crack extension (or to reach a maximum load condition) in a standard specimen containing a fatigue pre-crack. The result is expressed in terms of toughness parameters such as K_{Ic} , critical J , or critical $CTOD$. The measurement of fracture toughness is covered by several standards, such as BS7448 and ASTM E1820.

For this research, the tests were carried out in accordance to ASTM E1820. A total of 6 fracture toughness tests were carried out. Samples were machined from the same

position as the Charpy specimens, using the same specimen size and orientation. The samples were tested at 0 °C. Prior to the tests pre-cracks were generated for all the 6 specimens including a 3.5 mm notch depth located centrally and transverse to the weld, plus a targeted minimum of 1.3 mm fatigue crack growth.

A monotonically increasing load was applied during testing, and both load and crack mouth opening were monitored.

5.3.2. Weld geometry and chemical analysis

Figure 5-2 highlights the various weld regions under examination across the SAW joint. It is clear from the image that the combined heat input of the two pass SAW process has produced a defect free, fully penetrated weld, with a good weld bead shape. The high heat input from the SAW process also created a visible HAZ of between 2 – 4 mm in width at either side of the fusion zone.

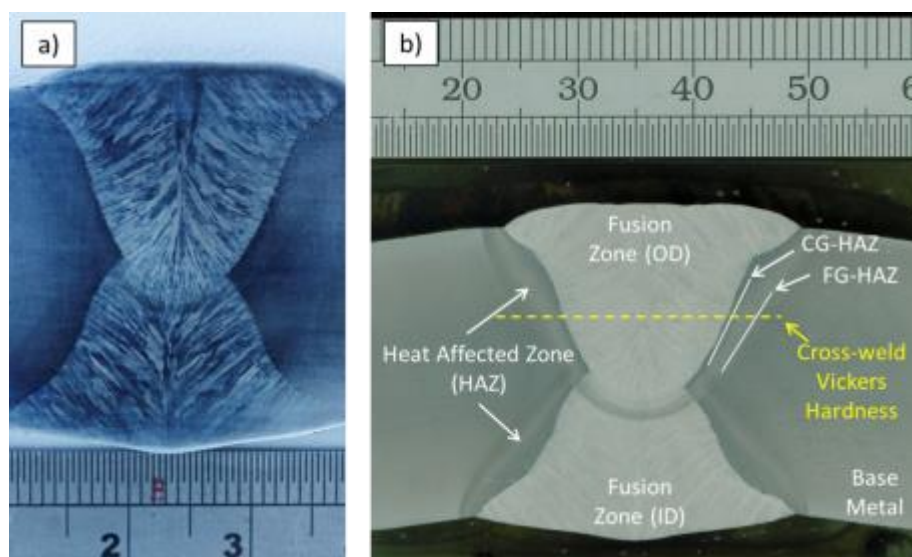


Figure 5-2: Transverse weld macrograph highlighting the various weld region: fusion zone, fine grain heat affected zone (FG-HAZ), coarse grain heat affected zone (CG-HAZ), base metal, and location of Vickers hardness indentations.

Table 5-2 summarises the measured chemistries of the as-welded SAW joint, obtained through optical emission spectroscopy (OES). The extremely low C content (0.04 wt.%) in the X65 base metal ensures excellent weldability (0.135 C_{eq}). Yet, by lowering the materials C content to this level, its strength would also have been reduced as a result of the decreased volume fraction of the relatively hard, cementite enriched, pearlite phase present in the microstructure. However, compensation has been made by the addition of small amounts (< 0.04 wt.%) of grain refining elements, such as V, Nb, and Ti. These elements pin the austenite boundaries with second-phase particles which allow for fine grain sizes (<10 μm) to be produced by TMCR [267].

Similarly low levels of V (0.003 wt.%) were found within the weld, however the weld exhibits higher levels of Ti (0.025 wt.%) and lower Nb (0.025 wt.%) concentrations in comparison to the base metal. The Ti and N contents play an important role in the formation of TiN particles. Higher contents of Ti and N can result in the formation of coarse TiN particles before solidification ends. Therefore, Ti and N contents should be controlled to be less than the solubility limits at solidus temperature to avoid the formation of coarse TiN particles. Also, the Ti/N ratio is significant to the growth of TiN particles during cooling. If Ti/N ratio is greater than the stoichiometric TiN (3.42), then TiN can coarsen at a faster rate [127].

A significant increase in Mo levels found within both the ID and OD weld, combined with the presence of Ni, has been found to decrease the volume fraction of grain boundary ferrite (GBF) within the fusion zone of SAW joints, while also giving rise to a microstructure which is predominantly fine acicular ferrite (AF) [141]. Similarly, the presence of B within the weld has also been found to promote AF formation [200]. However, the referenced work also demonstrated that by increasing the B content above the 0.003 wt.% present in the weld under examination in this paper, the volume of AF actually reduces and eventually induces the formation of an undesirable bainite microstructure as B level is increased above 0.01 wt.%.

As well as these intrinsic features within the respective weld regions, increased levels of Si and Mn in both the ID and OD weld are seen in Table 5-2 as a result of the diffusion of small amounts of Si (0.1 wt.%) and Mn (0.15 wt.%) from the flux into the fusion zone during the SAW process. Also, the mix of both the base metal and welding wires during the SAW process has led to a low Cr content within the fusion zone (about 0.1%) compared to the base metal (0.156%). However, the overall overmatching chemistry of the consumable selected in terms of C and other alloying elements such as Mo, V and B has resulted in an overmatching weld metal as intended in terms of the C equivalent values.

The effect that these alloying additions have on microstructure and mechanical properties will now be discussed in the proceeding sections.

		C	Si	Mn	P	S	Cr	Ni	Mo	Cu
Nominal Chemistries	X65 Base Metal	0.026	0.32	1.49	0.004	0.0003	0.17	0.009	0.002	0.011
	Welding Wire 1	0.07	0.26	1.1	0.013	0.003	0.04	0.021	0.51	0.02
	Welding Wire 2	0.08	0.27	1.14	0.013	0.002	0.035	0.024	0.5	0.02
Results of OES	X65 Base Metal	0.04	0.315	1.499	0.006	0.001	0.156	0.013	0.003	0.014
	ID Weld	0.049	0.335	1.531	0.011	0.003	0.105	0.018	0.174	0.04
	OD Weld	0.051	0.336	1.509	0.012	0.003	0.104	0.016	0.207	0.041
		V	Al	Nb	Sn	B	N	Ti	C _{eq}	Ti/N
Nominal Chemistries	X65 Base Metal	0.004	0.034	0.043	--	0.0002	0.005	0.012	0.122	2.4
	Welding Wire 1	0.006	0.011	--	0.001	0.017	0.003	0.012	0.274	4
	Welding Wire 2	0.007	0.011	--	--	0.01	0.002	0.01	0.233	5
Results of OES	X65 Base Metal	0.002	0.034	0.041	0.002	0	0.004	0.013	0.135	3.25
	ID Weld	0.003	0.02	0.026	0.002	0.003	0.005	0.024	0.171	4.8
	OD Weld	0.003	0.018	0.023	0.002	0.004	0.005	0.026	0.179	5.2

Table 5-2: Nominal and measured chemistries obtained through optical emission spectroscopy.

$$C_{eq} = \text{Carbon equivalent value} = C + \frac{Si}{30} + \frac{Mn+Cu+Cr}{20} + \frac{Ni}{60} + \frac{Mo}{15} + \frac{V}{10} + 5B \text{ wt\%}$$

[266]

5.3.3. Microstructure analysis

5.3.3.1. Base metal

Analysis of the base metal microstructure revealed a very fine grain structure with an average grain size of approximately 7 μm x 4 μm (calculated using the mean linear intercept technique). The grains are elongated along the rolling direction and consist of predominantly (90% volume fraction) of primary ferrite, as seen in Figure 5-3(a) It is concluded that the second phase is degenerate pearlite (DP) (10% volume fraction), highlighted in Figure 5-3(b). The structure of the DP phase, which is referred as pseudo-pearlite without the banding pattern, was different from that of typical pearlite evolved by normalizing and slow cooling. The high cooling rate associated with the accelerated cooling process retards the C diffusion efficiency during cooling to a point at which is insufficient for the lamellar structure of cementites, more commonly associated with pearlite, to form [70].

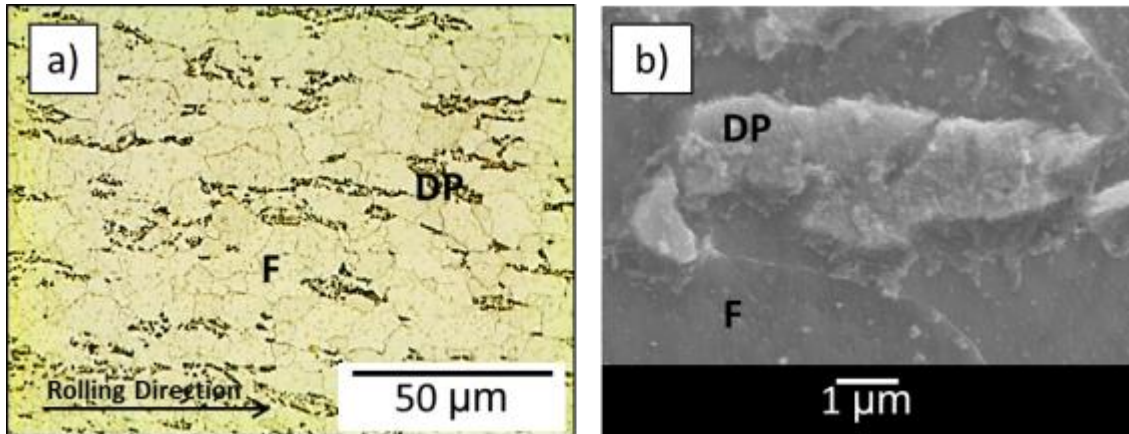


Figure 5-3: Primary ferrite (F) and second phase degenerate pearlite (DP) microstructure observed in the API 5L grade X65 base metal under a) optical microscope, b) SEM.

A small number of large (1.5 μm) cuboidal precipitates were found pinned to grain boundaries, as highlighted in Figure 5-4(a). SEM – EDX line mapping analysis, depicted in Figure 5-4 (b) and (c), show the precipitates to be enriched in Ti and V; particularly at the extremities, while also being depleted in Fe. Increased counts for both C and N in the region lead to the assumption that the precipitates are in fact Ti(V) carbonitrides (C, N).

The EDX line mapping analysis also encompassed a globular Al enriched inclusion. Al is added to steels in small amounts to act as a deoxidiser [268]. Al_2O_3 (Alumina), also known as Corundum ($\alpha\text{-Al}_2\text{O}_3$) is a common inclusion phase found in steel as a result of de-oxidation [269]. Some studies have found that the relative coarseness (2 μm) of the inclusion under examination can influence the ductile failure characteristics of the steel [270].

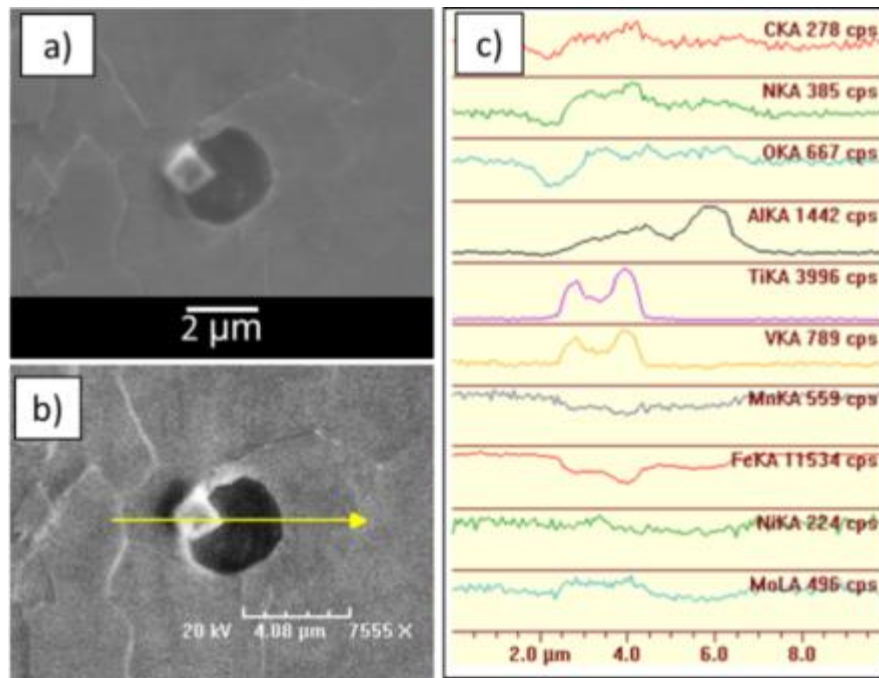


Figure 5-4: a) SEM image of large cuboidal Ti (C, N) precipitate and Al₂O₃ inclusion, b) Direction of EDX line mapping, c) Qualitative EDX line mapping results.

5.3.3.2. Heat affected zone

The visible HAZ was assessed as two entities; the CG-HAZ, and the FG-HAZ with their relative locations being defined in Figure 5-2. For the purpose of this study, only the observations made from the CG-HAZ will be presented as the CG-HAZ region has been a recent area of focus in the assessment of local brittle zones (LBZ) and their effect on HAZ toughness [73].

Figure 5-5(a) shows the CG-HAZ microstructure observed in the immediate vicinity to the fusion zone. The CG-HAZ exhibits an average grain size of approximately 11 μm x 7 μm. The intense thermal exposure from the SAW process in the CG-HAZ led to the dissolution of some of the strong carbide and nitride precipitation in the region. As previously discussed, small (<0.1 μm) precipitates form from strong, micro-alloyed, carbide and nitride formers (Ti, V, Nb) and pin grain boundaries to inhibit grain growth within the base metal at high temperature. The dissolution of these precipitates reduces the influence that grain pinning has in the controlling of grain size, and as a result, grain growth occurs. The 60% increase in grain size within the CG-HAZ, when compared to

the grain size in the unaffected base metal, can lead to reduced strength and toughness properties within the region [13].

Figure 5-5(b) highlights the polygonal ferrite (PF), and upper bainite (UB) microstructure found at higher magnifications in the CG-HAZ, close (<100 μm) to the fusion line. The relatively low cooling rate, in comparison to the accelerated cooling used in the X65 base metals manufacture, retained the CG-HAZ in the 550 – 400°C region for a period sufficient enough to allow the formation of upper bainite. The low C content (0.04 wt.%) in the API-5L grade X65 base metal produces small discrete particles of cementite precipitating from the residual austenite layers in between the ferrite sub-units, as seen in Figure 5-5(b).

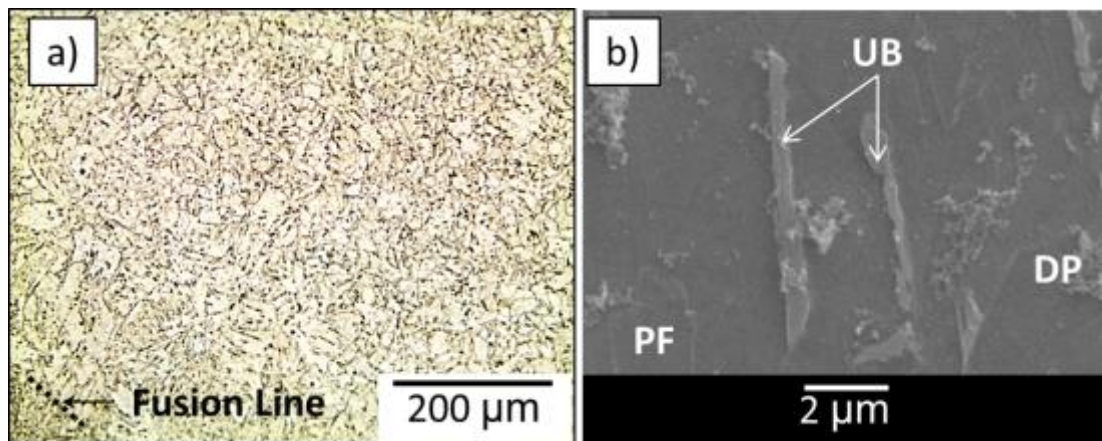


Figure 5-5: CG-HAZ observed under a) optical microscope, showing the grain growth region in the immediate vicinity to the fusion line, b) SEM, illustrating the upper bainite (UB), polygonal ferrite (PF), and degenerate pearlite (DP) microstructure

5.3.3.3. *Fusion zone*

When welding materials of a similar composition, epitaxial growth rather than nucleation occurs [108]. The solidifying grains grow anisotropically towards the heat flow resulting in the coarse and columnar fusion zone grain structure depicted in Figure 5-2(a).

Closer examination of the columnar grains in Figure 5-6(a) and (b) show a fine (2 μm) acicular ferrite microstructure (30% volume fraction) with small amounts of grain boundary phases in the columnar grains within the fusion zone. The Ni addition to the welding wire chemistry, along with relatively high Mo (0.107-0.204 wt.%) [141], and B (0.003 wt.%) [200] decreases the volume fraction of grain boundary ferrite within SAW joint, and give rise to the predominantly fine acicular ferrite microstructure as shown in Figure 5-6(b). Figure 5-6(c) shows the plates of acicular ferrites nucleated heterogeneously on small non-metallic inclusions and radiated in many different directions from these 'point' nucleation sites. It is believed that propagating cleavage cracks are frequently deflected as they cross an AF microstructure with its many different orientations [40]. This gives rise to superior mechanical properties, especially toughness. In pipeline steel welds, AF is regarded as the most desirable microstructural feature in view of these strength and toughness properties.

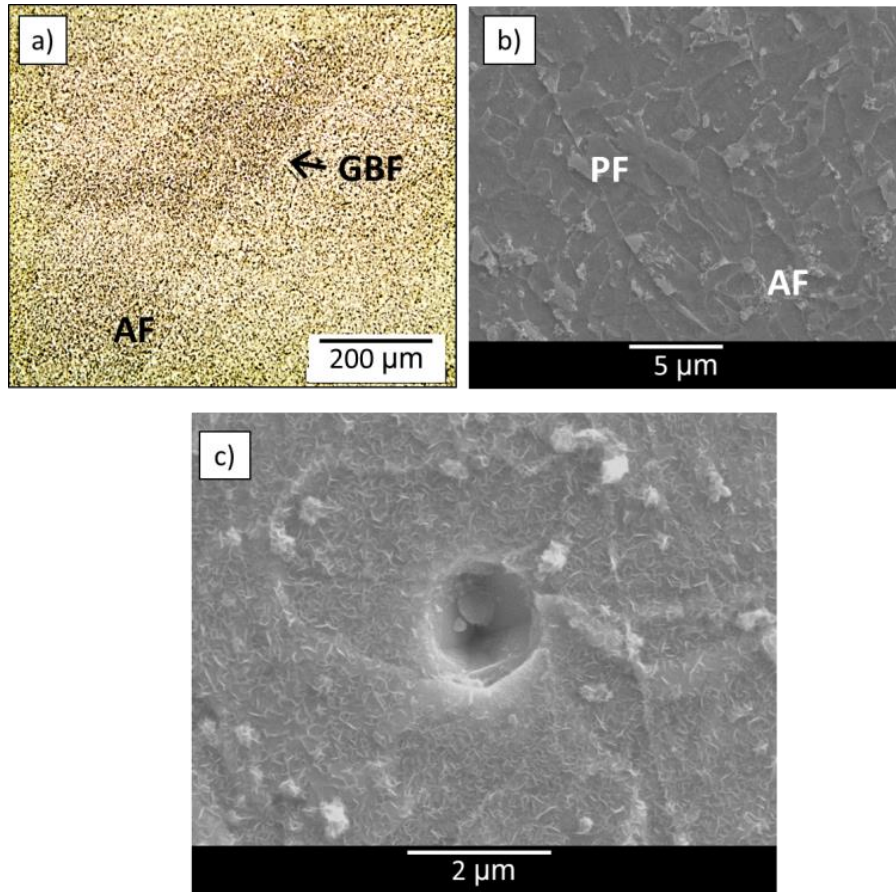


Figure 5-6: Predominantly acicular ferrite (AF) microstructure found in the fusion zone, observed under a) optical microscope, showing AF, and grain boundary ferrite (GBF) phases SEM, b) showing AF and polygonal ferrite (PF) phases, and c) SEM, showing small AF plates which have nucleated heterogeneously and grown from a non-metallic inclusion.

Figure 5-7 shows a typical example of coarse Ti enriched particles in the fusion zone. Crystallographic analysis was carried out and revealed that the Ti enriched particles have a mixture of alumina (solid circle) and Ti enriched phases (broken circle). The solid and broken circles in Figure 5-7 correspond to the positions where the selected area diffraction patterns (SADP) were taken in the TEM bright field image. The SADP shown in Figure 5-7(b) suggests that the crystal has a long lattice parameter in at least one lattice direction. The other SADP is shown in Figure 5-7(c), where the structure was confirmed as cubic with $a = 0.43 \text{ nm}$. Figure 5-8 shows the EDX mapping of the same particle. It is noted that the areas where the diffraction patterns in Figure 5-7(b) and (c) were acquired correspond to the Al and Ti rich regions, respectively.

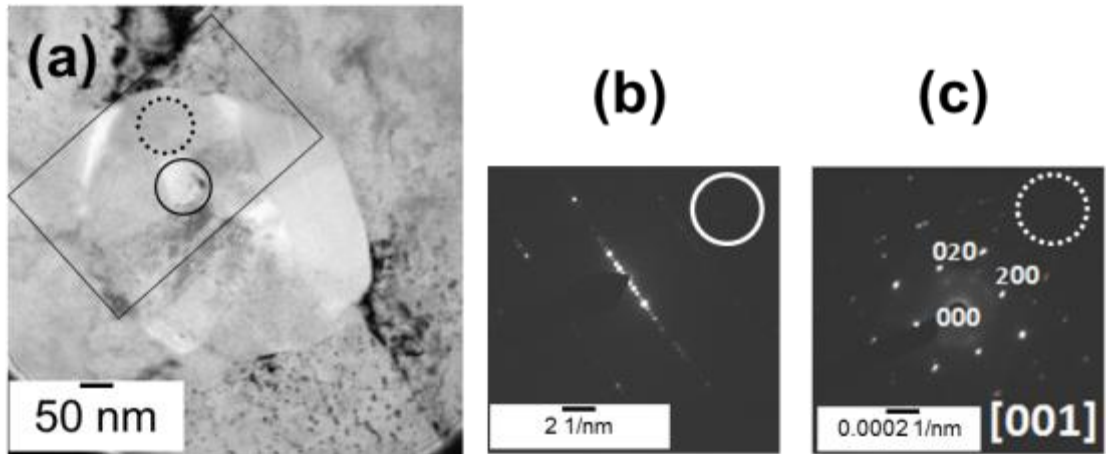


Figure 5-7: TEM bright field image of a coarse particle in the weld fusion zone (a) and two SADPs (b) and (c). The circles in the figures correspond to the area chosen in (a) for the acquisition of the diffraction patterns in (b) and (c). The rectangle box in (a) will be explained in Figure 5-8.

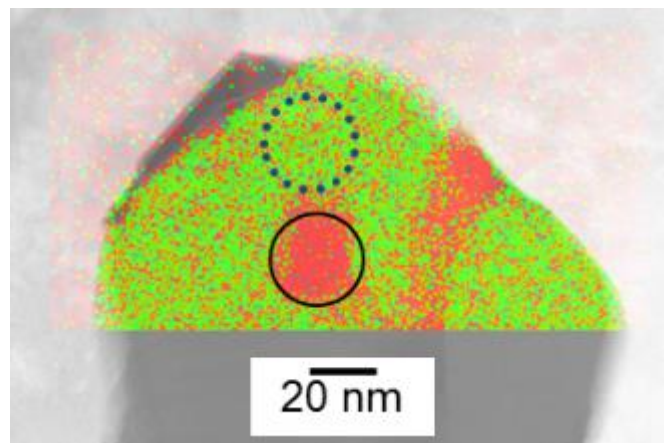


Figure 5-8: EDX mapping results for Al (red) and Ti (green) of the same precipitate in Figure 5-7. The region analysed by EDX mapping was indicated by the rectangle box in Figure 5-7. The positions of the SADP circles from Figure 5-7 are also shown.

In order to quantify the size and distribution of the particles reported on in Figure 5-7 and Figure 5-8, imaging software was used to analyse lightly-etched optical micrographs (see Figure 5-9(a)), as suggested by Yoo *et al* [271]. The scatter of the

results is presented in Figure 5-9(b). From the analysis the mean particle diameter was found to be 0.85 μm with a relative volume fraction of 0.103.

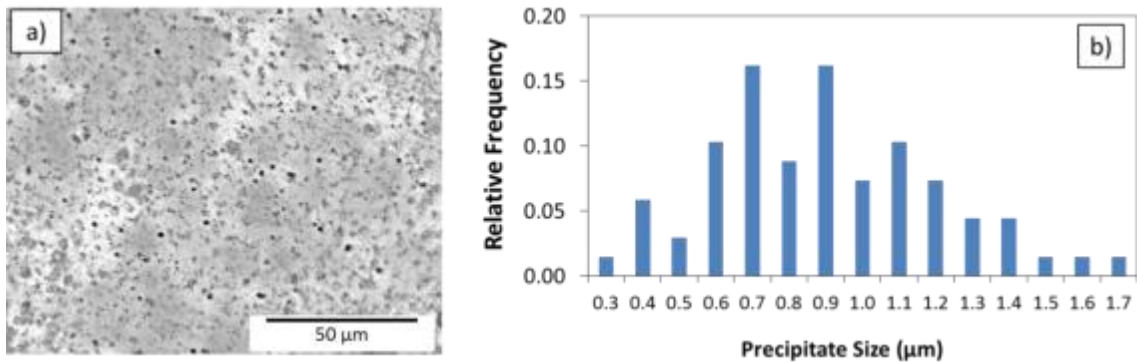


Figure 5-9: a) Lightly-etched optical micrograph showing the distribution of coarse particles (dark circular phase) in the weld fusion zone, b) the distribution of particle size observed in Fig.5-9(a).

5.3.4. Mechanical properties of the welded joint

Figure 5-10 shows the Vickers hardness and impact toughness across the welded joint. All results satisfy the minimum hardness and impact toughness values set out in API standard [86, 266]. The fusion zone exhibits high hardness (230 HV10) coupled with low impact toughness (223 J) properties, and as such is a key area of interest from a fracture mechanics perspective. As such, further fracture toughness tests were carried out with the mean of the measured fracture toughness summarised in Table 5-3. It shall be noted that the average fracture toughness in terms of stress intensity factor, K_{Ic} , of the weld joint is 40.8 $\text{MPa}\cdot\text{m}^{1/2}$. The base metal reveals high impact toughness (362 J) along with moderate hardness properties (192 HV10) in respect to the rest of the SAW joint. HAZ softening occurs in the fine grained HAZ (FG-HAZ), while it appears that the hardness also decreases sharply in the coarse grained HAZ (CG-HAZ).

Young's Modulus (E)	Yield Strength (Ys)	Fracture Toughness (K_{Ic})	C.T.O.D (δ)	Area under the curve (U_{pl})	Plastic part of J (J_{pl})	Elastic part of J (J_{el})	Total J (J_{Ic})
207 GPa	500 MPa	40.80 $\text{Mpa}\cdot\text{m}^{1/2}$	0.28 mm	4.78 kN.mm	0.26 J/mm^2	0.02 J/mm^2	0.28 J/mm^2

Table 5-3: Mean results from six fracture toughness (ASTM 1820) tests made on the fusion zone.

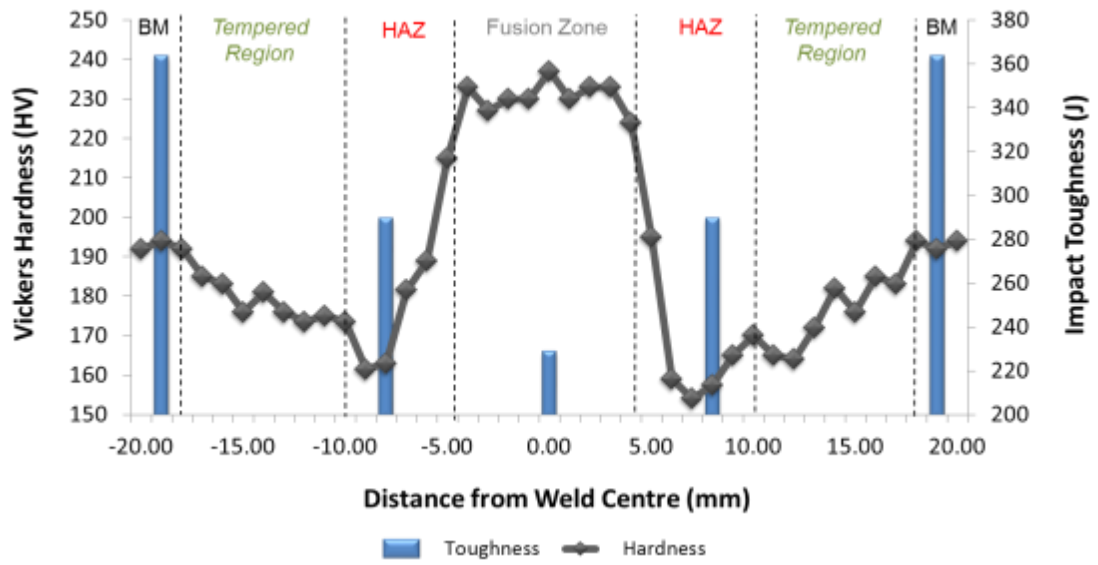


Figure 5-10: Vickers hardness and impact toughness measured by Charpy V-notch tests over a weld joint.

5.3.5. Fractography analysis of toughness samples

5.3.5.1. Base metal

Analysis of the base metal CVN fracture surfaces revealed delamination phenomenon. Specifically, on the base metal CVN fracture surface parallel to the rolling plane, as emphasized by the white box on Figure 5-11(a). Closer examination of the delaminated region in Figure 5-11(b) reveals mixed fracture morphologies. Close to the delamination origin, ductile dimples, or microvoids are observed. Yet, towards the edge of the delaminated terrace, a somewhat dendritic topology is found.

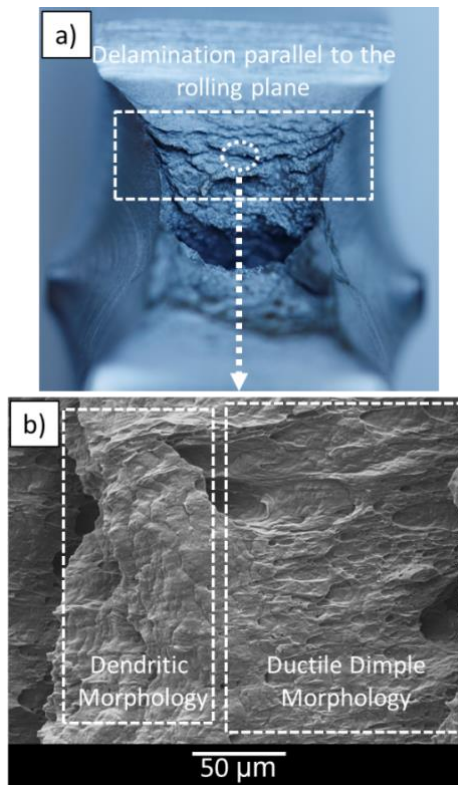


Figure 5-11: a) Macro image identifying delamination on the X65 base metal CVN fracture surface, b) SEM image detailing dimpled fracture surfaces close to the delamination origin.

5.3.5.2. Heat affected zone

The HAZ CVN sample achieved lower impact toughness results (288 J) in comparison to the base metal. Figure 5-12(b) reveals the increased coarseness to the fracture surface of the HAZ CVN sample. The increased coarseness of the microvoids and lower impact toughness values can be attributed to the coarser grain structure (11 μm x 7 μm) of the HAZ.

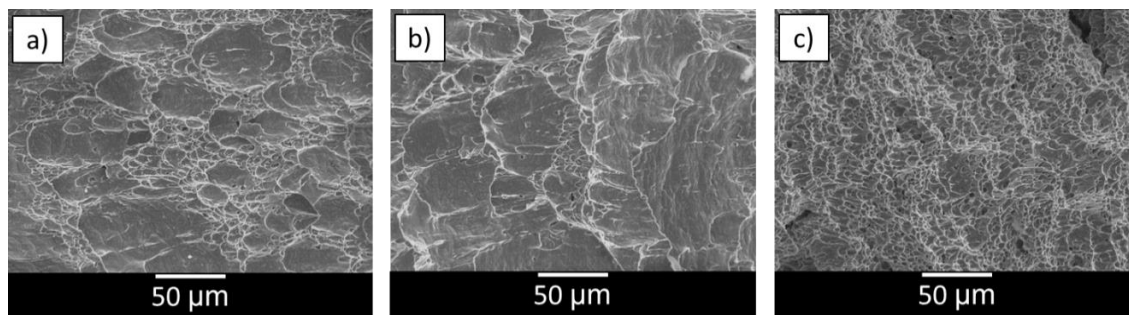


Figure 5-12: Ductile dimple fracture surfaces observed in CVN samples tested at 0°C under SEM; a) base metal, b) HAZ, and c) fusion zone

5.3.5.3. Fusion zone

The lowest impact toughness (228 J) was recorded in the fusion zone, yet the value was considerably higher than the minimum acceptance criteria (23 J) stipulated in API standard [266]. The fracture surface observed in the fusion zone CVN sample (Figure 5-12(c)) reveals a fully ductile fracture surface with a high density microvoid matrix and no delaminated regions.

Fractography examination on the fracture surface of the fusion zone CVN sample in Figure 5-13 reveals a high population of the coarse Ti enriched particles characterised in Figure 5-7 and Figure 5-8 to be located within the centre of the microvoid matrix.

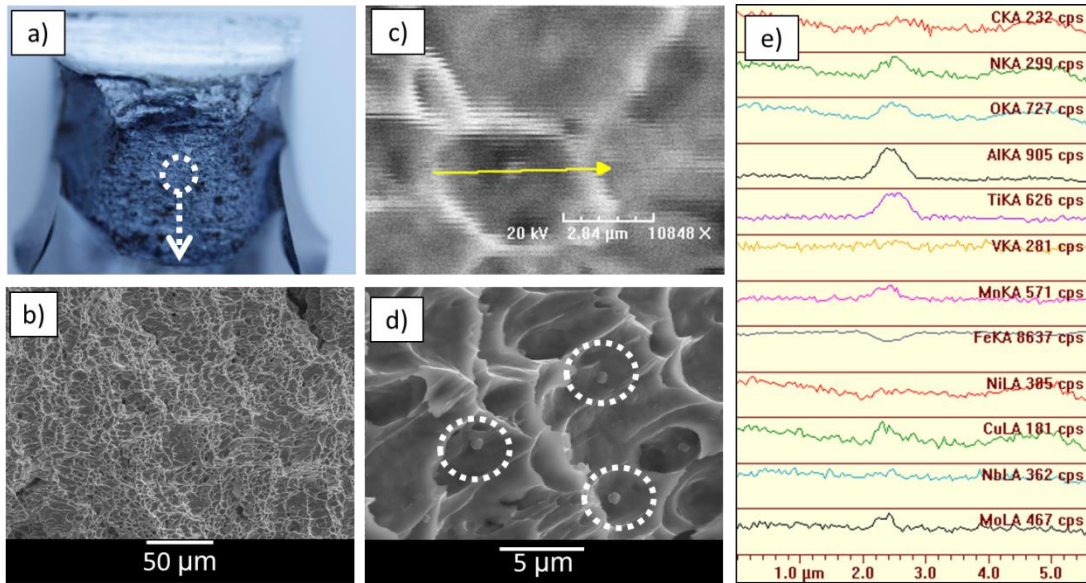


Figure 5-13: a) Macro image of fusion zone Charpy V-notch fracture surface, b) SEM image showing fully ductile fracture in centre of CVN sample, c) Direction of EDX line mapping across a chosen particle, d) SEM image showing large particles in the centre of microvoids, e) Qualitative EDX line mapping results along direction marked in c).

Figure 5-14 shows macrographs of the fracture surface of a K_{Ic} specimen tested at $0\text{ }^{\circ}\text{C}$. The ductile fracture in Figure 5-14(b) reveals that the fracture toughness of the weld metal determined by the experiment was upper-shelf values. For this type of material the ductile-to-brittle transition temperature is expected to be lower than $-80\text{ }^{\circ}\text{C}$ [272]. Further analysis in Figure 5-14(c) and (d) reveals a high number of large spherical particles to be located in the centre of the fracture microvoids. Qualitative EDX spectra (Figure 5-15(b)) and line mapping (Figure 5-15(c)) analysis, confirmed the particles to be of a similar composition to those presented in Figure 5-7, Figure 5-8 and Figure 5-13.

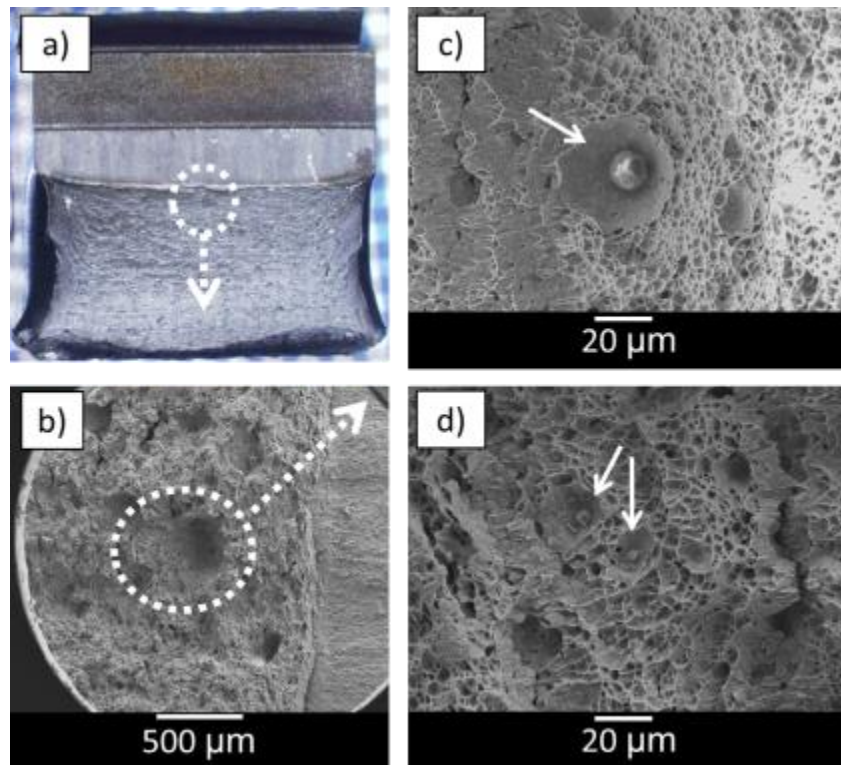


Figure 5-14: Fractography analysis of K_{Ic} fracture toughness specimens, showing; a) macrograph of specimen fracture surface, b) Secondary electron micrograph of area under examination showing fully ductile fracture, c) Very large ($12\ \mu\text{m}$) second phase particle inherent to the centre of the large fracture void under investigation, d) some of the smaller and more frequently distributed second phase particles.

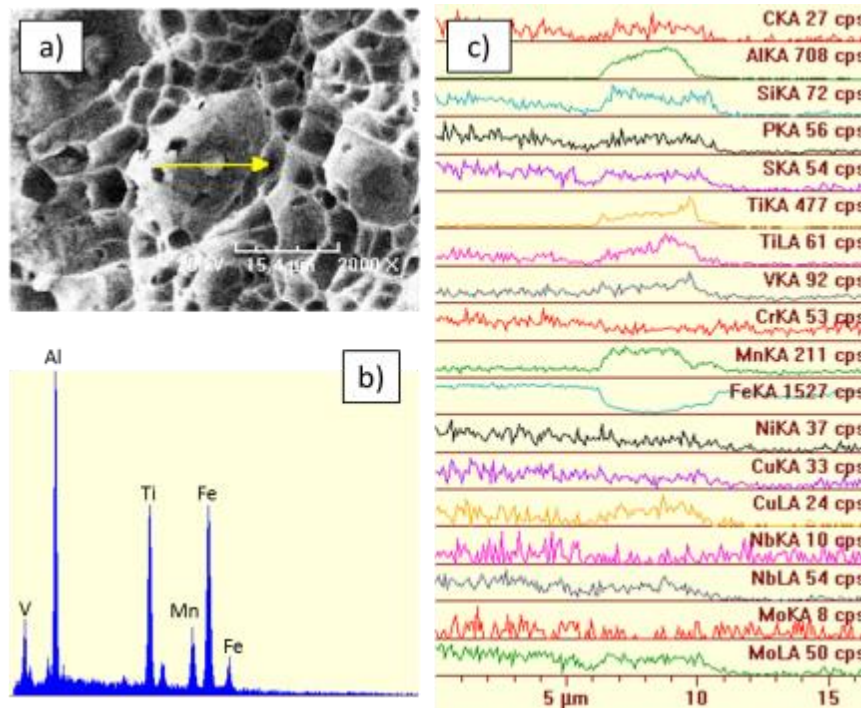


Figure 5-15: Chemical analysis of second phase particles found within the ductile fracture micro voids of the K_{Ic} fracture toughness specimens defining, a) particle under investigation and direction of EDX line map, b) EDX spectra of particle showing Al and Ti enrichment, c) Qualitative line mapping analysis highlighting Al, Ti, Mn, and V enrichment.

5.3.6. Discussion

In terms of the base metal microstructure, the large cuboidal Ti(V) (C, N) precipitates observed in Figure 5-4 are particularly interesting features where mechanical property improvements can be achieved. The particles do not aid in inhibiting austenite grain growth at high temperatures, despite their stability, because they are too large: $\geq 0.5 \mu\text{m}$, rather than the $0.1 \mu\text{m}$ required [125, 273]. Furthermore, they remove Ti, Nb, and V from solution; reducing precipitation hardening. It is therefore desirable to avoid the formation of large cuboidal Ti(V) (C, N) precipitates, and to reduce their size.

In practice, the control of precipitate size can be difficult. The multi-phase microstructure of HSLA steels is always unstable if the total interfacial free energy is not a minimum [274]. Therefore, a high density of small precipitates will tend to coarsen into a lower density of larger precipitates with a smaller total interfacial area. Due to the Gibbs-Thomson effect [156], the solute concentration in the matrix adjacent to a precipitate will increase as the radius of curvature decreases. Therefore, there will be concentration gradients in the matrix which will cause solute to diffuse in the direction of the largest precipitates away from the smallest. The overall result is that the total number of particles decreases and the mean radius (\bar{r}) increases with time. By assuming volume diffusion is the rate controlling factor, it has been shown that the following relationship should be obeyed [157]:

$$(\bar{r})^3 - r_0^3 = kt \quad (5-2)$$

and,

$$k \propto D\gamma X_e \quad (5-3)$$

where, r_0 is the mean radius at time $t = 0$, D is the diffusion coefficient, γ is the interfacial energy and X_e is the equilibrium solubility of very large precipitates. Since D and X_e increase exponentially with temperature, the rate of coarsening will increase

rapidly with increasing temperature – a key consideration in view of the austenitic (~1000°C) temperature conditions during the TMCR process.

It is reasonable to assume that the growth rate of Ti (C, N) particles is controlled by the diffusion of Ti, since the diffusion rate of substitutional Ti in austenite is significantly lower than that of either interstitial C or N. In addition, as the precipitate is local to the grain boundary, it is possible to conclude that the coarsening of the precipitates is controlled by the grain boundary diffusion of Ti away from smaller precipitates during the high temperature TMCR process. The TMCR process is a key part of the manufacturing process - essential in facilitating the high strength and toughness properties of the base metal, and cannot be discounted. One method of controlling the size of the large Ti (C, N) has been suggested by reducing the Ti and N alloying concentrations. This would then reduce the segregation of Ti and N in the liquid. However, by decreasing the amount of N too far, the volume fraction of nitride precipitates in austenite would significantly reduce, and is therefore undesirable. Chen *et al* [125] proposed the reduction of only the Ti content, while the size of the Ti(V) (C, N) precipitates may also be reduced by using a faster cooling rate during solidification.

Other than strengthening the base metal, as previously discussed, Ti and Nb are also added to the steel in order to lower interstitial C and N. The reduction of these interstitial elements reduces the ductile to brittle transition temperature through the mitigation of locking dislocations [275]. Previous studies [76, 276] have found the ductile to brittle transition temperature for similar grades of steel to be in the region of -50°C to -100°C.

Toughness testing in the upper-shelf region revealed the base metal has the highest impact energy (362 J). This is a result of the small grain size (7 µm x 4 µm) found within the base metal working to increase dislocation pile up at grain boundaries. The dislocation pile up then increases the amount of applied stress necessary to move a dislocation across a grain boundary and as a result increases toughness, as described by the Hall-Petch relationship [65]. However, research by Ju *et al* [76] found there to be anisotropy in the fracture toughness of API-5L grade X65 steel. The study found that the longitudinal notch orientation as utilized for the CVN tests presented in this research achieved almost 100% lower toughness properties in comparison to CVN's

made transverse to the weld. The root cause of this was proposed as the lower volume fraction of the densely packed “110” preferential slip plane in the longitudinal direction when compared to the transverse. More recently, Bhadeshia *et al* [77] proposed that rather than the alignment of preferential slip planes, directionally dependent delamination and texture effects were a more likely basis for reduced CVN impact toughness in hot rolled HSLA steels. The study found the delamination to be much more pronounced in CVN samples machined with longitudinal notch orientations, as used in this research.

It is known that orientation-dependent properties in linepipe steels are related to inclusions, microstructural anisotropy and unfavourable crystallographic texture [77]. In the context of inclusions, Mn sulphides and silicates become elongated during the rolling process and are commonly accepted to be the initiator of delamination. Also, the bands of degenerate pearlite observed in Figure 5-3(a) result from solidification-induced chemical segregation and lead to further directionally dependant toughness properties.

As future research, it is suggested casting trials are implemented to vary the Ti content of the base metal. SEM/TEM should be used to quantify the size and distribution of the Ti (C,N) precipitation. The results should then be compared against mechanical properties (strength and toughness) to ascertain if any minor Ti adjustments in chemistry can be favourable to strengthening and fracture/impact toughness. Further work is also required to study directionally dependant fracture properties of the TMCR base metal.

Table 5-4 summaries the average Vickers hardness values for each respective weld region, while Table 5-5 summaries the average micro-Vickers hardness values for the individual phases present within the respective weld regions.

BM	TR	FGHAZ	CGHAZ	FZ
193 HV10	171 HV10	160 HV10	195 HV10	232 HV10

Table 5-4: Average weld region Vickers hardness (10 kg load) results.

F	DP	UB	AF
189 HV0.1	232 HV0.1	283 HV0.1	243 HV0.1

Table 5-5: Average micro-Vickers hardness (10 g load) values for the individual phases present in the respective weld regions.

Hashemi *et al* [277] recently published Vickers hardness results of 212 HV10 for an API-5L grade X65 steel with an AF-B microstructure, produced through an alternative TMCR process with accelerated cooling. In this study, the F-DP microstructure observed in the unaffected X65 base metal achieved an average hardness value of 193 HV10, a 9% reduction in hardness in comparison to the AF-B microstructure reported in the aforementioned study. The overall macro-scale hardness property of the base metal can be measured with the micro-hardness values and relative volume fractions of the individual phase constituents within the region using Eq. 5-4.

$$HV_{Base\ Metal} = (VF_F \cdot HV_F) + (VF_{D,P} \cdot HV_{D,P}) \quad (5-4)$$

Where, VF_F , is the volume fraction (90%) and, HV_F , is the micro-Vickers hardness value (189 HV0.1) for the ferrite phase. Similarly, $VF_{D,P}$, is the volume fraction (10%) and, $HV_{D,P}$, is the micro-Vickers hardness value (232 HV0.1) for the degenerate pearlite phase. Using these inputs, the predicted macro-hardness of the base metal is 193.3 HV. When comparing to the experimental value of 193 HV10 it is possible to conclude that the base metal hardness is directly related to the volume fraction and hardness of the respective microstructure constituents. As such, it can also be deduced that the decreased hardness in respect to the previously presented results [277] is due to the absence of the hard bainitic (283 HV0.1) and AF (243 HV0.1) phases, in comparison to the low volume (10%) of relatively soft DP (232 HV0.1) in the material under investigation in this paper.

The HAZ is outside of the main scope of study, and as such will only be discussed briefly. The area between the unaffected base metal and the FG-HAZ was subjected to maximum temperatures of just below 730°C, the A_1 temperature, during the SAW process. These temperatures facilitate tempering within the area, reducing hardness, while also being anticipated to increase toughness within the region.

The FG-HAZ revealed the lowest hardness results across the SAW joint, with an average hardness of 160 HV10. This region was subjected to temperatures sufficient enough to cause the coarsening and dissolution of some of the grain boundary pinning precipitates, facilitating grain growth. The increased grain size, along with the decreased volume fraction of the small ($<0.1 \mu\text{m}$), hard carbides and nitrides can be defined as the source of the low hardness.

Although the CG-HAZ witnessed further precipitate dissolution and grain growth when compared to the FG-HAZ, the region recorded 22% higher hardness values. The increased hardness (195 HV10) in the CG-HAZ can be attributed to the introduction of the hard (283 HV0.1) UB phase in the region, which counterbalances the softening effects of further grain boundary precipitate dissolution and grain growth. It is also clear that there is a steep increase in hardness towards the fusion line within the CG-HAZ. Although it is hard to quantify using the techniques (imaging software) previously used within the paper, there is a clear increase in the volume fraction of UB towards the fusion line. The increased volume of the hard UB phase close to the fusion line can be defined as the cause for the high (218 HV10) individual CG-HAZ hardness results seen in Table 5-5. The increased hardness can also lead to the manifestation of local brittle zones (LBZ) within the CG-HAZ close to the fusion line [73].

5.4. The role of Ti carbonitride precipitates on strength-toughness

Some of the mechanisms for solidification crack formation and propagation have been elucidated from observations of fracture surfaces. Based on these observations, the following crack nuclei have been suggested: 1) liquid film or liquid pool [36]; 2) pore or series of pores [24, 37]; 3) grain boundary located in the place of stress concentration; and 4) inclusions or precipitates that can be easily separated from the liquid or solid phase [38, 39].

The results presented in the previous sections show significant evidence of numerous Ti (C,N) particles to be located within the weld joint. Based on the solidification crack nucleation mechanisms presented in the paragraph above, it appears the nucleation of solidification cracks on the Ti (C,N) particles is feasible. The Ti (C,N) will be quantified comprehensively in the following chapters.

5.4.1. Identification and distribution of precipitates

Image analysis presented in Figure 5-9 revealed the approximate volume fraction of particles to be 0.103. Unfortunately, calculating the mean particle spacing using the same techniques has proved difficult. To aid the calculation of mean particle spacing, Somekawa *et al* [138] described the relative volume fraction, f_p , in terms of mean particle diameter, D_p , and mean particle spacing, d_p , as described in Eq. 5-5.

$$f_p \cong \frac{\left(\frac{\pi D_p^2}{2}\right)}{(\sqrt{3} d_p + \sqrt{2} D_p)} \quad (5-5)$$

To obtain the mean particle spacing d_p in Eq. 5-5, the mean particle diameter ($D_p = 0.85 \mu\text{m}$) and relative volume fraction of the particles (0.103) were used and d_p was calculated as $\sim 5.67 \mu\text{m}$.

Chemical analysis of the particles, seen in Figure 5-7, Figure 5-8, Figure 5-13, and Figure 5-15 found the particles to be particularly enriched in both Ti and Al, suggesting the particle is a mixture of the two crystallographic structures. It is proposed, that taking advantage of the high diffusivity of the liquid phase, the highest melting temperature

phase in the weld component – alumina – forms first. It acts as a favourable nucleation site for precipitation to arise. Yan *et al* [278] found that TiN formed in the liquid often manifest as inclusions with a cubic morphology and well over 1 micron in size. As the TiN particles characterised in this study have a spherical morphology and a mean particle diameter of only 0.85 μm , it is proposed that the TiN precipitate upon the alumina inclusions during solidification. TiN exhibits a higher forming temperature and lower solubility than that of TiC, and as such is first to precipitate upon the favourable site created by the alumina. Yu *et al.* [279] reported that the carbide and nitride of Ti do not form in the liquid phase. TiN forms after the melt has solidified more than 40%, while TiC forms at the end of solidification. After this event, they form a continuous solid solution – Ti (C,N) – as TiN and TiC have the same crystallographic structure and approximate lattice constant [280]. From now on, the particles will be referred to as Ti (C,N) precipitates. As the ratio of Ti/N (~ 5) found during optical emission spectroscopy (Table 5-2) is greater than the stoichiometric TiN (3.42), a faster coarsening rate during cooling can be expected. To summarise, the particles are Ti (C,N) precipitates formed during solidification. The precipitates have a mean diameter of approx. 0.85 μm and mean spacing of 5.67 μm . The relative volume fraction of the coarse Ti (C,N) within the fusion zone is 0.103. The link between these properties on the weld strength and toughness will be discussed in the proceeding sections.

5.4.2. Effect of size and volume fraction of precipitates on strength

Strengthening is the core function of the Ti (C,N) precipitates within the fusion zone, and as such will be discussed first. The Ashby – Orowan equation is commonly used to assess precipitate strengthening assuming that all the precipitates are incoherent globular particles [122-124]:

$$\Delta\sigma_p = \frac{0.538.Gb.f_p^{1/2}}{x} \ln\left(\frac{D_p}{2b}\right) \quad (5-6)$$

where $\Delta\sigma_p$ is increment of yield strength in MPa, G is shear modulus ($81,600 \text{ MPa}$), b is Burger's vector in mm (0.248 nm), D_p is the average diameter of precipitates ($0.85 \text{ }\mu\text{m}$) in mm, and f_p is the volume fraction (0.103) of precipitates.

Figure 5-16 shows the increment of yield strength contribution for a range of precipitate sizes and volume fractions. For the SAW joint with a 0.103 volume fraction and $0.85 \text{ }\mu\text{m}$ average diameter Ti (C,N) precipitates, a strengthening contribution of around 32.1 MPa is achieved. Figure 5-16 also indicates that significant increase in weld metal strength could be achieved if the average precipitate size is below $0.5 \text{ }\mu\text{m}$ due to the exponential nature of the curve. By plotting at $\pm 20\%$ of the measured 0.103 volume fraction, it is also clear that an increase in the volume fraction of precipitates could also increase yield strength contribution, although not as significantly as in the case of controlling the precipitate size below $0.5 \text{ }\mu\text{m}$.

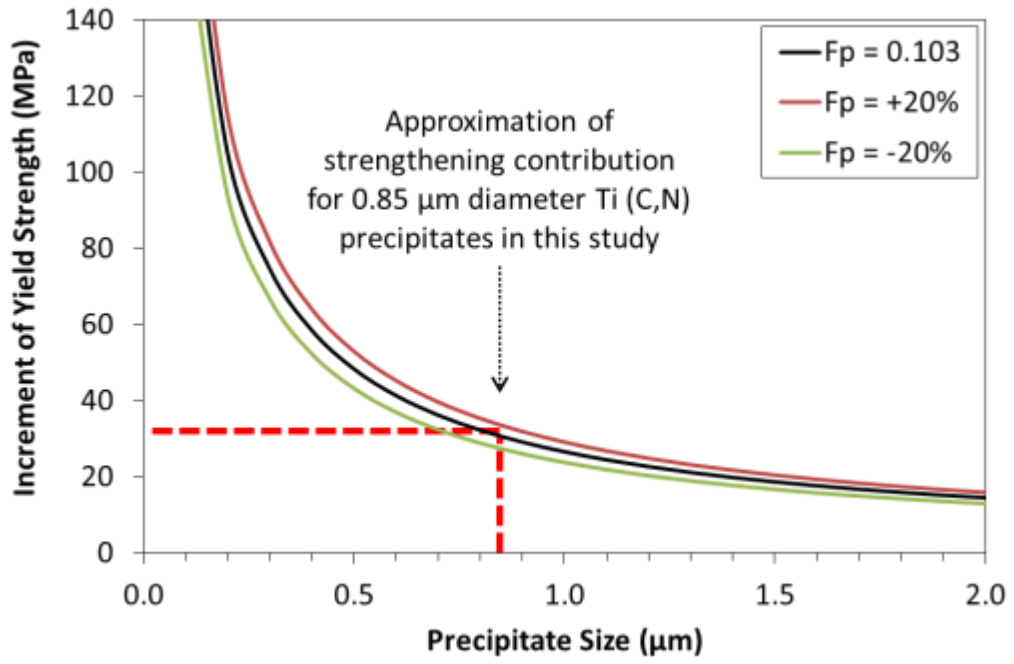


Figure 5-16: Variation in precipitate strengthening contribution calculated from the Ashby-Orowan equation for a range of average precipitate sizes at varying volume fractions.

5.4.3. Effect of the size/spacing of precipitates on fracture toughness

As discussed in the previous section, reducing precipitate size below 0.5 μm significantly improves the precipitate strengthening contribution. The experimental results in Figure 5-13 and Figure 5-14 illustrate that the coarse (0.85 μm) Ti (C,N) precipitates act as nucleation sites for ductile fracture during Charpy impact tests and fracture toughness tests, reducing toughness properties in the fusion zone.

Fracture toughness is commonly predicted from a critical crack tip opening displacement (CTOD) and a critical stress intensity factor, K_I . This is a macroscopic criterion, based on K_I or J_I , resulting from asymptotic continuum mechanics characterisation. Therefore, when using this method, the evaluation of toughness using K_{Ic} or J_{Ic} does not necessitate any microscopic understanding of the fracture events involved. In the interest of a full comprehension of a fracture process and specifically to define which microstructural features contribute to materials toughness; it is often beneficial to construct microscopic models for specific fracture mechanisms. Such models are generally referred as “fracture micro-mechanisms”. Unlike the macroscopic continuum approach, they require a microscopic model for the particular fracture model. In this case, that is a microscopic model for ductile fracture via microvoid coalescence. This model incorporates a local failure criterion and considers salient microstructural features such as size and spacing of void initiating precipitates. Using the well-known CTOD-stress intensity relation, we lose these key input parameters (precipitate size, spacing, and volume fraction) and instead, the magnitude of stress intensity factor, K , only depends on sample geometry, the size and location of the crack, and the magnitude/modal distribution of loads on the material.

In order to quantify how size and spacing of precipitates affect fracture toughness in terms of initiation and propagation of ductile fracture, several models have been developed to predict the fracture toughness based on these so-called “fracture micro-mechanisms”. For small scale yielding (ssy), a stress-modified critical strain criterion was proposed by various authors [135, 136]. According to Rice and Johnson [137], at the fracture initiation toughness in terms of J-integral, J_{Ic} , or critical CTOD, δ_{Ic} , the

local equivalent plastic strain, $\bar{\epsilon}_p^*$, must exceed a critical fracture strain or ductility, $\bar{\epsilon}_f^*(\sigma_m/\bar{\sigma})$, where the stress triaxiality, $(\sigma_m/\bar{\sigma})$, can be written as [138, 281]:

$$(\sigma_m/\bar{\sigma}) = \frac{1}{3} \left[1 + 2 \ln \left(1 + \frac{2d_p}{\delta} \right) \right] \quad (5-7)$$

For initiation of ductile fracture by microvoid coalescence, McClintock [282], Rice and Johnson [137], and Rice and Tracey [283] considered the criterion that the CTOD must exceed half the mean void initiating particle spacing, d_p . This implies that:

$$\delta = \delta_{Ic} \approx (0.5 \text{ to } 2)d_p \quad (5-8)$$

The critical fracture strain or ductility, $\bar{\epsilon}_f^*(\sigma_m/\bar{\sigma})$, is specific to the relevant stress state over a characteristic distance, l_0^* , comparable with the mean spacing (d_p) of the void initiating particles, as shown schematically in Figure 5-17.

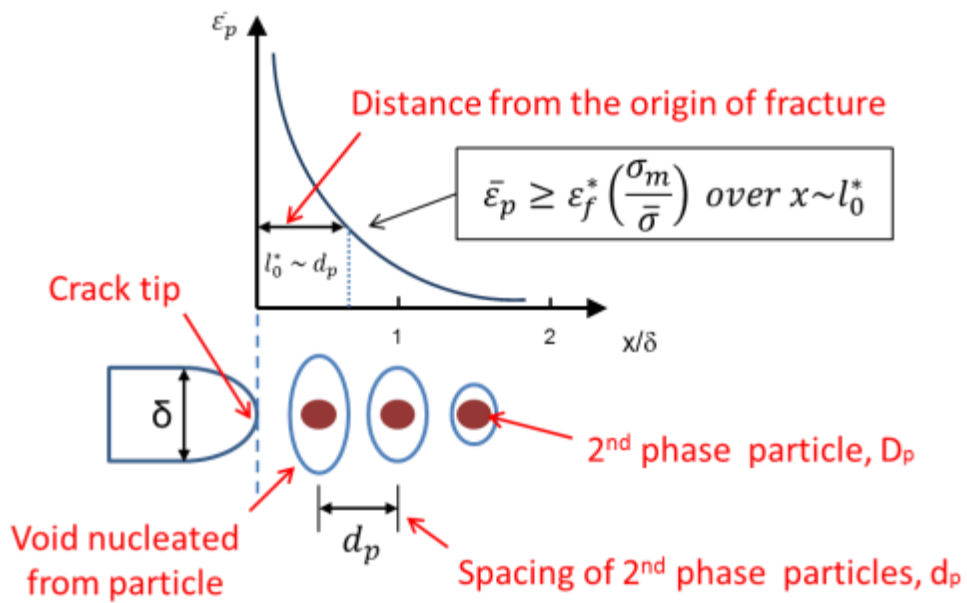


Figure 5-17: Schematic idealization of microscopic fracture criteria pertaining to critical stress-modified, critical strain controlled model for microvoid coalescence. Adapted from [137, 138, 271].

Following the approach of Ritchie *et al.* [139], the near tip strain distribution, $\bar{\epsilon}_p$, is considered in terms of distance ($r = x$) directly ahead of the crack, normalised with respect to the CTOD, δ .

$$\bar{\varepsilon}_p \propto \left(\frac{J}{\sigma_0 r}\right)^{\frac{1}{n}+1} \sim c_1 \left(\frac{\delta}{x}\right) \quad (5-9)$$

Where c_1 is of order unity and n is the strain hardening exponent. The crack initiation criterion of $\bar{\varepsilon}_p$ exceeding the critical fracture strain or ductility, $\bar{\varepsilon}_f^*(\sigma_m/\bar{\sigma})$, over $x = l_0^* \sim d_p$ at fracture initiation, J_{Ic} , now implies a ductile fracture toughness of: [139]

$$\delta_i = \delta_{Ic} \approx \bar{\varepsilon}_f^* l_0^*, \quad (5-10)$$

or,
$$J_{Ic} \approx \sigma_0 \bar{\varepsilon}_f^* l_0^*$$

or,
$$K_{Ic} \equiv \sqrt{J_{Ic} E'}$$

Where σ_0 is the yield strength (500 MPa) of the material and $E' = E/(1-\nu^2)$ in plain strain conditions, where, E is the young's modulus (207 GPa) and ν the poisons ratio (0.3). The stress modified critical strain criterion (Eq. 5-10), now implies that fracture initiation toughness, J_{Ic} for ductile fracture is proportional to strength times ductility. This is a physically realistic concept and permits rationalization of the toughness-strength relationship for cases where microstructural changes which increase strength also cause a more rapid reduction in the critical fracture strain.

While there is no conceptual difficulty with the term $\bar{\varepsilon}_f^*$, various methods have been proposed for its derivation. According to Ritchie and Thompson [140], for an array of void initiating particles of diameter (D_p) and mean spacing (d_p), the critical fracture strain ($\bar{\varepsilon}_f^*$) is given by:

$$\bar{\varepsilon}_f^* \approx \frac{\ln(d_p/D_p)}{0.28 \exp(1.5\sigma_m/\bar{\sigma})} \quad (5-11)$$

The amalgamation and reduction of Eq. 5-7, 5-8, 5-10 and 5-11 and taking $\delta = 2d_p$, results in a new expression (Eq. 5-12) that allows the prediction of fracture toughness based upon the size and distribution of second phase particles within the fusion zone.

$$K_{Ic} \equiv \sqrt{1.19\sigma_0 d_p \ln(d_p/D_p) E} \quad (5-12)$$

Using the mean D_p (0.85 μm) and d_p (5.67 μm) values calculated from microstructural observations in our study, it is possible to assess the effect of mean size and spacing of precipitates on plane-strain fracture toughness. The results in Figure 5-18 show a fracture toughness value of 36.6 $\text{MPa}\cdot\text{m}^{1/2}$ using the input data presented. This offers a conservative estimate around 11% below the fracture toughness values determined experimentally in Table 5-3. The low deviation and conservative nature of the prediction validates the integrity of the model presented. The stress triaxiality values predicted using Eq. 5-7 and 5-8 give slightly low values (~ 1.5) but offer good fracture toughness estimates in the case of this study. As shown in Figure 5-18, fracture initiation toughness increases as the size of precipitates become smaller. The drop in fracture toughness as a result of coarsening is attributed to the reduced local ductility around the precipitate as a direct result of growth. Once nucleated, the cracks develop into spherical and ellipsoidal holes by plastic deformation, with the fine acicular ferrite within the prior austenite grains providing the microvoids with a relatively straight, transgranular, fracture path to coalesce along with minimal energy. It is proposed that spherical Ti (C,N) precipitates act as microvoid initiation sites and render the relatively low impact toughness (228 J) and fracture toughness (40.8 $\text{MPa}\cdot\text{m}^{1/2}$) properties in the SAW joint. It has to be stated that the current study has only considered the effect of mean precipitate size and spacing. In reality, the largest precipitates will be the most active in initiating fracture, and this may cause some errors in fracture toughness estimation using Eq. 5-12.

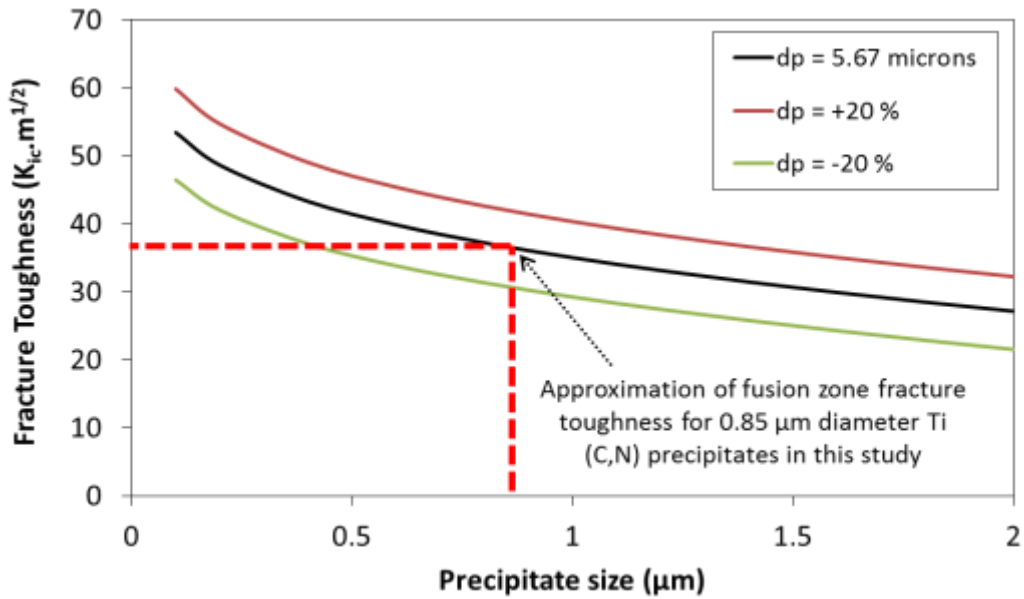


Figure 5-18: Predicted fracture initiation toughness in the fusion zone as a function of precipitate size, calculated from Eq. 5-12.

From both fracture mechanics and strengthening perspective, an optimum combination of toughness and strength can be achieved by controlling the size of Ti (C,N) precipitates to less than $0.5\mu\text{m}$ in the SAW weld X65 linepipes. However, if the volume fraction of particles is kept the same, reducing the precipitate size will cause the spacing of the precipitates to also reduce, as demonstrated in Figure 5-19. This will lead to a reduction in fracture toughness according to Eq. 5-12. So, in order to be certain that K_{Ic} could be increased, while reducing mean precipitate size, the volume fraction of particles also needs to be reduced in order to increase the particle spacing or to at least to maintain its same level. But a reduction in the volume fraction of particles will cause yield strength to drop, as presented in Figure 5-16. This is the classical scenario that an increase in yield strength of the steel will have to be compromised by a reduction in toughness, which is adequately demonstrated through the mathematical equations presented in the thesis. Therefore these equations could be used the guide the design or selection of the steel chemistries for the feedstock plate as well as welding consumables.

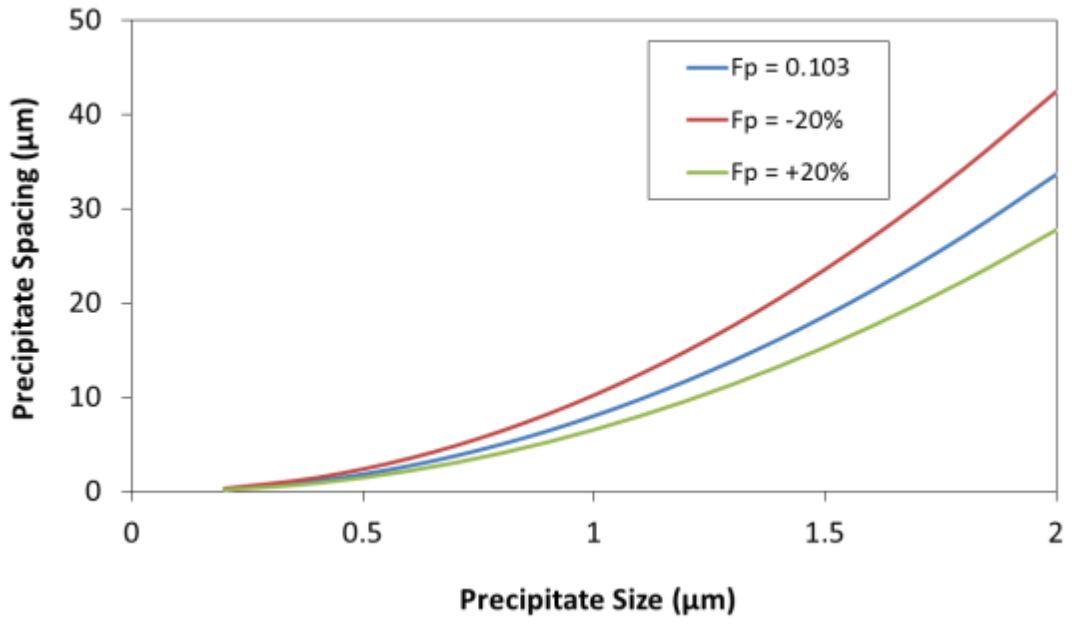


Figure 5-19: Relationship between mean particle size and spacing at different volume fractions.

5.5. Residual stress in UOE linepipe seam weld

5.5.1. Neutron diffraction experiment

ISIS is the world's brightest pulsed neutron source. It was home to one of the first dedicated neutron stress diffractometers, ENGIN [284]. Following increased demand from the engineering community, ENGIN was replaced by ENGIN-X [285], which was designed to provide at least an order of magnitude improvement in performance [286].

Second-generation neutron strain scanners were built on diffractometers originally designed to balance the competing requirements of various experiment types. This limited their utility for engineering measurements, particularly in large components. In contrast, ENGIN-X has been designed with the sole aim of making engineering strain measurements: essentially the accurate measurement of polycrystalline material lattice parameters, at a precisely determined location in an object. This approach has allowed considerable performance improvements to be made compared with previous instrumentation. Therefore, ISIS ENGIN-X instrument was utilised for the neutron diffraction experiments. The underlying theory of the neutron diffraction technique has been discussed in Chapter 2.2.8 and so experimental methods and results are only discussed in this chapter.

5.5.1.1. Sample preparation

A small length (~300 mm) was machined from each of the pipes described in Chapter 5.2, as depicted in Figure 5-20. A 100 mm block containing the weld joint was machined from the sub-ring and used to machine 6 mm thick stress relieved D_0 samples. Stress release in the D_0 samples was achieved via electrical discharge machining (EDM) thin (0.5 mm) slots in the sample (toothcomb method). The EDM was carried out with the minimum wire diameter and ample coolant. Two styles of D_0 sample were made (type 1 = tooth in weld centre, type 2 = slot in weld centre) to allow for measurements to be taken at 3.25 mm intervals away from the weld centre. After slots were machined, the D_0 samples were polished and etched to reveal the weld, as shown in Figure 5-22.

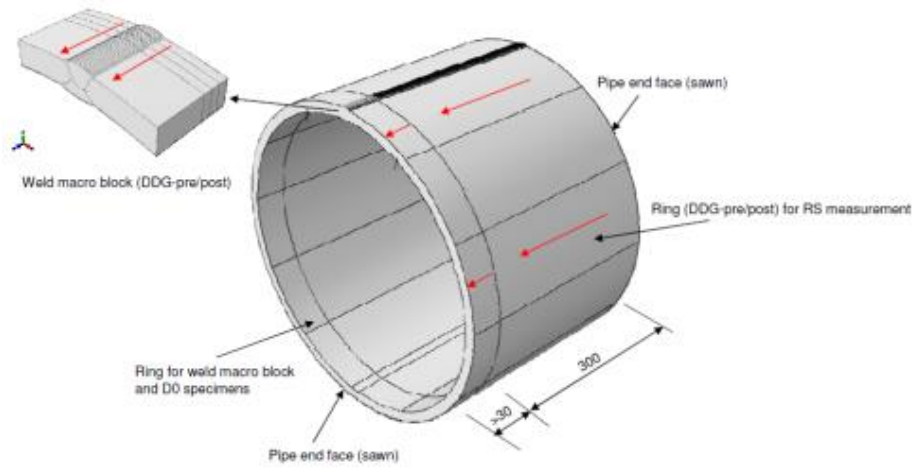


Figure 5-20: Schematic illustration of pipe section showing sub-ring to be removed to machine stress relieved D_0 samples.

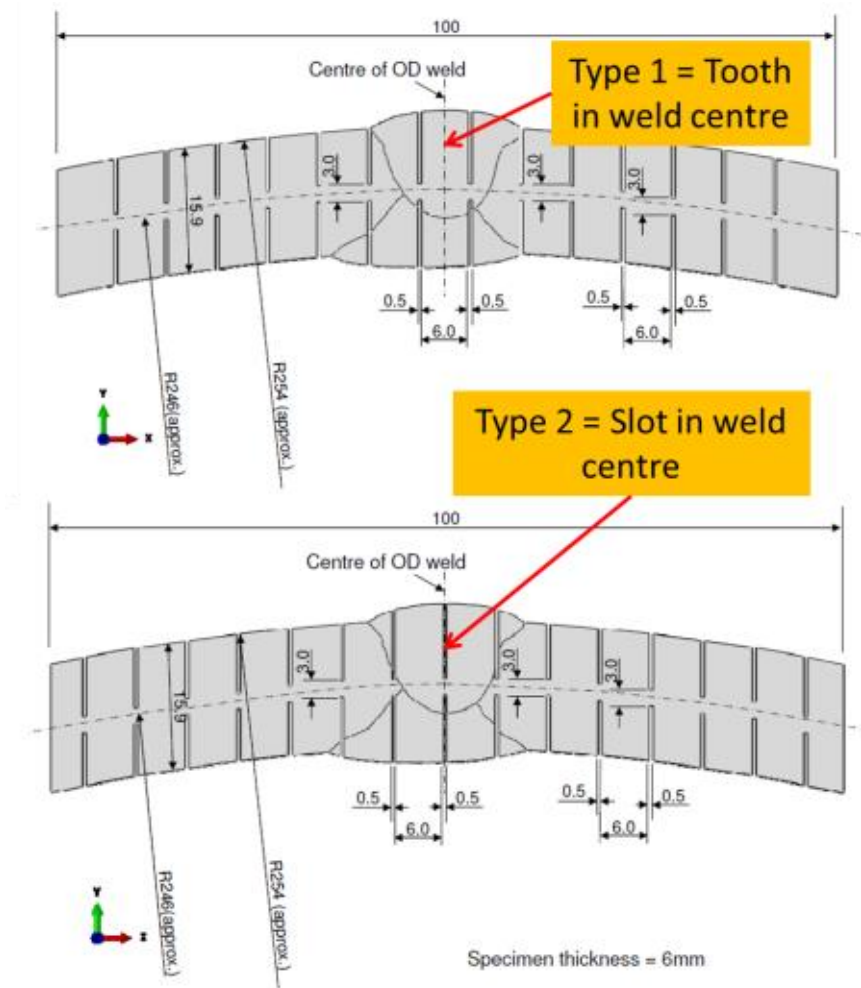


Figure 5-21: Schematic illustration and geometry of the stress relieved D_0 samples.

5.5.1.3. *ENGIN-X virtual laboratory*

Sample positioning is achieved using detailed three-dimensional virtual models of the samples, and a pair of theodolites for precise alignment on the instrument. The processes of planning, alignment and data analysis have been simplified by using SSCANSS [287], a computer program that:

- Provides computer aids in setting up the initial measuring strategy.
- Automates sample alignment and all routine aspects of the measurement process.
- Provides data analysis in near real-time, allowing decisions on changes to the measurement strategy.

A three-dimensional model of the pipes was created using a coordinate measuring machine. The virtual model is then uploaded to SSCANSS and the co-ordinates of the desired measurement locations are transposed onto the virtual model (Figure 5-24(b)). Once measurement points have been uploaded, simulations can be run to determine:

- 1) The translation path of the stage (Figure 5-24(c)) to check that there will be no collisions with collimators, etc.
- 2) The path length (and, in-directly, the measurement time) for each measurement co-ordinate specified (Figure 5-24(d)).

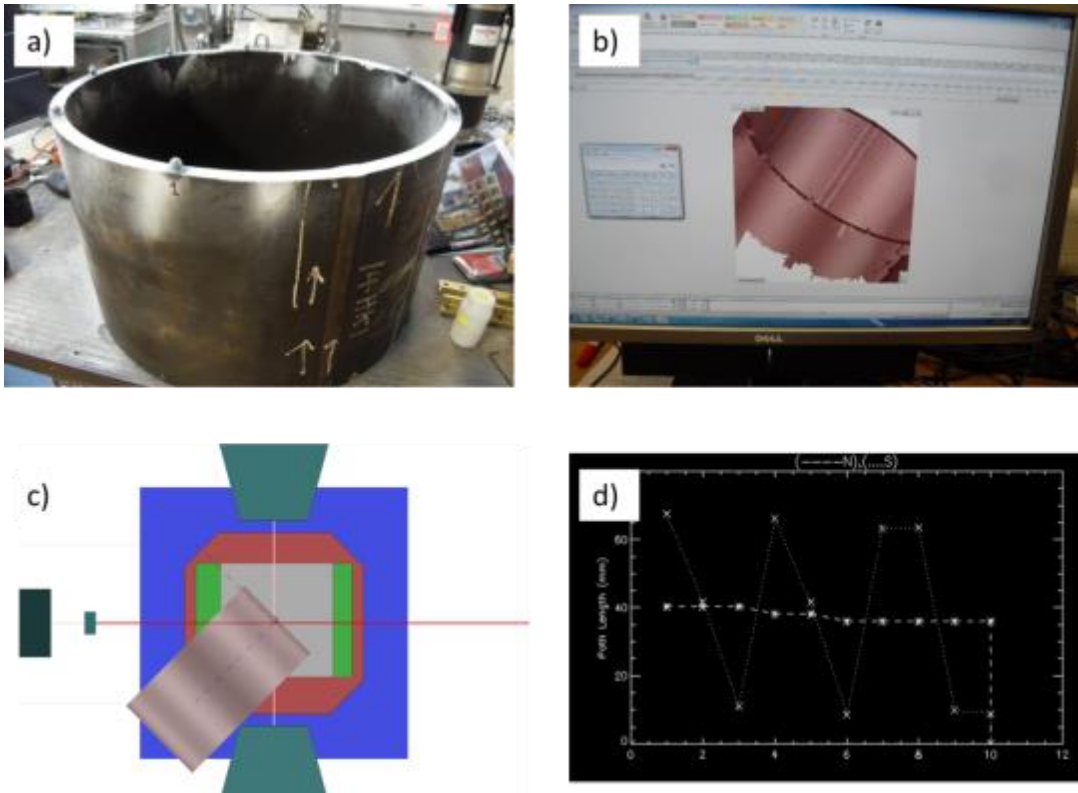


Figure 5-24: The ENGIN-X virtual laboratory. Three-dimensional models of the laboratory and sample are used for planning of experiments, in this case to measure the axial and radial directions of the strain tensor of the pipe. The three-dimensional model of the sample is produced by a co-ordinate measuring machine. The virtual model is then uploaded to SSCANSS to input measurement co-ordinates and scan times (Fig. b). Simulations are then ran to determine stage translation sequence (Fig. c) and path lengths (Fig. d)

5.5.1.4. Sample orientations for strain measurements

To obtain the stress tensor at each measurement location, hoop, axial and radial strain must be measured. To obtain the strain components, the orientation of the samples was adjusted. The pipe sample was initially laid on its outer circumference on supporting frames and orientated 45° to the neutron beam line, as shown in Figure 5-25(a), for measurement of lattice spacing (d) in the axial (along the longitudinal direction of the pipe) and radial (through the wall thickness) direction. For measurement in the hoop (along the circumference of the pipe) direction, the pipe sample was laid on a specially made frame to angle the sample at 45° to the beam and 45° to the floor.

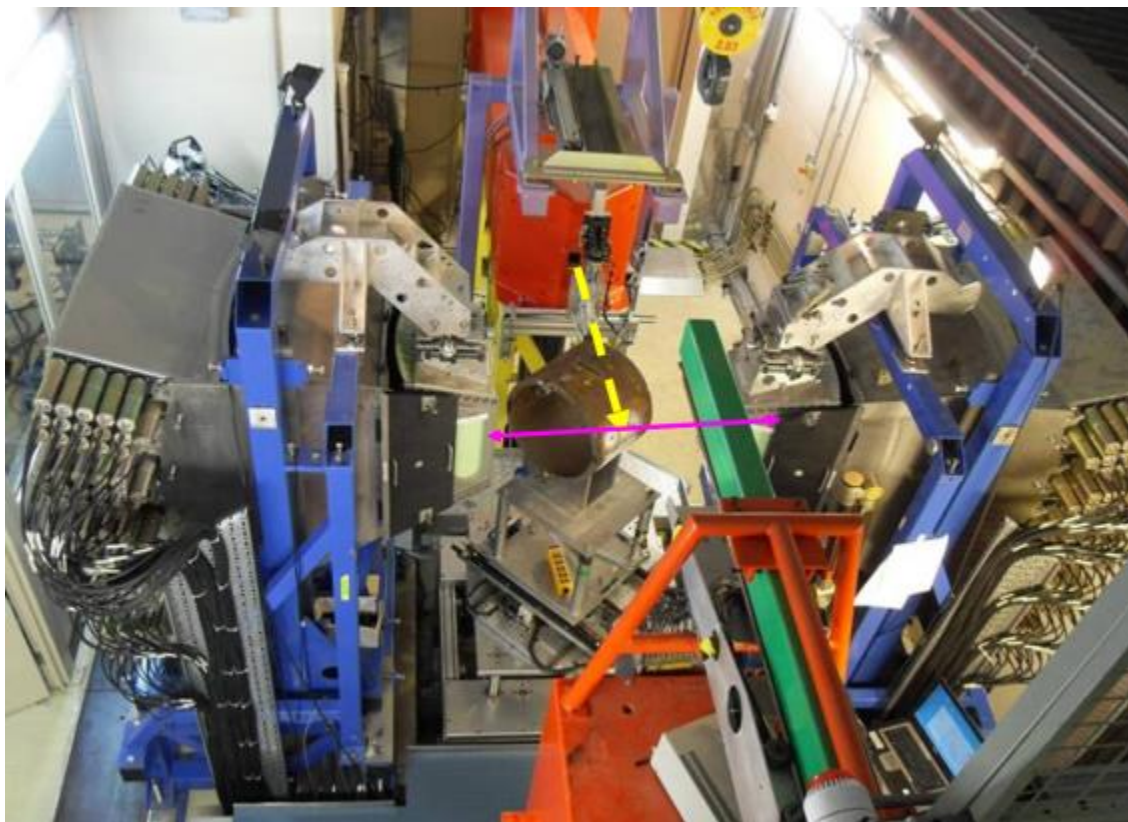


Figure 5-25: Orientation of pipe samples for axial and radial strain measurements.

5.5.1.5. *Experiment execution and data analysis*

Provided with the transformation between sample and laboratory coordinate systems, SSCANSS can drive the positioning table in order to visit all of the measurement points within the scan. At each measurement position, the spectra recorded by the individual detectors are time-focused. The program provides automatic single-peak and full-pattern refinement of the diffraction spectra specially devised for strain determination, through a library of common engineering materials. Full-pattern refinements use the computer code GSAS [288]. As most samples are textured, the refinement is performed leaving the peak intensities unconstrained, as described by Pawley [289]. To ensure the convergence of the refinement, initial guesses of the lattice parameters are obtained from single-peak refinement of the most intense peak.

5.5.2. Results

5.5.2.1. Raw data – TOF diffraction spectrums

TOF diffraction spectra with well-defined peaks were obtained quickly and with small error. An example of typical TOF diffraction spectra obtained from scans in the weld of the pipe is shown in Figure 5-26.

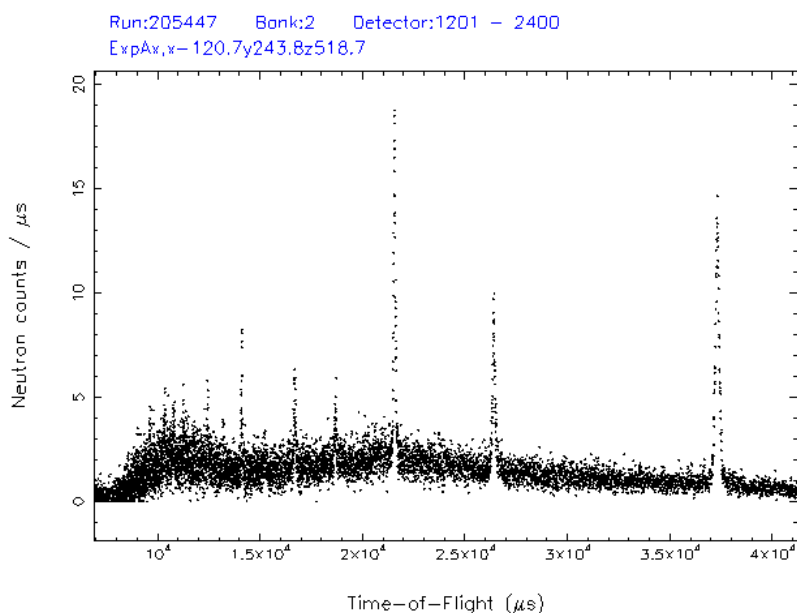


Figure 5-26: TOF diffraction spectrum in radial direction of linepipe, showing clearly defined peaks relating to lattice planes.

From the TOF diffraction spectra, GSAS computes the lattice spacing. Then, the normal elastic strain in a given direction can be calculated from the lattice spacing parameters in that direction under stressed and stress-free conditions using Eq. 2-21. The d -spacing parameter was only considered valid and used in residual stress calculations if the error was less than 100 μ strain.

Assuming that the principal axes of the residual stress field are aligned with the axial, radial and hoop directions, the corresponding residual stress components can then be calculated based on the Hook's Law of linear elasticity (Eq. 2-20)

In the calculation it was also assumed that the material was elastically isotropic. A Young's modulus of 210MPa and Poisson's ratio of 0.3 were used for all the analysis.

5.5.2.2. *Calculated weld residual stresses*

The through-thickness residual stress profiles were measured in the expanded and unexpanded pipes. The through-thickness residual stress profiles were calculated through the centre of the weld (Line 1) and through the weld toe/HAZ (Line 2), as schematically illustrated in Figure 5-23. The results of residual stress measurements in these locations are plotted in Figure 5-27 and Figure 5-28. The method of error bar calculation is described in Appendix B.

The through-thickness residual stress distribution profiles are well defined and clearly show that the highest residual stress is measured in the unexpanded pipe, in the axial direction with a maximum value of 277 MPa (Axial – unexpanded, Figure 5-27). The peak residual stress is located in the weld centre and is almost 50% of the actual yield strength of the parent material (516 MPa). After the mechanical expansion process, the residual stress in the corresponding location reduces significantly in both magnitude (277 MPa to 115 MPa, approx. a 58% reduction) and orientation (tensile residual stress to compressive residual stress). This trend (~58% reduction in residual stress magnitude and change of orientation from tensile to compressive) is consistent across all through-thickness axial residual stress measurements.

The hoop residual stress has a similar profile to that of the axial residual stress through the wall thickness along both lines, having a maximum value of only about 232 MPa (Hoop – unexpanded, Figure 5-28). The hoop residual stresses are tensile before and after the mechanical expansion process. The expansion process does appear to give a slight reduction to the hoop residual stress magnitude, although not significant or consistently through-thickness.

The radial residual stress forms the lowest profiles (below 55 MPa).

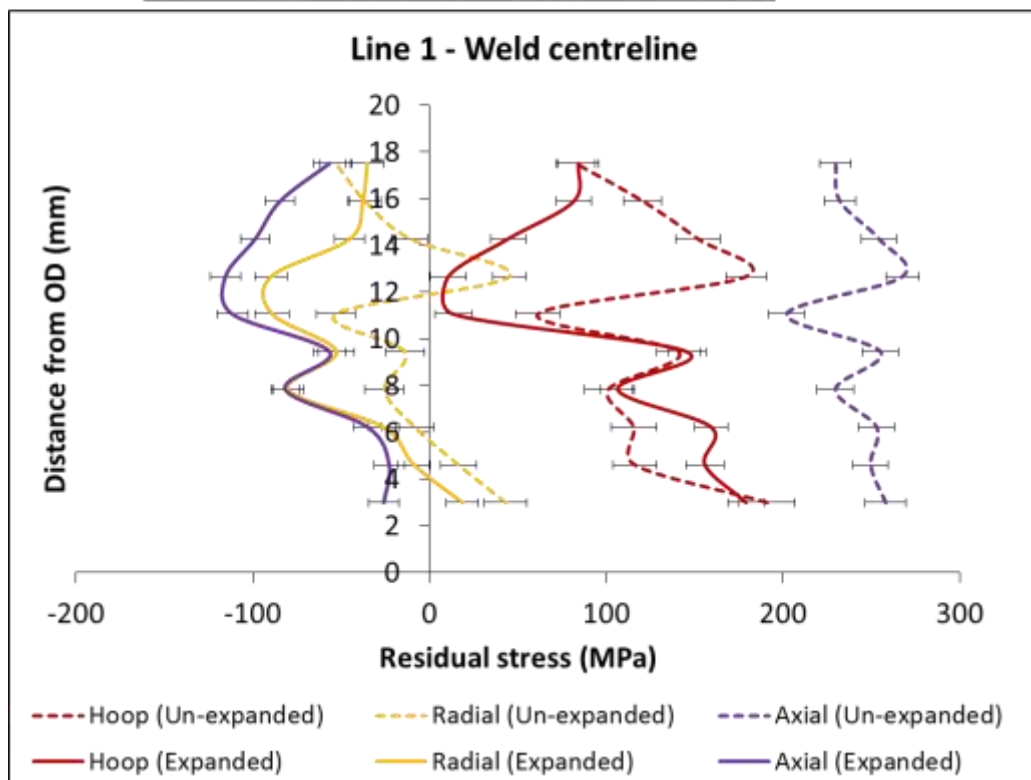
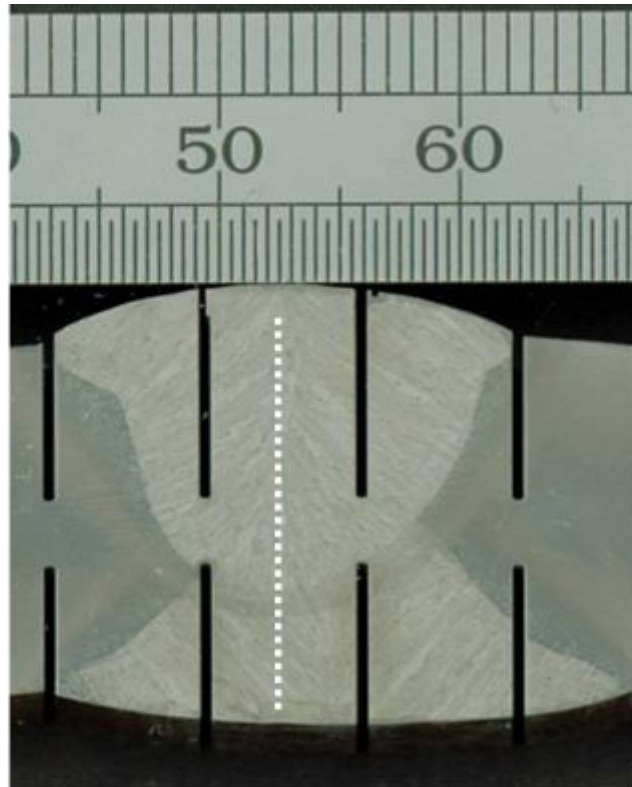


Figure 5-27: Residual stresses measured in the unexpanded and expanded 15.4 mm walled pipe. Measurements taken through thickness in the weld centre line.

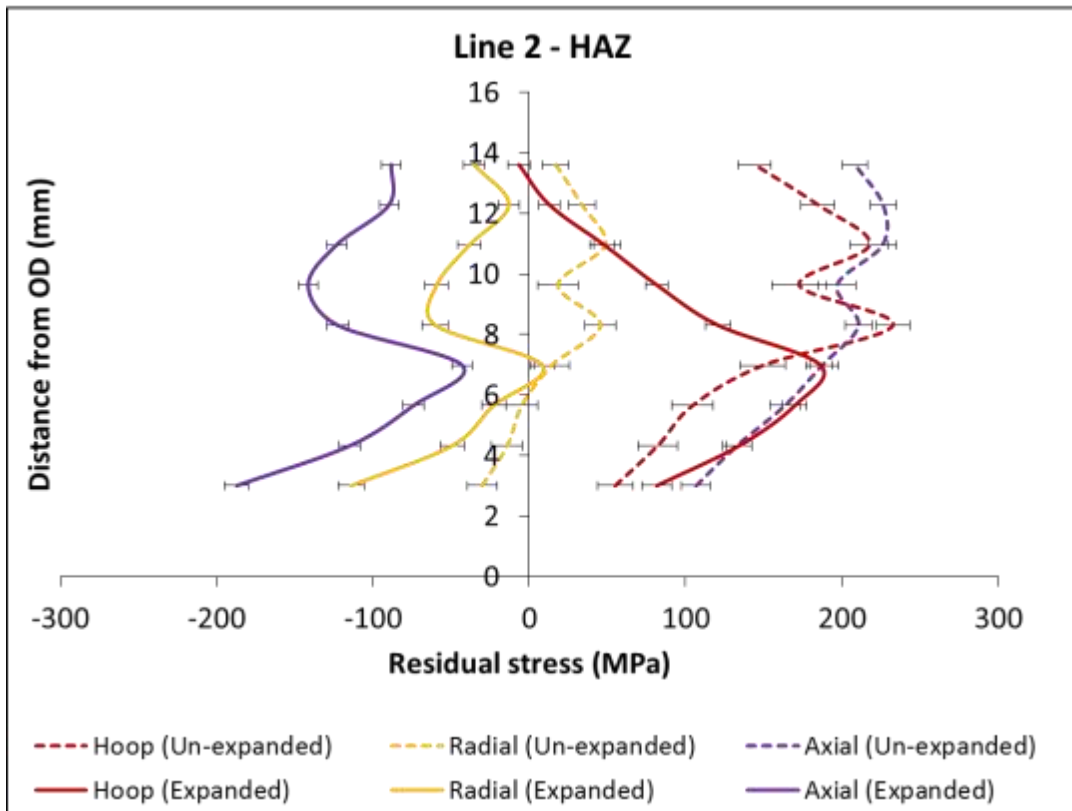
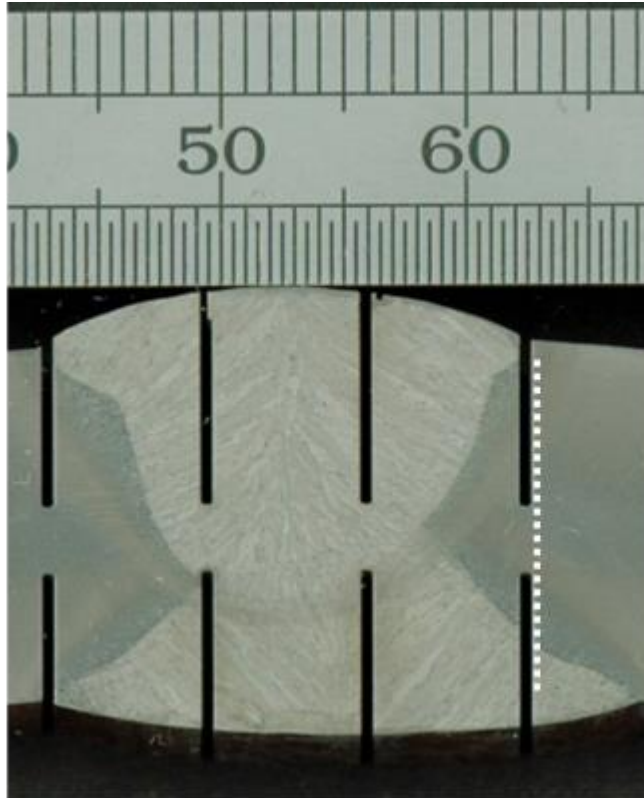


Figure 5-28: Residual stresses measured in the unexpanded and expanded 15.4 mm walled pipe. Measurements taken through thickness in the heat affected zone.

Figure 5-29 to Figure 5-31 display the results of residual stress measurements made horizontally away from the weld centreline in both the expanded and unexpanded pipes. The method of error bar calculation is described in Appendix B. The largest measured residual stress is still the 277 MPa axial stresses reported previously within the weld centre. As with the through-thickness measurements, the axial residual stress is consistently reduced in magnitude and orientation as a result of the mechanical expansion process. However, an even larger 72% mean reduction of axial residual stress magnitude is measured horizontally away from the weld when compared to the 58% mean reduction of axial residual stress measured through-thickness. Note that the mean reduction of 72% is calculated from the mean average of the difference (relative difference, not absolute) between axial residual stress measured in expanded and unexpanded pipes using measurement points defined in Figure 5-23.

It appears that the mechanical expansion process has two favourable effects on the axial residual stress component induced by welding;

- 1) It reduces the magnitude of the axial residual stress by an average of 65%
- 2) It transfers the derogatory tensile residual stress into a desirable compressive residual stress.

The hoop residual stresses show a similar profile to the axial residual stresses at a smaller magnitude. The hoop residual stresses are tensile before and after the mechanical expansion process. The expansion process does appear to give a slight reduction to the hoop residual stress magnitude, particularly along the outer diameter of the pipe.

Radial residual stresses are lowest of the stress components within the pipe. The radial stress is mostly compressive and under 55 MPa. The mechanical expansion process appears to have little effect on the size and distribution of the stresses.

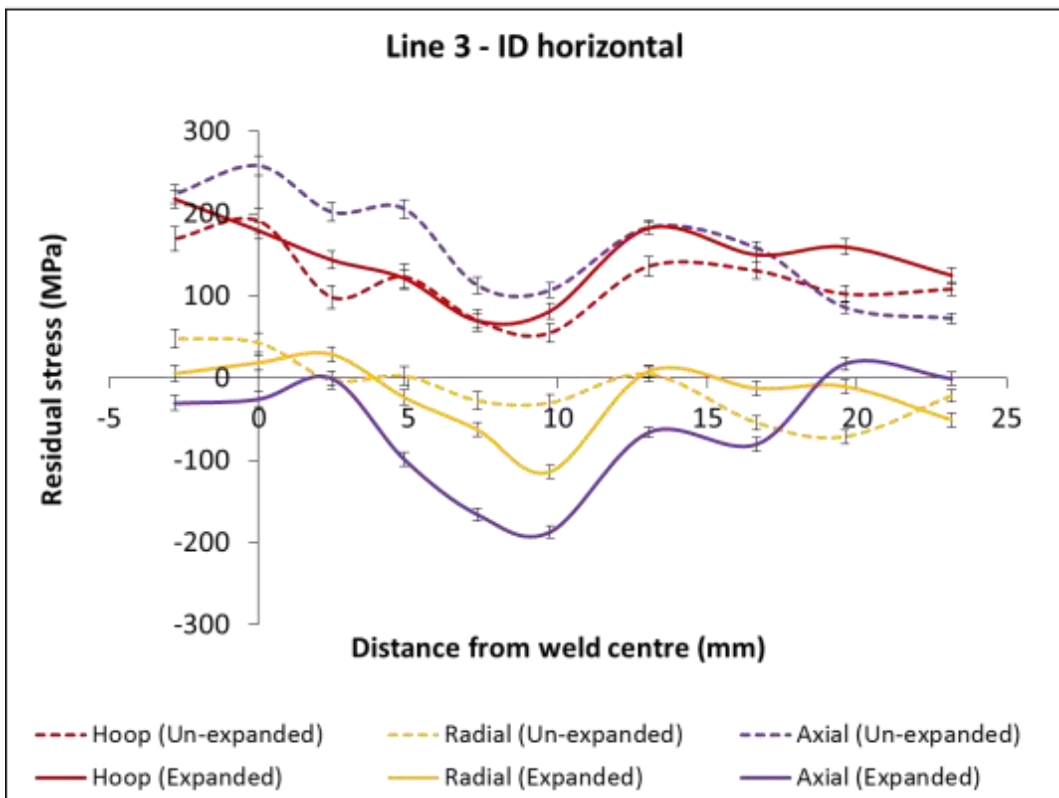
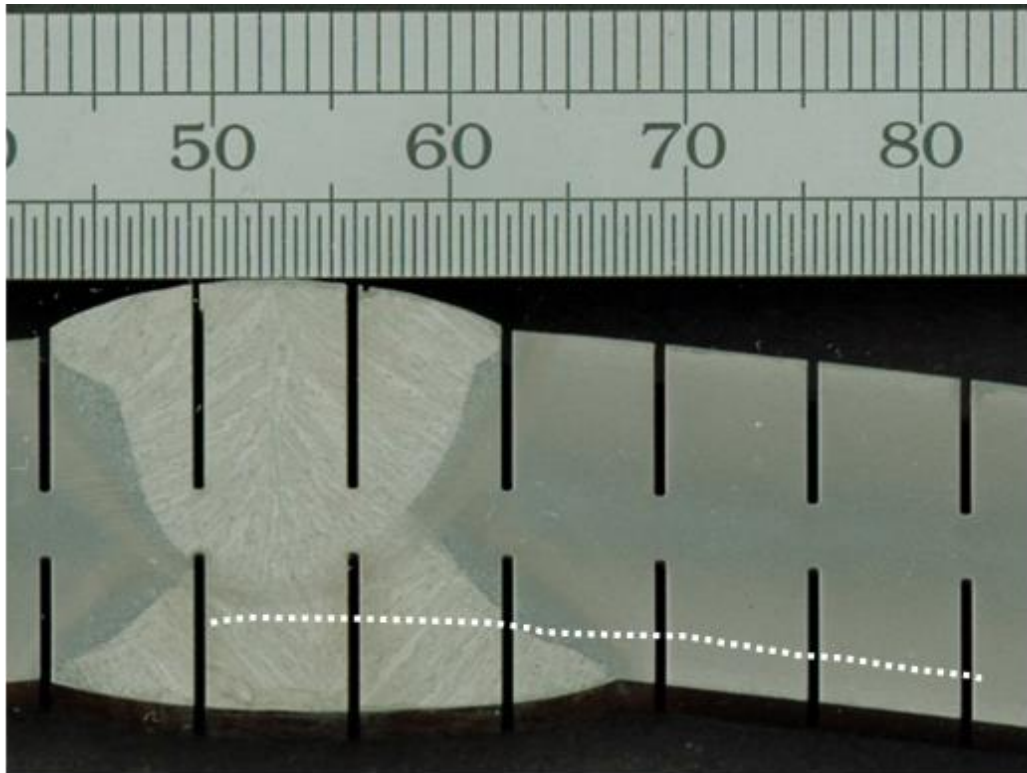


Figure 5-29: Residual stresses measured in the unexpanded and expanded 15.4 mm walled pipe. Measurements taken horizontally away from the weld centre line, 3 mm in from the inner diameter.

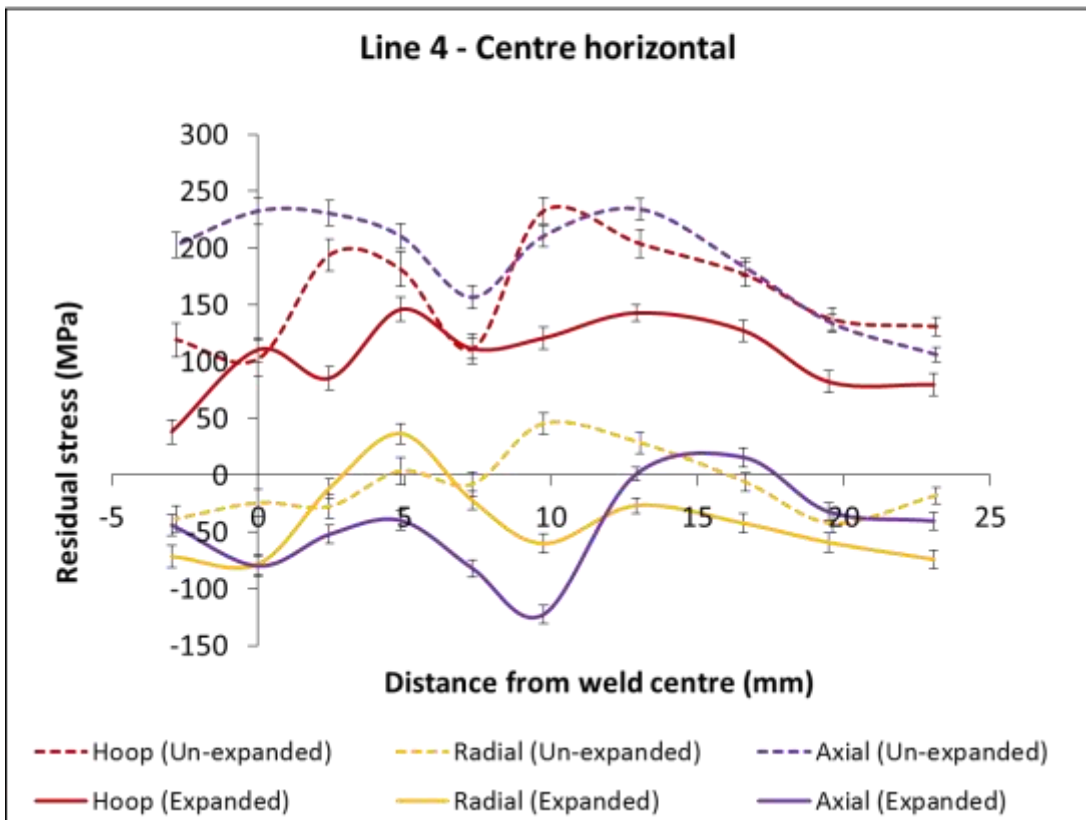
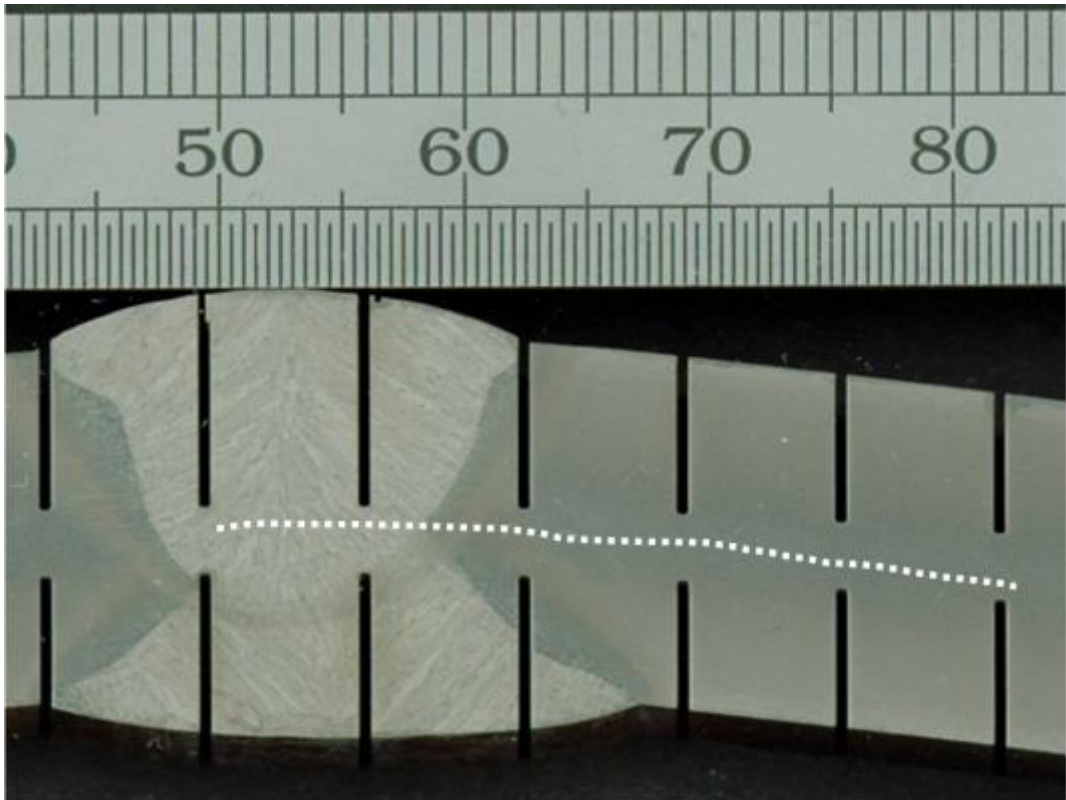


Figure 5-30: Residual stresses measured in the unexpanded and expanded 15.4 mm walled pipe. Measurements taken horizontally away from the weld centre line, 3 mm in from the outer diameter.

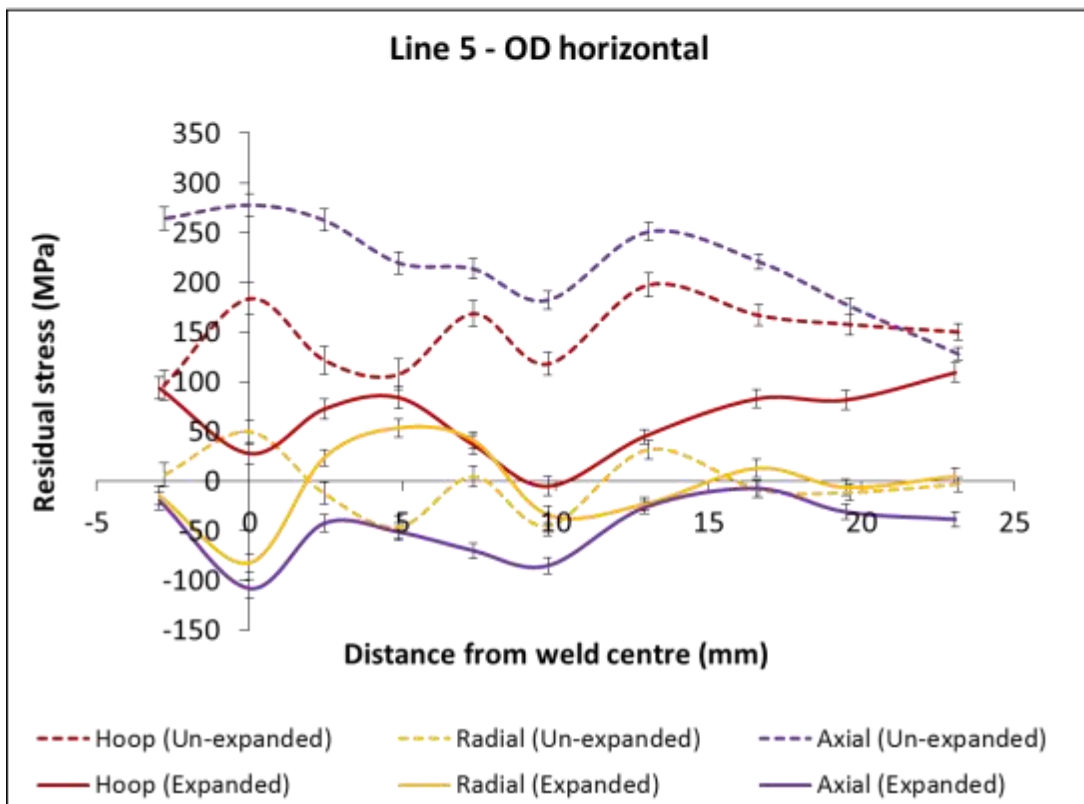
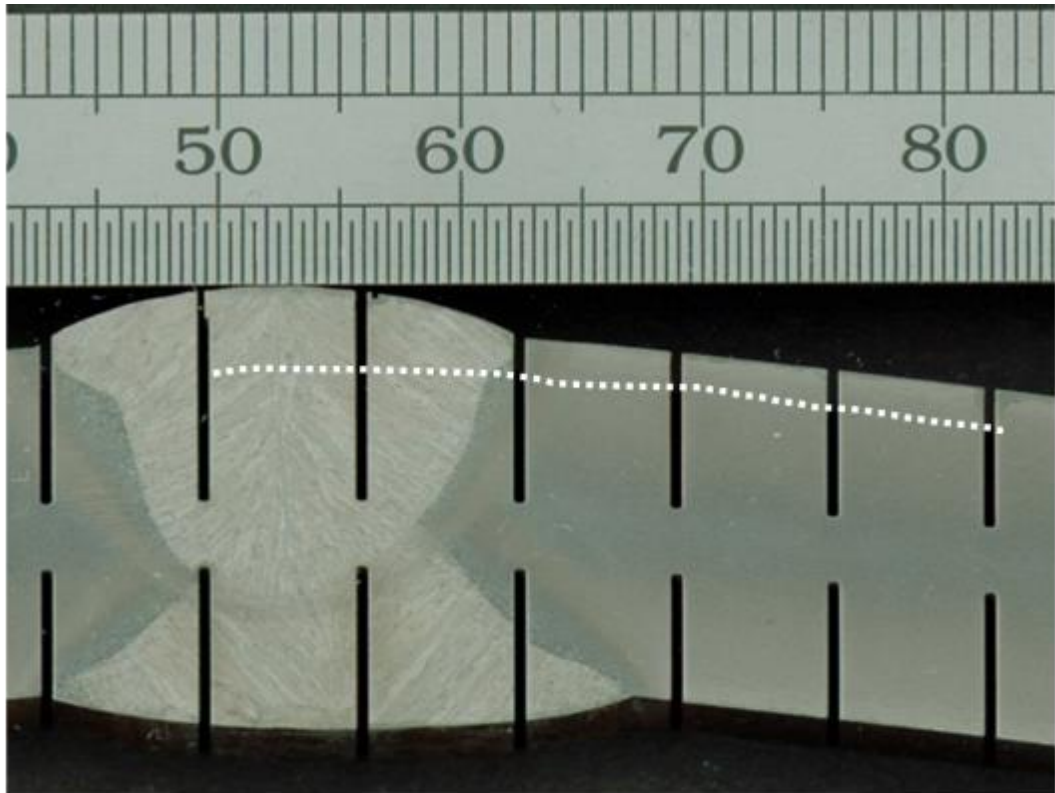


Figure 5-31: Residual stresses measured in the unexpanded and expanded 15.4 mm walled pipe. Measurements taken horizontally away from the weld centre at mid-thickness.

5.5.3. Discussion

It is well understood that residual stresses induced by welding could reach or even exceed the YS of the material [167, 186-189, 290]. However, the current study has showed that the maximum value of residual stress found in and near the seam weld of the linepipe was only about 277 MPa (un-expanded pipe in axial direction), approximately 53% of the actual YS of the parent material (516 MPa).

However, the primary revelation of the research presented in the thesis is the observations made on the effect of the mechanical expansion applied to the linepipe as the last step operation in the UOE process. After SAW seam welding, high levels (200-277 MPa) of tensile axial residual stress exist in and near the seam weld area (broken purple line in Figure 5-27 to Figure 5-31). After mechanical expansion, the residual stress distribution and magnitude are completely modified by plastic deformation resulting from the expansion operation, (solid purple line in Figure 5-27 to Figure 5-31). The axial residual stresses in the weld area are now mainly compressive, ranging between -20 and -125 MPa.

The residual stresses measured via the neutron diffraction technique are in agreement with the FE model of Wen [162] in terms of pattern and magnitude.

The welding thermal cycle causes non-uniform thermal expansion and contraction to the local material. The net effect of this is that the weld seam has a tendency to contract which is restrained by the surrounding parent material, generating high tensile residual stress (strain) within the weld due to misfit. The significant (277 MPa) tensile stress can stimulate solidification cracking in the terminal stages of weld solidification. With increasing solid fraction, liquid is isolated in pockets or immobilized by surface tension. During these sub stages, as liquid is trapped between interlocking dendrites, the free passage for liquid is blocked, transforming continuous liquid films into isolated liquid droplets. As a result, the strength of the material is very low due to the existence of this non continuous liquid film between the primary dendrites. If an external stress is applied to the material, such as tensile residual stress, then solidification cracking can easily occur.

The mechanical expansion imparts plastic deformation to the pipe for improvement of its roundness and straightness. The positive expansion strain applied in the hoop direction of the pipe (0.8% for the current pipe in consideration according to the FE calculation [185]), will at the same time cause negative strains in the radial direction (tending to slightly reduce the pipe wall thickness) and axial direction (tending to slightly reduce the pipe length). However, due to the geometry of the pipe (weld reinforcement, Figure 5-22) and expander die recesses, the expansion strain (in the hoop as well as axial and radial directions) is mainly distributed in the pipe body and the amount received by the seam weld is minimal [185]. As a result, the misfit between the weld and its adjacent parent material originally induced by welding is eased. The misfit relaxation results in a significant reduction in tensile residual stresses. The misfit can even be reverted depending on the operational conditions (e.g. expansion strain, etc.), giving rise to compressive residual stress in the weld area after expansion as demonstrated by the experimental results presented in this chapter.

Once solidified, it is greatly beneficial to transform tensile residual stresses in to compressive residual stresses. Tensile residual stresses are generally harmful since they can contribute to, and are often the main cause of fatigue failure and stress corrosion cracking. Compressive residual stresses are usually beneficial since they prevent origination and propagation of fatigue cracks, and increase wear and corrosion resistance.

5.6. Chapter summary

Basic characterisation of the linepipe SAW seam weld has been carried out following the industrial standard requirement. The characterisation found the base metal of the welded linepipe has a fine grain structure as a result of grain pinning and thermo-mechanically controlled rolling. It exhibits high impact toughness of 362 J. The hardness of base metal was found to be directly linked to the volume fraction and hardness properties of the individual microstructural phases within the region. A small number of large (1.5 μm) cuboidal Ti (C, N) precipitates were found pinned to the grain boundaries within the base metal. It is proposed that the coarsening of the precipitates occurred via grain boundary diffusion of Ti during the austenitic processing conditions of the rolling process. Within the fine grained HAZ, grain growth occurred due to the dissolution and coarsening of the precipitates, therefore reduced hardness and toughness properties were measured. However, a hard (283 HV) upper bainite microstructure was induced to the coarse-grained-HAZ close to the molten weld joint which contributed to higher hardness for the region. It is proposed that the induced bainitic microstructure could lead to the formation of local brittle zones within the coarse-grained HAZ. The fusion zone has high hardness (232 HV) coupled with low impact toughness (227 J).

In order to identify the underlining factors affecting the microstructure-mechanical property relationship in the fusion zone of the weld joint, advanced characterisation techniques have also been employed. Using the techniques, the microstructural features in the weld metal at micro, sub-micro and nano-scale have been characterised. Coarse (0.85 μm) precipitates are found in the predominantly acicular ferrite fusion zone of a submerged arc welded X65 linepipe. The precipitates are a mixture of Ti (C,N) and alumina phases. The strengthening contribution of the coarse Ti (C,N) precipitates was calculated at 32.1 MPa from the Ashby – Orowan equation. To improve the yield strength of welds, the average precipitate size shall be reduced while increasing the volume fraction.

However the Ti (C,N) precipitates act as nucleation sites for ductile fracture via microvoid formation. The fracture toughness can be increased by reducing the average precipitate size. To increase K_{IC} , while reducing the average precipitate size, the volume fraction of particles needs to be reduced. Unfortunately, reducing the volume fraction

will cause the yield strength to drop. This is the classical scenario that an increase in yield strength of the steel will have to be compromised by a reduction in toughness.

Through the current study an analytical equation has been derived to establish the relationship between precipitate size and spacing (and indirectly volume fraction) on fracture toughness of the SAW seam weld:

$$K_{Ic} \equiv \sqrt{1.19\sigma_0 d_p \ln(d_p/D_p) E}$$

The new approach developed should generally be applicable to base plate development, HAZ as well as fusion zone microstructure-mechanical property characterisation and quantification for future improvement of quality and integrity of UOE linepipe SAW seam weld. The above equation and the Ashby – Orowan equation shall be used to guide the selection of weld chemistry and the control of welding processes. For submerged arc welded X65 linepipes, the weld metal is designed to be overmatched with base metal, it is reasonable to suggest that the fracture toughness of welded X65 linepipes can be increased by reducing the Ti content in the filler wire.

The area of weld residual stress is a grey area in terms of detailed characterisation due to the complexity and cost aspects involved in the work. In British Standard, BS 7910 - "Guide to methods for assessing the acceptability of flaws in metallic structures" [291] a general assumption that residual stresses are equal to the material yield strength is required as input for pipeline structural integrity assessment if no information (either measured or predicted) is available. This has long been recognised as a potential cause for over conservatism in modern pipeline design.

The current neutron diffraction measurements have revealed that significant tensile residual stresses are induced from the welding process. Tensile residual stresses have significant influence on solidification cracking during welding. Once solidified, the mechanical expansion process imparts plastic deformation to the pipe. As a result, the misfit between the weld and its adjacent parent material originally induced by welding is eased. The misfit relaxation results in a significant reduction in tensile residual stresses. The misfit is also reverted, giving rise to favourable compressive residual stress in the weld area after expansion.

The current study has showed that the maximum value of residual stress found in and near the seam weld of the linepipe was only about 277 MPa (un-expanded pipe in axial direction), approximately 53% of the actual YS of the parent material (516 MPa). This can be used to challenge linepipe design over-conservatism and drive efforts to reduce material usage, which will promote cost savings in linepipe manufacturing.

Although the weld that has been extensively characterised in this chapter is sound and of good quality, it is generally perceived that welds are prone to flaws, defects or imperfections, one of which is solidification cracking during welding. It is therefore of vital importance to understand the formation mechanisms and influencing factors for solidification cracking to prevent the defects in full scale industry production. As such, solidification cracking in welding is the subject of the next chapter.

6. X-ray imaging of solidification cracking during welding of steel

6.1. Introduction

The literature review in Chapter 3 has identified that the potential driving forces for solidification cracking are well-established: solid contraction in a thermal gradient, solidification shrinkage, and a high sensitivity to solute segregation. However, the nucleation and propagation mechanism for solidification cracking is a severely understudied phenomenon. The literature presented in Chapter 3.4 on recent synchrotron X-ray imaging studies goes some way to addressing this issue. However, the previous research is biased in its application to the casting of favourable Al alloys.

This chapter is specifically designed to address the important issues relating to understanding the mechanisms and direct factors involved with solidification cracking in steel welds.

An innovative small-scale weldability test rig was designed to observe solidification cracking in steel welds *in situ* using a novel Vareststraint test method for high speed, high energy micro-radiography. Ex-situ μ CT scans are used to rebuild the complex 3D cracking networks and analyse the void distribution ahead of the bulk crack tip. Microscopy analysis is focused in the region of fracture nucleation, with fracture mechanisms being identified.

6.2. Materials and thermodynamic property characterisation methods

6.2.1. Materials

For the X-ray imaging experiments, 8 mm square samples were created 300 mm long from three steels with poor weldability. The chemistry of the materials is defined in Table 6-1.

	C	Mn	Si	P	S	Cr	Ni
Mild Steel - EN1A	0.15	1	0.35	0.06	0.6	--	--
Stainless Steel - S303	0.15	2	1	0.2	0.15	19	10
Carbon Steel	0.4	0.8	0.2	0.06	0.6	--	--

Table 6-1: Nominal chemistries of sample materials used for X-ray imaging experiments.

6.2.2. Methods of thermodynamic property characterisation

6.2.2.1. Thermo-Calc computational thermodynamics

The STR, solidification sequence, and primary solidification phase were predicted in Thermo-Calc computational thermodynamics software. Thermo-Calc has over the past 30 years gained a world-wide reputation as a powerful software package for thermodynamic calculations. It is widely used for a variety of calculations including calculating:

- Amounts of phases and their compositions
- Thermochemical data such as enthalpies, heat capacity and activities
- Transformation temperatures, such as liquidus and solidus
- Phase diagrams (binary, ternary and multi-component)
- Solidification applying the Scheil-Gulliver model
- Thermodynamic properties of chemical reactions

All calculations are based on thermodynamic data which is supplied in a database. For this research the TCFE7 - TCS Steels/Fe-Alloys Database was used. The database is produced by experts through critical assessment and systematic evaluation of experimental and theoretical data, following the well-established CALPHAD (CALculation of PHase Diagrams) technique.

The background of the CALPHAD method was laid by Kaufman and Hillert *et al* [292, 293] and the practical use of the theoretical modelling started by the development of several software packages [294-297]. A detailed and comprehensive description of the CALPHAD method was published by Saunders and Miodownik [298].

Using the input chemistries presented in Table 6-1, Thermo-Calc simulations were carried out in both equilibrium and non-equilibrium Scheil conditions. In comparison to the equilibrium model, the non-equilibrium Scheil model [299, 300] accounts for solute redistribution based the assumption that no diffusion occurs in solid phases once they are formed, and infinitely fast diffusion occurs in the liquid at all temperatures by virtue of a high diffusion coefficient, thermal convection, Marangoni convection, etc.

6.2.2.2. *Gleeble hot ductility tests*

The Gleeble test was developed in the welding research laboratory at Rensselaer Polytechnic Institute in 1949 by Nippes and Savage [301]. The Gleeble testing system uses resistance heating for the heating of a small test specimen according to a pre-programmed temperature cycle. The temperature is monitored through percussion welded thermocouples in a closed circuit loop. At a selected temperature and strain rate tensile testing is performed and the reduction of area (RA) is later measured and used as a means to evaluate the hot ductility. With this type of testing it is possible to produce ductility temperature curves to understand the point at which the material becomes brittle on-heating but also when ductility recovers on-cooling [205]. The characterization of a material's hot ductility based on Gleeble testing mainly consists of determining the zero ductility temperature (ZDT) and zero strength temperature (ZST). The ZDT corresponds to a temperature where the ductility is virtually zero. The ZST is defined as the temperature during cooling at which forces can first be transmitted perpendicular to the solidification

direction [302]. The ZST corresponds to a fraction of solid in the range of 0.65 to 0.80. As the steel solidifies and cools further, the strength and ductility of the material increases and at some point the material acquires plasticity [302]. The temperature at which the transition occurs from brittle to ductile behaviour is known as the ZDT and is commonly associated with a fraction of solid between 0.98 and 1.

For this research a 3800 Gleeble machine was used. Reduced centre diameter tensile samples were made and a platinum rhenium thermocouple welded in the reduced centre diameter. Samples were resistance heated to a series of temperatures across the solidification temperature range and held for 20s. The samples were then pulled apart and temperature, elongation and force measured. After testing, the reduced diameter % was measured on a shadow graph.

6.3. Equipment and experimental methods for X-ray imaging

6.3.1. Design and manufacture of test apparatus

A novel small-scale Varestraint weldability test rig was designed and manufactured for the *in situ* X-ray imaging experiments. A schematic illustration of the equipment is given in Figure 6-1(a), while Figure 6-1(b) shows the test rig integrated to the ESRF's ID19 experimental hutch. Rig operation is described in detail within the following section.

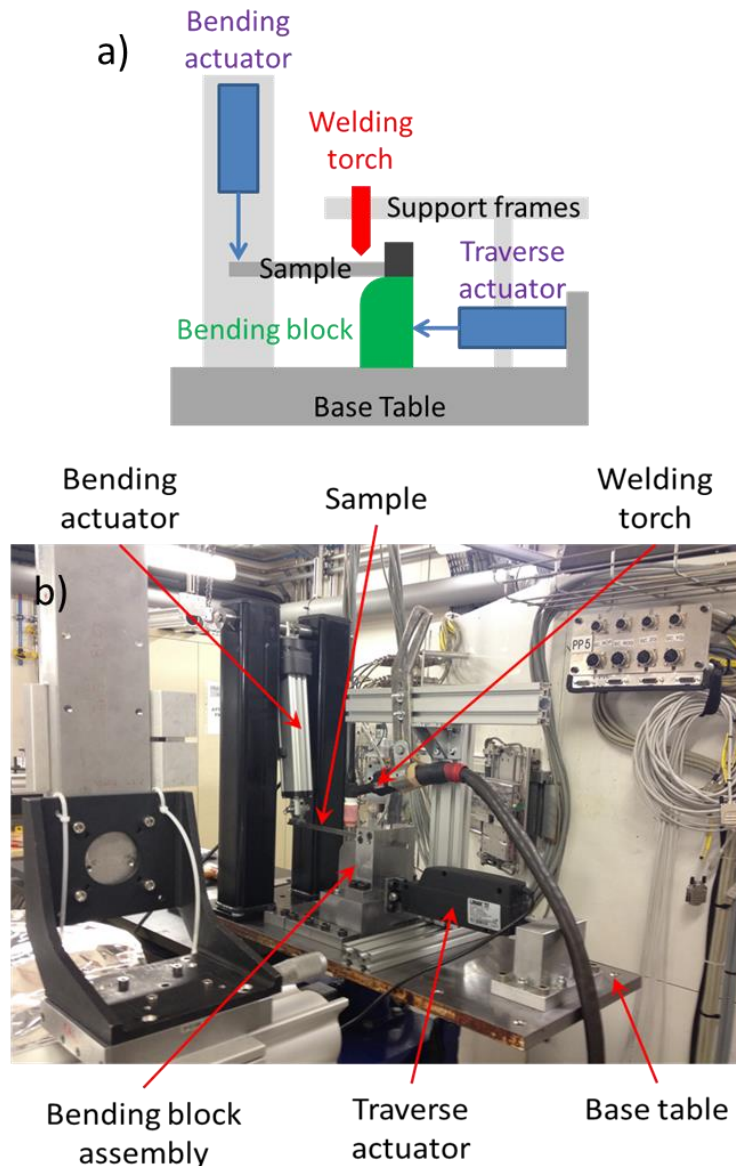
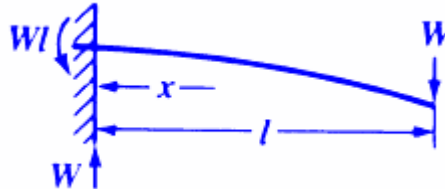


Figure 6-1: a) Schematic illustration of Varestraint weldability test rig, b) Varestraint test rig integrated to the ESRF's ID19 experimental hutch.

6.3.1.1. Design considerations

Sample deflection calculations

Assuming the bar to be a cantilevered beam:



Maximum deflection at point W can be expressed as,

$$(6-1) \quad W(L) = -\frac{PL^3}{3EI}$$

Where,

P = Load, L = length of bar, E = Young's Modulus, I = Moment of inertia

Description	Value	Units	SI Units	
Length of Beam	230	mm	0.23	m
Load	500	N		
Young's Modulus (Steel)	210	GPa		
Young's Modulus (Steel)	69	GPa		
Thickness	8	mm	0.008	m
Distance to Neutral Axis	4	mm	0.004	m
Moment of Inertia	341.33	mm ⁴	3.41E-10	m ⁴

Table 6-2: Input parameters for sample deflection calculations.

Angular displacement calculations

Angular displacement can be defined as:

$$\theta_{max} = -\frac{PL^2}{2EI} \quad (6-2)$$

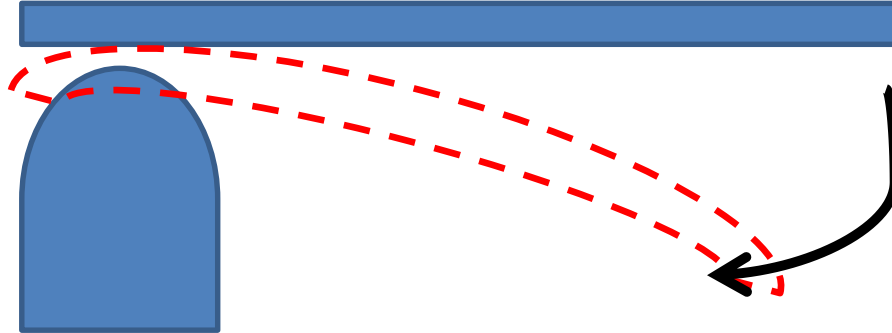


Figure 6-2: Schematic of angular displacement.

As material will be at an unknown, but high temperature the following deflections are possible, dependant on actual sample temperature when bending.

Temperature	Reduction factor (E_t/E_{normal})	Revised E	Maximum Deflection (m)	Maximum Deflection (mm)	Angular Displacement (Rads)	Angular Displacement (Degrees)
22	1	2.10E+11	0.02829	28.29	0.12	7.05
60	1.04	2.18E+11	0.02720	27.20	0.12	6.78
120	1.01	2.12E+11	0.02801	28.01	0.12	6.98
150	1.04	2.18E+11	0.02720	27.20	0.12	6.78
180	1.02	2.14E+11	0.02774	27.74	0.12	6.91
240	0.98	2.06E+11	0.02887	28.87	0.13	7.19
410	0.92	1.93E+11	0.03075	30.75	0.13	7.66
460	0.94	1.97E+11	0.03010	30.10	0.13	7.50
540	0.87	1.83E+11	0.03252	32.52	0.14	8.10
600	0.73	1.53E+11	0.03875	38.75	0.17	9.65
660	0.73	1.53E+11	0.03875	38.75	0.17	9.65
720	0.51	1.07E+11	0.05547	55.47	0.24	13.82
770	0.49	1.03E+11	0.05773	57.73	0.25	14.38
830	0.33	6.93E+10	0.08573	85.73	0.37	21.35
940	0.12	2.52E+10	0.23575	235.75	1.03	58.72

Table 6-3: Predicted deflection and angular displacement as a function of sample temperature.

6.3.1.2. 3D Solidworks model

The rig is designed to operate as a stand-alone setup offline, while also complying with necessary regulations for use in synchrotron experimental hutches. A 3D assembly was generated, visualised and validated using Solidworks CAD package.

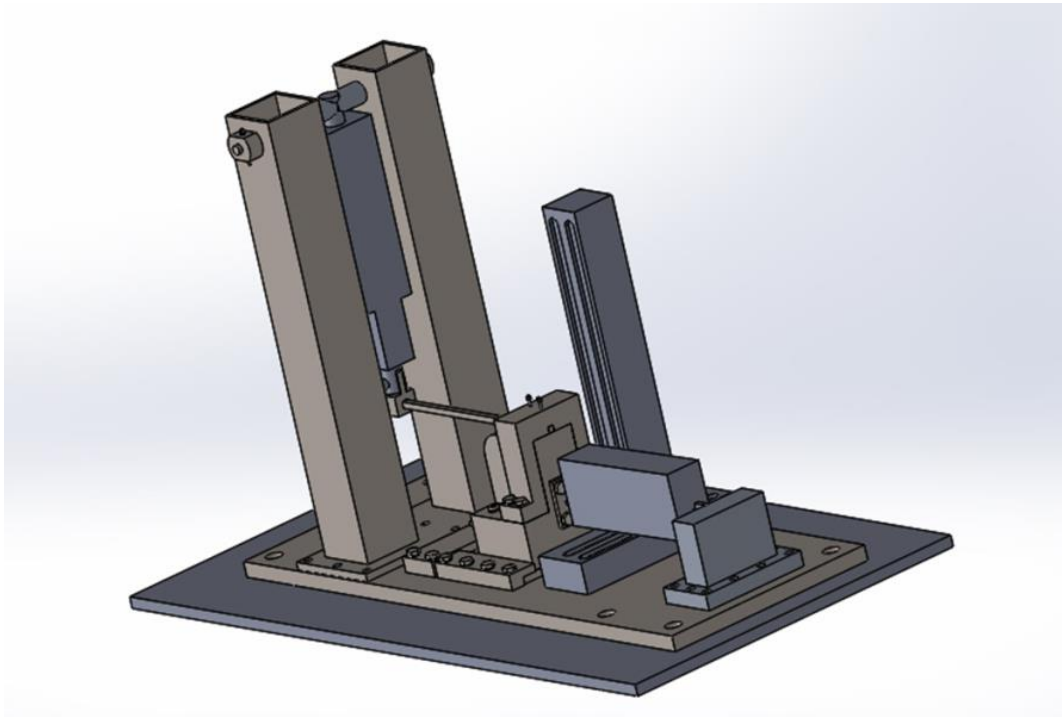


Figure 6-3: 3D Solidworks model of Vareststraint test rig assembly.

6.3.2. Procedure for the *in situ* imaging of weld solidification cracking

6.3.2.1. *Varestraint weldability test*

The Varestraint weldability test rig described in section 6.3.1 was integrated to the ESRF's ID19 beamline as depicted in Figure 6-5. The broken red box highlights the location of the sample and test rig. The broken blue box highlights the location of the detector, 7.2 m down beam. All other equipment within the hutch is not used in the *in situ* radiography experiments.

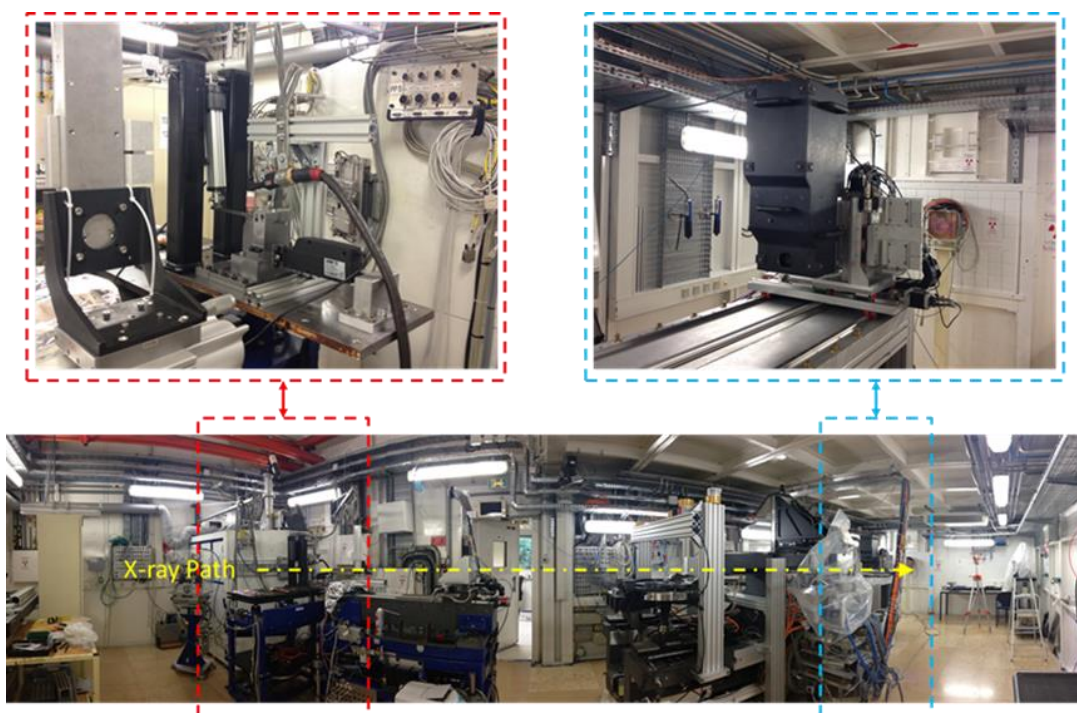


Figure 6-5: Varestraint test rig integrated into the ESRF's ID19 experimental hutch. The broken red boxes highlight the location of sample and test rig, while the broken blue boxes highlight the detector location (7.2 m away from the sample)

Figure 6-6 shows two photographs of the experimental setup both before, and after testing. The equipment is designed to carry out stand-alone small scale Varestraint weldability tests, while also allowing for integration to ESRF ID19 experimental hutch. A summary of the welding and test parameters is made in Table 6-4. The welding was carried out using a tungsten inert gas (TIG) weld method at 10 V and 98-108 A with a non-consumable tungsten electrode in DC-ve polarity. Adaptable Al fixings were used to support the welding torch and allow for easy adjustments to be made during testing.

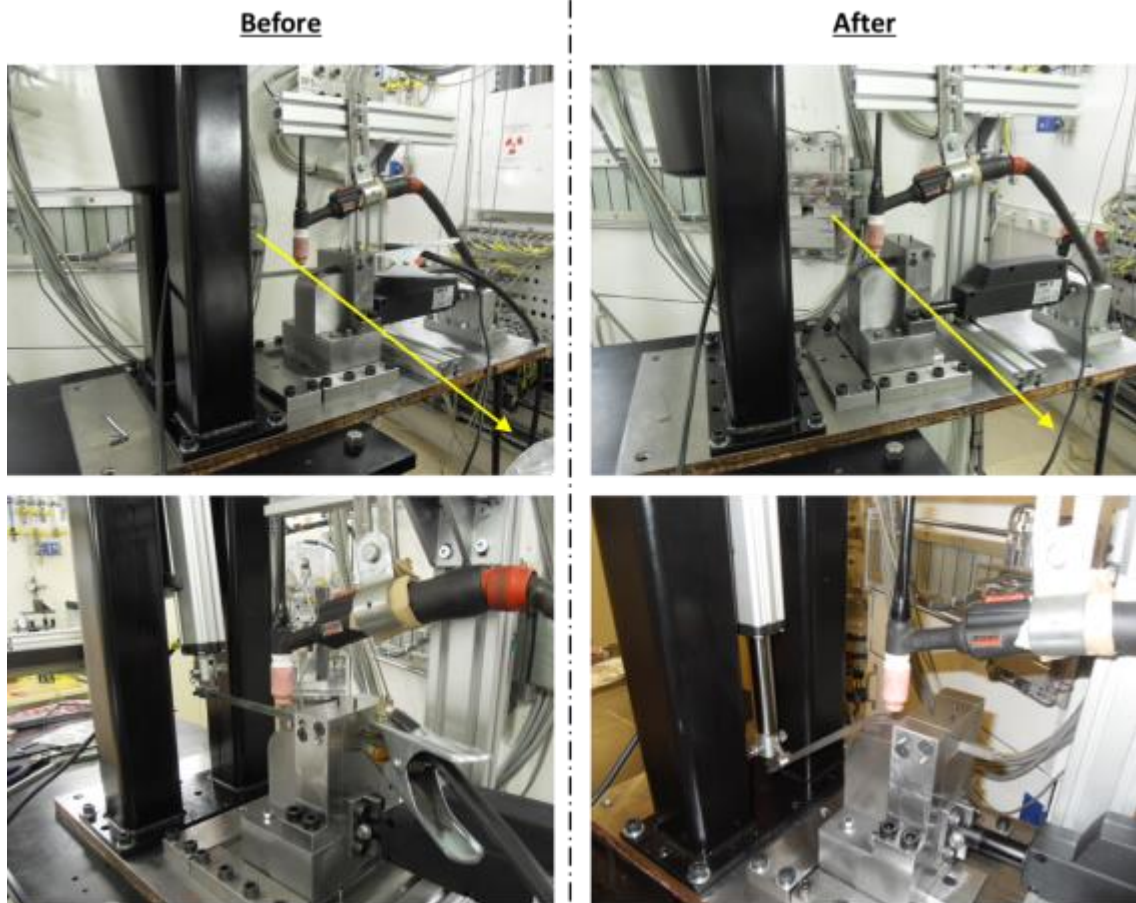


Figure 6-6: Experimental setup within ID19 showing the test apparatus both before testing (showing an un-deformed sample, with both the horizontal and vertical actuators retracted) and after testing (showing the sample deformed around the bending radius with both the vertical and horizontal actuators fully extended). The yellow arrow dictates the approximate path of the X-ray through the 8 mm thickness of the samples towards the detector.

8 mm square samples were created 300 mm long from three steels with poor weldability. The chemistry of the materials is defined in Table 6-1. To improve image quality, it is imperative to obtain the smallest path length for the beam to travel through the sample. The 8 mm sample thickness was selected as it was the smallest feasible in order to create a weld upon. The samples were locked into the clamping device on top of the bending radius with a 30 mm overhang to attach the earth clamp for welding.

The bending block assembly (with the sample clamped in) is attached to one of two electric actuators powered by a 12 V battery. The actuator to the right in the images in Figure 6-6 (horizontal orientation) supplies a 750 N load at speeds of up to 14 mm/s

across a 40 mm stroke length (Linak LA12 actuator). This actuator is connected to the bending block assembly and traverses it along the table to create the motion for welding a 40 mm length along the sample. Guide rails located on the surface of the base table interlink with the bending block assembly to ensure a straight travel path, normal to the beam.

The opposite side of the test sample is then attached to a second actuator, seen to the left in the figures (vertical orientation). This provides a 500 N load at speeds of up to 135 mm/s across a 150 mm stroke length (Linak LA36 actuator). This actuator was used to bend the sample during welding. The bending causes the sample to deform around the radius (30 mm) of the bending block and induces a strain to the sample in order to stimulate solidification cracking. The induced strain is calculated by $\epsilon = t/2R$ where, t is the material thickness and R is the radius of deformation on the outer surface of the sample.

The speed of both actuators is controlled from a motor control unit and programming interface from 0-100% of the bending speeds stipulated in the previous paragraphs. For the tests, welding velocity was controlled at 2.5 mm/s by the LA12 actuator, and the bending speed was assessed at three different increments (100%, 85%, and 70% of LA36 full speed). The bending load was initiated during welding at $t = 14$ s (approx. 35 mm weld length). After bending was completed (approx. 1 second later), the welding arc was turned off, but the traverse continued for a further ~1 second until the full 40 mm stroke length was reached, as illustrated in Figure 6-7. The weld pool solidification temperature was measured by tungsten-rhenium Type C thermocouples.

Parameter	Value used for tests
Weld method	TIG
Polarity	DC-ve
Current	98-108 A
Voltage	10 V
Arc length	1 mm
Weld length	40 mm
Weld velocity	2.5 mm/s
Bending speed	135, 115, and 95 mm/s
Bending strain	13%

Table 6-4: Summary of Vareststraint weldability test parameters.

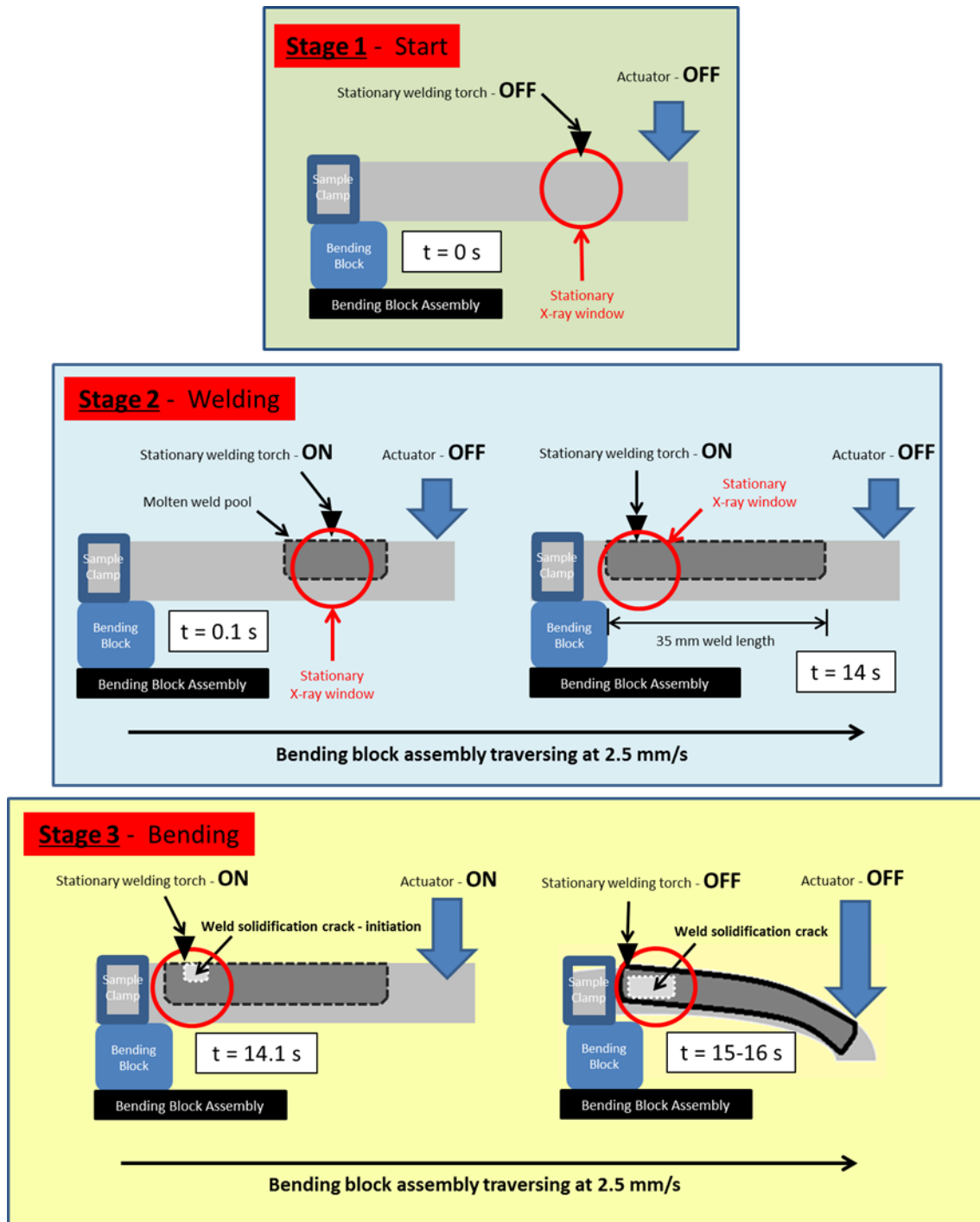


Figure 6-7: Schematic illustration of the Vareststraint test for in situ synchrotron X-ray micro-radiography experiments.

6.3.2.2. Synchrotron based micro-radiography

The X-ray beams produced at third generation synchrotron radiation facilities exhibit a high degree of coherence. This arises from the small source size σ (in the 50 μm range) and the large source to sample distance L (in the 100 m range). The transverse coherence length $d_c = \lambda L / 2\sigma$, is in the 100 μm range, and allows the recording of “phase images” by varying the sample-to-detector distance. This is known as propagation based imaging. Therefore, the European Synchrotron Radiation Facilities (ESRF) high resolution imaging beamline, ID19, was chosen for the experiments. The beamline is installed on a low-beta section of the storage ring. ID19 has a small source size (30 μm vertical x 120 μm horizontal) and long 145 m straight section from the source to experimental hutch. This allows for the coherence properties of the beam to be exploited [303]. In order to reach a sufficiently high photon flux density at the desired X-ray energy of around 110 keV, ID19 was operated in white beam mode. The light of the beamlines wiggler (gap 45) was filtered by a diamond window, 5.6 mm Al and 6 mm Cu. The resulting bandwidth is comparably large ($\Delta E/E = 90\%$, peak around 117 keV) but allows for radiography imaging at frame rates up to 1 kHz. The resultant photon flux density was approximately 7×10^{11} photons $\text{mm}^{-2}\text{s}^{-1}$. The corresponding indirect detector consisted of two identical objectives in tandem geometry (Hasselblad, type: HC 2.2/100 MM) leading to an effective 1:1 magnification: the lens-system projects the luminescence image of a 750 μm -thick LuAG:Ce single-crystal scintillator (Crytur, Czech Republic) onto the sensor of a camera. A periscope-like design with a folded optical path via a mirror is utilised in order to keep the objectives and electronics out of the intense hard X-ray photon beam. A pco.dimax camera was chosen (PCO AG, Germany; 2016 x 2016 pixels, 11 μm pixel size, 50% peak quantum efficiency at 500 nm, 36 GB on-board memory for fast intermediate storage, 1279 full images per second (fps) maximum frame rate). For the imaging, a view window of 1872 x 1000 pixels was employed with a 10 μm /pixel resolution. The camera recorded continuously images at a rate of 1000 fps to satisfy the temporal demands in observing the solidification cracking *in situ*. In order to enhance the contrast of the cracks by means of X-ray inline phase contrast, a propagation distance of 7.3 m between sample and detector was realised [304].

All post-processing was performed with freely available ImageJ software. A simple processing routine was implemented for all analysis. Firstly a “median Z stack” was made from a 500 frames of a reference image (I_0) without the sample and equipment present in the field of view. This stage is implemented to average out the high contrast noise speckles. Next, the raw data (I) was normalised against the reference image by a $-\log(I/I_0)$ math function. This stage effectively masks the background noise created by the beam to focus on the test specimen.

6.3.3. Procedure for *ex situ* synchrotron X-ray micro-tomography

For the ex-situ scans of the post-mortem samples, a similar configuration to that described in Chapter 6.3.2.2 was employed and used for synchrotron-based micro-tomography scans. The insertion device settings and filters remained the same. Experiments were carried out while the ESRF was operated in so-called 4bunch operation, resulting in a reduced photon flux which is still sufficient for the comparable long scans of the static samples.

A FReLoN CCD camera (type: 2k / F_A7899, ESRF in-house development, 2048 x 2048 pixels, 14 μm pixel size) detector was combined with 4:1 magnification optics resulting in an effective pixel size of 3.5 μm . As scintillator a 250 μm LuAG:Ce was chosen. The propagation distance was 1.2 m.

1200 projection images were recorded per sample in order to ensure good tomographic reconstruction quality. For the image reconstruction the ESRF in-house software PyHST_2 was used which is based on the filtered-backprojection approach. The resultant image stacks were then filtered using a 3D median filter to remove high contrast speckle noise, and then sharpened to enhance the edges using ImageJ. 3D reconstruction of the stacks and volumetric analysis was carried out in freely available Drishti volume exploration software.

6.4. Results

6.4.1. Visual analysis of welds and solidification cracking

The novel small-scale Varestraint test rig commissioned for the tests successfully produces consistent and repeatable solidification cracks. Figure 6-8 highlights a typical post-test sample. The sample exhibits good TIG weld quality with solidification cracks induced to the weld. A total of nine samples were selected for analysis and the region of solidification cracking removed from bulk of the samples for further analysis.

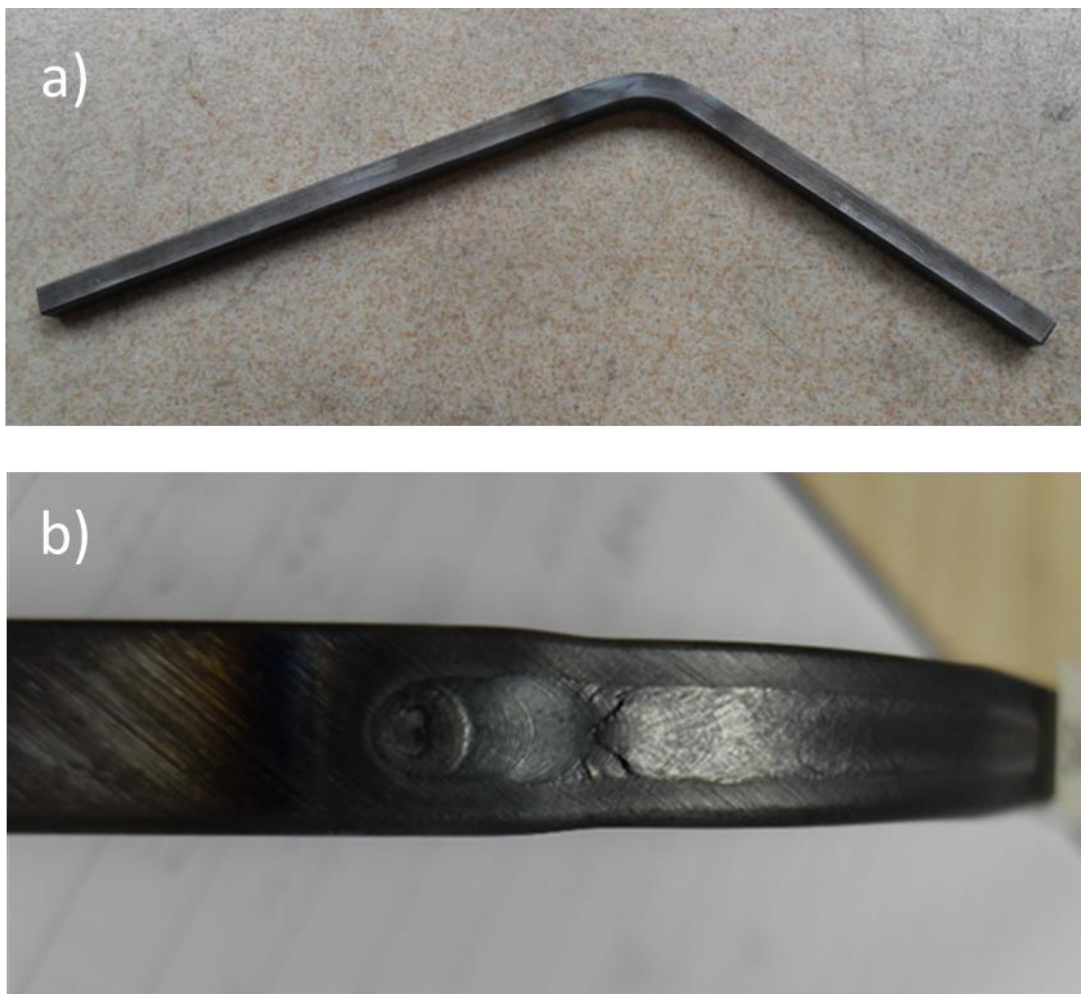


Figure 6-8: a) Macro image of typical deformed sample, b) detailed view of the weld which exhibits good quality with induced solidification cracking defects.

Figure 6-9 displays macro images of the surface cracking observed in the samples selected for analysis. Each of the nine tests depicted in Figure 6-9 was repeated three times to ensure that the results obtained were consistent. It is evident from initial inspection of Figure 6-9 that both the material type and bending speed employed during Varestraint testing has significant impact on solidification cracking.

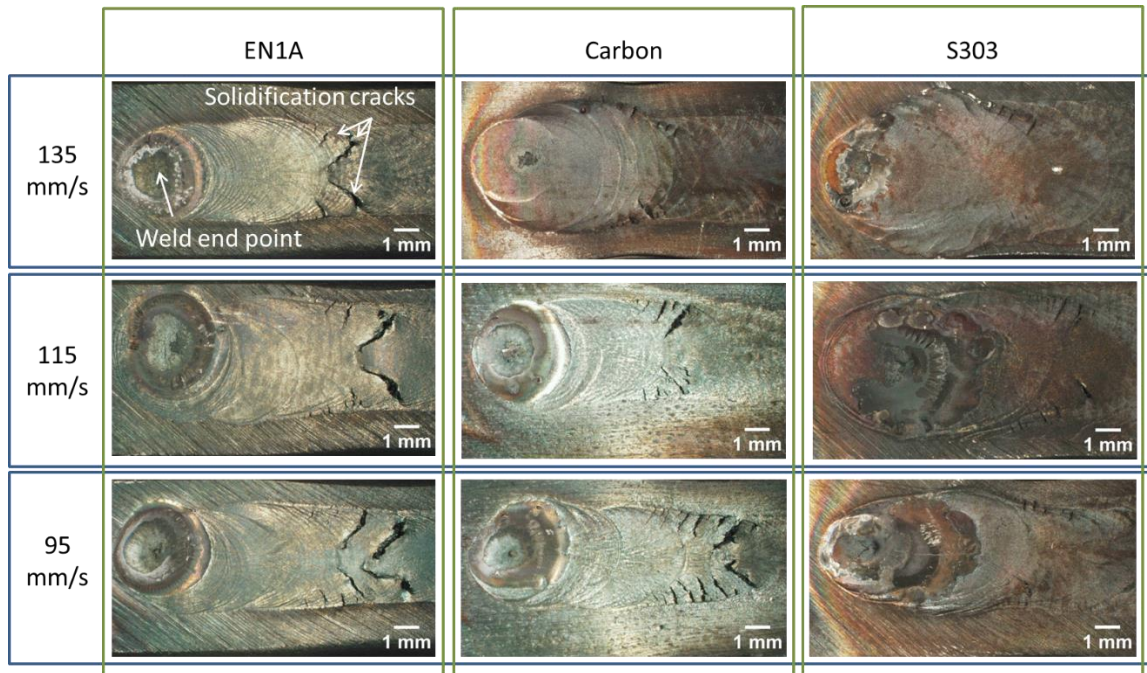


Figure 6-9: The array of weld solidification cracking observed in EN1A, C, and S303 materials tested at 135, 115, and 95 mm/s bending speeds.

ImageJ software was used to quantify the surface cracking observed in the samples in terms of total crack length criterion (TCL) with the results plotted in Figure 6-10. TCL is derived from:

$$TCL = \sum Crack_1 + Crack_2 + \dots + Crack_N \quad (6-3)$$

Analysis of Figure 6-10 confirms that both material type and bending speed influence solidification cracking. There is clearly a 3 tier susceptibility based on material type, with the EN1A sample being the most susceptible, and the S303 being the least susceptible. It is also evident from Figure 6-10 that the TCL of solidification cracks is also heavily dependent upon the bending speed utilised during Varestraint testing. In

the proceeding section, the initiation and propagation of the weld cracking defects is observed *in situ* using a novel micro-radiography approach.

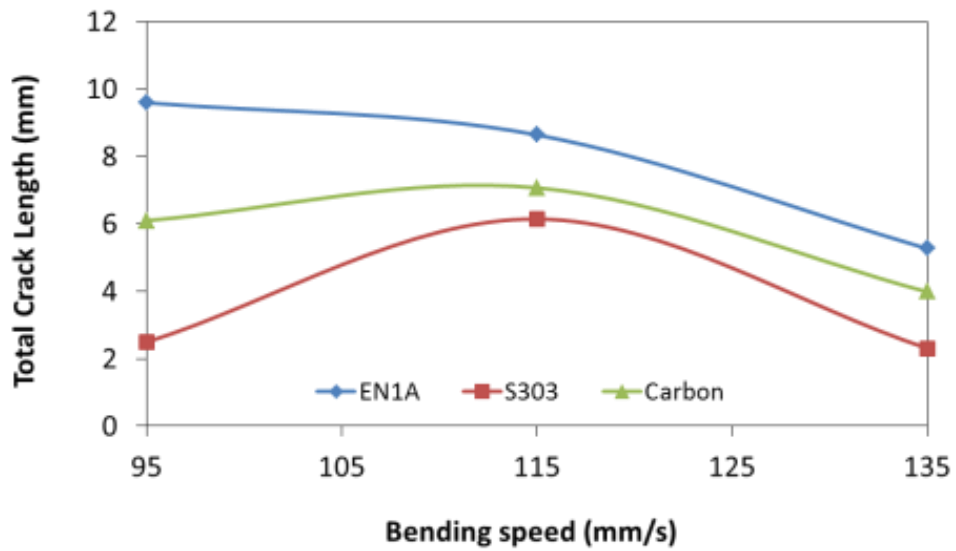


Figure 6-10: Total length of surface solidification cracking observed in the weld after Vareststraint testing at a range of bending speeds.

6.4.2. *In situ* radiography imaging of weld solidification cracking

Figure 6-11 displays a series of processed radiographs. The white tip in the top left of the images is the tungsten welding electrode. The large white part in the centre of the images is an EN1A test sample. Figure 6-11(a) highlights the point at which weld solidification cracking were observed to initiate in the radiography sequence. The cracks are easily distinguishable, being darker than the bulk sample. This is due in part to a lower attenuation through the cracking interface. However, the main source of the interface clarity can be attributed to the refraction based coherent imaging technique and wide propagation distance between the sample and detector.

The cracks appear after 0.134 s of bending under a loading rate of 135 mm/s. The approximate strain at cracking initiation is 3.25%. Detailed analysis of the cracking shown in Figure 6-11(c) reveals that the solidification cracks appear to initiate trailing the welding electrode by 2.69 mm at 1.45 mm sub-surface, approximately 0.22 mm away from the fusion boundary within the weld. Upon further loading, the cracks appear to propagate vertically and penetrate the upper surface of the sample after 0.324s of loading. The velocity of the fracture propagation is measured at approximately 2.2 mm/s in the 2D plane of imaging. However, due to the 3D nature of the cracking, this could equate to speeds of up to 2.8 mm/s when considering propagation at angles up to 38° in the z plane, as detailed in Appendix C.

Analysis of the sequence reveals that after the initial cracks have penetrated the surface, further cracking then begins to initiate sub-surface in the region to the left of the initial initiation site (closer to the heat source) and follow the same vertical propagation path. This time however, it appears that the cracks also begin to converge laterally with the initial crack. Cracking continues to develop in this manner until 0.832s of bending (Figure 6-11(b)). The cracks then cease to develop, with the total cracking observed displayed in Figure 6-11(d) at 10.53% strain. From the analysis it is possible to conclude that the weld solidification cracking occurred in the EN1A sample (tested at a 135 mm/s bending rate) over a 3.25-10.53% strain range and 0.698s time period.

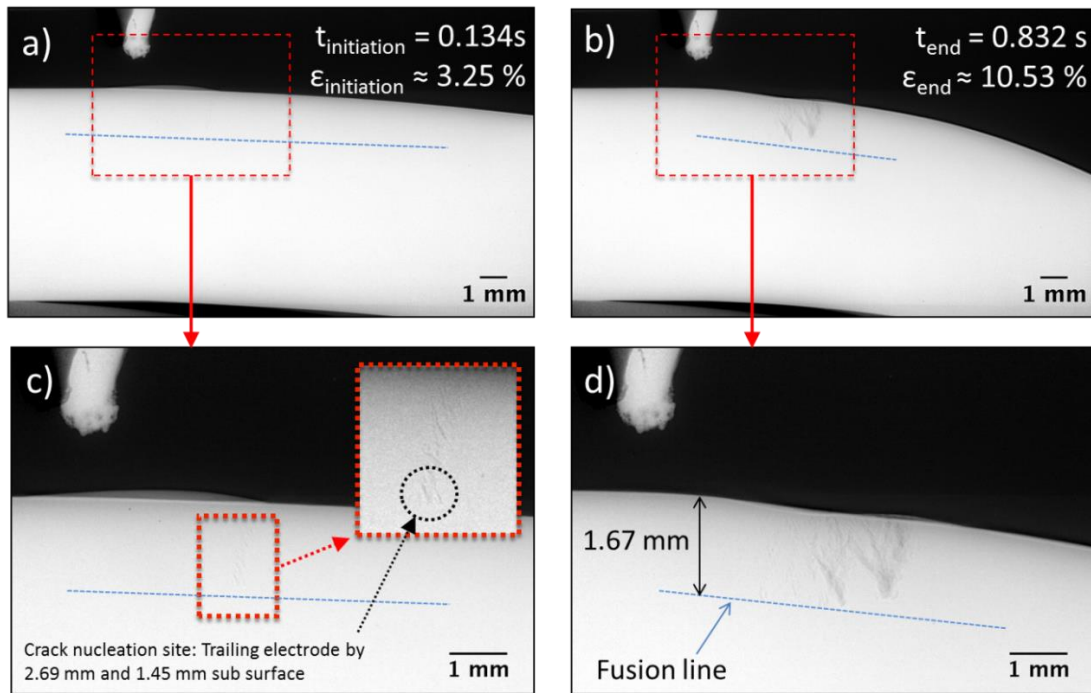


Figure 6-11: Results of synchrotron radiography analysis on the EN1A sample tested with a 135 mm bending speed, showing a) the initiation of weld solidification cracking at 0.134 s of bending with an approximate strain of 3.25 %, the broken blue line depicts the fusion boundary measured from post-test microscopic observations b) the end of solidification cracking at 0.832 s of bending and an approximate strain of 10.53 %, c) a magnified image of the weld solidification crack initiating trailing the welding electrode by 2.69 mm at 1.45 mm sub-surface, d) a magnified image of the full solidification cracking at the end of testing, showing propagation through the surface.

The same analysis was completed for all samples referenced in Figure 6-9. The results are presented in Table 6-5. All solidification cracks were found to initiate sub-surface during analysis of micro-radiographs. Figure 6-12 plots the measured nucleation depths as a function of the bending speed employed in V-restraint testing. It is clear that the least susceptible material – the S303 alloy – initiates at a shallower (0.47 – 0.98 mm) location when compared to the more susceptible EN1A and Carbon alloys. Furthermore, Figure 6-13 also demonstrates that solidification cracks initiate at lower strains (2.42 – 3.42 %) in the more susceptible materials - the EN1A and carbon alloys. In the less susceptible S303 alloy, the cracks do not appear until strains have reached 4.00 – 5.06 %. A similar trend is observed in Figure 6-14 for the strain range over which solidification cracking was observed to propagate in. The most susceptible material in terms of the commonly applied TCL criterion (Figure 6-10) – the EN1A

sample – exhibits the widest strain range in which solidification cracking propagates. The least susceptible alloy – the S303 sample – exhibits the shortest strain range. Again, it is apparent that all of the features are again heavily dependent upon the Vareststraint bending speed. However, the measured fracture velocity remains fairly consistent throughout the experiments with an average velocity of 2.33 mm/s calculated.

	EN1A			S303			Carbon		
	95 mm/s	115 mm/s	135 mm/s	95 mm/s	115 mm/s	135 mm/s	95 mm/s	115 mm/s	135 mm/s
Crack initiation time (s)	0.15	0.11	0.13	0.52	0.26	0.22	0.19	0.16	0.18
Cracking end time (s)	1.33	0.88	0.83	1.15	0.87	1.00	1.22	0.87	0.71
Cracking period (s)	1.19	0.77	0.70	0.63	0.61	0.78	1.03	0.71	0.52
Crack initiation strain	2.47	2.58	3.25	5.06	4.00	4.35	2.42	2.56	3.42
Cracking end strain	8.33	8.89	10.53	9.52	8.70	10.13	7.69	8.16	9.52
Cracking strain range	5.86	6.31	7.27	4.46	4.70	5.78	5.27	5.60	6.11
Crack nucleation depth (mm)	1.18	1.63	1.45	0.47	0.86	0.98	0.82	1.05	1.73
Fracture velocity (mm/s)	1.66	2.46	2.20	2.48	2.54	2.53	2.33	2.18	2.59

Table 6-5: Summary of properties observed from in situ micro-radiography.

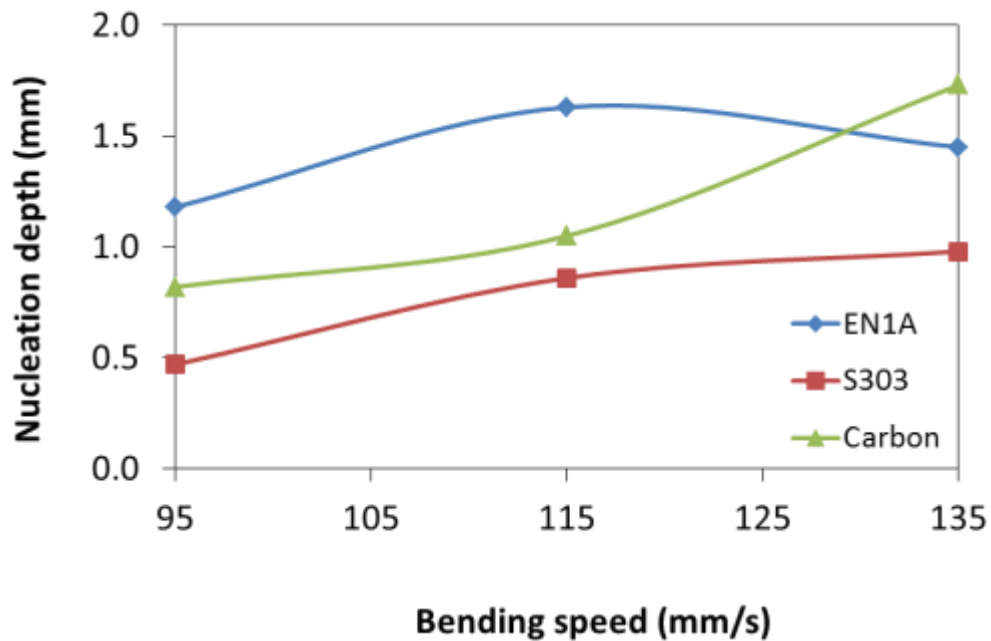


Figure 6-12: Sub-surface depth of solidification cracking nucleation site, plotted as a function of Vareststraint bending speed.

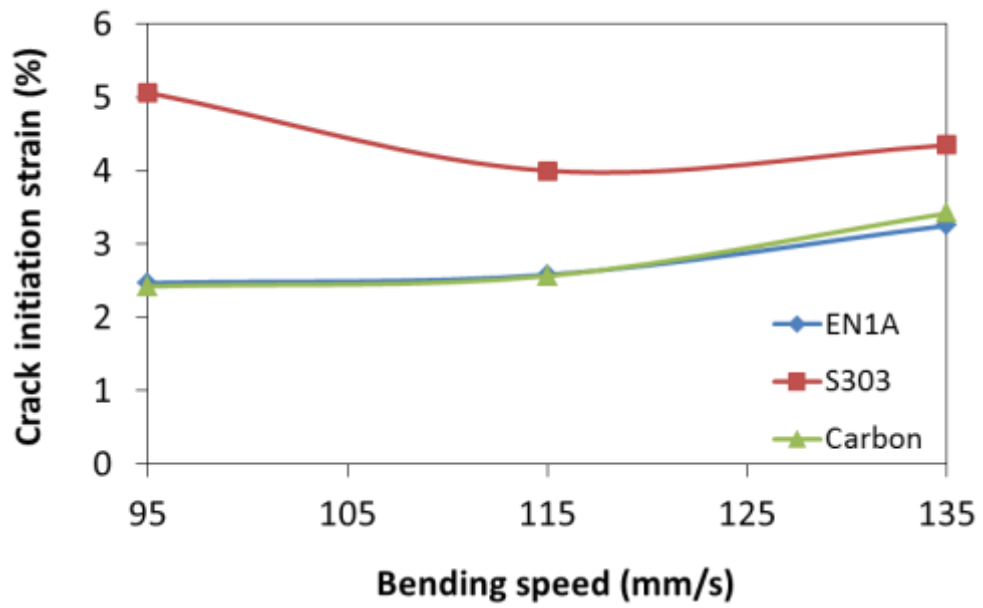


Figure 6-13: Strain that initiated solidification cracking plotted as a function of bending speed.

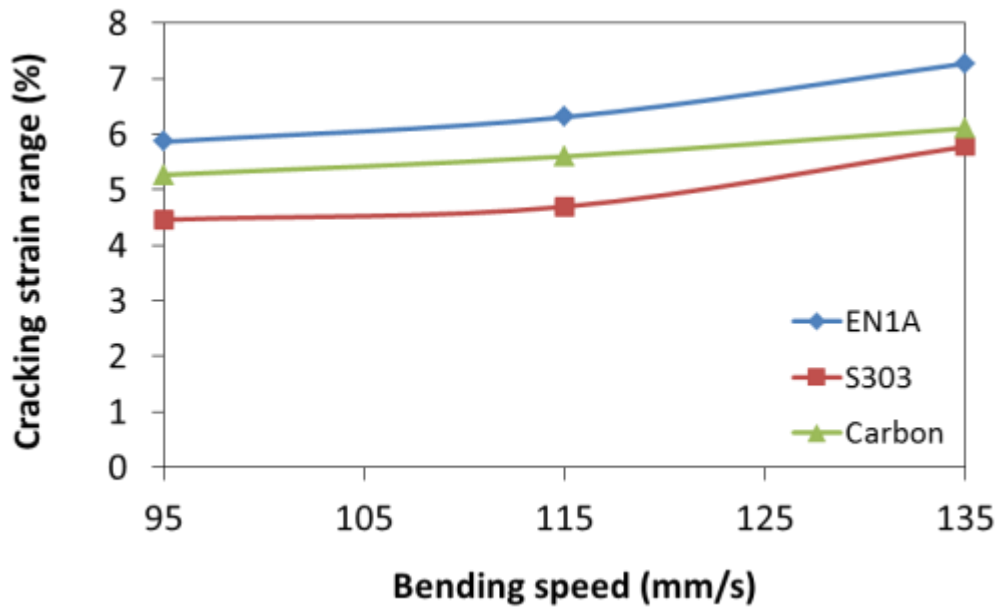


Figure 6-14: Strain range over which solidification cracking was observed to propagate plotted as a function of Varcstraint bending speed.

6.4.3. Temperature and phase when solidification cracking initiates

In this section, the temperature and phase when solidification cracking initiates is investigated. Figure 6-15 illustrates solidification stages, in terms of temperature and volume fraction of solid, which relate to solidification cracking. The values are calculated from Thermo-Calc simulations for the EN1A alloy under both equilibrium and non-equilibrium (Scheil) solidification conditions. The brittle temperature range (BTR) where solidification cracking can occur is determined by the ZST-ZDT. Based on the Thermo-Calc simulations presented in Figure 6-15, the BTR is between 41°C and 368°C dependent upon solidification conditions.

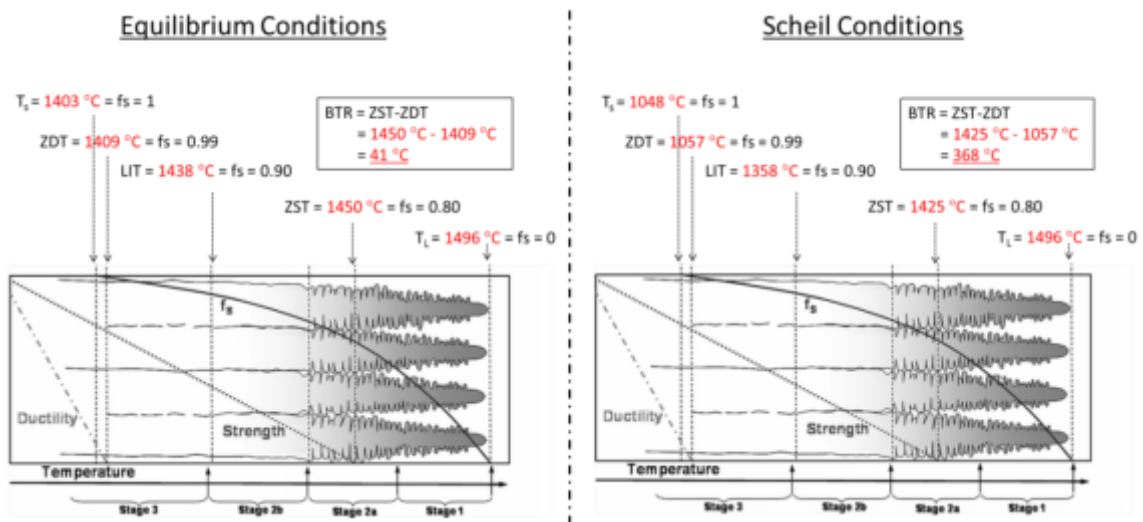


Figure 6-15: Schematic illustration of solidification stages relating to solidification cracking, adapted to include values calculated from the results of EN1A alloy Thermo-Calc simulations under equilibrium and non-equilibrium (Scheil) conditions.

To determine the high temperature mechanical properties more accurately, Gleeble hot ductility tests were performed on the EN1A alloy. Figure 6-16(a) displays images of the fracture samples and their corresponding test temperatures. Figure 6-16(b) shows the results of the stress vs temperature and corresponding reduced area % for the samples tested in Figure 6-16(a).

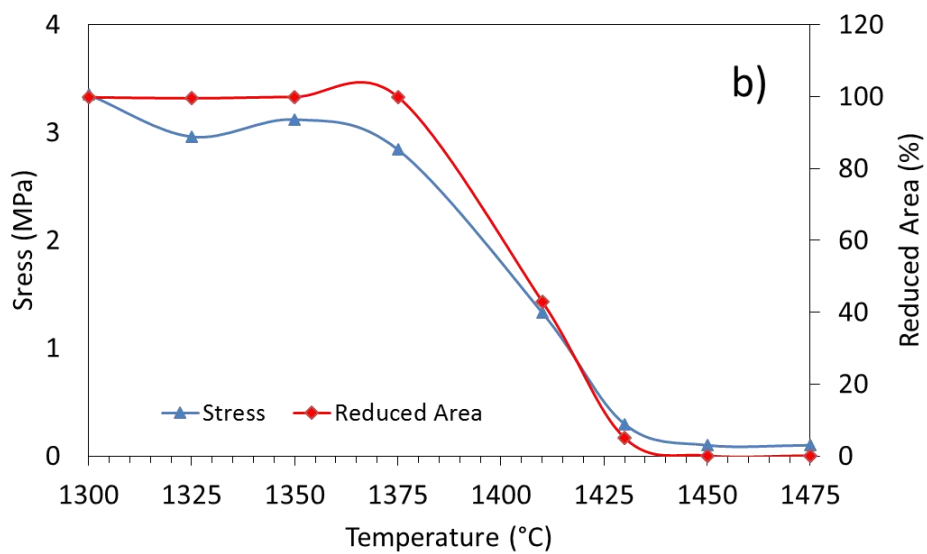
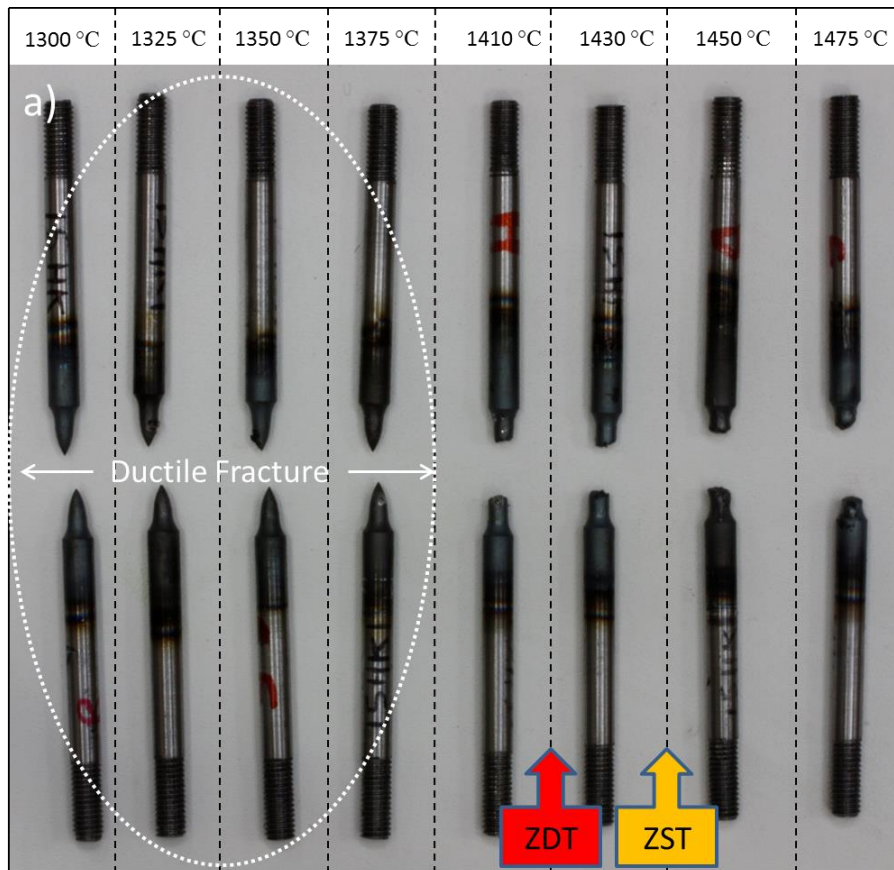


Figure 6-16: Results of Gleeble hot ductility tests showing, a) Fracture samples and corresponding test temperatures. The lower temperature samples show clear elongation and ductile fracture. Based on visual observations, it appears the ZDT is between 1410-1430 °C and the ZST between 1430-1450 °C, b) Plot of stress and reduced area vs temperature from the Gleeble hot ductility tests on the EN1A alloy.

Based on examination of the hot ductility results, the onset of elongation is first observed on the sample tested at 1410 °C. Therefore, the ZDT is deduced to lie between 1410 °C and 1430 °C. Similarly, the ZST is deduced to lie between the points when the brittle fracture surface at 1430 °C becomes molten at 1450 °C. As such, the approximate BTR obtained directly from hot ductility tests is between 20 and 40 °C showing good correlation with the equilibrium Thermo-calc results in Figure 6-15, as tabulated in Table 6-6.

Test method	Solidus (Fs = 1)	ZDT (Fs = 0.99)	LIT (Fs = 0.90)	ZST (Fs = 0.80)	Liquidus (Fs = 1)	BTR (ZST-ZDT)
Thermocalc simulation - Scheil conditions	1048	1057	1358	1425	1496	368
Thermocalc simulation - Equilibrium conditions	1403	1409	1438	1450	1496	41
Gleeble hot ductility test		1410-1430		1430-1450		20-40

Table 6-6: Summary of solidification thermodynamic results

Although the temperature range over which the cracking occurs has been identified, it is also interesting to understand the localised temperature and phase fraction when the solidification cracks first initiate. To achieve this, the temperature within the molten weld joint was recorded via thermocouples during welding. The distance (2.69 mm) trailing the heat source where solidification cracks were observed to initiate in the radiography sequence (Figure 6-11(c)) is used to extrapolate an approximate cracking initiation temperature from the weld temperature curve in Figure 6-17. Using the 1433 °C value extrapolated from Figure 6-17 for cracking initiation temperature, the volume fraction of solid is then predicted from Thermo-Calc (equilibrium, Figure 6-15) and hot ductility data (Figure 6-16). Based on predictions presented in Figure 6-17, the cracks initiate as stage 3 “hot cracks” at the terminal stage of solidification when small amounts (~0.08 volume fraction) of liquid remain. Stage 3 hot cracks typically develop on thin inter-granular liquid films present after the transformation from the dendritic to grain structure. The films form at grain boundaries due to segregated elements in the liquid, lowering the melting point of this film. Solid-state creep is the only way to accommodate solidification shrinkage and thermal stresses at this stage.

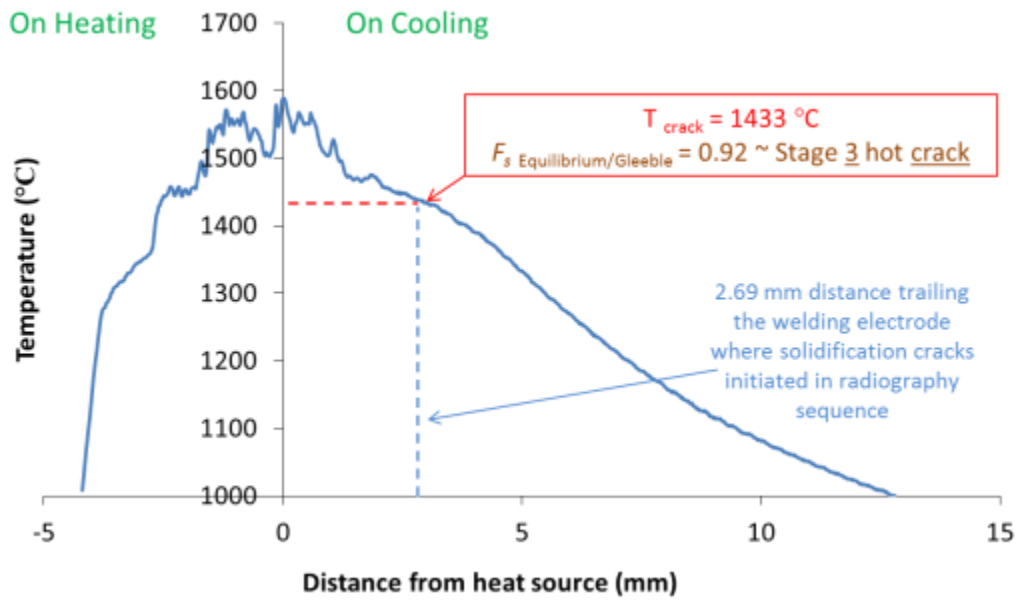


Figure 6-17: Results of thermocouple recordings within the molten weld pool during Varestraint testing. T_{cracking} has been extrapolated from the observations on crack initiation made in the in situ radiography sequence reported in Figure 6-11.

6.4.4. Tomographic reconstruction of the crack network

Thermodynamic analysis suggests that the solidification cracks initiate as stage 3 hot cracks. In this section, the 3D morphology of the solidification cracking network and fracture initiation site is examined from reconstructions of micro-tomography images. Figure 6-18 displays a 3D tomographic reconstruction of the solid EN1A sample tested at 135 mm/s bending speed.

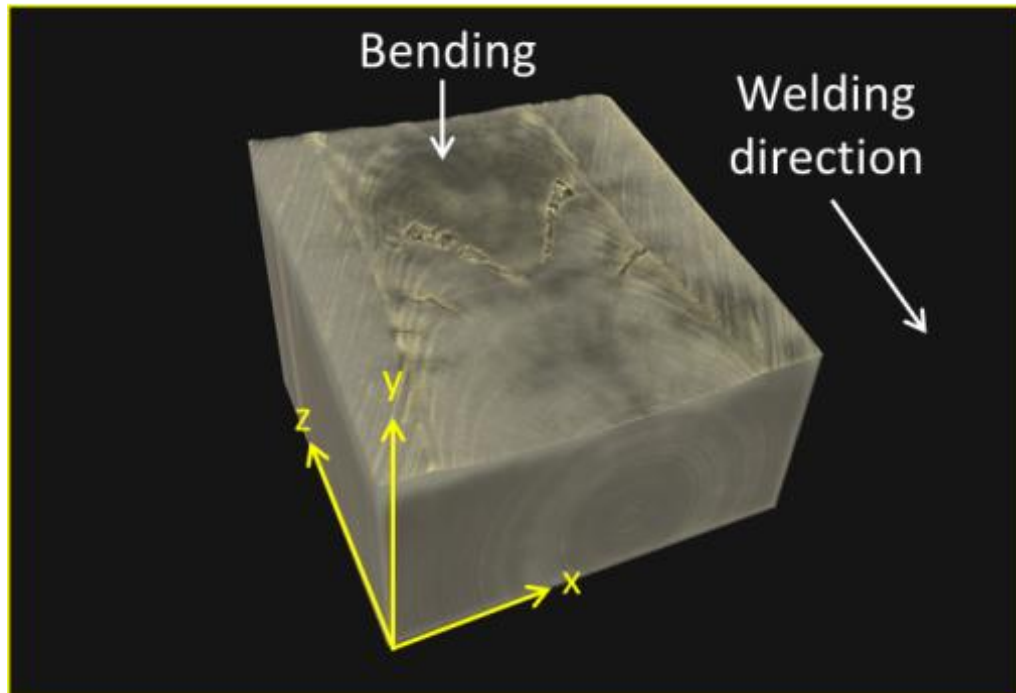


Figure 6-18: 3D reconstruction of the solid EN1A sample tested at 135 mm/s bending speed with weld and solidification cracks visible on the surface of the reconstruction. An orthogonal co-ordinate system is defined in the image.

Figure 6-19(a) illustrates the surface cracking observed in the sample and Figure 6-19(b) displays the air which is inherent to the crack network. The network has been further divided into two regions depicted by the broken line boxes in Figure 6-19. The blue box represents the bulk of the solidification cracking (~75%) and propagates the largest surface area on sample surface. It essentially one crack and is the point at which the cracks first initiate. The red box represents solidification cracking that is primarily sub-surface and invisible from Figure 6-19(a). These cracks initiate at a later stage in

the *in situ* radiography sequence. There are hundreds of separated and interlinked cracks in this region and the majority of those are sub-surface cracks.

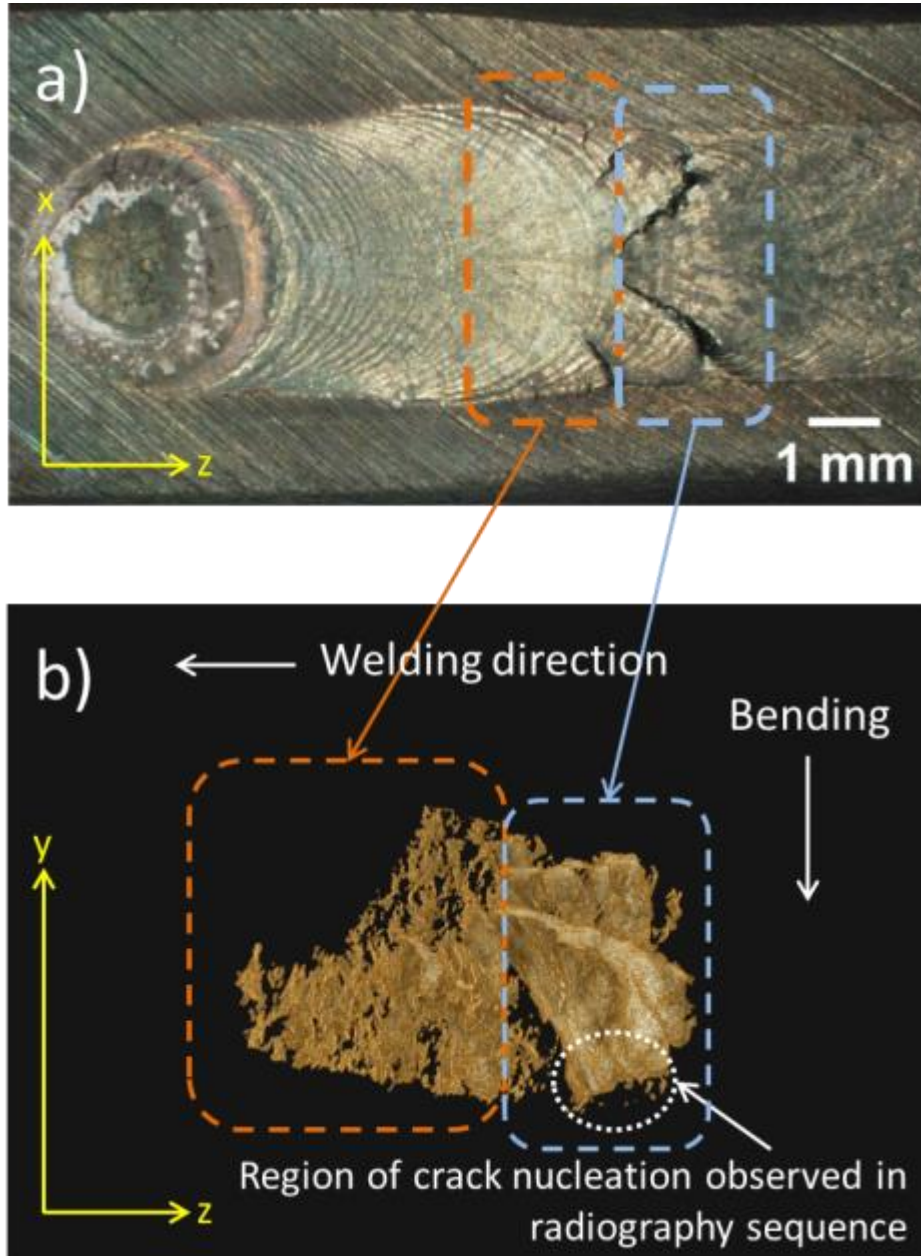


Figure 6-19: a) Macro image of surface cracking visible to the eye, b) View of the air (solidification cracking network) inherent to the sample from the z-y plane. The broken blue line highlights the bulk of the solidification cracking. It essentially one crack that propagates the largest surface area on sample surface and is the point at which the cracks first initiate. The broken red line highlights the solidification cracks initiated at later times during testing. This region is made up of hundreds of isolated cracks, the majority of which are sub-surface

A plan view on the x-z plane of the cracking network in Figure 6-20 reveals symmetric features in terms of the orientation of the angle of cracking either side of the weld centreline.

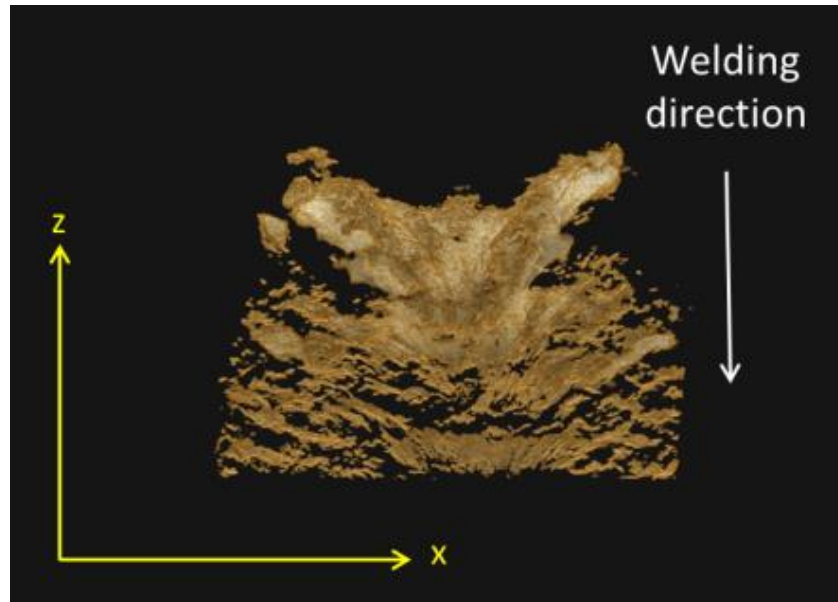


Figure 6-20: Plan view on the z-x plane of the solidification cracks showing somewhat symmetric features in terms of the angle of cracking either side of weld centreline.

The location of the fracture initiation site observed in the radiography sequence has been transposed onto the corresponding region on the 3D volume in Figure 6-21. The shape of the cracks appears to be related to the weld geometry as the network resembles arches that loop from the lateral edges of the weld around the semi-circle weld geometry. What is interesting from the Figure 6-21 is the presence of the isolated pores/cavities/cracks that are situated away from the bulk crack. Detailed analysis of the features in Figure 6-22 reveal the size of the cavities to be between 5-40 μm in size and often isolated. Sometimes the cavities coalesce with each other, but not the bulk crack, and in the case of the cavities highlighted in Figure 6-22, some also coalesce with each other and the bulk crack.

From the experimental evidence provided with this novel synchrotron X-ray imaging approach, it appears there is significant evidence to suggest that weld solidification cracks are initiating from these isolated pores/cavities/cracks. It is therefore essential to characterise the features.

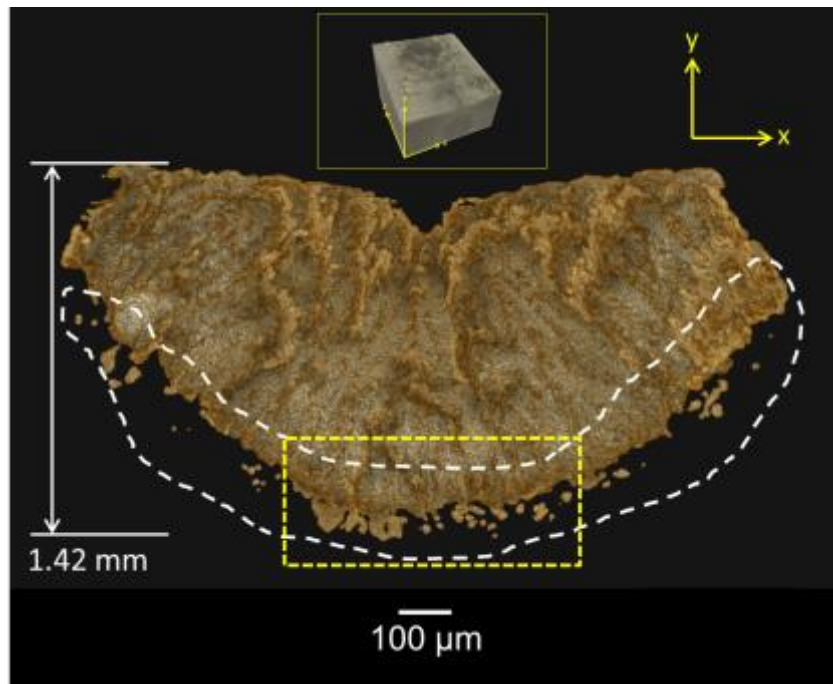


Figure 6-21: Detailed observation of fracture initiation site. The yellow broken square highlights the fracture initiation site observed in the micro-radiography sequence and is viewed in more detail in Figure 6-22.

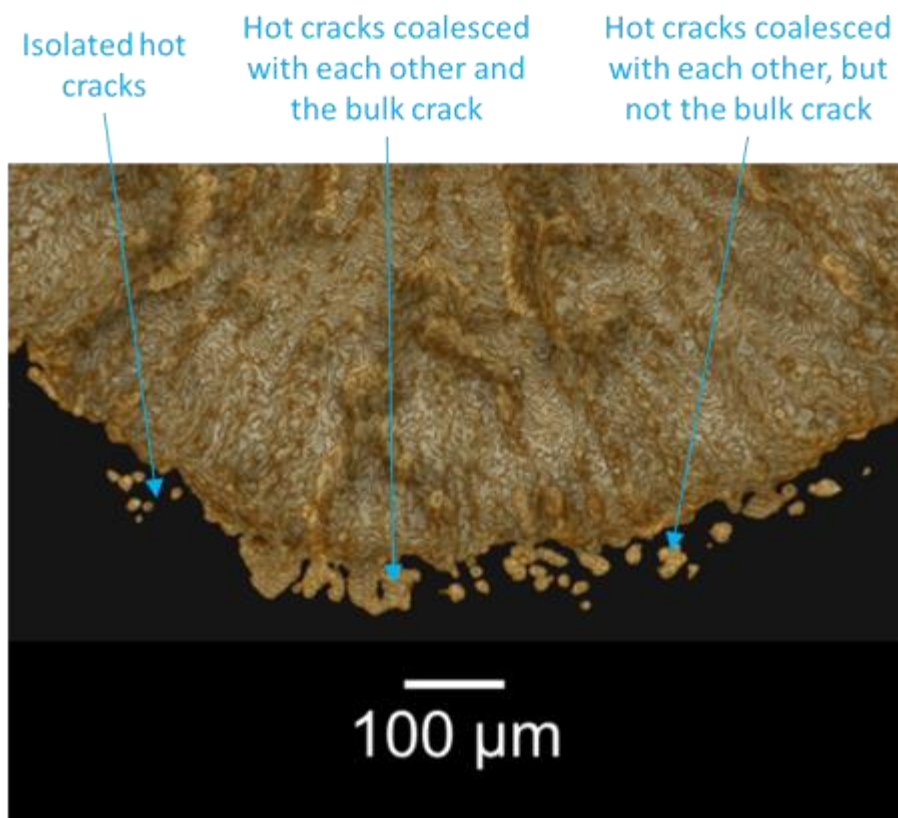


Figure 6-22: Cavitation ahead of the crack tip. Some of the cracks are isolated, some coalesce with each other, but not the bulk crack and some coalesce with each other and the bulk crack.

6.4.5. Microscopic examination of fracture surfaces

In this section, the EN1A fracture surfaces features resulting from Gleeble hot ductility and Vareststraint testing are characterised by microscopy and chemical analysis. Analysis in Figure 6-17 predicts the solidification cracking initiation temperature to be 1433 °C. Therefore, microscopic analysis has been focussed on the Gleeble hot ductility sample tested at 1430 °C - the closest temperature to the predicted 1433 °C cracking initiation temperature.

Figure 6-23 presents observations made on the Gleeble hot ductility sample tested at 1430 °C. Figure 6-23(b) shows an as-solidified faceted ferritic grain structure observed in the centre of the fracture surface. The fracture is inter-granular and brittle with a high volume of porosity inherent to the facets as detailed in Figure 6-23(c). The damage in the sample at this temperature is by hot cracks; only the grains are observed and no dendrite morphology is present on the fracture surface. Hot cracks develop due to the segregation of solute elements at grain boundaries in the final stages of solidification when the volume fraction of liquid is <0.1 .

Evidence presented in Figure 6-23(d) points towards two segregation-related features that could initiate the fracture. The orange circles in Figure 6-23(d) highlight two MnS particles. Traditionally, sulphides can be classified as types I, II, and III. Type I particles appear as individual spheroids of a wide size distribution scattered randomly in the inter-dendritic spaces. Type II particles appear as a degenerate eutectic network made of irregular cylindrical rods, spread out in the inter-dendritic spaces, delineating the dendrite arm boundaries. Type III particles appear as idiomorphic crystals scattered through the whole dendritic structure but frequently are situated in inter-dendritic spaces. They often project arms that join type II particles [305]. From analysis of Figure 6-23(d) it is clear that the MnS particles under observation are type III sulphides. The broken red circle Figure 6-23(d) also displays the presence of globular particles more numerous in population. The particles are inherent to the grain boundaries of the fracture surface and enriched in solute elements Mn, Al, and in particular, Si. The size (approximately between 5-20 μm) and globular morphology of the particles correlate well with the size and shape of the cavities which are observed in Figure 6-22 – the region of solidification crack initiation.

The evidence presented in Figure 6-23 further supports the argument that solidification cracking in welding initiates as hot cracks in the final stages of solidification after the dendrite to grain transition when the volume fraction of liquid is <0.1 . It appears that the cracking initiates in the form of cavities that are established on low melting point solute enriched films which segregate at the grain boundaries.

Figure 6-24 displays the fracture surface observed on the bulk crack presented in Figure 6-21. The fracture observed in Figure 6-24 is inter-dendritic and categorised as hot tearing. From the analysis provided, it is clear that there are multiple cracking mechanisms active through the solidification cracking process. Hot tears occur at higher volume fractions of liquid prior to the dendrite to grain transformation, in comparison to the hot cracks which occur after the dendrite to grain transformation.

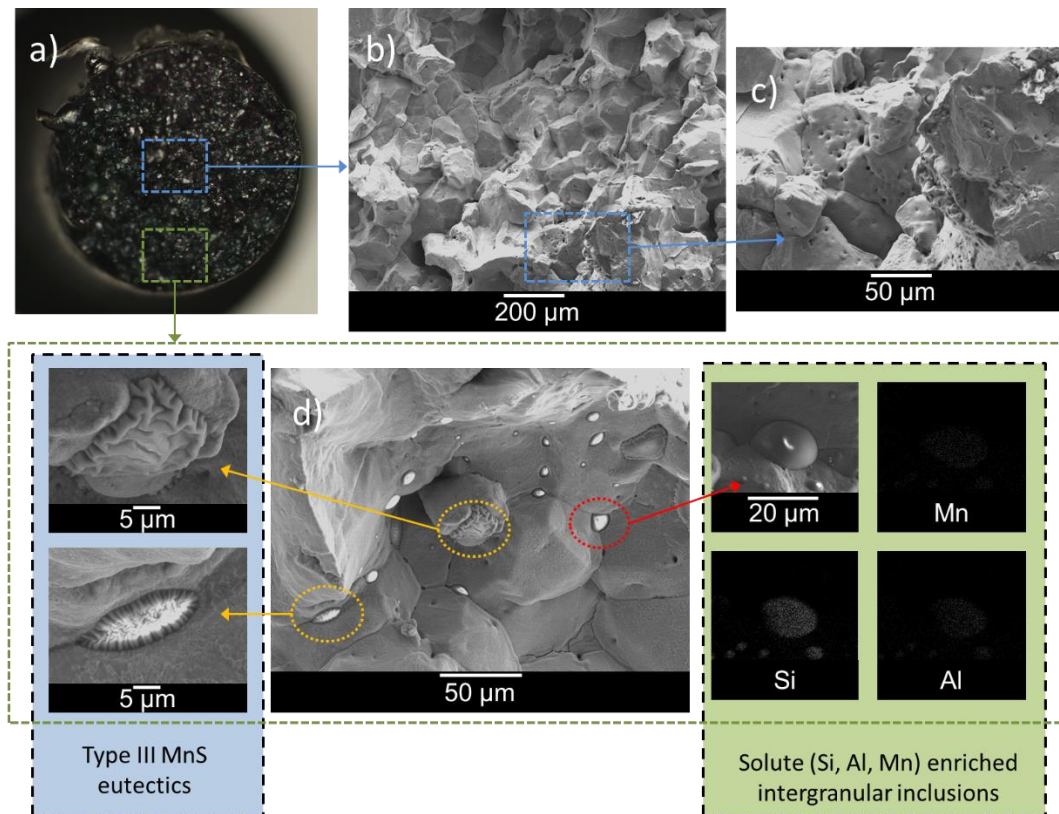


Figure 6-23: Observations made on the fracture surface of the Gleeble hot ductility sample tested at 1430 °C showing, a) macro image of the full fracture surface, b) SEM image of the as-solidified faceted ferritic grains in the centre of the Gleeble sample. The facets results from brittle inter-granular fracture, c) magnified SEM image of the porosity inherent to the faceted grains in the centre of the Gleeble sample, d) SEM image of the fracture surface typical to the outer fracture surface. The orange broken circles highlight two low melting point Type III MnS particles while the broken red circle highlights the presence of numerous globular particles enriched in solute elements (Si in particular) inherent to grain boundaries.

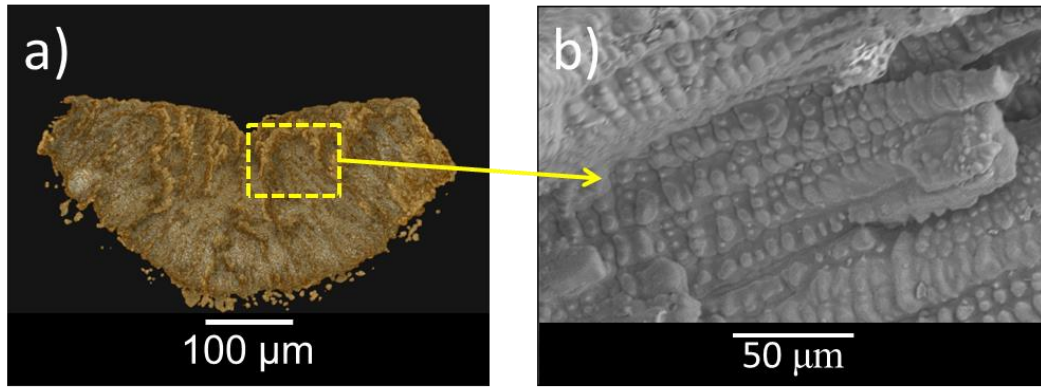


Figure 6-24: Dendritic fracture morphology observed on the bulk fracture surface at later stages of cracking showing clear inter-dendritic fracture associated with stage 2 hot tearing.

6.5. Mechanisms proposed for solidification cracking during welding of low-alloy high-impurity steels

Stage 1: Sub-surface initiation of inter-granular hot cracks after the transition from dendrite to grain structure (nucleation mechanism)

During weld pool solidification, after the transition from the dendrite to the grain structure when the volume fraction of liquid is <0.1 and temperature is $\sim 1430^\circ\text{C}$, solute elements (Mn, Si, Al) and impurities (S) segregate to grain boundaries. As a result, low melting point films with eutectic chemistries form in the inter-granular regions. Under tensile strains of $\sim 3.25\%$, hot cracks form sub-surface at the inter-granular sites where the eutectic liquid films are concentrated, as illustrated in Figure 6-25 and evidenced in Figure 6-11 and Figure 6-23.

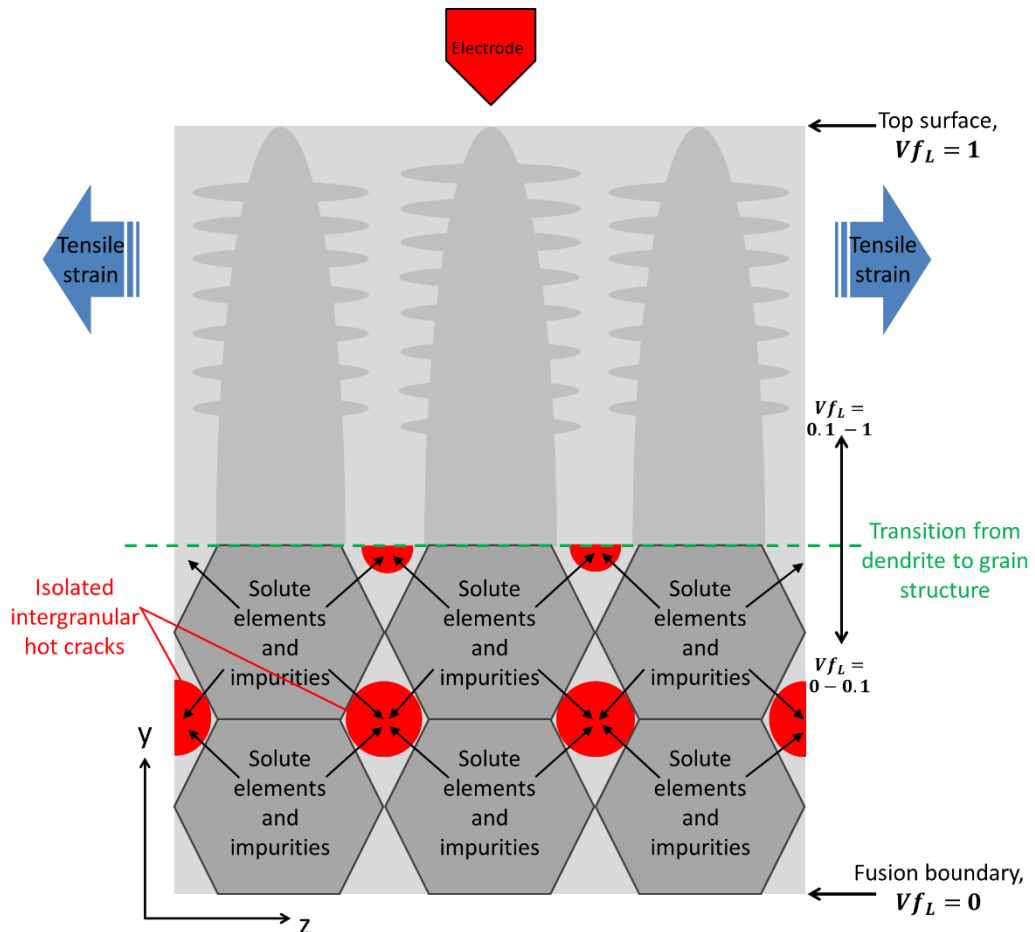


Figure 6-25: 2D schematic of inter-granular hot crack initiation, formed upon low melting point eutectic segregates after the transition from the dendrite to the grain structure. Coordinate system used in bottom left of the figure is defined in Figure 6-26.

The cavities initially form sub-surface in the weld centre, as illustrated in Figure 6-26(a) by the red globules and evidenced in Figure 6-11 and Figure 6-21. Similarly, FE models by project partners predict the peak volumetric strain to be localised sub-surface in the weld centre during loading. Shortly after, further hot cracks begin to form sub-surface around the circumference of the weld pool as illustrated in Figure 6-26(b) and evidenced in Figure 6-21.

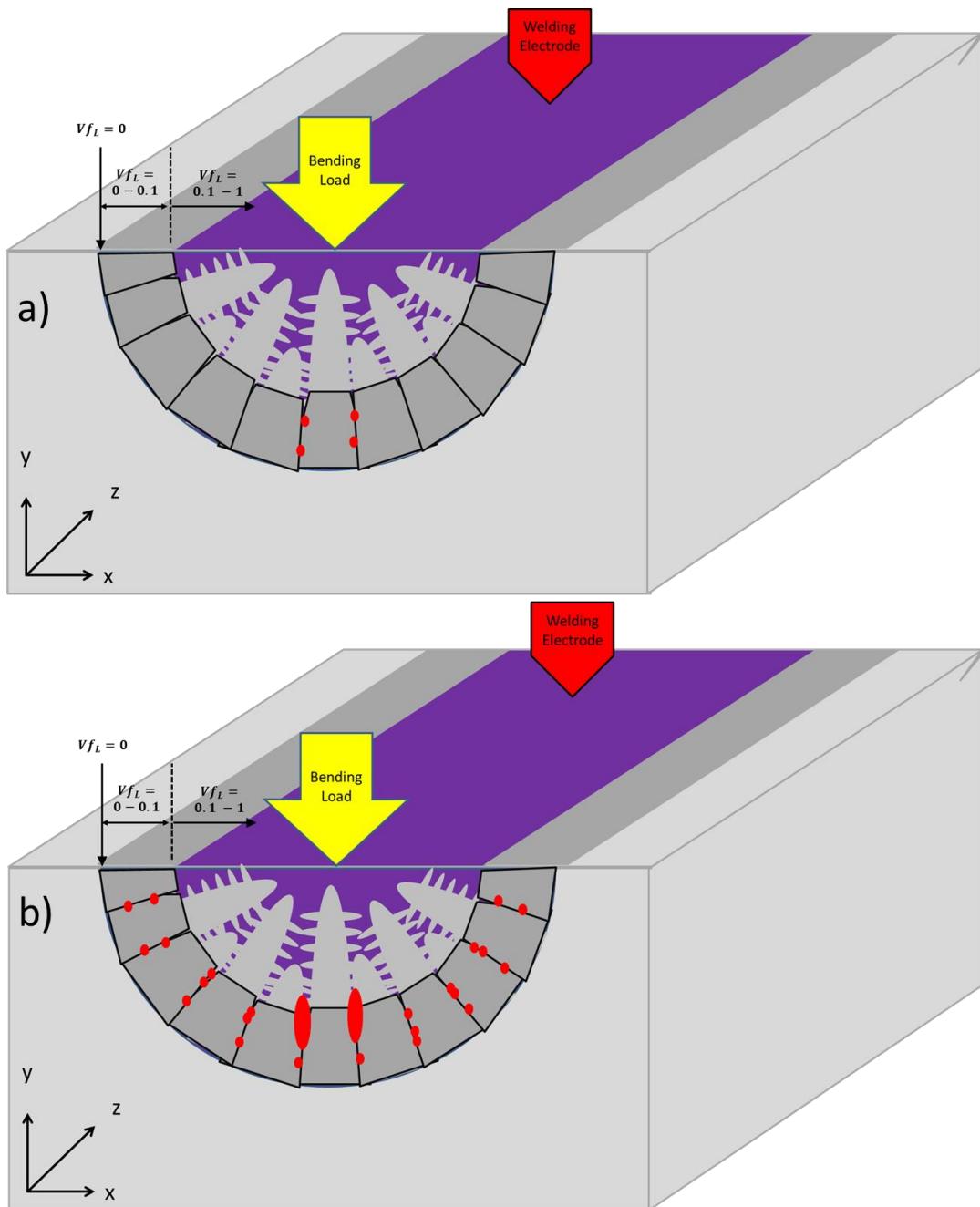


Figure 6-26: 3D schematic of hot crack initiation in respect to weld pool. The red globules depict hot cracks initiated in the solidifying weld.

Stage 2: Coalescence of hot cracks

In the Varcstraint test, the load is applied along the length of the weld, as illustrated in Figure 6-26. As the loading increases, the hot cracks then coalesce, predominantly in the “y” direction through the fracture of network separating bridges. Sometimes the hot cracks remain isolated and sometimes they coalesce with each other but not the bulk crack, as evidenced in Figure 6-22. Eventually, it is proposed that the coalescence of the hot cracks propagates through the grain structure to the solidifying dendritic structure, as described in Figure 6-27.

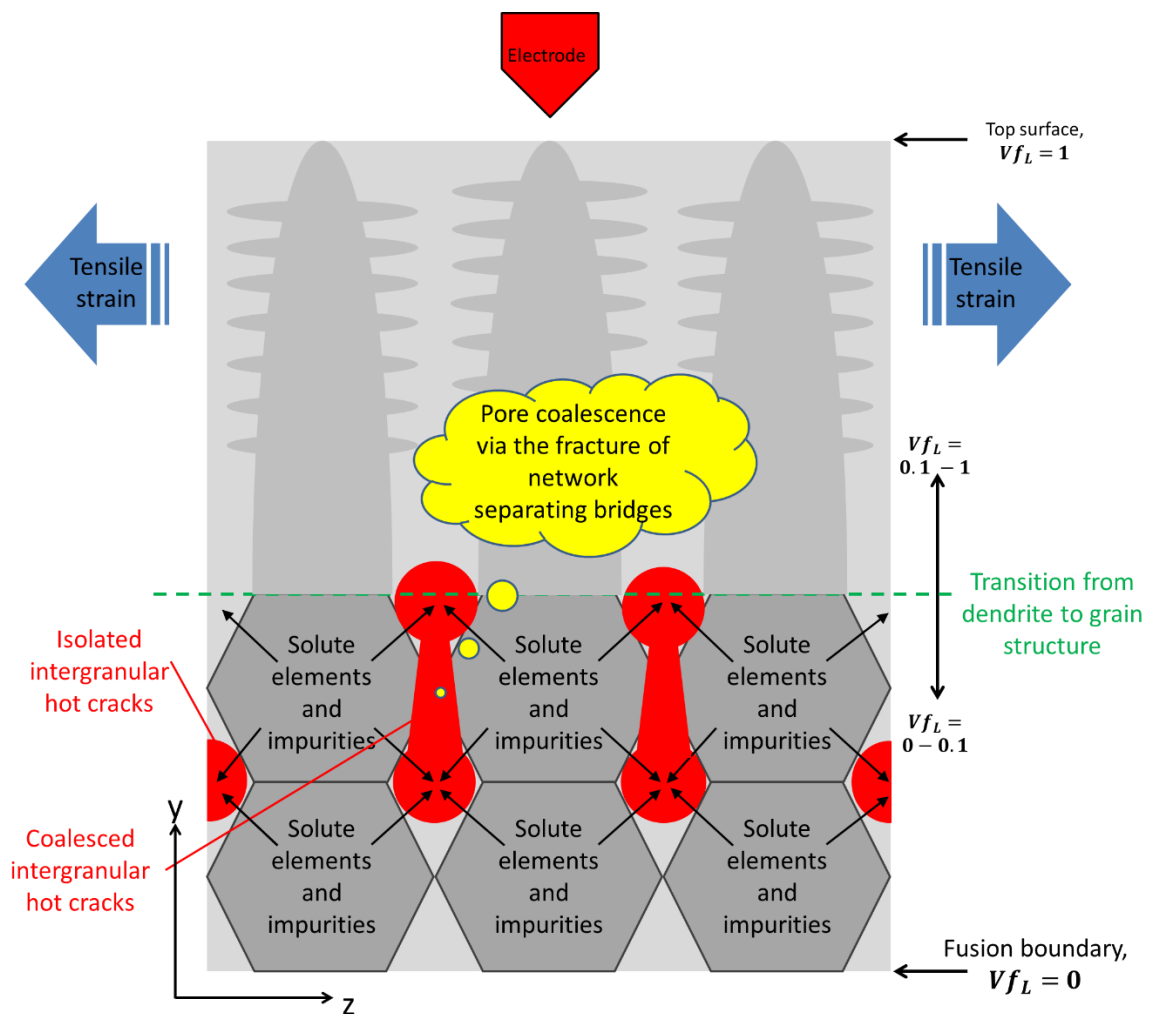


Figure 6-27: 2D schematic illustration of the hot crack coalescence mechanism. Sometimes the hot cracks remain isolated and sometimes they coalesce with each other but not the bulk crack. Eventually the coalescence of the hot cracks propagates through the grain structure to the solidifying dendritic structure.

Stage 3: Hot tearing (bulk propagation mechanism)

Once the coalescence of the inter-granular hot cracks has propagated through to the solidifying dendrite structure, hot tearing begins. At this stage, the volume fraction of liquid is higher and inter-dendritic fracture is observed from the separation of primary dendrite arms as a result of tensile deformation as described in Figure 6-28 and evidenced in Figure 6-24. As the propagation is linked to the solidifying dendrites, the propagation path is related to that of the growing dendrites in terms of direction (towards the heat source) and velocity ($\sim 2.2\text{-}2.8$ mm/s), as illustrated in Figure 6-29 and evidenced in Figure 6-11. However, as the load is applied along the length of the weld (z-axis), the tearing of the dendrites is also induced parallel to the x-axis, resulting in the somewhat angular cracking path towards the heat source as illustrated in Figure 6-29 and evidenced in Figure 6-9.

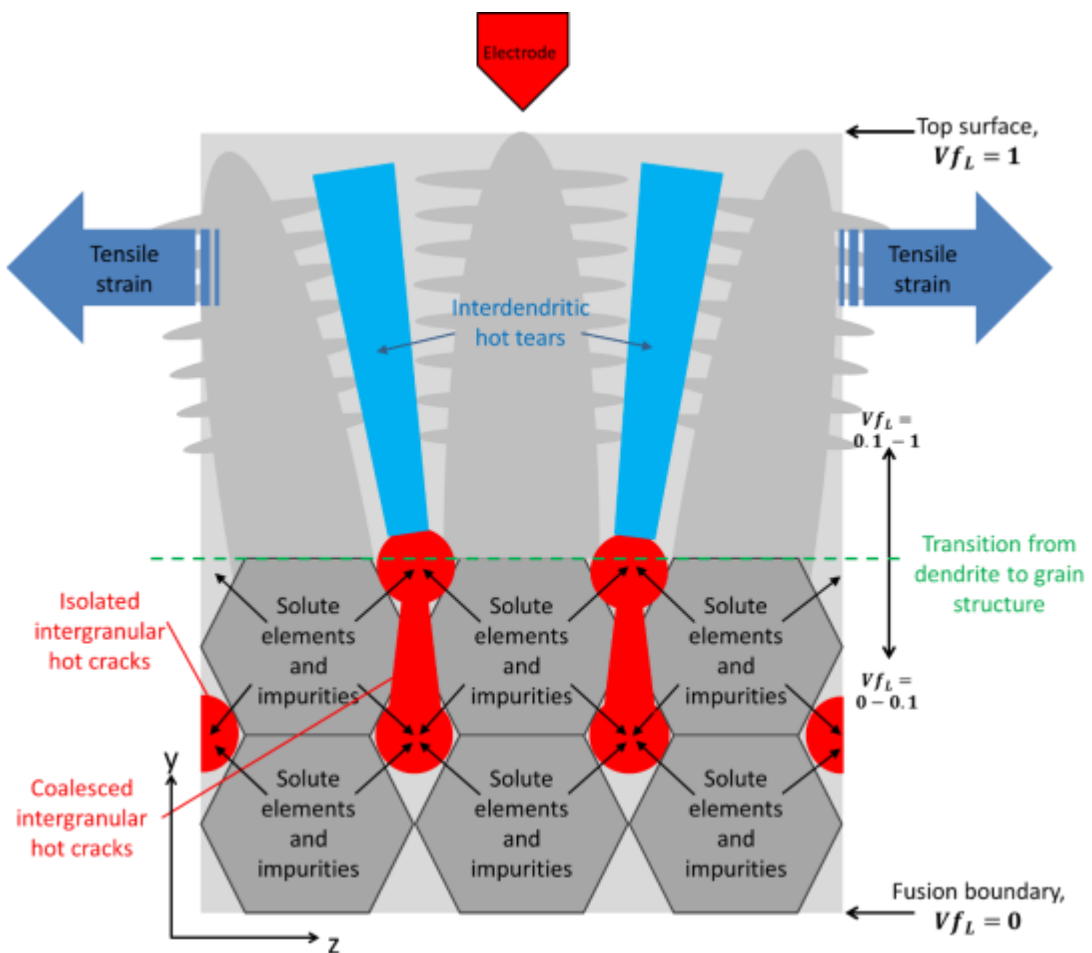


Figure 6-28: 2D schematic of hot tears nucleated from hot cracks. Hot tears form from inter-granular hot cracks that coalesce and propagate into the solidifying dendrite structure.

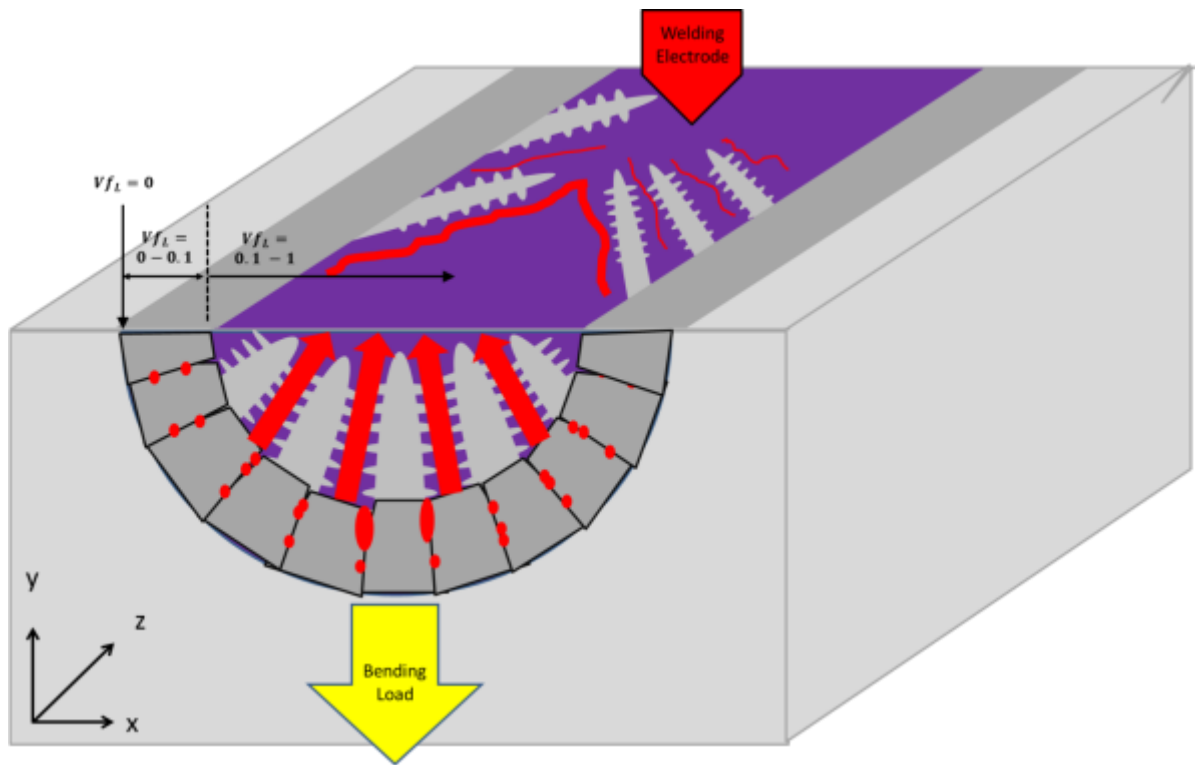


Figure 6-29:3D illustration of hot tearing propagation direction towards the heat source.

6.6. Discussion

Weld solidification cracking in steel has been successfully observed *in situ* using a high speed, high energy, synchrotron X-ray radiography approach. Analysis of the *in situ* radiography sequence revealed the solidification cracking initiates in the weld sub-surface trailing the welding electrode. Cavities are then observed in ex-situ 3D tomographic reconstructions of the cracking network, exclusive to the region of solidification crack initiation observed through *in situ* radiography. The process of void formation leading to solidification cracking is complex and poorly understood. Farup *et al.* [23] tried to identify the underlying mechanisms of solidification cracking and observed three different mechanisms for solidification crack nucleation: (1) directly as elongated pores or tears, (2) on pores caused by solidification shrinkage, or (3) as round pores nucleated in the liquid constituting a healed hot tear. Thus, it is clear that in the early stages, solidification cracking is controlled by the formation and growth of internal voids. In another study, Fredriksson *et al.* [17] presented a thermodynamic description of solidification crack nucleation. In this work, it was proposed that solidification crack nucleation is enhanced by the supersaturation of vacancies, since these vacancies will cluster to form voids at grain boundaries. After nucleation, solidification crack growth would occur by a combination of vacancy diffusion and also by the decrease in free energy when stored elastic energy from thermal and mechanical stress is released as crack growth. Void nucleation in semisolid metals has also been investigated. Piwonka proposed that dissolved gases aid in void nucleation [306]. Campbell [39] has shown that the cavitation pressure required to form voids is large in comparison to the expected shrinkage pressure drop during solidification. Instead, it was proposed that voids form via separation of the solid-liquid interface and at entrained oxides or other heterogeneous nuclei. Hirth *et al.* [307] proposed a thermodynamic analysis to describe the rate of void nucleation due to cavitation, boiling, and degasification processes. However, in all these cases, the initial size of these nucleating voids was not discussed. Nor was any relationship to semisolid microstructure or stress state presented. Both of these features are important relationships for understanding the underlying mechanisms of solidification crack nucleation.

In this study, a local temperature of 1433 °C is extrapolated from the temperature profile within the weld for the temperature at which the first solidification cracks form. Based on thermodynamic analysis, the damage at this temperature is predicted as inter-granular hot cracking as the metal is in the final stages of solidification when the volume fraction of liquid is <0.1. *Ex situ* tomography reveals the damage initiating hot cracks are between 5-40 µm in size. Sometimes they are isolated, sometimes they coalesce with each other but not the bulk crack and sometimes they coalesce with each other and the bulk crack. Microscopic analysis of fracture surfaces on corresponding fracture samples confirms that the damage at ~1430 °C is indeed brittle inter-granular hot cracking. Hot cracks initiate on liquid films formed from the segregation of solute elements at grain boundaries during the final stages of solidification. Microscopic analysis on the fracture surface attributes the formation of the hot cracks to the segregation of type III MnS and also solute (Si predominantly) enriched globular segregates. Microscopic analysis of the bulk fracture surface reveals an inter-dendritic propagation mechanism characteristic of hot tearing at later stages of solidification cracking.

So, evidence has been provided to explain the mechanisms for initiation (hot cracking) and propagation (hot tearing) at later stages of damage. What is still unclear and lacking in experimental evidence is the mechanism for the transformation from inter-granular hot cracks to inter-dendritic hot tearing. I.e. the coalescence of inter-granular hot cracks into the solidifying dendrite structure and transformation to inter-dendritic hot tears.

It is hypothesised that the speed of hot crack coalescence (through the fracture of network bridges in the solid skeleton) exceeds the speed of solidification and eventually (quite quickly in fact) the coalescence of the inter-granular hot cracks propagates through the grain and into the dendritic structure at which stage inter-dendritic hot tearing becomes the dominant propagation mechanism.

The results presented from the novel X-ray imaging approach will now be up-scaled to guide industrial scale weldability tests on HSLA linepipe steel.

7. Industrial application

7.1. Introduction

Guided by the results presented in Chapter 6, experimental methods are then scaled-up to assess industrial scale weldability tests on HSLA steel used for oil and gas transportation applications. Transvarestraint tests are carried out at an industrial scale using a novel weldability susceptibility testing machine at Tata Steel. The test is numerically modelled by project partners to understand the temperature and volumetric strain distribution in the sample during testing. The solidification cracking mechanisms are then identified in the alloy from comprehensive fractography studies.

7.2. Materials

For industrial scale weldability tests two grades of material were selected. Firstly, a non-production – non-alloyed steel was produced for use as a reference within the study. The second material was a HSLA API-5L grade X65 steel. This grade is widely used as the main pipeline material for transporting oil and gas in harsh deep sea environments. The chemistries of the materials are highlighted in Table 7-1. All sample dimensions were 130 mm x 300 mm x 12.5 mm (L x W x H).

	C	Si	Mn	P	S	Cr	Mo	Ni
X65	0.07	0.36	1.47	0.01	0.001	0.019	0.001	0.019
Model Alloy	0.145	0.014	1.02	0.001	0.0005	0.005	0.005	0.005
	Cu	Al	N	Nb	Ti	V	O	Ceq
X65	0.014	0.035	0.006	0.033	0.003	0.069	--	0.1644
Model Alloy	0.005	0.005	0.001	0.001	0.0001	0.001	0.0009	0.1975

Table 7-1: Chemical composition of the alloys used for industrial scale weldability tests.

7.3. Industrial scale Transvarestraint weldability test

7.3.1. Test rig setup

Figure 7-1 shows the Transvarestraint weldability test rig that was used for industrial scale weldability testing. The test rig was designed and built by Tata Steel. The rig essentially consists of a steel base frame connected to a steel top frame. The connection between the upper and lower frame is made by a hydraulic loading cell. The equipment is controlled by a standalone PC with custom built control software. The rig has integrated strain (strain gauge) and temperature (thermocouple) recording capabilities. The exact bending force applied is unknown, but is easily capable of bending steel plates 1” thick. The testing method will be discussed in more detail in section 7.3.2.

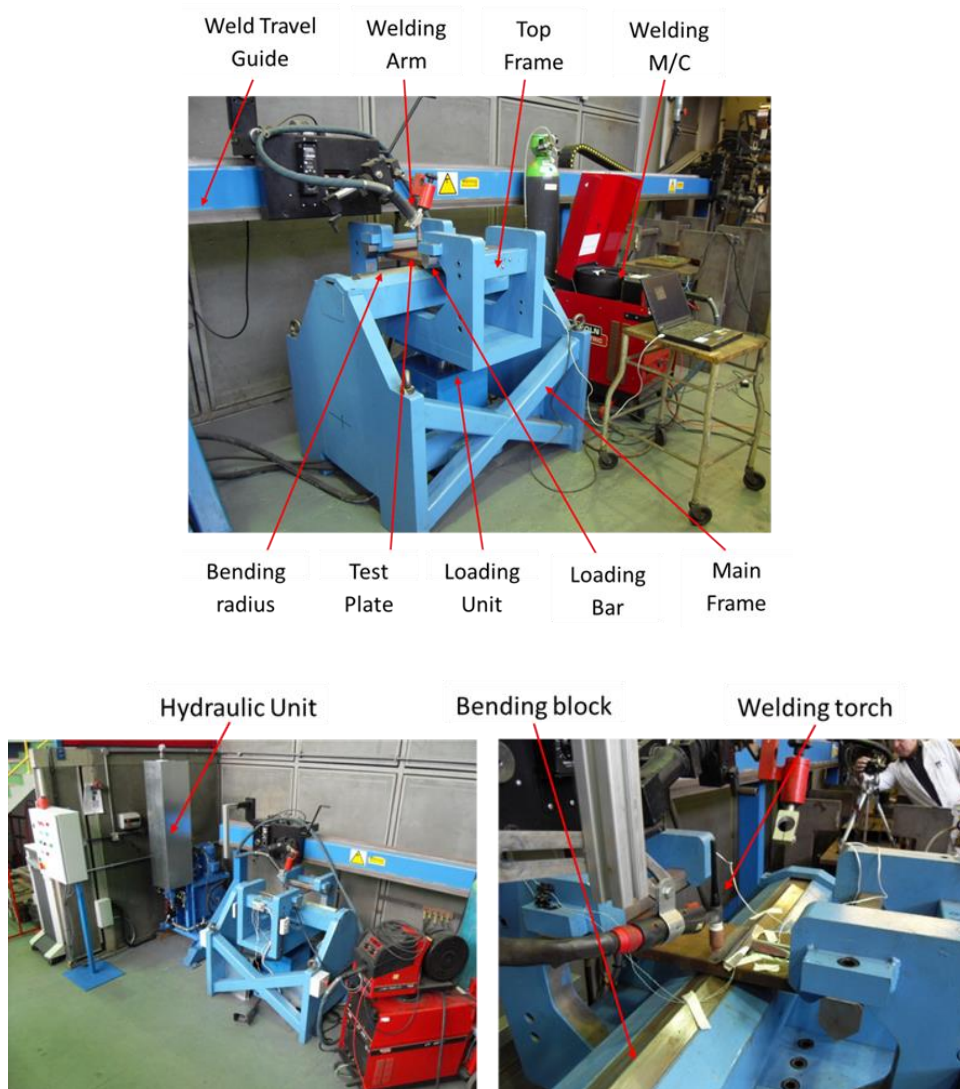


Figure 7-1: Transvarestraint weldability test rig.

7.3.2. Transvarestraint weldability test procedure

An autogenous bead-on-plate tungsten inert gas weld was laid centrally on the surface of the test plates. A summary of the test parameters is defined in Table 7-2. The plates were bent at high (6%) augmented strains in order to achieve cracking in the saturated regime. The strain was controlled using $\varepsilon = t/(2R)$ where, t is the material thickness (12.5 mm) and R is the radius of deformation. The bending stroke was initiated during welding (Point B in Figure 7-2). The welding arc and traverse were extinguished once the bending stroke was complete (Point C). Fine wired tungsten-rhenium Type C thermocouples were used to measure weld pool temperature. The thermocouples were located in holes drilled underneath the plates. The holes were drilled to coincide with the centre of the weld bead to a depth that left 1.5 mm of material to shield the thermocouple from the intense arc heat during welding. The 1.5 mm of material and thermocouple were then engulfed as the welding arc passed overhead.

Weld type	Polarity	Weld Velocity	Amps	Volts	Arc Energy	Weld Length	Bending Stroke	Bending Speed
TIG	DC+ve	3.5 mm/s	220 A	12 V	0.76 KJ/mm	110 mm	80 mm	80 mm/s

Table 7-2: Summary of welding and Transvarestraint test parameters.

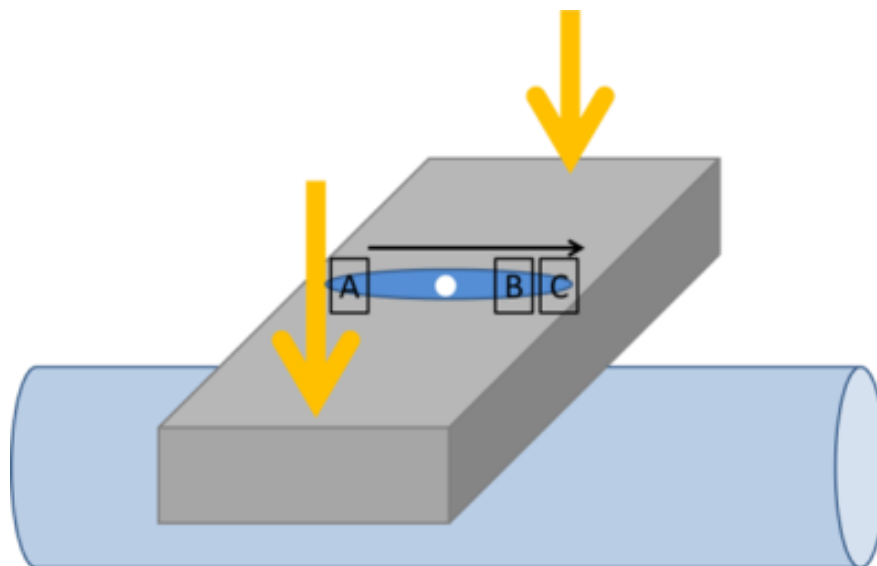


Figure 7-2: Schematic illustration of welding and bending points during Transvarestraint test.

7.4. Results

7.4.1. Material solidification characteristics

Using input chemistries from Table 7-1, phase equilibria in the solidification temperature range for the experimental alloys is simulated using the CALPHAD method from Thermo-Calc's TCFE7 database. According to the results, the model alloy and API-5L grade X65 alloys solidify similarly with the primary formation of BCC δ -ferrite, then proceeding in the three-phase region ($L + \delta + \gamma$) with the formation of the FCC γ -phase. The STR under equilibrium conditions for the API-5L grade X65 sample is 40°C, slightly wider than the STR of only 31°C in the model alloy. A summary of the Thermo-Calc simulation results are depicted in Table 7-3.

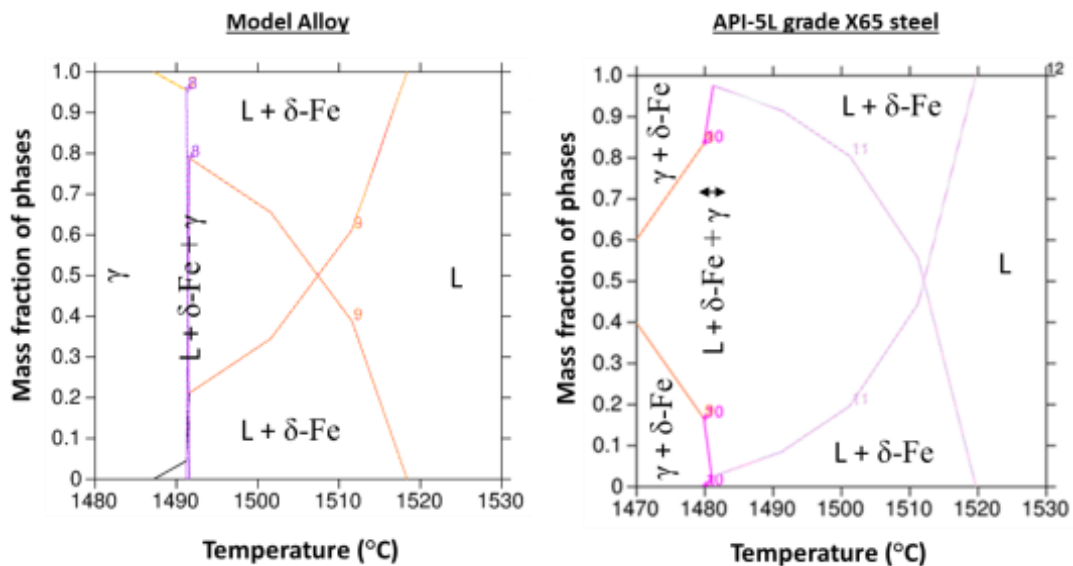


Figure 7-3: Results of thermodynamic analysis displaying the mass-fraction of equilibrium phases during solidification of the experimental alloys.

Alloy	Equilibrium STR	Peritectic Reaction	Primary Solidification Phase
Model	31 °C	Yes	δ -ferrite (b.c.c.)
X65	40 °C	Yes	δ -ferrite (b.c.c.)

Table 7-3: Summary of the thermodynamic parameters predicted in Thermo-Calc simulations that affect weld solidification cracking susceptibility.

7.4.2. Quantification of weld geometry and solidification cracking

Analysis of the model alloy welds after Transvarestraint testing revealed no visible solidification cracking defects. The alloy appears to be highly resistant to the defects. Conversely, in the X65, solidification cracks were visibly inherent to the weld.

An image of the fusion zone cracking resulting from the Transvarestraint tests upon the X65 alloy is presented in Figure 7-4(a). Closer examination of the cracking region circled in the figure under backscattered electron microscopy revealed a much large number of cracks, as depicted in Figure 7-4(b). Quantification of the cracking observed in the backscattered electron micrograph was carried out using imaging software with the results being summarised in Table 7-4.

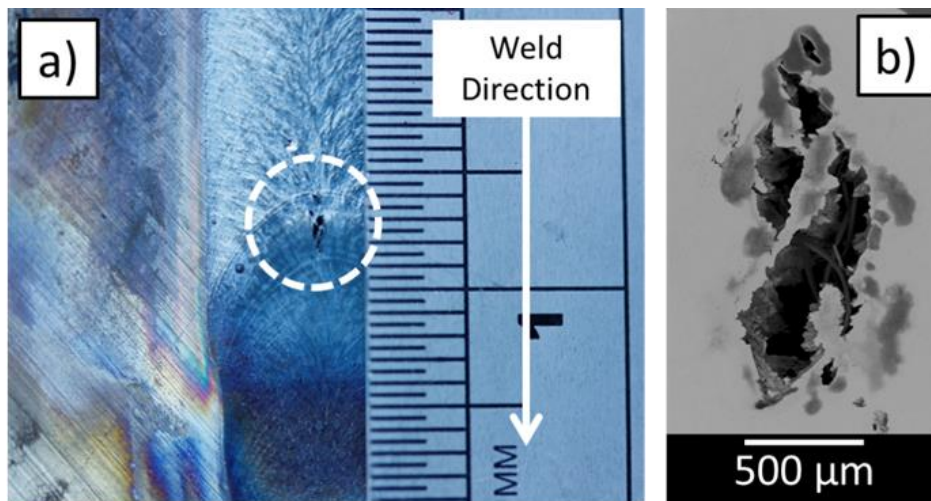


Figure 7-4: Weld solidification cracking observed in: a) initial observations on the X65 weld bead; b) backscattered electron micrograph of metallographically prepared X65 specimen.

	X65	Model
Number of cracks	22	0
TCL (mm)	3.07	0.00
MCL (mm)	1.24	0.00
ACL (mm)	0.14	0.00

Table 7-4: Quantification of cracking observed in the weld bead after Transvarestraint testing.

Transverse cross-sectional macrographs of the weld joints (Figure 7-5) were taken from the weld centre and quantified in terms of weld width and depth with the results presented in Table 7-5.

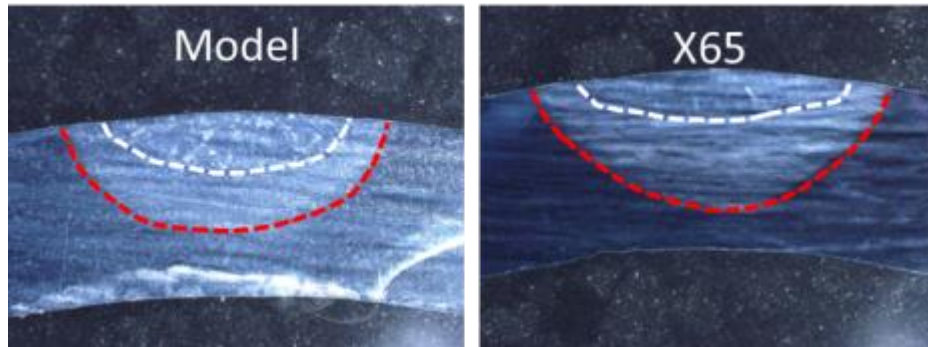


Figure 7-5: Transverse weld macrographs of weld geometries in test alloys showing, the fusion zone (area enclosed by the white broken line) and HAZ (area enclosed by the red broken line) shape and size.

	Model	X65
Width (mm)	8.2	8.9
Depth (mm)	1.9	1.6

Table 7-5: Measured weld geometries (width and depth) mid-weld on Transvarestraint test samples.

7.4.3. Identification of solidification crack initiation sites

Guided by the findings in chapter 6, the focus on identifying fracture nucleation sites is concentrated in the sub-surface fracture region trailing the weld electrode, close to the fusion boundary.

The cracked samples were opened out to reveal the solidification cracking fracture surface. The dark region encircled by the broken white line in Figure 7-6(a) represents the large centreline solidification crack in the X65 sample. The SEM image in Figure 7-6(b) displays the fracture surface highlighted by the broken yellow square in Figure 7-6(a) trailing the welding electrode. The specific region of interest in terms of possible fracture nucleation site is highlighted in Figure 7-6(b) by the broken yellow circle, trailing the welding electrode and around 1.8 mm sub-surface. Closer examination of the region in Figure 7-6(c) reveals the presence of several ductile microvoids. The microvoids appear within the solidification cracking region and are surrounded by smooth dendritic fracture surfaces. The smooth surfaces hint towards the presence of liquid at the time of fracture. Figure 7-6(d) displays detailed analysis of the microvoid encircled by the broken yellow circle in Figure 7-6(c). Within the microvoid, the presence of a void initiating Ti (C,N) precipitate is evident. It is also clear that the fracture surface in and around the microvoid is smooth and dendritic.

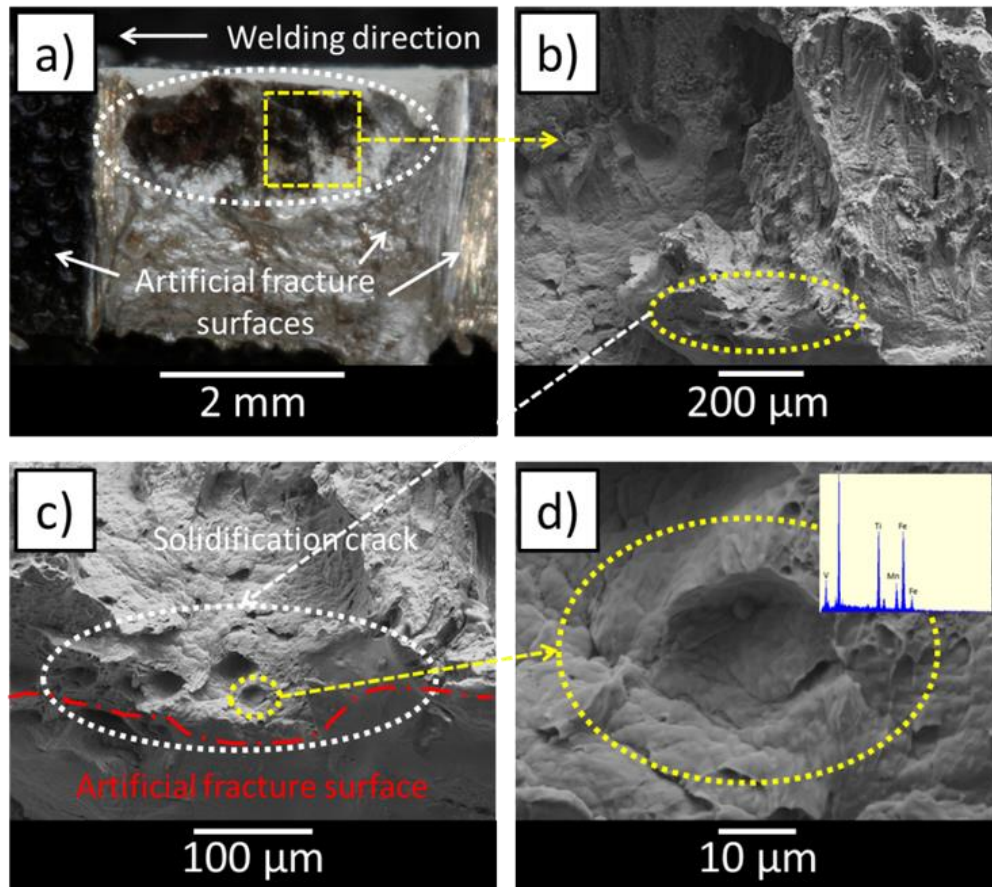


Figure 7-6: Fractography examination of solidification cracking in X65 steel, showing; a) macro image of full solidification crack interface (dark region encircled by broken white line), b) SEM image of fracture surface highlighted by the broken yellow square in Fig. a., c) SEM image of ductile microvoids at the base of the solidification crack around 1 mm sub-surface. The microvoids are located within the solidification cracking region and are surrounded by dendritic fracture morphologies, d) SEM image of microvoid detailed in Fig. c by broken yellow arrow, showing the presence of a void initiating second phase particle. The fracture surface in and around the microvoid appears to be smooth highlighting possible presence of liquid at failure.

7.4.4. Identification of solidification crack propagation mechanism

Figure 7-7(a) presents the bulk fracture surface observed on the X65 alloy. The fracture surface is almost entirely smooth and dendritic, although there is evidence of some ductile fracture of coherent bridges within the fracture zone. There are well defined primary dendrite arms that are both interlocked and separated. The fracture surfaces are covered with eutectics. Figure 7-7(b) details such eutectics at higher magnification in the X65 alloy. EDX line mapping analysis revealed that the eutectics are enriched in solute elements (C, N, Al, Si, P, S, and Cu) and strengthening (solution and precipitation) elements (Ti, Mo, Nb). From the results, it is proposed that the propagation mechanism for solidification cracking is inter-dendritic fracture through-liquid-film by grain separation. The films manifest as a result of segregation of solute elements (C, N, Al, Si, and Cu) and impurities (S and P) forming eutectics at grain boundaries in the terminal stages of solidification.

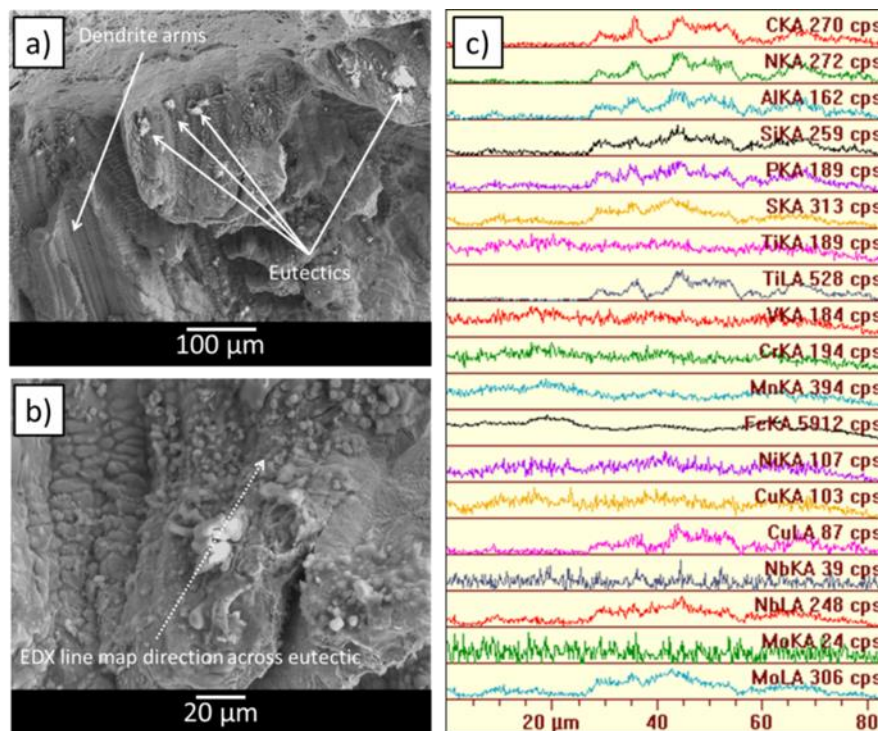


Figure 7-7: Results of SEM and EDX analysis depicting the through-liquid-film, inter-granular, fracture propagation mechanism in X65 alloy, showing; a) SEM image of upper fracture surfaces displaying both interlinked and separated primary dendrite arms. The fracture surface is covered in eutectics. b) detailed SEM image of a eutectic with direction of EDX line scan transposed, c) results of EDX line mapping across the eutectic presented in Fig. b, showing enrichment in solute elements (C, N, Al, Si, P, S, and Cu) as well as strengthening (solution and precipitation) elements (Ti, Mo, Nb).

7.5. Mechanisms proposed for solidification cracking during welding of HSLA subsea linepipe steel

Stage 1: Pre-cursors to cracking:

1) Base metal microstructure

The microstructure of the subsea linepipe was extensively characterised in Chapter 5. Importantly, the presence of Ti (C,N) particles were characterised within the base metals fine grained microstructure. To improve HAZ toughness, Ti is commonly added to HSLA linepipe steel to enhance weldability. The enhanced weldability is due to the Ti forming thermally stable Ti (C,N) particles which at a suitable size will suppress austenite grain coarsening in the weld HAZ [125, 146]. The Ti (C,N) are illustrated in Figure 7-8 by the black circles and the fine grain structure is illustrated by the grey hexagons.

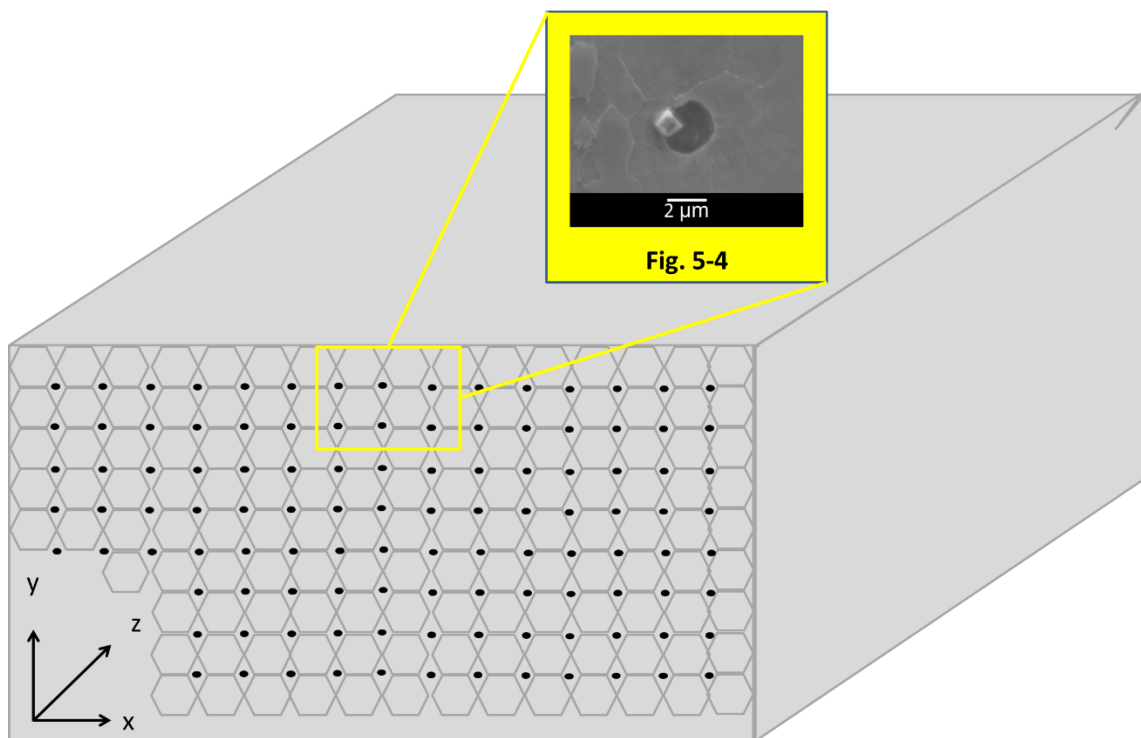


Figure 7-8: 3D schematic illustration of base metal microstructure prior to welding, the black circles represent Ti (C,N) particles inherent to the fine grained microstructure depicted by the grey hexagons.

2) Weld pool formation, grain growth in the HAZ

As the welding arc is initiated, the base metal is melted to form a molten weld pool (purple semi-circle in Figure 7-9). The weld pool fluid flow and geometrical evolution have been extensively characterised in chapter 4. The Ti (C,N) close to the heat source dissolve into the molten steel weld pool. A thermal gradient exists away from the heat source. The region where temperature lies between the solidus ($\sim 1450\text{ }^{\circ}\text{C}$) and austenitic transformation ($\sim 730\text{ }^{\circ}\text{C}$) temperature is the HAZ. In the HAZ the temperature induced by welding isn't high enough to cause melting, but is significant enough to stimulate substantial solid state phase transformations. Most notably, precipitate growth (large black circles in Figure 7-9) which allows for grain growth (large green hexagons in Figure 7-9) by reduced Zener pinning efficiency.

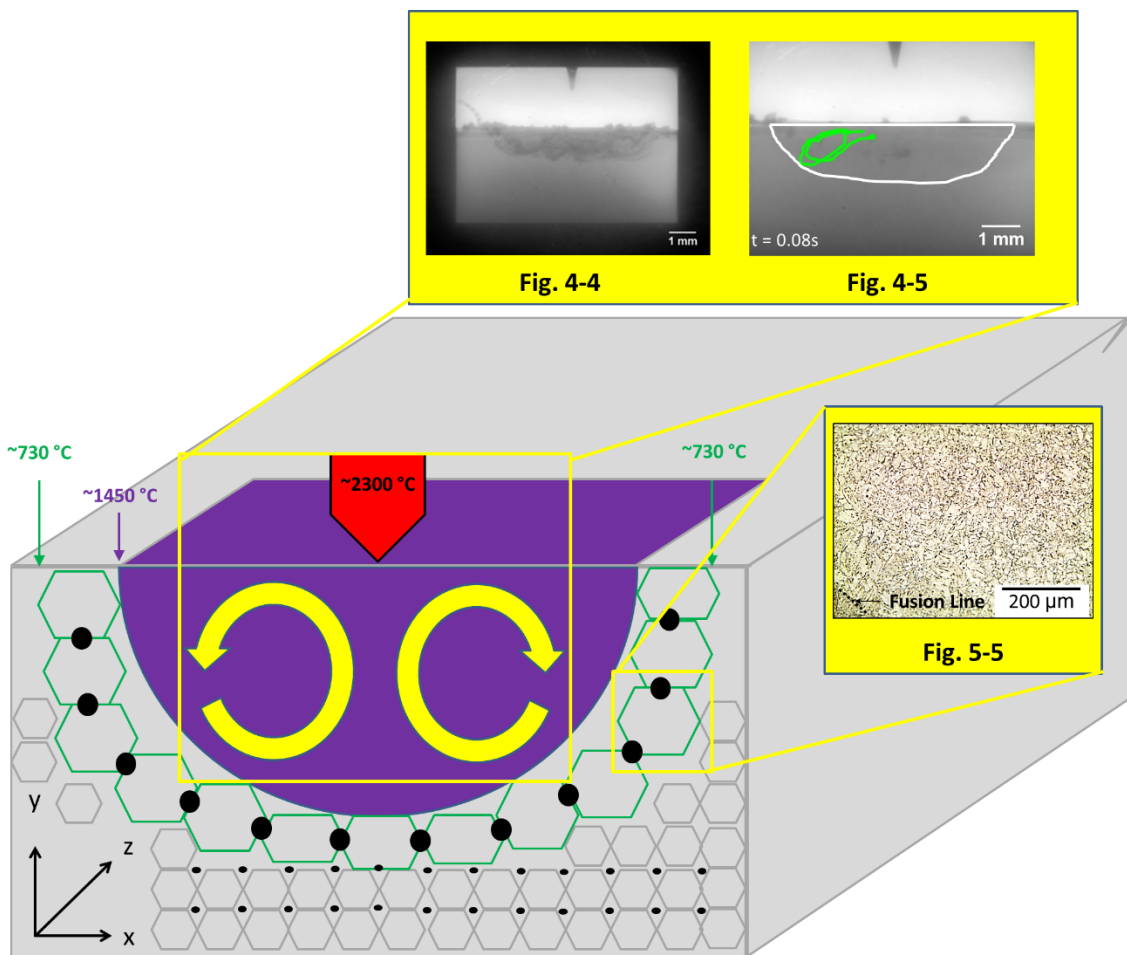


Figure 7-9: 3D schematic of weld pool formation and grain growth in the HAZ. The large black dots represent Ti (C,N) enlarged from thermal exposure during welding. The large green hexagons represent the HAZ grain growth region and the purple semi-circle depicts the molten weld pool.

Stage 2: Solidification and the precipitation of Ti (C,N):

As the welding electrode moves away and the temperature begins to cool, solidification begins. As the chemistry of the weld pool and base metal are identical, epitaxial growth occurs. Epitaxial growth describes the process by which the molten liquid solidifies and develops new grains directly from the solid in the underlying HAZ as illustrated in Figure 7-10.

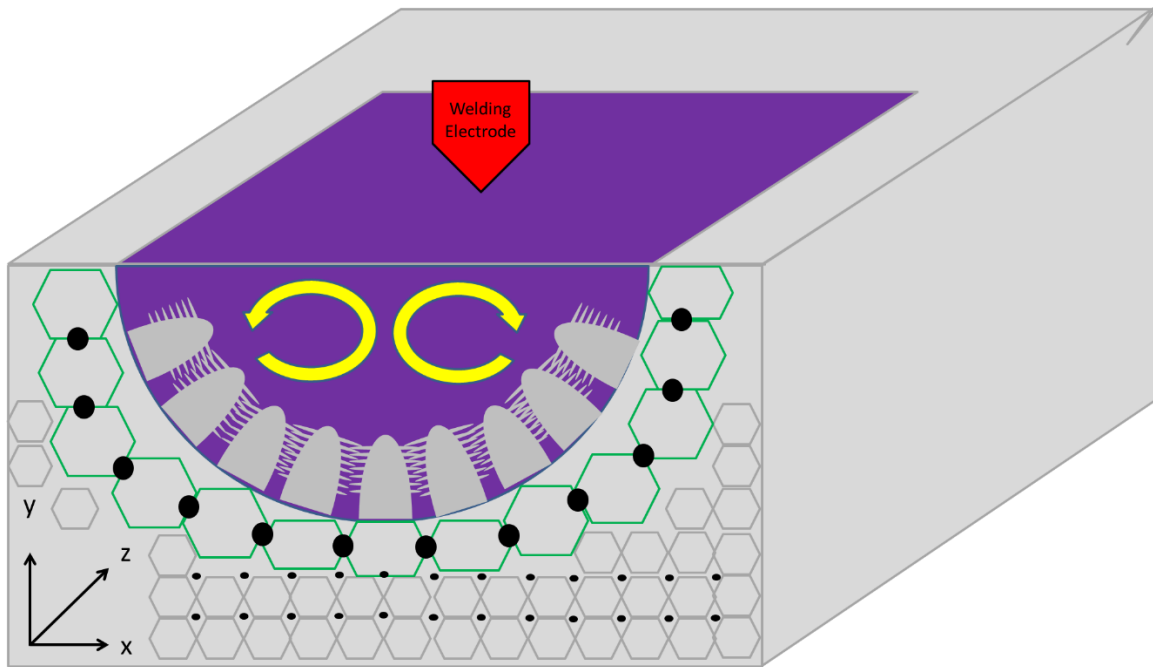


Figure 7-10: 3D schematic of solidification initiation. Coarse and columnar grains grow directly from the coarse HAZ grains.

The grains are anisotropic because they grow along the direction of heat flow. Those grains with their (100) directions parallel to the heat-flow direction grow fastest and stifle the growth of unsuitably oriented grains. This solidification path results in a columnar solidification structure depicted in Figure 7-11, with the width of the columns related to the size of the grains in the underlying base material. Eventually fluid flow is hampered and Ti (C,N) precipitates to trigger the coalescence of primary dendrite trunks as illustrated in Figure 7-12.

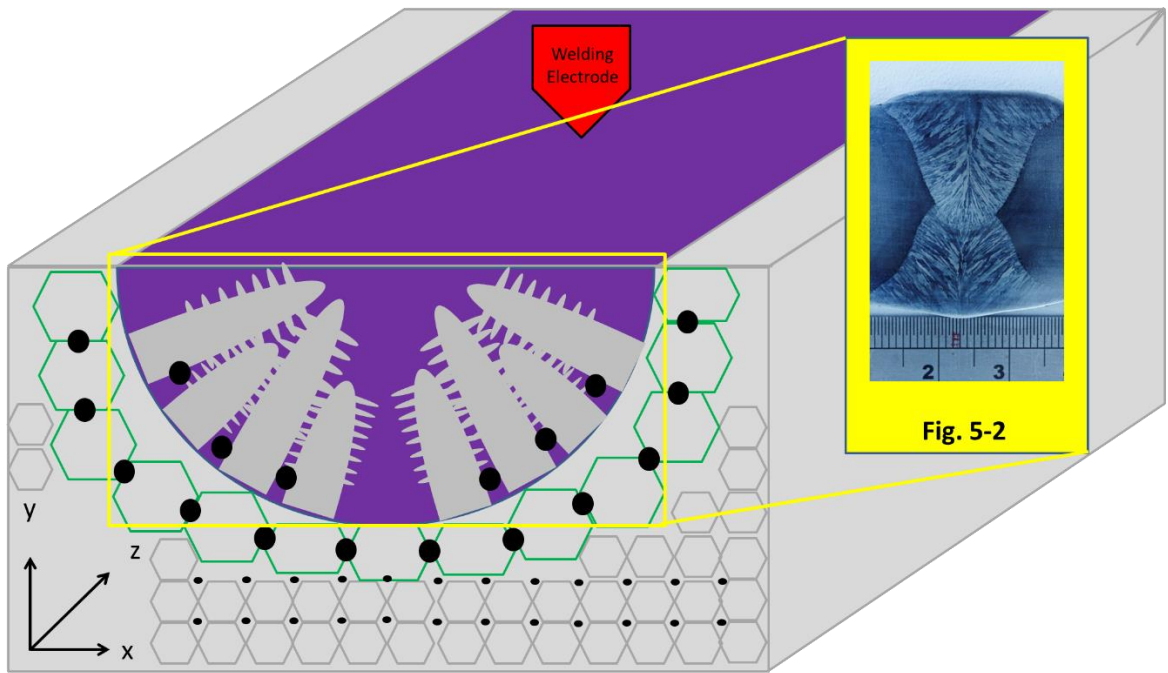


Figure 7-11: 3D schematic of competitive growth of columnar dendrites and precipitation of Ti (C,N) which triggers coalescence of primary dendrite trunks.

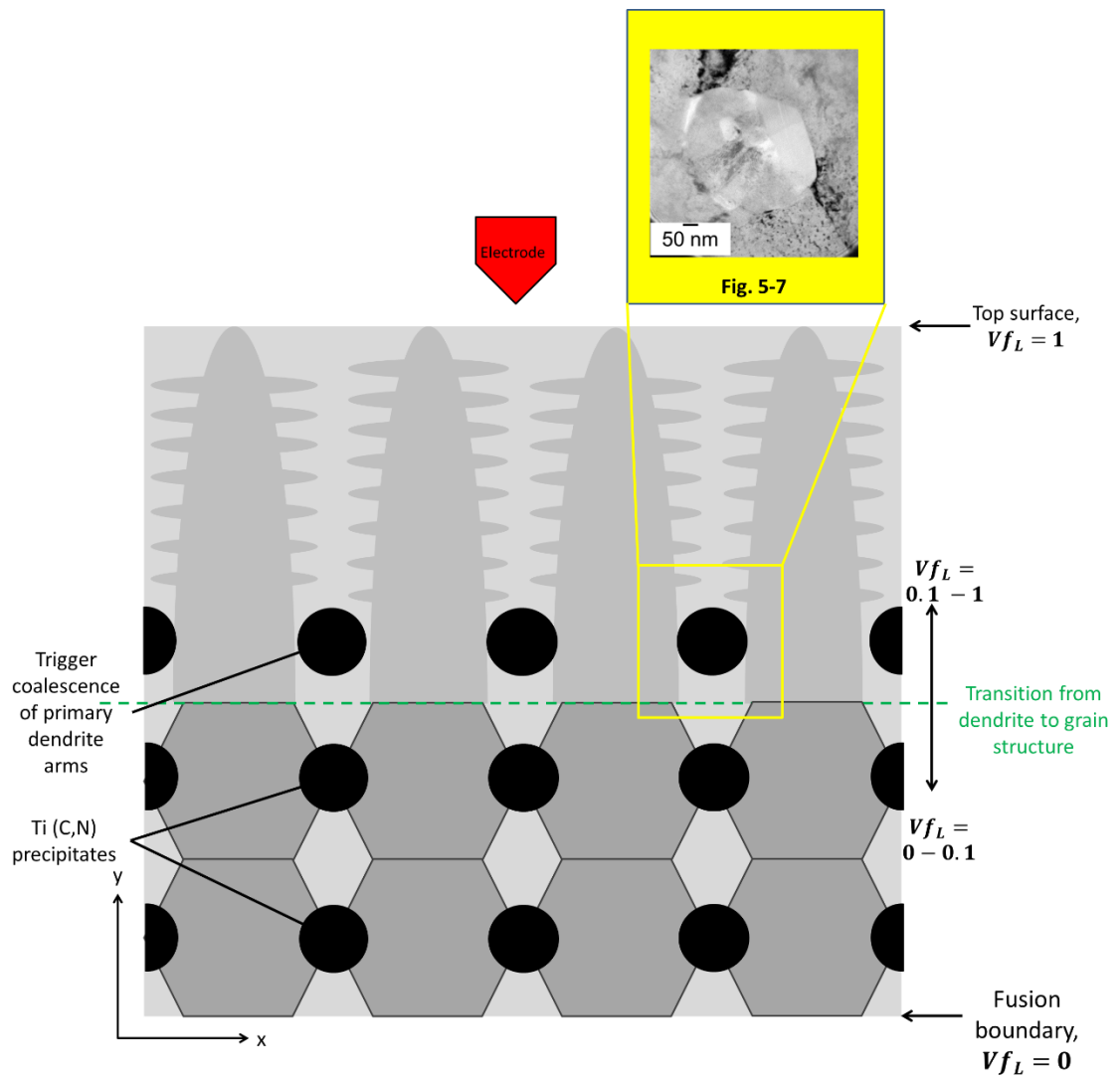


Figure 7-12:2D schematic of Ti (C,N) precipitation and dendrite coalescence.

Stage 3: Microvoid nucleation around Ti (C,N) precipitates:

Tensile strain is applied transverse to the weld, as illustrated in Figure 7-13, and ductile fracture is induced on the favourable site created by the Ti (C,N) precipitation, as depicted in Figure 7-14.

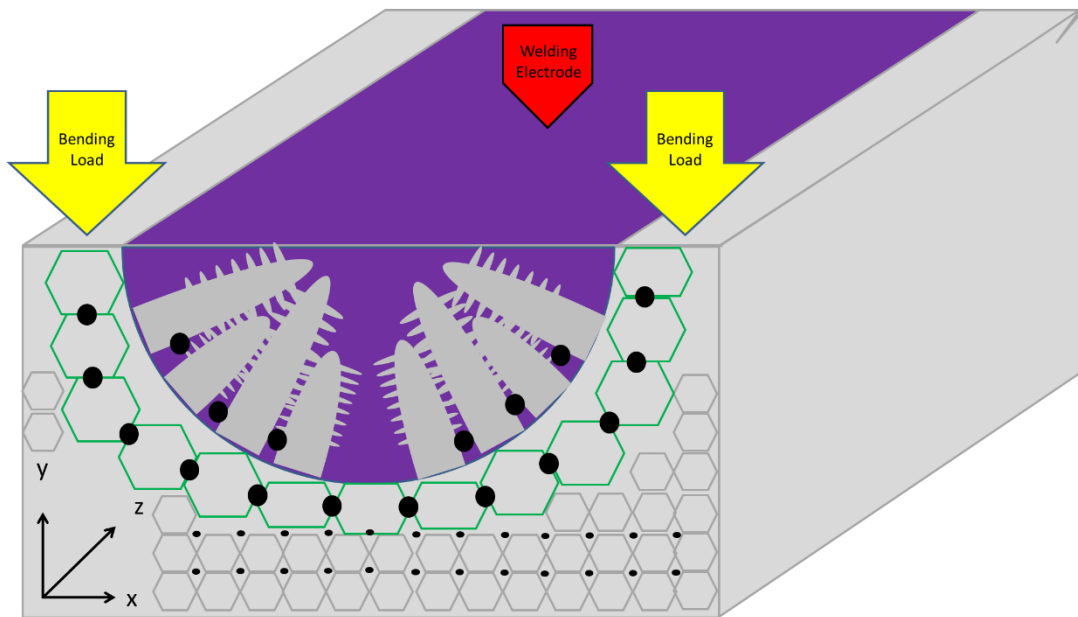


Figure 7-13: 3D schematic of transverse tensile strain application.

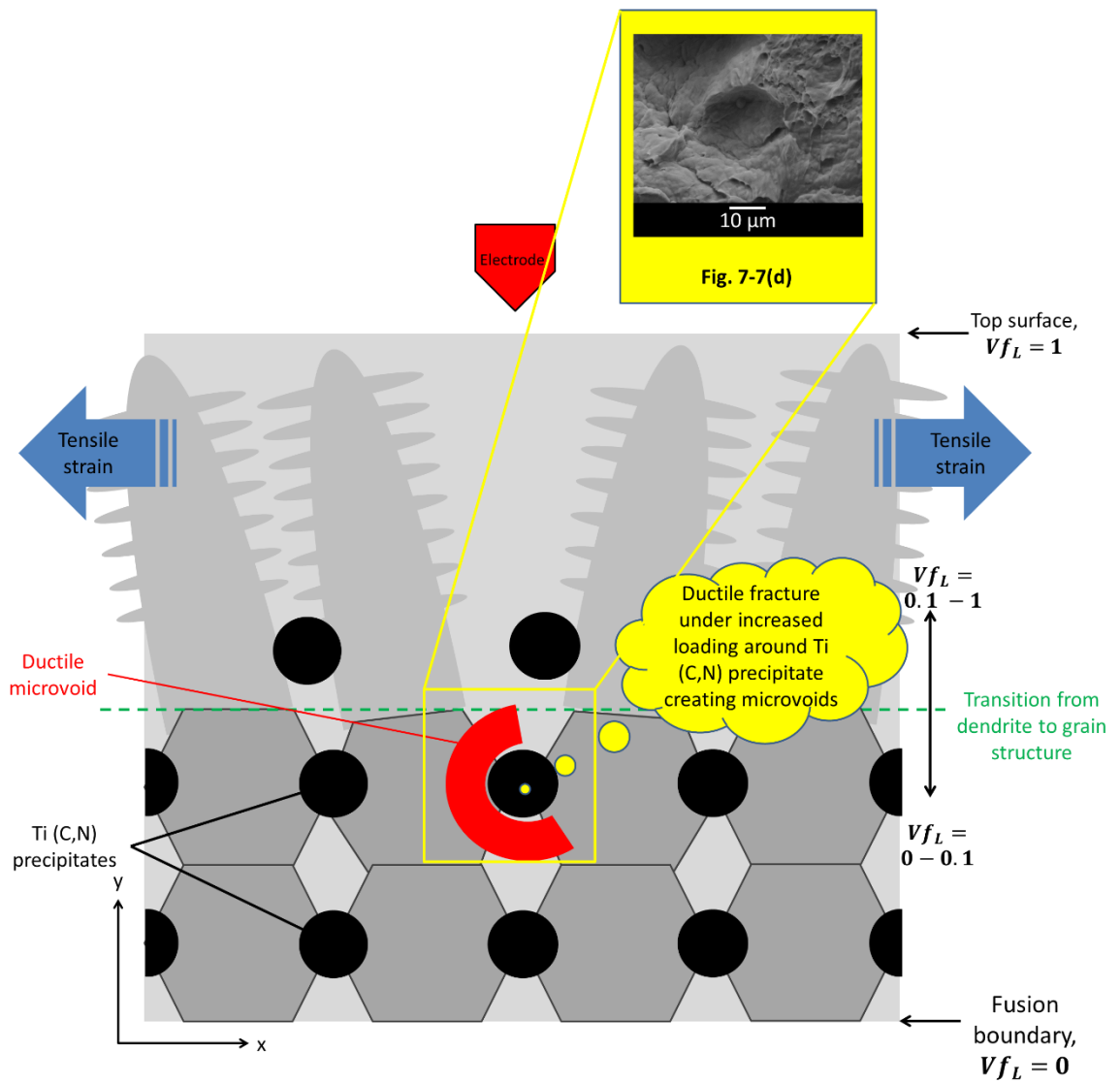


Figure 7-14: 2D schematic of microvoid nucleation mechanism.

Stage 4: Microvoid coalescence and propagation:

As the loading increases, the microvoids coalesce, predominantly in the y direction through the fracture of network separating bridges. Sometimes the microvoids remain isolated and sometimes they coalesce with each other but not the bulk crack. Eventually the coalescence of the microvoids propagates through the grain structure to the solidifying dendritic structure, as described in Figure 7-15.

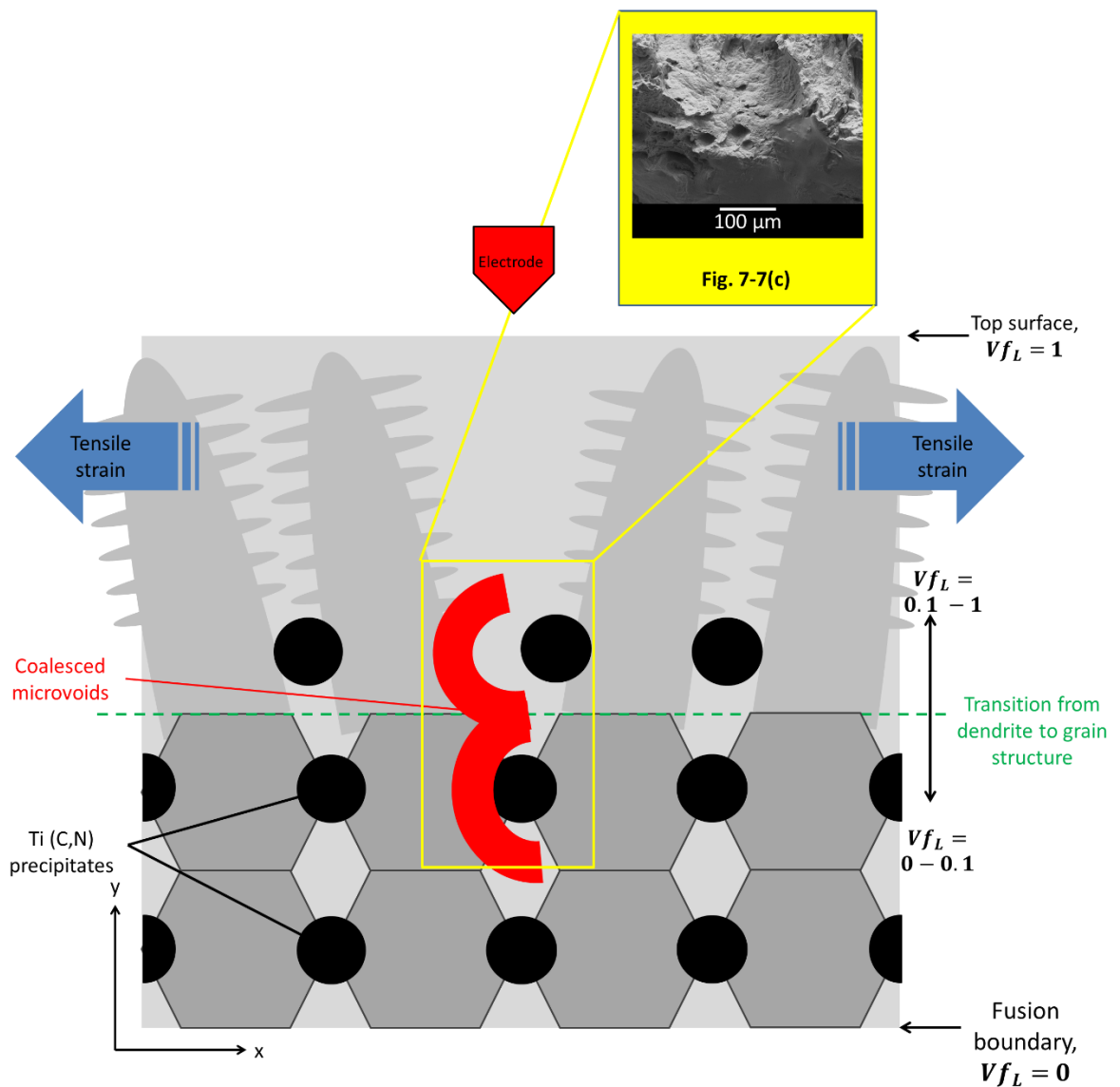


Figure 7-15: 2D schematic of microvoid coalescence mechanism.

Stage 5: Hot tearing:

Once the coalescence of the microvoids has propagated through to the solidifying dendrite structure, hot tearing begins. At this stage, the volume fraction of liquid is higher and inter-dendritic fracture is observed from the separation of primary dendrite arms as a result of tensile deformation as described in Figure 7-16. As the propagation is linked to the solidifying dendrites, the propagation path is related to that of the growing dendrites in terms of direction (towards the heat source) and velocity, as illustrated in Figure 7-17. However, as the load is applied transverse to the weld (x -axis), the tearing of the dendrites is also induced parallel to the z -axis, resulting in a centreline crack path towards the heat source.

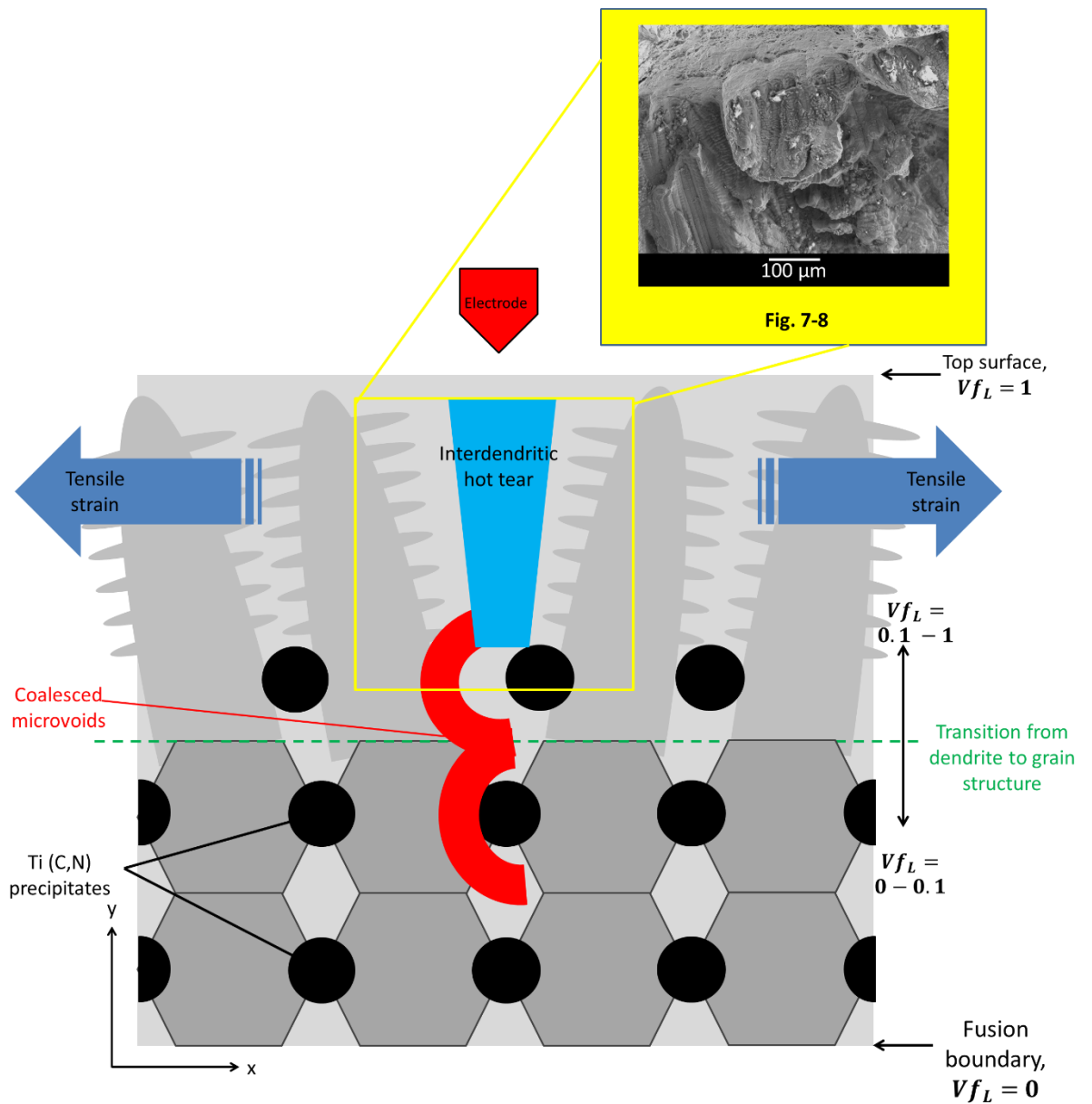


Figure 7-16: 2D schematic of hot tears nucleated from microvoids. Hot tears form from microvoids that coalesce and propagate into the solidifying dendrite structure.

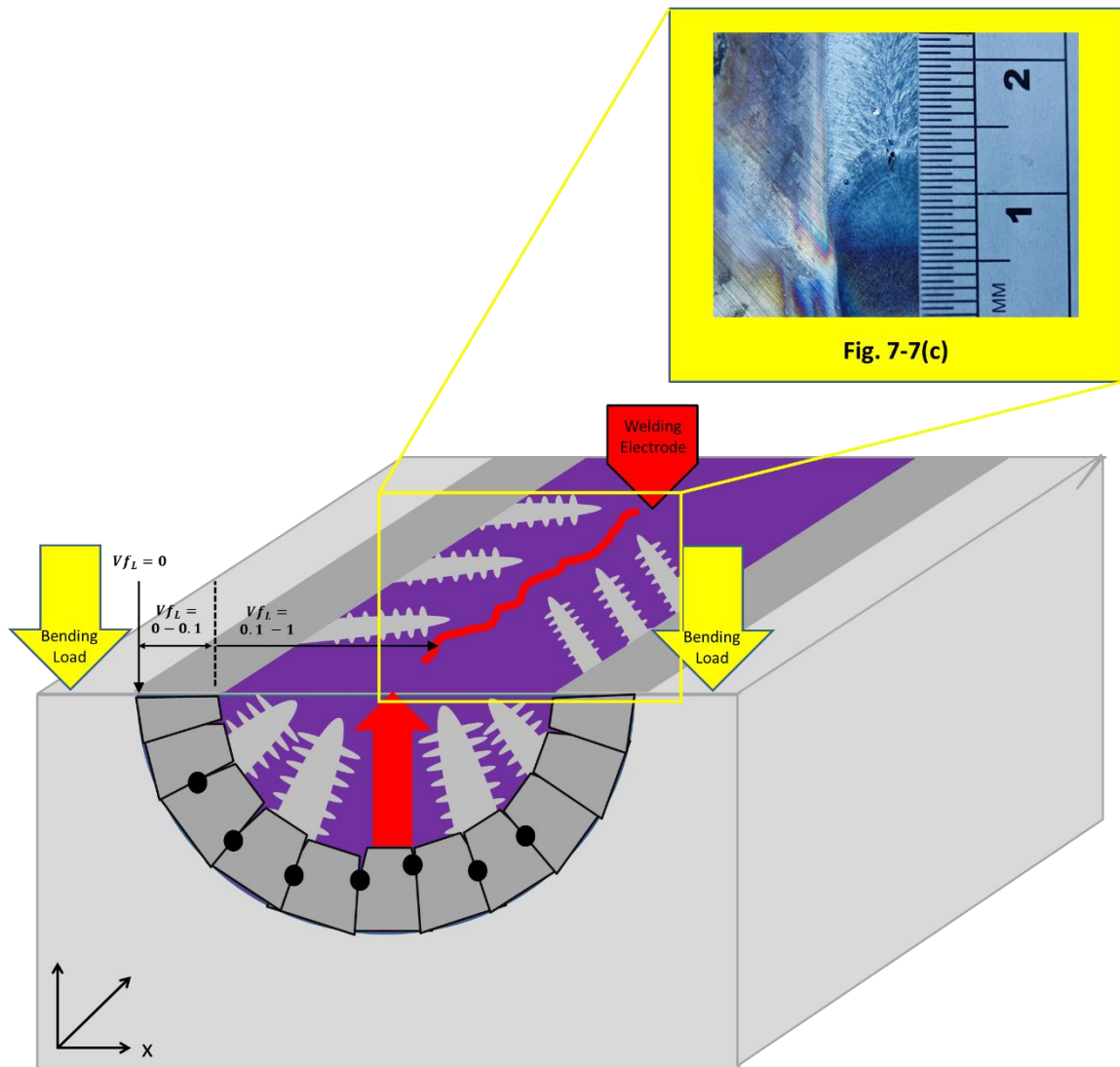


Figure 7-17: 3D illustration of hot tearing propagation direction towards the heat source.

7.6. Discussion

Guided by the information presented in Chapter 6, industrial-scale weldability tests on two steel alloys; non-alloyed steel and pipeline steel used for oil and gas transportation applications have been completed. The non-alloyed steel resisted solidification cracking during Transvarestraint weldability testing. Conversely, the same tests produced distinct solidification cracking in the steel used for oil and gas applications. This shows that the alloy used for oil and gas applications has some susceptibility to these welding defects when compared to the non-alloyed steel. The purpose of this discussion is to elucidate the direct factors and mechanisms which cause solidification cracking in the oil and gas transportation alloy.

In terms of solidification thermodynamics presented in Figure 7-3, it is hard to associate the thermodynamic properties to cracking susceptibility. I.e. The X65 and model alloys have identical solidification sequences, similar STR's and peritectic solidification reactions. However, the X65 alloy was subject to solidification cracking, whereas the model alloy was resistant. This somewhat disproves simple assumptions of cracking susceptibility being based solely upon the size of an alloys STR [20, 30, 217] and points towards a strong dependency on specific microstructural or chemistry related factors.

Guided by the results presented in chapter 6, fractography analysis on the solidification crack fracture surfaces has been focussed on the sub-surface region to identify the features nucleating solidification cracking defects in steel linepipe welds. Fractography analysis 1.8 mm sub-surface on the X65 alloy solidification crack fracture surface revealed the presence of Ti (C,N) precipitates. The precipitates have been characterised within the fusion zone in chapter 5. Notably, recent phase field studies on the continuous casting of HSLA steel [14] have found that TiN can precipitate during the latter stage of bulk solidification and trigger coalescence of dendrite trunks. As such, the precipitation of TiN was deemed favourable in improving solidification cracking resistance due to improved coherence of solidification structure. Conversely, in this study, analysis of Figure 7-6 hints towards the Ti (C,N) acting as nucleation sites for fracture. To explain this, the strain induced by the Vrestraint test needs to be considered. The strain induced by the Vrestraint test is significantly larger than that induced by only the solidification and shrinkage strains associated with continuous

casting. Therefore it is reasonable to conclude that Ti (C,N) particles close to the heat source during welding of the X65 base metal are heated to melting point and form part of the molten metal weld. As the bending load and solidification proceed, Ti (C,N) particles precipitate during solidification at high temperatures (around 1770 K [14]). The precipitates trigger coalescence of dendrite trunks and under further loading they provide favourable sites for high temperature ductile fracture within the semi-solid matrix. The remaining liquid is deposited on the surface of the newly formed cavity. The fracture is a high temperature ductile fracture mechanism allowing easy matrix decohesion. It is proposed that the cavities then coalesce and propagate by interdendritic fracture through-liquid-film.

There are some indications of ductile fracture of coherent bridges within the fracture zone. However, it is evident from the results presented in Figure 7-7 that the primary fracture propagation mechanism is inter-dendritic fracture through-liquid-film by dendrite separation. Therefore, the manifestation of these liquid films needs to be assessed in terms of both chemistry and solidification sequence. Thermo-Calc computational thermodynamic analysis (Figure 7-3) has revealed the X65 alloys primary solidification phase is BCC ferrite. This primary solidification phase is favourable because impurity elements found in steel (S and P) have significantly lower solubility in austenite than in ferrite. Consequently, during ferritic solidification these impurities are more readily retained within the bulk. As a result, the time in which the weld stays in its semi-solid and brittle state during solidification is reduced. Despite this favourable solidification sequence, segregation of S and P is still observed in EDX analysis (Figure 7-7c). The analysis clearly shows enrichment of the eutectic phase with solute elements (C, N, Al, Si, P, S, and Cu). To improve cracking resistance within the X65 alloy, it appears that efforts to control segregation would be beneficial. However, reducing the alloying contents would most probably reduce mechanical properties, and as such would be unfeasible.

The model alloy contains considerably fewer micro-alloying elements in comparison to the X65 alloy. The alloy has essentially four chemical components (Fe-C-Mn-Si). The micro-alloying elements are added to the oil and gas alloys to facilitate high strength and toughness properties through phenomenon like solution strengthening, precipitation hardening, and Zener pinning. Evidence (Figure 7-6) has suggested that the second

phase particles are acting as nucleation sites for solidification cracking. It is possible to assume that the model alloy is likely to contain no such second phase particles, due to the lack of alloying additions. The lack of particles which can easily separate from the semi-solid matrix under loading would significantly increase the materials resistance in nucleating solidification cracks.

8. Conclusions and recommendations

8.1. Conclusions

In situ imaging of weld pool evolution and fluid flow

- Flow within molten welds has been characterised at dynamic speeds between 0.3 and 0.52 m/s using synchrotron X-ray radiography for *in situ* imaging.
- The direction of the flow pattern is governed primarily by Marangoni flow and the Marangoni flow is controlled by the surface tension gradient within the weld pool.
- If the surface tension within the weld pool is negative, a flow pattern that promotes wide and shallow weld geometries results from the transport of the warmest liquid weld metal under the welding electrode laterally to the weld toes.
- If the surface tension within the weld pool is positive, a flow pattern that promotes deep and narrow weld geometries results from the transport of the warmest liquid weld metal under the welding electrode vertically downwards stimulating improved penetration.
- The novel *in situ* X-ray radiography approach provides a useful tool to further understand the link between the resultant weld geometry (penetration in particular) from prior fluid flow. The tool can be used to develop welding processes and chemistries of welding consumables to achieve optimised width/penetration characteristics, especially useful for high speed arc welding process used to join subsea sea oil and gas linepipes.

Characterisation of microstructure and mechanical properties of linepipe SAW seam weld

- Through the current study an analytical equation has been derived to establish the relationship between precipitate size and spacing (and indirectly volume fraction) on fracture toughness of the SAW seam weld:

$$K_{Ic} \equiv \sqrt{1.19\sigma_0 d_p \ln(d_p/D_p) E}$$

- The strengthening contribution of coarse Ti (C,N) precipitates was calculated at 32.1 MPa from the Ashby – Orowan equation.
- To improve the yield strength of welds, the average precipitate size shall be reduced while increasing the volume fraction.
- The fracture toughness can be increased by reducing the average precipitate size. To increase K_{Ic} , while reducing the average precipitate size, the volume fraction of particles needs to be reduced.
- For submerged arc welded X65 linepipes, the weld metal is designed to be overmatched with base metal, it is reasonable to suggest that the fracture toughness of welded X65 linepipes can be increased by reducing the Ti content in the filler wire.
- The current study has showed that the maximum value of residual stress found in and near the seam weld of the linepipe was only about 277 MPa (un-expanded pipe in axial direction), approximately 53% of the actual YS of the parent material (516 MPa).
- Once solidified, the mechanical expansion process imparts plastic deformation to the pipe. As a result, the misfit between the weld and its adjacent parent material originally induced by welding is eased. The misfit relaxation results in a significant reduction in tensile residual stresses. The misfit is also reverted, giving rise to favourable compressive residual stress in the weld area after expansion. This can be used to challenge linepipe design over-conservatism and drive efforts to reduce material usage, which will promote cost savings in linepipe manufacturing.

Nucleation of weld solidification cracks

Solidification cracking nucleates/initiates from sub-surface cavities. The cavities are associated with:

i) Residual liquid high in solute and impurity concentration (hot cracks):

- Hot cracks have globular morphologies between 5-40 μm in size.
- They nucleate at grain boundaries where segregated residual liquid is concentrated.
- The hot cracks form after the dendrite to grain transformation when the volume fraction of liquid is <0.1 .
- The residual liquid is enriched in solute elements (Mn, Si, Al) and impurities (S).
- The hot cracks initiate at a specific temperature and strain ($\sim 1433\text{ }^\circ\text{C}$ and $\sim 3.25\%$ in the case on the EN1A alloy presented) around the circumference of the solidifying weld pool, nucleating solidification cracking.

ii) Ti (C,N) precipitated during solidification (that induce ductile microvoids):

- Microvoids were observed on the solidification crack fracture surface of subsea linepipe steel, near the fusion boundary.
- Ti (C,N) precipitates were found within the microvoids, hinting towards their role in nucleating the fracture.
- TiN can precipitate during the latter stage of bulk solidification and trigger coalescence of dendrite trunks. The particles trigger the coalescence of the primary dendrite trunks, but under the tensile loading induced by the test method, the particles provide favourable sites for high temperature ductile fracture to occur. The microvoids are covered with the remaining residual liquid and a solidification crack is nucleated.

Propagation of weld solidification cracks

Two propagation stages are proposed during weld solidification cracking:

Stage 1: Coalescence of cavities or microvoids:

- Evidence suggests that in the early stages of solidification cracking, once initial cavities or microvoids have nucleated, the mechanism for propagation is via cavity or microvoid coalescence.
- It is proposed that the cavities coalesce via the fracture of network separating bridges in the solid skeleton under tensile loading.
- The fracture at this stage is a brittle inter-granular fracture.
- It is hypothesised that the coalescence of the cavities occurs at a rate exceeding solidification and quite quickly the infant cracks propagate into the solidifying dendrite structure where larger volume fraction of liquid exists. At this stage, hot tearing becomes the dominant propagation mechanism.

Stage 2: Hot tearing (bulk propagation mechanism):

- Hot tearing is characterised as the dominant propagation mechanism in all materials tested.
- Hot tears are characterised by inter-dendritic fracture through a liquid film by dendrite separation under tensile strain.
- Hot tearing occurs at higher volume fractions of liquid (>0.1).
- The hot tears were observed to propagate at a rate of between 2.2 – 3.2 mm/s and over a strain range between 4.7 – 7.3 %.

8.2. Recommendations for further work

The scope for continuation of the study on solidification cracking during welding is abundant. The analysis presented in chapter 6 only considers one of the experimental alloys at one testing bending speed. As such, the data is available for the analysis of solidification cracking mechanisms in further steel alloys allowing comparisons to be made between further material types and correlate the effect of Vrestraint bending speed to a greater extent.

The mathematical models used to simulate weldability tests are quite simple in nature and only broadly capture the observed damage development as a precursor to cracking, but further development of these models is required to provide a full description of the development of solidification cracks. These models capture some, but not all, of the physical processes observed experimentally and described above and they do not fully model the shape and micro-distribution of the evolving cavities. Despite this, our preliminary results are encouraging and provide a basis for developing more complete mechanical models of damage and crack development.

To do so, an application has been submitted to the EPSRC funding committee seeking support for the continuation of the research theme. Specifically, **“A novel approach towards understanding the mechanisms of weld solidification cracking using synchrotron X-ray imaging and CT with computational modelling”**.

Appendix

Appendix A – Evaluation of measurement errors in Chapter 4.

In Chapter 4, weld pool fluid flow is measured at maximum velocities of between 0.3-0.52 m/s. The velocity is calculated from manually selecting the location of a tracking particle in consecutive radiographs. It is therefore essential to accurately locate the centroid of the particle to ensure precise results. Similarly, only particles which flow along the extremities of the visible weld pool are considered in the analysis to negate the effects of error arising from viewing a 3D flow in a 2D space, as described in Figure 4-3. Due to the above discussion, the maximum flow velocities reported in the thesis are therefore susceptible to errors in the following forms:

- 1) Inaccurate selection of the centroid of tracking particles.

The first thing to consider is the possibility of particles being blurred or elongated in appearance due to the high flow velocity (~ 0.5 m/s) coupled with the 0.96 ms exposure time. Figure A illustrates the phenomenon in more detail. Figure A(a) illustrates an ideal case whereby the imaging is accomplished using an instantaneous exposure time. Using an instantaneous exposure time, the ~ 50 μm particles would appear identical to their actual size of ~ 50 μm as illustrated in Figure A(a). However, this is an ideal case and not achievable in real terms. Figure A(b) illustrates the effect that the 0.96 ms exposure time, which is used in this research, has upon the accuracy of the tracking particle size, shape and location. A maximum elongation effect of 500 μm is calculated from the product of the maximum measured particle velocity (0.52 m/s) and exposure time (0.96 ms). Given particle size is ~ 50 μm , the 500 μm elongation effect results in an order of magnitude decrease in the accuracy of locating the particle. For the image analysis in this research, the centroid of the resultant “ellipse” described in Figure A(b) is taken as the particle location in each frame. Human error resulting from manually locating the centroid of the ellipse is minimized by zooming to high magnification in the image sequence.

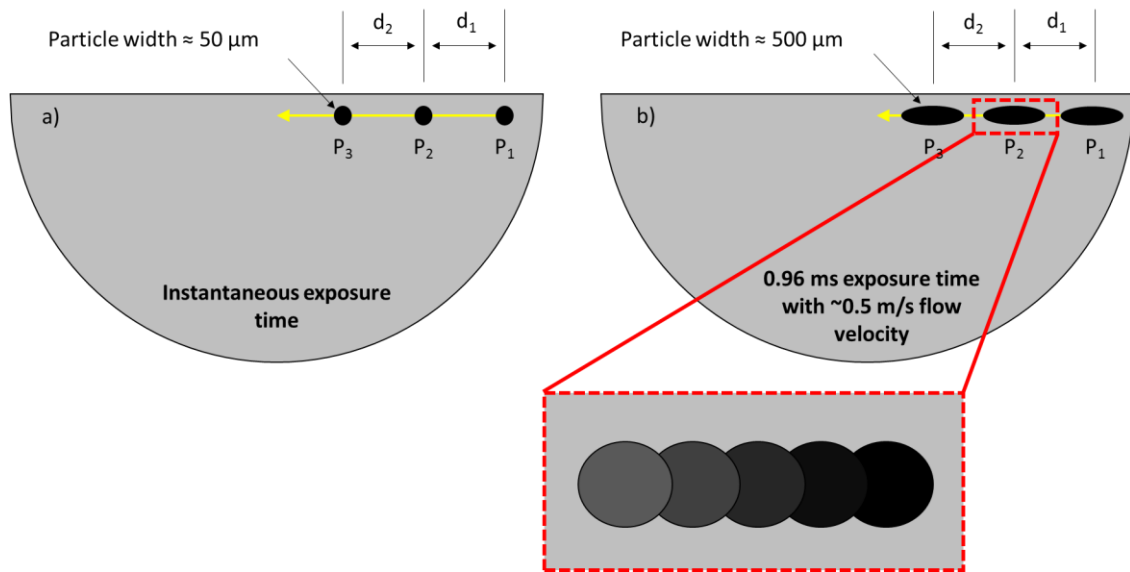


Figure A: Schematic illustration of particle visualisation in *in situ* radiography sequence of weld pool fluid flow under a) idealised conditions with instantaneous exposure time, and b) under actual imaging parameters with a 0.96 ms exposure time highlighting the elongated appearance of the tracking particle.

2) Tracking out-of-plane flow patterns.

The largest possible error in the measurements reported in Chapter 4 results from the possibility of out-of-plane flow patterns being tracked. Figure B illustrates the issue whereby the 2D flow pattern observed in the *in situ* radiography sequence can appear identical for various 3D flow patterns. The maximum measured flow velocity of 0.52 m/s assumes that the tracking particle is moving parallel to the 2D viewing plane. This assumption will give the lowest possible velocity, therefore, it is essential to consider the upper boundary of possible flow velocities.

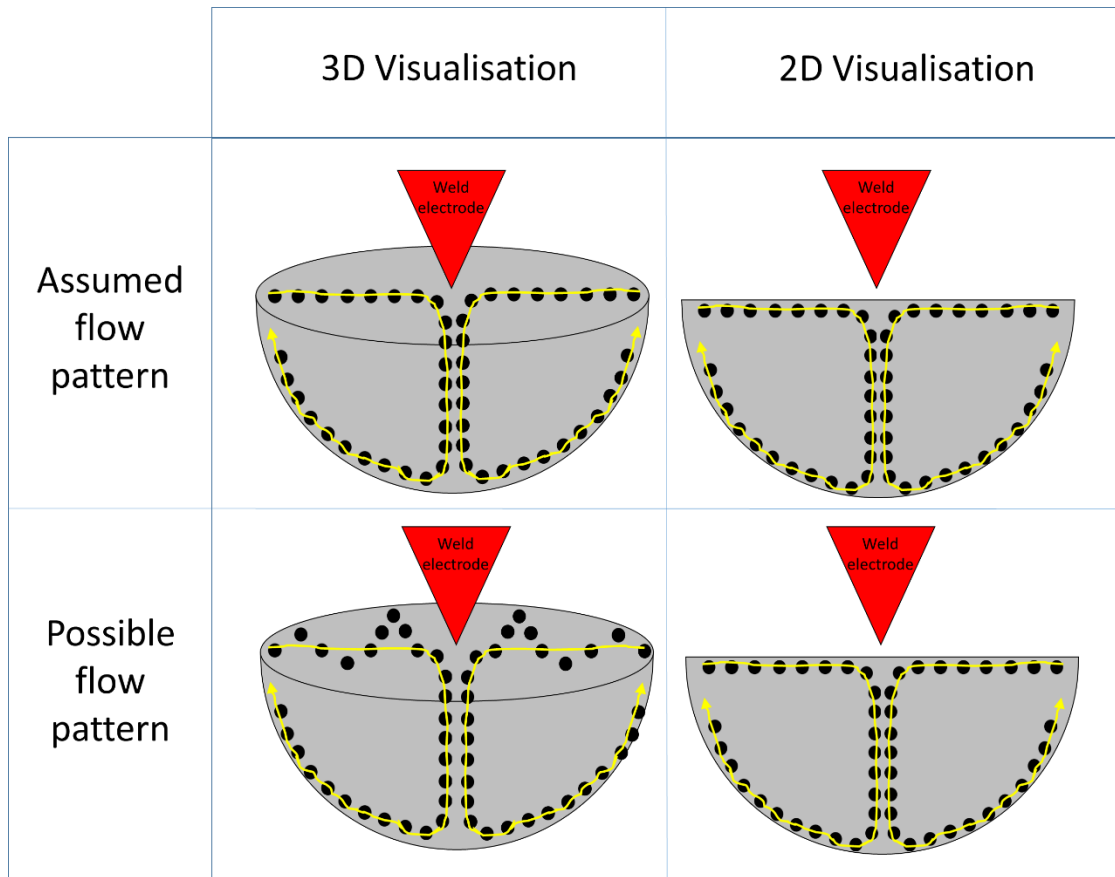


Figure B: Schematic illustration highlighting the assumed and possible flow patterns observed during *in situ* observations of fluid flow. Note that the two flow patterns appear identical in 2D, but may differ significantly in real terms (3D).

Figure C illustrates plan views of the flows described in Figure B. The schematic at the top of Figure C illustrates the idealised flow path that is assumed to calculate the flow velocities reported in the main body of the thesis. However, as described in the previous paragraph, the flow could deviate from this assumed path and would be unnoticeable from the 2D imaging plane used for *in situ* radiography. The lower illustration in Figure C quantifies the largest possible deviation from the assumed flow path. Using the maximum width of the weld pool (~5.85 mm) at the time when the flow is tracked (~2 s), along with the largest measured particle travel distance (0.52 mm) between two consecutive radiographs, it is possible to construct a triangle and solve for the hypotenuse (d_4 in the bottom illustration of Figure C) using Pythagoras theorem, as illustrated in Figure D.

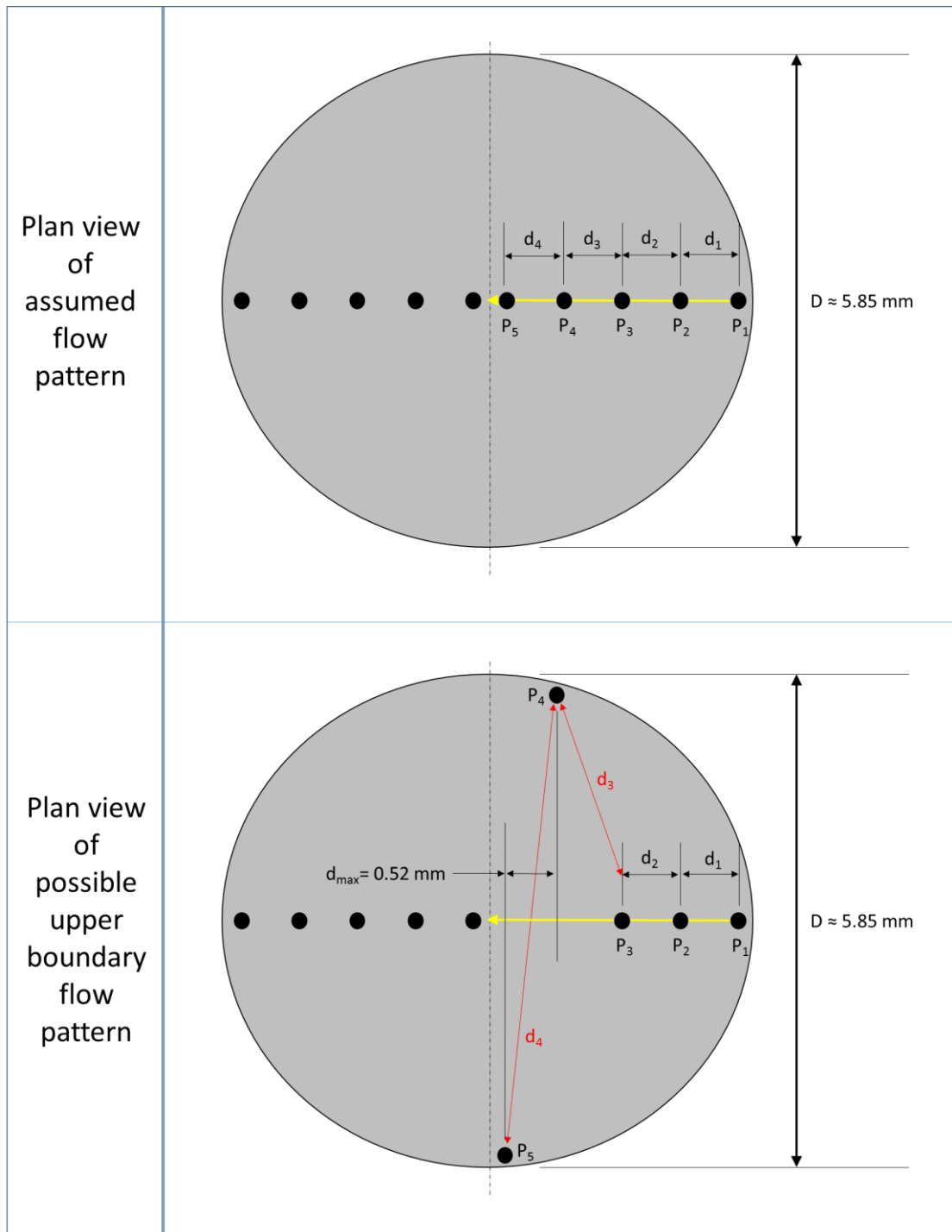


Figure C: Plan view of the flow within the TIG spot weld. The top image illustrates the idealized flow that is assumed in order to measure the lower bound 0.52 m/s flow velocity. The lower image illustrates the longest possible deviation (d_4) from the flow path depicted in the ideal case above between points 4 and 5 close to the weld centre.

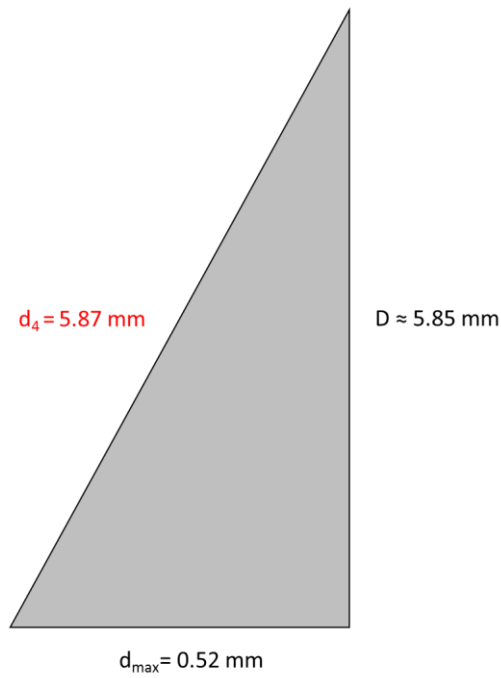


Figure D: Calculation of the upper boundary travel distance possible for tracking particles to have travelled between frames under non-idealised conditions. The upper boundary distance calculated using Pythagoras theorem shows an order of magnitude increase in distance compared with idealised scenario.

Using the calculated upper boundary inter-radiograph particle travel distance of 5.87 mm it is possible to derive an upper boundary flow velocity of 5.87 m/s. As a result, the fluid flow is reported as between 0.52 and 5.87 m/s.

Appendix B – Evaluation of measurement errors in Chapter 5.

In Chapter 5, error bars are included in Figure 5-27 through Figure 5-31 - the plots of residual stress measurement results. To calculate the residual stress error, first, the error in each of the strain component measurements is calculated using:

$$\Delta\varepsilon = \frac{d}{d_0} \sqrt{\left(\frac{\Delta d}{d}\right)^2 + \left(\frac{\Delta d_0}{d_0}\right)^2}$$

Where, d , is the measured lattice parameter in the full sample and d_0 is the measured lattice parameter in the unstressed samples. The equation is implemented for all individual measurement points in the hoop, axial or radial direction.

Using the calculated errors in strain measurements described above, the residual stress error is then calculated in each measurement direction as follows:

$$\Delta\sigma_{axial} = \frac{E}{(1 + \nu)} \sqrt{\left(\frac{\nu}{1 - 2\nu}\right) \Delta\varepsilon_{axial}^2 + \left(\frac{\nu}{1 - 2\nu}\right)^2 (\Delta\varepsilon_{axial}^2 + \Delta\varepsilon_{radial}^2 + \Delta\varepsilon_{hoop}^2)}$$

Appendix C – Evaluation of measurement errors in Chapter 6.

In Chapter 6, fracture propagation speed is measured at 2.2 mm/s in the 2D plane of imaging. However, due to the 3D nature of the cracking, it is important to consider cases where the propagation path is not parallel with the 2D imaging plane. Figure E reveals that propagation path could possibly be at an angle of approximately 38° to the radiography imaging plane. As such, the 2.2 mm/s fracture propagation speed reported will only give a lower boundary estimate of fracture velocity. It is therefore important to evaluate the upper boundary fracture propagation velocity resulting from the 38° propagation path described in Figure E. Using trigonometry, an upper boundary fracture propagation speed is calculated in Figure F as 2.8 mm/s. Therefore, the fracture propagation speed is reported between 2.2-2.8 mm/s.

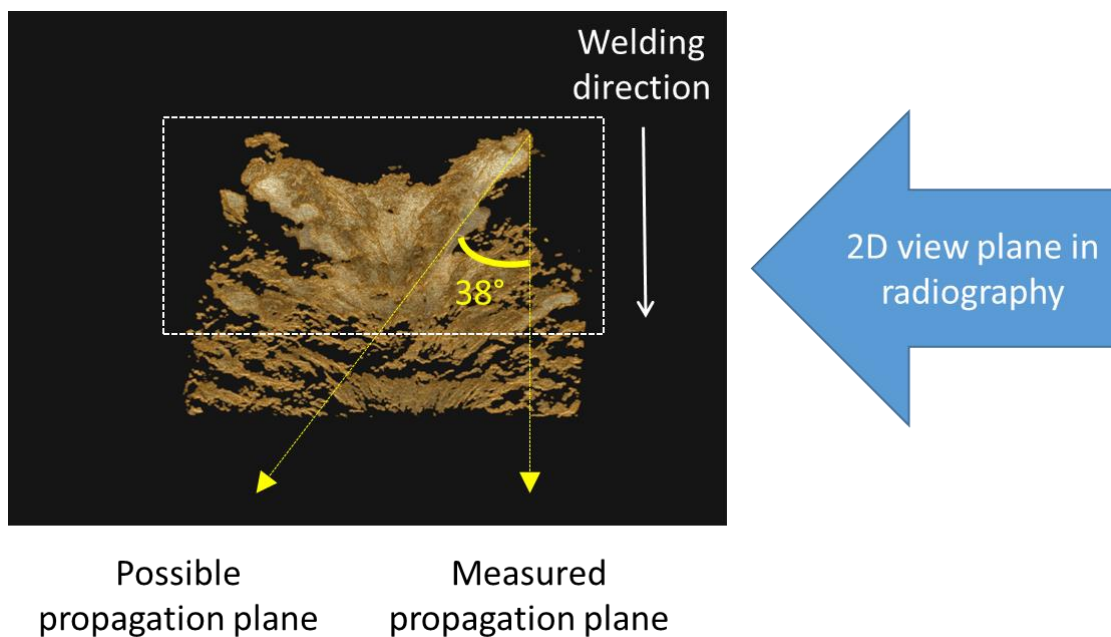


Figure E: Illustration of the possible out-of-plane propagation path for solidification cracking.

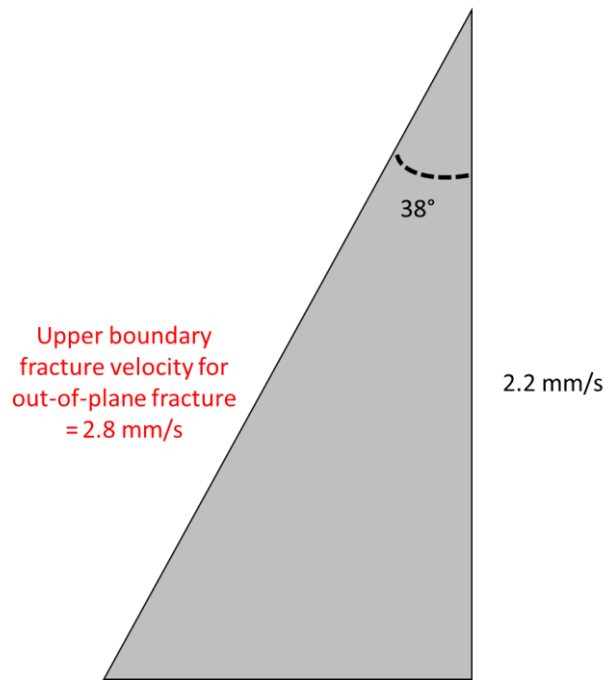


Figure F: Calculation of the upper boundary fracture propagation speed for out-of-plane propagation path. The upper boundary distance calculated using trigonometry shows only a small increase in distance in the 2.2 mm/s observed and quantified during radiography.

References

1. Gray, J. and F. Siciliano, *High strength micro-alloyed linepipe: Half a century of evolution*, Microalloyed Steel Institute: Houston, TX 77056 USA.
2. Barkow, A.G., *Columbium steel in high-pressure line pipe service*, in *Regional Technical Meeting No. 591960*, American Institute of Steel and Iron: Buffalo, N.Y.
3. Carruth, M., *Design Optimization Case Study: Deep Sea Linepipe*, in *WellMet20502011*, University of Cambridge.
4. Shankar, V. and J.H. Devletian, *Solidification cracking in low alloy steel welds*. *Science and Technology of Welding and Joining*, 2005. **10**(2): p. 236-243.
5. Park, S., *A study of hydrogen and solidification cracking in steel weld metal related to solidification behaviour*, 1989, Ohio State University.
6. Davis, J., *Corrosion of weldments*. 2006, Materials Park, OH, USA: ASM International. 227.
7. Herynk, M.D., *Effects of the UOE/UOC pipe manufacturing processes on pipe collapse pressure*. *International Journal of Mechanical Sciences*, 2007. **49**(5): p. 533-553.
8. Engr, M., *Contrasting welding techniques used on pipelines and refinery piping: Uphill versus downhill*. *Pipeline & Gas Journal*, 2012. **239**(1).
9. Europe, T.S., *UOE double submerged arc welded (DSAW pipe)*, 2012.
10. Society, A.W., *AWS A3.0:2001 - Standard Welding Terms and Definitions*. 2001.
11. Anderson, J., *Weldability of precipitation hardening superalloys - Influence of microstructure*, in *Materials Technology Department2011*, Chalmers University of Technology.
12. TWI. *Weld solidification cracking (hot cracking)*. Technical Knowledge 2015; Available from: <http://www.twi-global.com/technical-knowledge/faqs/material-faqs/faq-what-is-hot-cracking-solidification-cracking/>.
13. Kou, S., *Welding metallurgy, second edition*. 2002: Wiley978-0-471-43491-7.
14. Böttger, B., et al., *Relationship between solidification microstructure and hot cracking susceptibility for continuous casting of low-carbon and high-strength low-alloyed steels: A phase-field study*. *Metallurgical and Materials Transactions A*, 2013. **44**(8): p. 3765-3777.
15. Nishimoto, K., et al., *Influence of Minor and Impurity Elements on Hot Cracking Susceptibility of Extra High-Purity Type 310 Stainless Steels*, in *Hot Cracking Phenomena in Welds III*, T. Böllinghaus, J. Lippold, and C.E. Cross, Editors. 2011, Springer Berlin Heidelberg. p. 183-208.
16. Korojy, B., A Fredriksson, *Hot crack formation during peritectic reaction in steels*. *J Ironmaking & steelmaking*, 2010. **37**: p. 63-72.
17. Fredriksson, H., et al., *Theory of hot crack formation*. *Materials Science and Technology*, 2005. **21**(5): p. 521-530.
18. Shankar, V., *Criteria for hot cracking evaluation in austenitic stainless steel welds using longitudinal vareststraint and transvareststraint tests*. *Science and Technology of Welding and Joining*, 2000. **5**(2): p. 91-98.
19. Sistaninia, M., et al., *3-D granular modeling and in situ X-ray tomographic imaging: A comparative study of hot tearing formation and semi-solid deformation in Al-Cu alloys*. *Acta Materialia*, 2013. **61**(10): p. 3831-3841.

20. Eskin, D.G. and L. Katgerman, *A Quest for a New Hot Tearing Criterion*. Metallurgical and Materials Transactions A, 2007. **38**(7): p. 1511-1519.
21. Phillion, A., S.L. Cockcroft, and P.D. Lee, *X-ray micro-tomographic observations of hot tear damage in an Al-Mg commercial alloy*. Scripta Materialia, 2006. **55**(5): p. 489-492.
22. Davidson, C., et al., *Observation of crack initiation during hot tearing*. International Journal of Cast Metals Research, 2006. **19**(1): p. 59-65.
23. Farup, I., J.M. Drezet, and M. Rappaz, *In situ observation of hot tearing formation in succinonitrile-acetone*. Acta Materialia, 2001. **49**(7): p. 1261-1269.
24. Rappaz, M., J.M. Drezet, and M. Gremaud, *A new hot-tearing criterion*. Metallurgical and Materials Transactions A, 1999. **30**(2): p. 449-455.
25. Sigworth, G.K., *Hot tearing of metals*. AFS Trans., 1996. **104**: p. 1053-1062.
26. Guven, Y. and J.D. Hunt, *Hot-tearing in aluminium copper alloys*. Cast Met., 1988. **1**(2): p. 104-111.
27. Aveson, J. *Observation of the initiation and propagation of solidification cracks by means of in situ synchrotron radiography*. in *IOP Conference Series: Materials Science and Engineering*. 2012.
28. Arantes, F. and R.E. Trevisan, *Experimental and theoretical evaluation of solidification cracking in weld metal*. Journal of Achievements in Materials and Manufacturing Engineering, 2007. **20**(1-2).
29. Shankar, V., *Solidification cracking in austenitic stainless steel welds*. Sandhana, 2003. **28**: p. 359-382.
30. Kou, S., *Solidification and liquation cracking issues in welding*. JOM, 2003: p. 37-42.
31. Brooks, J.A. and A.W. Thompson, *Microstructural development and solidification cracking susceptibility of austenitic stainless steel welds*. International Materials Reviews, 1991. **36**(1): p. 16-44.
32. Matsuda, F., H. Nakagawa, and S. Tomita, *Quantitative evaluation of solidification brittleness of weld metal during solidification by in-situ observation and measurement*. Transactions JWRI, 1986. **15**(2).
33. Kujanpaa, V., *Effect of steel type and impurities in solidification cracking of austenitic steel welds*. Metal Construction, 1985. **17**(1): p. 40-46.
34. *The influence of composition on solidification cracking susceptibility in binary alloys*. Br. Found., 1985. **74**: p. 79.
35. Santillana, B., et al., *High-temperature mechanical behavior and fracture analysis of a low-carbon steel related to cracking*. Metallurgical and Materials Transactions A, 2012. **43**(13): p. 5048-5057.
36. Van Haafden, W., W.H. Kool, and L. Katgerman, *Hot tearing studies in AA5182*. Journal of Materials Engineering and Performance, 2002. **11**(5): p. 537-543.
37. Gregson, P. and S. Harris, *Micro-mechanical model of hot tearing at triple junctions in DC casting*, in *Aluminium Alloys 2002 - ICAA8 2002*. p. 179-184.
38. Rappaz, M., et al., *Solidification of aluminum alloys 2005*: TMS, Warrendale, PA. p. 179-90.
39. Campbell, J., *Castings*. 2003: Elsevier Science.
40. Bhadeshia, H., *Steels - microstructure and properties*. Third ed. 2006.
41. El-Danaf, E., et al., *Mechanical, microstructure and texture characterization of API X65 steel*. Materials & Design, 2013. **47**(0): p. 529-538.

42. Lee, S., et al., *Transformation strengthening by thermomechanical treatments in C-Mn-Ni-Nb steels*. Metallurgical and Materials Transactions A, 1995. **26**(5): p. 1093-1100.
43. Becket, F.M. and R. Franks, *U.S. Patent No. 2,158,621*, 1939.
44. Becket, F.M. and R. Franks, *Steel, U.S. Patent No. 2,264,355*. 1941.
45. Peters, P. and J.M. Gray. *Genesis and development of specifications and performance requirements for modern linepipe - Strength, toughness, corrosion resistance and weldability*. in Australian Pipeline Industry Association, Inc. 1992. Hobart-Tasmania, Australia.
46. Gray, J. and P.A. Peters. *Technical demands and specifications for linepipe during the past decades*. in CBMM/TSNIICHERMET Seminar - 25 Years of Cooperation. 2002. Moscow, Russia.
47. Beiser, C.A., *The effect of small columbium additions to semi-killed medium-carbon steels*, in ASM Preprint No. 1381959: Buffalo, NY.
48. DeKazinczy, F., A. Axnas, and P. Pachleitner, *Some properties of niobium treated mild steel*. Jernkontorets, Annglar, 1963. **147**.
49. Morrison, W., *The influence of small niobium additions on the properties of carbon-manganese steels* JISI, 1963. **201**: p. 317.
50. Baird, J. and R.R. Preston, *Relationships between processing structure and properties in low carbon steels* Processing and Properties of Low Carbon Steel. The Metallurgical Society of AIME, 1973.
51. Irani, J., et al., *Beneficial effects of controlled rolling in the process of structural steels "strong tough structural steels"*. ISI Special Publication No. 104, 1967.
52. Cuddy, J. *The effect of microalloy concentration on the recrystallisation of austenite during hot deformation*. in Proc. Thermomechanical Processing of Microalloyed Austenite. 1981. Pittsburgh, PA: AIME.
53. Kozasu, I. *Hot rolling as a high-temperature thermo-mechanical process*. in Microalloying '75 Conference Proceedings. 1975. Washington, DC.
54. Barsanti, L., R. Bruschi, and E. Donati. *From X80 to X100: Know-how reached by ENI Group of High Strength Steel*. in Proc. of Application & Evaluation of High Grade Linepipe in Hostile Environments. 2002. Yokohama.
55. Petersen, C., et al. *Improving long distance gas transmission economics-X120 development overview*. in 4th Int'l Pipeline Technology Conf, Oostend. 2004. Belgium, May 9-13.
56. Papka, S.D., et al., *Full-Size Testing and Analysis of X120 Linepipe*. Oil & Gas J. **102**(8).
57. Asahi, H., et al. *Metallurgical design of high strength steels and development of X120 UOE linepipe*. in 4th Int'l Pipeline Technology Conf 2004. Oostend, Belgium, May 9-13.
58. Ohm, R., J.T. Martin, and K.M. Orzessek. *Characterization of ultra high strength linepipe*, . in Pipeline Technology. 2000. Brugge, Belgium, May.
59. Choi, B., D. Seo, and J. Jang, *A nanoindentation study on the micromechanical characteristics of API X100 pipeline steel*. Metals and Materials International, 2009. **15**(3): p. 373-378.
60. Yoshie, A. and J. Sasaki, *Niobium bearing structural steels*. The Minerals, Metals and Materials Society, 2010: p. 291.
61. Tanaka, Y. in ASME Pressure Vessels and Piping Division Conf. 2005. Denver, Colorado, USA.

62. Kiyoshi, N. and I. Kazutoshi, *Progress in thermomechanical control of steel plates and their commercialization*. Science and Technology of Advanced Materials, 2012. **13**(2): p. 023001.
63. Hall, E.O., *The deformation and ageing of mild steel: III discussion of results*. Proceedings of the Physical Society, 1951 **64**(9): p. 747.
64. Petch, N.J., J. Iron Steel Inst., 1953. **174** p. 25.
65. Hansen, N., *Hall–Petch relation and boundary strengthening*. Scripta Materialia, 2004. **51**(8): p. 801-806.
66. Pickering, F., *Physical metallurgy and the design of steels*. 1978 London: Applied Science Publications Ltd.
67. Manohar, P., M. Ferry, and T. Chandra, *Five decades of the Zener equation*. ISIJ International, 1998. **38**(9): p. 913-924.
68. Smith, C.S., Trans. AIME., 1948. **175**(15).
69. Miodownik, M., *Zener pinning*. Materials: Science and Technology 2001. **2**: p. 9855–9859.
70. Park, G.T., et al., *Effect of microstructure on the hydrogen trapping efficiency and hydrogen induced cracking of linepipe steel*. Corrosion Science, 2008. **50**(7): p. 1865-1871.
71. Liao, C. and J.L. Lee, *Effect of molybdenum on sulfide stress cracking resistance of low-alloy steels*. Corrosion, 1994. **50**(9): p. 695-704.
72. Wang, W., Y. Shan, and K. Yang, *Study of high strength pipeline steels with different microstructures*. Materials Science and Engineering A, 2009. **502**(1-2): p. 38-44.
73. Katsina, I., *Effect of welding thermal cycles on the heat affected zone microstructure and toughness of multi-pass welded pipeline steels*, 2012, Cranfield University.
74. Wang, S.H., et al., Mater. Chem. Phys., 2002. **77**: p. 447.
75. Fragieli, A., R. Schouwenaarf, and R. Guardian, *Microstructural characteristics of different commercially available API 5L X65 steels*. Journal of New Materials for Electrochemical Systems, 2005. **8**: p. 115-119.
76. Ju, J.-B., J.-S. Lee, and J.-i. Jang, *Fracture toughness anisotropy in a API steel line-pipe*. Materials Letters, 2007. **61**(29): p. 5178-5180.
77. Jooa, M., et al., *Role of delamination and crystallography on anisotropy of Charpy toughness in API-X80 steel*. Materials Science and Engineering A 2012. **546**: p. 314-322.
78. Hashemi, S.H., *Strength–hardness statistical correlation in API X65 steel*. Materials Science and Engineering: A, 2011. **528**(3): p. 1648-1655.
79. Easterling, K., *Introduction to the physical metallurgy of welding*. 2nd ed. ed. 1992, Oxford: Butterworth-Heinemann Ltd.
80. Rorvik, G., et al., *High heat input welding of offshore structures — Procedures and weld properties*. Weld J, 1992. **09**: p. 331.
81. Kou, S. and Y. Le, *Three-dimensional heat flow and solidification during the autogenous GTA welding of aluminum plates*. Metallurgical Transactions A, 1983. **14**(11): p. 2245-2253.
82. Rosenthal, D., *Heat distribution during welding and cutting*. Weld J, 1941. **20**.
83. Xie, Y., H.B. Dong, and J.A. Dantzig, *Using the interface Peclet number to select the maximum simulation interface width in phase-field solidification modelling*. Computational Materials Science, 2013. **70**(0): p. 71-76.

84. Mathier, V., *Coalescence of equiaxed grains during solidification*. Modelling and Simulation in Materials Science and Engineering 2004 **12**(3): p. 479.
85. Aucott, L., H. Dong, and S. Wen, *The role of Ti carbonitride precipitates on fusion zone strength-toughness in submerged arc welded linepipe joints*. Materials Science and Engineering: A, 2015. **622**(0): p. 194-203.
86. Aucott, L., S. Wen, and H. Dong, *On the relationship of microstructure, toughness, and hardness properties in a submerged arc welded API-5L grade X65 pipeline steel section*, in *OMAE 2014*: San Fransisco.
87. Aucott, L., et al. *Assessment of the resistance to weld solidification cracking of X65 pipeline steel using a Transvarestraint test*. in *4th International Integrity of High Temperature Welds Conference*. 2012. London.
88. Blodgett, O., *Welding Innovation Quarterly*, 1985. **2**.
89. Tsai, M. and S. Kou, *Marangoni convection in weld pools with a free surface*. International Journal for Numerical Methods in Fluids 1989. . **9**: p. 1503.
90. Szekely, J., *Recent trends in welding science and technology in TWR1990*, ASM International: Materials Park, OH. p. 3–10.
91. Jönsson, P., R.C. Westhoff, and J. Szekely, *Arc characteristics in gas-metal arc welding of aluminum using argon as the shielding gas*. Journal of Applied Physics, 1993. **74**(10): p. 5997-6006.
92. Heiple, C. and J. Roper, *Mechanism for minor element effect on GTA fusion zone geometry*. Weld J, 1982. **61**(4): p. 97s-102s.
93. Zhao, Y. and Y. Lei, *Effects of surface active elements sulfur on flow patterns of welding pool* J. Mater. Sci. Technol. , 2005. **21**(3): p. 408-414.
94. Heiple, C.R., J.R. Roper, and R.T. Stagner, *Surface Active Element Effects on the Shape of GTA, Laser, and Electron Beam Welds*. Welding Journal, 1983: p. 72-77.
95. Kou, S., *Fluid flow and solidification in welding: Three decades of fundametnal research at the University of Wisconsin*. Supplement to the welding journal, 2012: p. 287.
96. Kou, S. and D.K. Sun, *Fluid flow and weld penetration in stationary arc welds*. Metallurgical Transactions A 1985. . **16A**: p. 203.
97. Kou, S. and Y.H. Wang, *Weld pool convection and its effect* Welding Journal 1986. **6**(3): p. 63-s.
98. Kou, S. and Y.H. Wang, *Computer simulation of convection in moving arc weld pools*. Metallurgical Transactions A 1986. **17**(A): p. 2271.
99. Pitscheneder, W., et al., *Role of sulfur and processing variables on the temporal evolution of weld pool geometry during multi-kilowatt laser welding of steels*. . Welding Journal 1996 **75** (3): p. 71-s to 80-s.
100. Hong, K., et al., *Modelling turbulent thermofluid flow in stationary GTA weld pools*. Science and Technology of Welding and Joining, 2002 **7**(3): p. 125-136.
101. Tong, M., et al., *Multiscale, multiphysics numerical modeling of fusion welding with experimental characterization and validation*. JOM, 2013. **65**(1): p. 99-106.
102. Kou, S. and D.K. Sun, *Fluid flow and weld penetration in stationary arc welds*. Metallurgical Transactions A, 1985. **16**(1): p. 203-213.
103. Limmaneevichitr, C. and S. Kou, *Visualization of Marangoni convection in simulated weld pools*. Welding Journal, 2000. **79** p. 126-s.

104. Limmaneevichitr, C. and S. Kou, *Experiments to simulate effect of Marangoni convection on weld pool shape*. Welding Journal, 2000. **79**(8): p. 231-s.
105. Limmaneevichitr, C. and S. Kou, *Visualization of Marangoni convection in simulated weld pools containing a surface-active agent*. Welding Journal 2000. **79**(5): p. 324-s.
106. Zabler, S., et al., *Particle and liquid motion in semi-solid aluminium alloys: A quantitative in situ microradioscopy study*. Acta Materialia, 2013. **61**(4): p. 1244-1253.
107. Dodge, M., *The effect of heat treatment on the embrittlement of dissimilar welded joints*, in *PhD Thesis in the Engineering Department of the University of Leicester* 2014.
108. Keehan, E., *Effect of microstructure on mechanical properties of high strength steel weld metals*, in *Department of Experimental Physics 2004*, Goteborg University.
109. Aronson, A. and W.F. Savage, *Preffered orientation in the weld fusion zone*. Welding Journal, 1966: p. 85.
110. Nakata, K. and F. Matsuda, *Evaluations of ductility characteristics and cracking susceptiblity of Al alloys during welding*. Trans. JWRI, 1995. **24**(1).
111. *Classification of microstructure in low carbon low alloy weld metal*. IIW Doc, 1983.
112. Onsoien, M., Weld J, 1996. **75**.
113. ASM, *Welding Brazing and Soldering*. Vol. 6. 1993.
114. Bhadeshia, H., *Case Study: Weld Microstructures*. Graduate Institute of Ferrous Technology, POSTECH, Korea.
115. Wu, K., *Three-dimensional analysis of acicular ferrite in a low-carbon steel containing titanium*. Scripta Materialia, 2006. **54**(4): p. 569-574.
116. Yamada., *Relation between inclusion surface and acicular ferrite in low carbon low alloy steel weld*. ISIJ International, 2009. **49**(7): p. 1059-1062.
117. Mills, A., G. Thewlis, and J.A. Whiteman, Mater. Sci. Technol., 1987. **3**: p. 1051.
118. Thewlis, G., Mater. Sci. Technol., 1994. **10**: p. 110.
119. Grong, O., et al., Mater. Sci. Technol., 1995. **26A**: p. 525.
120. Koçak, M., *Structural integrity of welded structures: process - property – performance (3P) relationship*, in *63rd Annual Assembly & International Conference of the International Institute of Welding 2010*: Turkey.
121. Andrew, C. and R. King, *Subsea pipeline engineering*. 2008.
122. Xu, G., et al., *The development of Ti-alloyed high strength microalloy steel*. Materials & Design, 2010. **31**(6): p. 2891-2896.
123. Ashby, M.F., *Oxide dispersion strengthening*. 1958: p. 143-205.
124. Orowan, E., *Internal stress in metals and alloys*. 1948.
125. Chen, Z., *Nature of large precipitates in titanium containing HSLA steels*. Materials Science and Technology, 1987. **3**: p. 836-844.
126. Zhuo, X., et al., *Nature of large (Ti, Nb)(C, N) particles precipitated during the solidification of Ti, Nb HSLA steel*. Journal of University of Science and Technology Beijing, Mineral, Metallurgy, Material, 2007. **14**(2): p. 112-117.
127. Yan, W., Y. Shan, and K. Yang, *Effect of TiN inclusions on the impact toughness of low-carbon microalloyed steels*. Metallurgical and Materials Transactions A, 2006. **37**(7): p. 2147-2158.

128. Echeverría, A. and J.M. Rodriguez-Ibabe, *Brittle fracture micromechanisms in bainitic and martensitic microstructures in a C-Mn-B steel*. Scripta Materialia, 1999. **41**(2): p. 131-136.
129. Fairchild, D., D.G. Howden, and W.A.T. Clark, *The mechanism of brittle fracture in a microalloyed steel: Part I. Inclusion-induced cleavage*. Metallurgical and Materials Transactions A, 2000. **31**(3): p. 641-652.
130. Zhang, L., C.L. Davis, and M. Strangwood, *Effect of TiN particles and microstructure on fracture toughness in simulated heat-affected zones of a structural steel*. Metallurgical and Materials Transactions A, 1999. **30**(8): p. 2089-2096.
131. Du, J., M. Strangwood, and C. Davis, *Effect of TiN particles and grain size on the charpy impact transition temperature in steels*. Journal of Materials Science & Technology, 2012. **28**(10): p. 878-888.
132. Chen, J.H., G.Z. Wang, and Q. Wang, *Change of critical events of cleavage fracture with variation of microscopic features of low-alloy steels*. Metallurgical and Materials Transactions A, 2002. **33**(11): p. 3393-3402.
133. Chen, J.H., L. Zhu, and H. Ma, *On the scattering of the local fracture stress σ_f^** . Acta Metallurgica et Materialia, 1990. **38**(12): p. 2527-2535.
134. Chen, J., G.Z. Wang, and Z. Li, *Effects of tensile prestrain on the notch toughness of low-alloy steel*. Metallurgical and Materials Transactions A, 2003. **34**(5): p. 1055-1068.
135. McClintock, F.A., *A criterion for ductile fracture by the growth of holes* Journal of Applied Mechanics 1968. **35** (2): p. 363-371
136. Mackenzie, A.C., J.W. Hancock, and D.K. Brown, *On the influence of state of stress on ductile failure initiation in high strength steels*. Engineering Fracture Mechanics, 1977. **9**(1): p. 167-188.
137. Rice, J. and M.A. Johnson, *The role of large crack tip geometry changes in plane strain fracture*, in *Inelastic Behavior of Solids* M.F. Kanninen, Editor. 1970 p. 641-672.
138. Somekawa, H. and T. Mukai, *Fracture toughness in an extruded ZK60 magnesium alloy*. Materials Transactions, 2006. **47**(4): p. 995 to 998.
139. Ritchie, R., W.L. Server, and R.A. Wullaert, Metallurgical Transactions A 1979 **10**(A): p. 1557–1570.
140. Ritchie, R. and A. Thomson, *On macroscopic and microscopic analyses for crack initiation and crack growth toughness in ductile alloys*. Metallurgical Transactions A, 1985. **16**(A): p. 233-248.
141. Bhole, S., et al., *Effect of nickel and molybdenum additions on weld metal toughness in a submerged arc welded HSLA line-pipe steel*. Journal of Materials Processing Technology, 2006. **173**(1): p. 92-100.
142. Bose-Filho, W., A. Carvalho, and M. Strangwood, *Effects of alloying elements on the microstructure and inclusion formation in HSLA multipass welds*. Materials Characterization, 2007. **58**(1): p. 29-39.
143. Beidokhti, B., A.H. Koukabi, and A. Dolati, *Effect of titanium addition on the microstructure and inclusion formation in submerged arc welded HSLA pipeline steel*. Journal of Materials Processing Technology, 2009. **209**(8): p. 4027-4035.
144. Moeinifar, S., A. Kokabi, and H. Hosseini, *Role of tandem submerged arc welding thermal cycles on properties of the heat affected zone in X80*

- microalloyed pipe line steel*. Journal of Materials Processing Technology, 2011. **211**(3): p. 368-375.
145. Ju, J., W. Kim, and J. Jang, *Variations in DBTT and CTOD within weld heat-affected zone of API X65 pipeline steel*. Materials Science and Engineering: A, 2012. **546**(0): p. 258-262.
 146. Kanazawa, S., et al., *Improved toughness of the weld fusion zone by fine TiN particles and development of a steel for large heat-input welding*. Tetsu-To-Hagane/Journal of the Iron and Steel Institute of Japan, 1975. **61**(11): p. 2589-2603.
 147. Linaza, M., et al., *Cleavage fracture of microalloyed forging steels*. Scripta Metallurgica et Materialia, 1995. **32**(3): p. 395-400.
 148. Linaza, M., et al., *Influence of the microstructure on the fracture toughness and fracture mechanisms of forging steels microalloyed with titanium with ferrite-pearlite structures*. Scripta Metallurgica et Materialia, 1993. **29**(4): p. 451-456.
 149. Deschamps, A. and Y. Brechet, *Influence of predeformation and ageing of an Al-Zn-Mg Alloy-II. Modeling of precipitation kinetics and yield stress* Acta Materialia, 1999. **47** (1): p. 293–305.
 150. Kampmann, R. and R. Wagner, Materials Science and Technology – A Comprehensive Treatment, , 1991. **5**.
 151. Strid, J. and K.E. Easterling, *On the chemistry and stability of complex carbides and nitrides in microalloyed steels*. Acta Metallurgica, 1985. **33**(11): p. 2057-2074.
 152. Suzuki, S., G.C. Weatherly, and D.C. Houghton, *The response of carbo-nitride particles in hsla steels to weld thermal cycles*. Acta Metallurgica, 1987. **35**(2): p. 341-352.
 153. Voorhees, P.W., *The theory of Ostwald ripening*. Journal of Statistical Physics, 1985. **38**(1-2): p. 231-252.
 154. Ostwald, W., Z. Phys. Chem., 1901. **37**: p. 385.
 155. Liu, S. and F.-C. Liao, *Precipitate stability in the heat affected zone of nitrogen-enhanced high strength low alloy steels*. Materials Science and Engineering: A, 1998. **244**(2): p. 273-283.
 156. Perez, M., *Gibbs–Thomson effects in phase transformations*. Scripta Materialia, 2005. **52**(8): p. 709-712.
 157. Lifshitz, I.M. and V.V. Slyozov, *The kinetics of precipitation from supersaturated solid solutions*. Journal of Physics and Chemistry of Solids, 1961. **19**(1–2): p. 35-50.
 158. Rossini, N.S., et al., *Methods of measuring residual stresses in components*. Materials & Design, 2012. **35**(0): p. 572-588.
 159. Macherauch, E. and K.H. Kloos, *Origin, measurement and evaluation of residual stresses*. Residual Stresses in Science and Technology, 1987: p. 3-26.
 160. Trufyakov, V., P. Mikheev, and Y. Kudryavtsev, *Fatigue strength of welded structures*. Harwood Academic, London, 1999.
 161. Park, M.J., et al., *Residual stress measurement on welded specimen by neutron diffraction*. Journal of Materials Processing Technology, 2004. **155–156**(0): p. 1171-1177.
 162. Wen, S., et al. *Neutron diffraction measurement of weld residual stresses in an uoe linepipe subjected to mechanical expansion*. in *Proceedings of the ASME 2013 32nd International Conference on Ocean, Offshore and Arctic Engineering, OMAE2013*,. 2013. June 9-14, 2013, Nantes, France.

163. Totten, G., *Handbook on residual stress* 2005. **1**.
164. Cosham, A. *ECAs: Are they fit-for-purpose?* . in *OPT* 2008. Amsterdam, the Netherlands.
165. Institute, B.S., *BS 7910: Guide on methods for assessing the acceptability of flaws in metallic structures*, , 2005.
166. Connelly, M., *Why over-conservatism in linepipe specifications should be challenged*. Pipeline & Gas Journal 2010. **237**(5).
167. Withers, P., *Residual stress and its role in failure*. Reports on Progress in Physics, 2007 **70**: p. 2211–2264.
168. James, M. *Residual stress influences in mechanical engineering*. in *Proceedings of the XVIII Congreso Nacional de Ingeniería Mecánica*. 2010. Ciudad Real.
169. Prime, M. and A. Gonzales. in *Proceedings of the sixth international conference on residual stresses*. . 2000. Oxford, UK IOM Communications Ltd.
170. Bueckner, H.F., *The propagation of cracks and the energy of elastic deformation*. Trans ASME, 1958. **80**: p. 1225–1230.
171. Ju, J.-B., et al., *Determination of welding residual stress distribution in API X65 pipeline using a modified magnetic Barkhausen noise method*. International Journal of Pressure Vessels and Piping, 2003. **80**(9): p. 641-646.
172. Gou, R., et al., *Residual stress measurement of new and in-service X70 pipelines by X-ray diffraction method*. NDT & E International, 2011. **44**(5): p. 387-393.
173. Hutchings, M., *Introduction to the characterisation of residual stress by neutron diffraction*. 2005.
174. Website, R.S.o.C.; Available from: <http://www.rsc.org/Education/EiC/issues/2011November/ResearchIsis.asp>.
175. Fitzpatrick, M. and A. Lodini, *Analysis of residual stress by diffraction using neutron and synchrotron radiation*. 2003, London: Taylor and Francis.
176. Santisteban, J., et al., *ENGIN-X: a third-generation neutron strain scanner*. Journal of Applied Crystallography, 2006. **39**: p. 812-825.
177. Bragg, W., *The diffraction of short electromagnetic waves by a crystal*. Proc. Cambridge Phil. Soc., 1913. **17**: p. 43-57.
178. Withers, P., *Depth capabilities of neutron and synchrotron diffraction strain measurement instruments. I. The maximum feasible path length*. J. Appl. Cryst. (2004. **37**: p. 596-606.
179. Law, M., et al., *Neutron residual stress measurements in linepipe*. Physica B: Condensed Matter, 2006. **385–386**, Part 2(0): p. 900-903.
180. Clapham, L., et al., *Characterization of texture and residual stress in a section of 610 mm pipeline steel*. NDT & E International, 1995. **28**(2): p. 73-82.
181. Wen, S., S. Church, and S. Parker. *Finite element modelling of weld residual stress, distortion and HAZ microstructure*, . in *Proceedings of 14th International Conference on Computer Technology in Welding and Manufacturing*, . 2004. Sheffield Hallam University, UK. .
182. Wen, S., P. Hilton, and D.C.J. Farrugia. *Finite element modelling of a submerged arc welding process*. in *Proceedings of the International Conference on Advances in Materials and Processing Technologies, AMPT'99 and 16th Annual Conference of the Irish Manufacturing Committee, IMC16*. 1999. Dublin, Ireland,.
183. Wen, S., P. Summerfield, and P. Hilton. *Modelling of UOE pipe forming for enhanced collapse resistance*. in *Presented at OPT (Offshore Pipeline Technology)* 2003. Amsterdam.

184. Slater, S., et al. *Manufacturing the thickest UOE 18" linepipe*. in *OPT 2010*. Amsterdam.
185. Wen, S. and M. Connelly. *Finite element analysis of weld residual stress in an UOE linepipe subjected to mechanical expansion*, . in *10th International Seminar on Numerical Analysis of Weldability*, . 2012. Graz, Austria.
186. Woo, W., et al., *Neutron diffraction measurements of residual stresses in friction stir welding: a review*. *Science and Technology of Welding and Joining*, , 2011. **16**(1): p. 23-32.
187. Zhang, W., Z. Feng, and P. Crooker, *Improved procedure for computing residual stresses from neutron diffraction data and its application to multipass dissimilar welds*. *Science and Technology of Welding and Joining*, 2011. **16**(3): p. 254-260.
188. Neeraj, T., et al., *Residual stresses in girth welds of carbon steel pipes: neutron diffraction analysis*. *Science and Technology of Welding and Joining*, , 2011. **16**(3): p. 249-253.
189. Lawa, M., et al., *Residual stress measurements in coil, linepipe and girth welded pipe*. *Materials Science and Engineering A*, 2006. **437**: p. 60-63.
190. Eskin, D., Suyitno, and L. Katgerman, *Mechanical properties in the semi-solid state and hot tearing of aluminium alloys*. *Progress in Materials Science*, 2004. **49**(5): p. 629-711.
191. Dantzig, J. and M. Rappaz, *Solidification*. 2009: Taylor & Francis Group.
192. Medovar, I., *On the nature of weld hot cracking*. *Avtomatich.* , 1954 **7**: p. 12–28.
193. Feurer, U., *Mathematical model by the hot cracking tendency of binary aluminum alloys*. *Giessereiforschung*, 1976. **28**(2): p. 75-80.
194. Rogberg, B., *Investigation on the hot ductility of steels by performing tensile tests on "in situ solidified" samples*. *Scandinavian Journal of Metallurgy*, 1983. **12**(2): p. 51-66.
195. Borland, J.C., *Generalized theory of super-solidus cracking in welds (and castings)*. *British Welding Journal*, 1960. **7**: p. 508-512.
196. Pellini, W.S., *Strain theory of hot tearing*. *Foundry*, 1952. **80**: p. 125.
197. Humphrey, W.I., *A consideration of the nature of brittleness at temperatures above the solidus in castings and welds in aluminum alloys*. *J. Inst. Metals*, 1948. **75**: p. 235.
198. Lees, D., *The hot tearing tendencies of aluminium casting alloys*. *J. Inst. Met.*, 1946. **72**: p. 343-364.
199. Lundin, *Varestraint test rig patent*. 1966.
200. Lee, H., *Effect of boron contents on weldability in high strength steel*. *Journal of Mechanical Science and Technology*, 2007. **21**: p. 771-777.
201. Wei, Y., et al., *Modeling the Trans-Varestraint test with finite element method*. *Computational Materials Science*, 2006. **35**(2): p. 84-91.
202. Finton, T., *Standardization of the Transvarestraint test*, 2003, The Ohio State University.
203. Lippold, J., *Recent developments in weldability testing for advanced materials*. *Joining of Advanced and Specialty Materials VII*, 2005. **7**.
204. Savage, W.F. and C.D. Lundin., *The Varestraint Test*. *Welding Journal*, 1966. **44**: p. 433s-442s.
205. Dupont, J. and J. Lippold, *Welding metallurgy and weldability of nickel-base alloys*. 2009: Wiley.

206. Scotti, A., *Performance assessment of the (Trans) Varestraint test for determining solidification cracking susceptibility when using welding processes with filler metal*. Institute of Physics Publishing, Measurement Science and Technology, 2004: p. 2215 – 2222.
207. Lundin, C. and A. Lingenfelter, *The Varestraint test*. Welding Research Bulletin, 1982. **280**: p. 1-19.
208. Novikov, I. and F.S. Novik, *Doklady Akademii Nauk SSSR*, 1963. **7**.
209. Prokhorov, N.N., *Resistance to hot tearing of cast metals during solidification*. Russian Castings Production, 1962. **2**(2): p. 172-175.
210. Clyne, T. and G.J. Davies, *Quantitative solidification cracking test for castings and an evaluation of cracking in aluminium-magnesium alloys*. Br Foundryman, 1975. **68**(pt 9): p. 238-244.
211. Williams, J. and A.R.E. Singer, *Deformation, strength, and fracture above the solidus temperature*. J. Inst. Met., 1968. **96**: p. 5-12.
212. Clyne, T. and G.J. Davies, *Comparison between experimental data and theoretical predictions relating to dependence of solidification cracking on composition*. Solidification and Casting of Metals, 1979: p. 275-278.
213. Katgerman, L., *Mathematical model for hot cracking of aluminum alloys during DC casting*. Journal of Metals, 1982. **34**(2): p. 46-49.
214. Drezet, J. and M. Rappaz. *Prediction of hot tears in DC-cast aluminum billets*. in *Light Metals: Proceedings of Sessions, TMS Annual Meeting (Warrendale, Pennsylvania)*. 2001.
215. Li, L., *The effects of P and sulfur on susceptibility to weld hot cracking in austenitic stainless steels*. Weld J, 1999. **78**(12): p. 387-396.
216. Lee, C., *Effect of minor elements on hot cracking susceptibility of austenitic stainless steel welds*. Metals and Materials, 1996. **2**(2): p. 81-91.
217. Hannu Hänninen, A.B., Tapio Saukkonen, et al, *Environment-assisted cracking and hot cracking susceptibility of nickel-base alloy weld metal*, 2011, VTT Tiedotteita.
218. Steiner Petrovič, D., et al., *Differential scanning calorimetry study of the solidification sequence of austenitic stainless steel*. Journal of Thermal Analysis and Calorimetry, 2011. **105**(1): p. 251-257.
219. Company, M.E.P., *Principles and Technology of the Fusion Welding of Metals*. 1979.
220. Borland, J. and R. Younger, Br. Weld. J., 1960. **7**: p. 22–60.
221. Kihara, H. and F. Matsuda, Trans JWRI, 1970. **2**(2): p. 103-114.
222. Masumoto, I., *Solidification, blowhole formation and cracking of steel weld metal*. Welding in the World, Le Soudage Dans Le Monde, 1993. **31**(3): p. 211-221.
223. Kim, J., K.T. Rie, and J. Ruge, Steel Res, 1985. **56**(12): p. 639-644.
224. Ohshita, S., et al., Weld. J., 1983. **62**(5): p. 129-s-136-s.
225. Hirabayashi, K., et al., Proc. Fourth Int. Symp, 1982: p. 383-388.
226. Nassar, H., B. Korojy, and H. Fredriksson, *A study of shell growth irregularities in continuously cast 310S stainless steel*. Ironmaking & Steelmaking, 2009. **36**(7): p. 521-528.
227. Nakata, *Evaluations of ductility characteristics and cracking susceptability of Al alloys during welding*. JWRI, 1995. **24**(1): p. 83-94.
228. Shankar, V. and J.H. Devletian, *Solidification cracking in low alloy steel welds*. Science and Technology of Welding and Joining, 2004. **10**(2): p. 236-243.

229. Lippold, J. and W. Lin, *Weldability of commercial Al-Cu-Li alloys*. Aluminium Alloys - Their Physical and Mechanical Properties, 1996: p. 1685-1690.
230. Diamond. *How diamond works*. 2015; Available from: <http://www.diamond.ac.uk/Home/About/How-Diamond-Works.html>.
231. Röntgen, W.C., *Über eine neue Art von Strahlen*, in: . Secretary of the Physical-Medical Society, , 1895.
232. Cormack, A.M., *Representation of a function by its line integrals, with some radiological applications*. Journal of Applied Physics, 1963. **34**(9): p. 2722-2727.
233. Hounsfield, G.N., *Computerized transverse axial scanning (tomography): I. Description of system*. British Journal of Radiology, 1973. **46**(552): p. 1016-1022.
234. Reimers, P. and J. Goebbels, *New possibilities of nondestructive evaluation by X-ray computed tomography*. Mater. Eval., 1983. **41**(6): p. 732-737.
235. Flannery, B., et al., *Three-dimensional x-ray microtomography*. Science, 1987. **237**(4821): p. 1439-1444.
236. Bonse, U. and F. Busch, *X-ray computed microtomography (μ CT) using synchrotron radiation (SR)*. Progress in Biophysics and Molecular Biology, 1996. **65**(1-2): p. 133-169.
237. Koch, A., et al., *X-ray imaging with submicrometer resolution employing transparent luminescent screens*. Journal of the Optical Society of America A: Optics and Image Science, and Vision, 1998. **15**(7): p. 1940-1951.
238. Phillion, A., et al., *Quantitative assessment of deformation-induced damage in a semisolid aluminum alloy via X-ray microtomography*. Metallurgical and Materials Transactions A, 2008. **39**(10): p. 2459-2469.
239. Phillion, A.B., S.L. Cockcroft, and P.D. Lee, *A new methodology for measurement of semi-solid constitutive behavior and its application to examination of as-cast porosity and hot tearing in aluminum alloys*. Materials Science and Engineering: A, 2008. **491**(1-2): p. 237-247.
240. Phillion, A.B., et al., *In situ X-ray observation of semi-solid deformation and failure in Al-Cu alloys*. Acta Materialia, 2011. **59**(4): p. 1436-1444.
241. Gourlay, C.M., et al., *Granular deformation mechanisms in semi-solid alloys*. Acta Materialia, 2011. **59**(12): p. 4933-4943.
242. Vernède, S., J.A. Dantzig, and M. Rappaz, *A mesoscale granular model for the mechanical behavior of alloys during solidification*. Acta Materialia, 2009. **57**(5): p. 1554-1569.
243. Vernède, S. and M. Rappaz, *A simple and efficient model for mesoscale solidification simulation of globular grain structures*. Acta Materialia, 2007. **55**(5): p. 1703-1710.
244. Vernède, S., P. Jarry, and M. Rappaz, *A granular model of equiaxed mushy zones: Formation of a coherent solid and localization of feeding*. Acta Materialia, 2006. **54**(15): p. 4023-4034.
245. Sistaninia, M., et al., *A 3-D coupled hydromechanical granular model for simulating the constitutive behavior of metallic alloys during solidification*. Acta Materialia, 2012. **60**(19): p. 6793-6803.
246. Puncreobutr, C., et al., *Influence of Fe-rich intermetallics on solidification defects in Al-Si-Cu alloys*. Acta Materialia, 2014. **68**(0): p. 42-51.

247. Puncreobutr, C., et al., *In situ quantification of the nucleation and growth of Fe-rich intermetallics during Al alloy solidification*. Acta Materialia, 2014. **79**(0): p. 292-303.
248. Puncreobutr, C., et al., *Coupling in situ synchrotron X-ray tomographic microscopy and numerical simulation to quantify the influence of intermetallic formation on permeability in aluminium–silicon–copper alloys*. Acta Materialia, 2014. **64**(0): p. 316-325.
249. Shirali, A. and K. Mills, *The effect of welding parameters on penetration in GTA welds*. Weld J, 1993. **07**.
250. Tszin, V. and A. Karasev, *Surface tension of iron-manganese and iron-sulfur melts*. Russian Metallurgy and Fuels, 1960. **2**: p. 33-34.
251. Gupt, K. and V. Yavoiski, *Study of the effect of concentration and temperature on surface tension of Fe-O-S system*. Trans. Indian Inst. Metals, 1976. **29**(4): p. 286-291.
252. Halden, F. and W. Kingery, *Surface tension at elevated temperatures: Effect of C, N, O and S on liquid iron surface tension*. J. Phys. Chem., 1955. **59**: p. 557-559.
253. Gogiberzide, M., *Effects of oxygen and sulfur on the surface tension of ShKh steel*. Bulletin of the Academy of Sciences of the Georgian SSR, 1968.
254. Kidess, A., et al., *An integrated model for the post-solidification shape and grain morphology of fusion welds*. International Journal of Heat and Mass Transfer, 2015. **85**(0): p. 667-678.
255. Heiple, C. and R. Roper, *Effects of minor elements on GTAW fusion zone shape, in Trends in welding research in the United States*. 1982, Am. Soc. for Metals.: Metals Park, Ohio. p. 489-520.
256. Brimacombe, K. and F. Weinberg, *Observations of surface movements of liquid copper and tin*. Metall. Trans., 1972. **3**: p. 2298-2299.
257. Campbell, J., *Invisible Macrodefects in Castings*. Journal de Physique IV, 1993. **3**: p. 861-887.
258. Cambridge, U. *Dissemination of IT for the Promotion of Materials Science - Microscopy (DoITPoMS)*. Available from: <http://www.doitpoms.ac.uk/tlplib/optical-microscopy/printall.php>.
259. Goldstein, J., *Scanning electron microscopy and X-ray microanalysis: Third edition*. 2003: Springer US.
260. Zworykin, V.K. and J. Hiller, ASTM Bull., 1942. **117**.
261. Lozano-Perez, S., et al. *Preparation of TEM specimens containing stress corrosion cracks in austenitic alloys using FIB*. in *Electron Microscopy and Analysis 2001. Proceedings, 5-7 Sept. 2001*. 2001. Bristol, UK: IOP Publishing.
262. Huang, Y.Z., et al., *Preparation of transmission electron microscopy cross-section specimens of crack tips using focused ion beam milling*. Journal of Microscopy, 2002. **207**: p. 129-36.
263. Smith, R.L. and G.E. Sandland, *An Accurate Method of Determining the Hardness of Metals, with Particular Reference to Those of a High Degree of Hardness* Proceedings of the Institution of Mechanical Engineers, 1922. **1**: p. 623–641.
264. Siewert, T., et al., *Pendulum impact testing: A century of progress*. ASTM STP 1380. ASTM, 1999.
265. Williams, M.L. and G.A. Ellinger, *Investigation of fractured steel plates removed from welded ships*. . National Bureau of Standards Rep., 1948

266. API, *API 5L*, in *Specifications for linepipe* 2004.
267. Smallman, R.E., *Physical Metallurgy and Advanced Materials Engineering* Vol. 7. 2007, Elsevier Ltd.
268. Dub, A. and V. Volkov, *Russian Metallurgy*, 2007: p. 585-590.
269. Peng, C. and P. Wu, *Inclusion characterization in high strength low alloy steel*, in *Materials Science and Engineering* 2009, University of Toronto.
270. Yoo, O., et al., *The effect of the carbon and nitrogen contents on the fracture toughness of Type 347 austenitic stainless steels*. *Materials Science and Engineering A*, 2005. **405**(1-2): p. 147-157.
271. Yoo, O., et al., *The effect of the carbon and nitrogen contents on the fracture toughness of Type 347 austenitic stainless steels*. *Materials Science and Engineering: A*, 2005. **405**(1-2): p. 147-157.
272. Capelle, J., et al., *Design based on ductile–brittle transition temperature for API 5L X65 steel used for dense CO₂ transport*. *Engineering Fracture Mechanics*, 2013. **110**(0): p. 270-280.
273. Gondoh, H., *Nippon Steel Tech. Rep.*, 1979. **14**: p. 55-65.
274. Porter, D. and K. Eastering, *Phase transformations in metals and alloys*. Second Edition ed. 1992.
275. Van Zwieten, A. and J.H. Bulloch, *The influence of interstitial solute level on the Charpy toughness properties of a 40% Cr-Fe stainless steel*. *International Journal of Pressure Vessels and Piping*, 1993. **56**(1): p. 69-91.
276. Shin, S.Y., et al., *Correlation of microstructure and charpy impact properties in API X70 and X80 line-pipe steels*. *Materials Science and Engineering: A*, 2007. **458**(1-2): p. 281-289.
277. Hashemi, S. and D. Mohammadyani, *Characterisation of weldment hardness, impact energy and microstructure in API X65 steel*. *International Journal of Pressure Vessels and Piping*, 2012. **98**(0): p. 8-15.
278. Yan, W., Y. Shan, and K. Yang, *Influence of TiN inclusions on the cleavage fracture behavior of low-carbon microalloyed steels*. *Metallurgical and Materials Transactions A*, 2007. **38**(6): p. 1211-1222.
279. Yu, H., et al., *Precipitation behaviors of X70 acicular ferrite pipeline steel*. *J. Univ. Sci. Technol. Beijing*, , 2006 **13**.
280. Zhou, M. and Y. Hao, *Effects of precipitates and inclusions on the fracture toughness of hot rolling X70 pipeline steel plates*. *International Journal of Minerals, Metallurgy and Materials*, 2012. **19**(9).
281. Thompson, A., *The relation between changes in ductility and in ductile fracture topography: Control by microvoid nucleation*. *Acta Metallurgica*, 1983. **31**(10): p. 1517-1523.
282. McClintock, F.A., *Physics of Strength and Plasticity*, 1969: p. 307-326.
283. Rice, J. and T. D.M., *J. Mech. Phys. Solids.*, 1969. **17**: p. 201-217.
284. Johnson, M., L. Edwards, and P.J. Withers, *ENGIN — A new instrument for engineers*. *Physica B: Condensed Matter*, 1997. **234–236**(0): p. 1141-1143.
285. Daymond, M., *The determination of a continuum mechanics equivalent elastic strain from the analysis of multiple diffraction peaks*. *J. Appl. Phys.* , 2004. **96**(8): p. 4263-4272.
286. Johnson, M. and M.R. Daymond, *An optimum design for a time-of-flight neutron diffractometer for measuring engineering stresses*. *J. Appl. Cryst.* , 2002. **35**(1): p. 49-57.

287. James, J., et al., *A virtual laboratory for neutron and synchrotron strain scanning*. Physica B: Condensed Matter, 2004. **350**(1–3, Supplement): p. E743-E746.
288. Von Dreele, R., J.D. Jorgensen, and C.G. Windsor, J. Appl. Cryst. , 1982. **15**: p. 581–589.
289. Pawley, G.S., J. Appl. Cryst. , 1981. **14**: p. 357–361.
290. Dong, P., *Residual stress and distortion in welded structures: a perspective for engineering applications*. Science and Technology of Welding and Joining, 2005. **10**(4): p. 389 – 398.
291. Institute, B.S., *BS 7910: Guide to methods for assessing the acceptability of flaws in metallic structures*, 2005.
292. Kaufman, L., *The lattice stability of metals-I. Titanium and zirconium*. Acta Metallurgica, 1959. **7**(8): p. 575-587.
293. Hillert, M., T. Wada, and H. Wada, J. Iron Steel Inst., 1967. **205** p. 539–546.
294. Andersson, J.O., et al., *Thermo-Calc & DICTRA, computational tools for materials science*. Calphad: Computer Coupling of Phase Diagrams and Thermochemistry, 2002. **26**(2): p. 273-312.
295. Davies, R., et al., *MTDATA - Thermodynamic and phase equilibrium software from the national physical laboratory*. Calphad: Computer Coupling of Phase Diagrams and Thermochemistry, 2002. **26**(2): p. 229-271.
296. Chen, S.L., et al., *The PANDAT software package and its applications*. Calphad: Computer Coupling of Phase Diagrams and Thermochemistry, 2002. **26**(2): p. 175-188.
297. Bale, C.W., et al., *FactSage thermochemical software and databases*. Calphad: Computer Coupling of Phase Diagrams and Thermochemistry, 2002. **26**(2): p. 189-228.
298. Saunders, N. and A.P. Miodownik, *Calphad (A comprehensive guide)*. 1998, Oxford Pergamon Press.
299. Gulliver, G.H., J. Inst. Met. , 1913 **9** (120).
300. Scheil, E., Z. Metallkd. , 1942. **34** (70).
301. Nippes, E.F. and W.F. Savage, *Development of specimen simulating weld heat-affected zones*. Welding Journal, 1949. **28**: p. 534-546.
302. Won, Y., et al., *A new criterion for internal crack formation in continuously cast steels*. Metallurgical and Materials Transactions B, 2000. **31**(4): p. 779-794.
303. Weitkamp, T., et al., *Status and evolution of the ESRF beamline ID19*. AIP Conf. Proc. (ICXOM20), 2010. **1221**: p. 35-38.
304. Cloetens, P., et al., *Phase objects in synchrotron radiation hard X-ray imaging* J. phys. D: Appl. phys., 1996. **29**(1): p. 133-146.
305. Bigelow, L.K. and M.C. Flemings, *Sulfide inclusions in steel*. Metallurgical Transactions B, 1975. **6**(2): p. 275-283.
306. Piwonka, T. and M.C. Flemings, Trans. TMS-AIME, 1966. **236**: p. 1157–65.
307. Hirth, J.P. and M. Cohen, *Authors' reply*. Metallurgical Transactions, 1970. **1**(7): p. 2026-2026.